Interfaces in motion in elementary liquid foams

Théo Lenavetier

Université de Rennes

THESE DE DOCTORAT DE

L'UNIVERSITE DE RENNES

ECOLE DOCTORALE N° 638
Science de la Matière, des Molécules et Matériaux
Spécialité : *Physique*

Par
Théo LENAVETIER

Mouvements aux interfaces de mousses liquides élémentaires

Traduit de l'anglais : Interfaces in motion in elementary liquid foams

Thèse présentée et soutenue à Rennes, le 13 décembre 2023
Unité de recherche : Institut de Physique de Rennes – UMR 6251

Rapporteurs avant soutenance :

Christophe YBERT Directeur de Recherche, CNRS, iLM
Jacco SNOEIJER Professeur, Université de Twente

Composition du Jury :

Président : Elisabeth CHARLAIX Professeur des universités, Université Grenoble Alpes, LiPhy

Examinateurs : Elise LORENCEAU Directrice de Recherche, CNRS, LiPhy
Thomas SALEZ Chargé de Recherche, CNRS, LOMA
Christophe YBERT Directeur de Recherche, CNRS, iLM
Jacco SNOEIJER Professeur, Université de Twente

Dir. de thèse : Isabelle CANTAT Professeur des universités, Université de Rennes, IPR

Ah! Mais ch'est èn Anguiais enco en pu c't'affaire?

(Normand du centre Manche)
Marie-Thérèse Gouesmel, ma grand-mère, en
découvrant la langue de ce manuscrit.

Remerciements

J'ai tricoté tous ces paragraphes de "Mercis" petit à petit, le long de l'écriture de ce manuscrit et jusqu'à quelques temps après ma soutenance. Cette période intense aura été ponctuée de moments de gratitude dont ces (longs) remerciements sont le fruit. Ma thèse représente pour moi la fin d'un parcours scolaire puis universitaire le long duquel j'ai pu faire de nombreuses rencontres, sans lesquelles il aurait été bien différent. Pour cette raison et parce que je m'y suis plu, je voudrais remercier pour cela les personnes qui m'ont permis de le réaliser.

Je remercie tout d'abord le jury de cette thèse, pour leur temps, leur intérêt pour ces travaux, et leurs lectures de mon manuscrit. Merci à Christophe Ybert et Jacco Snoeijer, les rapporteurs, pour leurs remarques qui ont mené à des discussions très riches, en amont, pendant la soutenance, et à continuer après. Mon travail et ma réflexion sur les systèmes physiques de ma thèse en sortent grandis. Merci à Thomas Salez et Elise Lorenceau, examinateurs, et Elisabeth Charlaix, présidente du jury, pour la séance de questions qui allaient de la physico-chimie utilisée/à essayer aux ingrédients physiques profonds derrière les équations des écoulements présentés dans cette thèse. Je n'ai pas vu le temps de question passer, c'était juste passionnant.

Je remercie Isabelle Cantat, ma directrice de thèse. J'ai passé trois années scientifiques et humaines incroyables à l'IPR, et je te dois beaucoup pour cela. J'ai eu les encouragements, les ressources, la présence et l'espace qu'il faut pour m'approprier les notions et les codes nécessaires à la thèse. Avec cela, j'ai eu la chance de m'engager dans la vie du laboratoire, enseigner, partir en conférence souvent, et bien sûr une superbe expérience d'avoir pu partir à Cambridge en stage. Tu m'as fait découvrir ton métier et communiqué ta passion. Tu as été une mentor et une collègue bienveillante, toujours présente et à l'écoute. J'ai énormément d'admiration et de gratitude pour tout cela, et je suis extrêmement fier d'avoir été à ton école.

Je remercie les employés de l'IPR et sa direction, pour leur accueil et leur aide: Bénédicte Faure et Valérie Ferry, pour leur assistance et présence auprès des non-permanents, Nathalie Mabic, pour sa gentillesse et sa disponibilité, Jean-Charles Potier, pour sa jovialité et les pièces de méca toujours nickel, Patrick Chasles, qui m'a bien aidé sur l'électronique de ma manipe, Jean-Christophe Sangleboeuf, pour son accueil et nos discussions, Florian Scholkopf, pour les pauses café, et Jérémy Gardais, pour nos discussions occasionnelles mais toujours très agréables.

Merci à Emmanuel Schaub, ingénieur de recherche au département matière-molle. Cela a été un vrai plaisir de travailler avec toi sur mon montage expérimental. Tu as toujours pris le temps de répondre à toutes mes questions sur l'optique, l'électronique et l'interfaçage, et ça a été très formateur pour moi.

Merci aux enseignants-chercheurs avec qui j'ai eu la chance de travailler et/ou partager mon environnement de travail: Axelle Amon, pour les discussions scientifiques et rôlistiques, Laurent Courbin, notre adoré et révéré chef, Sylvie Beaufils, avec qui c'est un plaisir d'enseigner, et Jérôme Crassous, généreux en miel et en explications apicoles.

Merci aux non-permanents de l'IPR qui ont vu mon arrivée au labo et m'y ont accueilli: Donatien Mottin, mon camarade rôliste et de théâtre de l'ESPCI, Nolwenn Delouche, qui m'a fait don des séminaires non-permanents, Raphaël Poryles, qui m'a lancé sur les manipes, Jean-Baptiste Besnard, et sa grande culture musicale, Jeanne Kergomard, pour nos importantes discussions,

Maxime Vassaux, pour avoir mis l'ambiance et les discussions scientifiques toujours passionnantes, Yoann Raffray, Theany To et Alexis Duval, avec qui je n'ai que des bons moments et n'ai pas fait assez de soirées, Gaël Privault, avec qui j'ai commencé la thèse et vécu les épreuves de la fin en simultané, et Elliot Speirs, qui m'a fait découvrir les whiskies écossais.

Merci aux non-permanents que j'ai vus arriver et dont je ne pourrai maintenant suivre le parcours qu'à distance en leur souhaitant bon vent: Amélie Godard-Palluet, la super représentante des non-permanents, Alberto Macario-Farto, pour ta sympathie et d'avoir repris les séminaires non-permanents, Marion Baudoin et Laurianne Chonchon, avec qui on se croise ponctuellement pour discuter.

Merci à Thomas Mabit, doctorant arrivé 1 an après moi, pour ta présence douce et tes explications de méthodes numériques toujours riches, claires et passionnantes. Bravo pour ton poste !

Merci à Alexy Brunel, doctorant arrivé 2 ans après moi, pour le support technique (et moral!) le jour de la soutenance. Ca m'a beaucoup aidé. Ta culture générale scientifique m'impressionne (de la physique à la bio/médecine), je suppose qu'il faut au moins ça pour rendre de l'eau comestible ;)

Merci à Noémie Ourvois-Maloisel, doctorante arrivée 1 an après moi en thèse, mais 1 an avant moi à l'IPR en stage. La vraie doyenne des non-permanents. Ta jovialité et les moments de détente que l'on a sont très rafraîchissants. C'était bien sympa de me faire découvrir l'analyse senso et de servir de cobaye pour tes formulations de faumage.

Merci à Youna Louyer et Nathan Chapelle, qui arrivent reprendre le flambeau en tant que doctorants et qui dynamisent déjà l'équipe. Venir en thèse en quête de défi intellectuel après une ou plusieurs années d'enseignement est une démarche pour laquelle j'ai un immense respect. Nul doute que ces trois années vous sourient.

Merci à Marion Berry, François Giavassis, Milène Aubry, Gaëlle Audéoud et Gabriel de Oliveira Rodrigues, stagiaires dans notre groupe tout au long de ma thèse. Partager ma salle de manipe avec chacun d'entre vous à été un plaisir, et encadrer Gaëlle et Gabriel ont été d'excellentes expériences dont je sors grandi.

Un gros merci en particulier à Thomas, Alexy, Noémie, Nathan, Lucas, Florian, Ambroise, Axelle, Isabelle, Milène et Youna pour l'aide apportée le jour de la soutenance et le magnifique pot que vous m'avez réalisé. Merci beaucoup à Marion Berry, Alice Etienne-Simonetti, Corentin Trégouët, Adrien Bussonnière, Louis Ginabat et Pierre Glidic, qui m'ont fait la magnifique surprise de venir à Rennes assister à ma soutenance: vous êtes des amis et consoeurs/confrères adorables ! Cette journée s'est passée exactement comme je l'ai rêvée, et c'est notamment grâce à votre aide et votre présence à toutes et tous :)

Merci à Corentin Trégouët, qui est un peu devenu mon grand frère du milieu académique, et pour tout ce que tu as fait pour moi depuis 3 ans. De la visite d'appartement pour mon compte lors de mon arrivée à Rennes en temps de covid, aux week-ends passés chez Chloé et toi pour relâcher un peu la pression pendant la rédaction. Partager avec toi tous ces moments en conférence, en GDR, ou simplement autour d'un tableau à craie sont des épisodes de vie scientifique et humaine que je chérie. Ton soutien, ton expérience et ton amitié m'ont rendu la vie plus douce.

Merci à Adrien Bussonnière, mon prédécesseur sur mon montage expérimental. Tu m'as refourgué un sacré bestiau ! Et j'ai eu 3 ans pour apprécier tout le travail, la minutie et la pugnacité que tu as mis dedans. Merci pour tes conseils toujours judicieux, tes offres de postdocs, tes matrices élevées à la puissance 22... et tous les coups que tu m'as payés en conf/GDR! (j'ai arrêté de compter)

Merci à Jacques-Teïva Baué, qui m'a précédé à la présidence du bureau 007 en son temps. Mon camarade, mon partner, pour tous les coups géniaux à foireux sur ces deux ans passés ensemble. Du mariage en tant que chauffeurs ensemble jusqu'au fin fond du Grand Canyon, en passant par un road trip andalou, tout est gravé et précieusement gardé. Tu as une énergie positive, un sens de la répartie et une détermination qui font de toi une rencontre qui m'a marqué, et un ami formidable. Les fous rire que tu m'as offerts pendant cette thèse résonneront longtemps dans ma mémoire !

Merci à Adrien Gans, le post-doc prodigue en café et en bons conseils, maintenant maître ~~pokémon~~ de conférence à Nancy. Tu es une force tranquille de l'ESR, une source intarissable d'enthousiasme pour les sciences... et de mèmes de qualité. J'ai beaucoup apprécié nos discussions craie-tableau, tes cours d'économie politiquement très neutres, et bien sûr partager ces instants en dehors du labo et à ton mariage. Cette année passée ensemble m'a beaucoup apporté.

Merci à Ambroise Mathey, mon ami arrivé 1 an après moi en tant que doctorant. "Little knowledge of lab earthquakes, large knowledge of Rennes' pubs", il se présente comme ça ! Tu as une grande humilité et un si bel éclectisme face aux sciences, discuter avec toi est toujours très riche. J'y ai trouvé des questions qui m'ont fait avancer sur ma compréhension de nos sujets respectifs, découvert des problèmes numériques que je ne m'étais jamais posés. Ta culture et ta capacité d'apprentissage sur ces sujets est impressionnante. Nos nombreuses soirées avec tes anecdotes incroyables à partir de 2 pintes vont beaucoup me manquer.

Merci à Lucas Jannin, mon ami arrivé 2 ans après moi en tant que doctorant et actuel président du bureau 007 (puisque Ambroise a préféré le rôle d'éminence grise). Derrière tout le sel que tu balances gentiment, il y a un coeur un or. J'ai beaucoup apprécié ces moments à l'escalade, autour d'un verre ou du tableau pour décider comment on va détecter tes fichues ellipses. Merci pour tout ça!

Merci à Maryam Sadeghiyan Dehaghani, doctorante arrivée peu de temps avant moi. My dear friend ! Échanger avec toi sur nos parcours a été très enrichissant. Merci de m'avoir fait découvrir l'incroyable cuisine iranienne et des bribes de persan à travers de belles musiques.

Merci à Pierre Glidic, mon binôme de TP à l'ESPCI et ami depuis les premiers jours où j'y ai mis les pieds. Ta curiosité, ta culture et ton humour sont précieux. Construire ma pensée scientifique, découvrir la physique avec un camarade comme toi a été une grande chance. Tu fais un fier docteur depuis le 24 novembre dernier, et je n'ai eu que trop hâte de te rejoindre en tant que confrère, mon ami.

Merci à Anaïs Gauthier, ma co-bureau pendant l'écriture de ce manuscrit. Tu es une force positive et une marraine des sciences qui m'a appris énormément pour ce qui est de naviguer dans ce vaste milieu académique. Discuter de la vie, trouver des idées de manipes, et s'enthousiasmer avec toi sur des résultats a été très riche et rafraîchissant. Je ne t'aurai pas convaincue avec ce que tu appelles mes "thés de princesse", mais ils auront été bus en si bonne compagnie.

Merci à Sylvain Deville et Félix Ginot, qui m'ont encadré durant mon premier stage de recherche en 2018 au LSFC. C'était mon premier contact professionnel avec le monde académique, et ma première expérience de recherche tout court. En plus de l'aspect scientifique qui m'a beaucoup passionné, j'ai eu avec vous 6 mois très importants qui ont très largement contribué à me faire commencer cette thèse et vouloir continuer en recherche.

Merci à Franck Lesieur, mon prof de maths en spé. Votre passion pour les maths m'a marqué, et j'en garde clairement un enthousiasme teinté de respect pour cette discipline. Votre dévotion pour vos élèves m'a beaucoup aidé dans un moment difficile d'orientation scolaire. Ah, et votre "boîte à outil" m'aura servi exactement 3 fois dans cette thèse !

Merci à Aline Barazer, ma prof de chimie en sup. Vous avez cru en mes capacités, et sans vos mots au bon moment je ne me serais probablement pas donné les moyens d'intégrer l'ESPCI.

Merci à Nicolas Guillouet, mon prof de physique en sup. Votre sens de la pédagogie et votre enthousiasme pour transmettre votre savoir ont beaucoup contribué à m'orienter vers la physique. J'essaye d'arriver devant mes élèves avec le même élan que vous.

Merci à Emmanuel Brouard, mon prof de maths en seconde et terminale. L'entrain et l'énergie que vous avez dans votre métier m'ont beaucoup marqué. Je m'en inspire le plus possible pour enseigner, et je m'y découvre une passion. Vous m'avez écouté, encouragé et orienté pour mon envol vers le supérieur. Cela a été très important pour moi. Surveillant le jour de mon bac de maths, un sourire aux lèvres: "Je me mets à côté de Théo, il triche tout le temps!". Passer cette épreuve sous votre égide a été un temps fort de mon lycée.

Merci à Fabrice Vimond, mon prof de physique-chimie de collège. Je me souviens de vos passionnantes petites expériences en fin de cours, et votre passion pour transmettre aux jeunes de la belle science. Mention spéciale pour celle où on relie un petit et un grand ballon de baudruches et on se demande lequel va se vider dans l'autre. C'était mon premier contact avec la pression de Laplace, qui, 15 ans plus tard, est un des phénomènes centraux de ce manuscrit. Merci pour la leçon d'avance!

Enfin, Merci à ma famille pour son soutien de chaque instant, à chaque étape de mon parcours: Annie, ma mère, Paul et Zoé, mon frère et ma soeur, Jean-Marie, Dominique, Colette et Françoise, mes oncles et tantes, Benjamin et Margot, mes cousins, Jean-Claude et Marie-Thérèse, mes grands-parents, et Swanny, ma conjointe. Votre amour, vos encouragements et votre présence sont un moteur qui m'a permis d'identifier tôt et vivre pleinement ma passion pour les sciences, et me donne les moyens pour que je puisse en faire mon métier. Sans tout ça, l'apprenti scientifique qui arrivait le matin au labo n'aurait pas eu le même épanouissement, la même envie, la même passion. En cela, cette thèse vous doit beaucoup.

Résumé en Français

Les travaux de cette thèse portent sur les écoulements dans le plan de films de savon. C'est un point de vue d'hydrodynamicien qui vise à aider à mieux comprendre la rhéologie et le vieillissement des mousses liquides en s'attaquant à des échelles locales: le film de savon unique et la mousse liquide élémentaire, c'est à dire trois films reliés entre eux à 120^o par un ménisque.

Dans l'introduction, je présente l'état de l'art sur la physique des films de savon et des mousses liquides élémentaires. Le lecteur y trouvera en premier lieu des définitions de quantités thermodynamiques importantes pour coupler la rhéologie d'une interface gas-liquide aux écoulements dans la phase liquide, puis une mise en équation pour les mouvements dans le plan des films de savon, qui représentent un cas extrême de confinement entre deux de ces interfaces. Cela fait poser et calculer quelques ordres de grandeurs nécessaires pour la suite en discutant notamment les échelles spatiales et temporelles pertinentes, ainsi que les propriétés physico-chimiques des solutions savonneuses (choix et propriétés des surfactants, viscosités etc...).

Ensuite, il est question de regarder plus spécifiquement la zone de jonction entre ces films plats et un ménisque courbé. Des régimes stationnaires et instationnaires d'évolution du profil d'épaisseur dans le film sont discutés selon l'écoulement imposé côté film.

Enfin, j'expose un état de l'art sur les mousses liquides élémentaires sous déformation imposée. Deux expériences précédentes (par Durand & Stone [1] et Besson & Debrégeas [2]) et des simulations numériques récentes (Titta [3]) ont montré la pertinence de cette échelle locale des mousses, que ce soit pour mieux comprendre la mécanique globale de ces matériaux, ou pour sonder la rhéologie de surface des interfaces qui les composent. Dans tous les cas, la réponse mécanique de la mousse élémentaire est montrée comme étant notamment déterminée par les quantités de surfactants échangées entre films, et entre les films et le ménisque. Ces échanges font systématiquement l'objet d'hypothèses fortes dans ces modèles, et tenter de les estimer par le calcul confronte la communauté à des variables physico-chimiques pas ou mal connues. Les connaître permettrait de résoudre le champ de vitesse dans la mousse élémentaire, pour lequel un modèle existe (Bussonnière & Cantat [4]), et de donner des lois rhéologiques locales physiques pour la rhéologie des mousses liquides.

La principale problématique de cette thèse est ainsi posée: peut-on quantifier ces échanges de surfactants entre films et entre films et le ménisque?

Le plan du manuscrit est construit avec un Chapitre 1 portant sur l'élasticité individuelle d'un film de savon, un Chapitre 2 sur une description théorique et une mesure d'une tension de ligne d'origine purement capillaire dans les films, et la modélisation des écoulements qu'elle génère dans le plan du film, et un Chapitre 3 portant sur la quantification des échanges de surfactants au sein d'une mousse liquide élémentaire entre films et entre les films et le ménisque.

Le Chapitre 1 commence par présenter un modèle d'élasticité de film de savon (Prins *et al.* [5]) qui résout complètement le couplage entre étirement et échanges volume-interface de surfactants pour des régimes sous-micellaires. Ce modèle est validé par des expériences faites à l'époque, et également présentées dans le manuscrit.

Mon apport est ici d'étendre ce modèle au régime micellaire grâce à des résolutions numériques, et de prédire les courbes de charge $\Delta\sigma = f(\epsilon)$, les variation de tension de surface $\Delta\sigma$ en fonction

de la déformation ϵ selon les axes du plan du film. L'élasticité d'un film est quantifié en prenant la pente à l'origine de ces courbes. Notamment, il apparaît ici qu'étant données les hypothèses du modèle, les surfactants en régime micellaire ne contribuent pas à cette élasticité. On attend donc à être dominé principalement par les contributions soit des impuretés, soit d'un co-surfactant peu soluble de la solution.

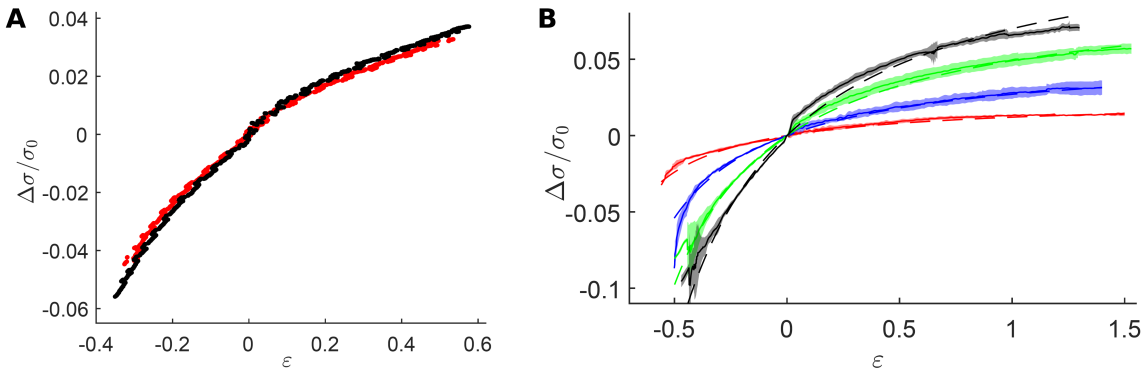

Figure 1: Courbes de charge: **(A)** pour différentes vitesses de déformation à chimie donnée $[DOH] = 35\,\mathrm{mg/L}$ ($U = 5$ et $10\,\mathrm{mm/s}$ resp. en rouge et noir) ; **(B)** Pour différentes chimies à vitesse $U = 10\,\mathrm{mm/s}$ (de rouge à noir, $[DOH] = 0,\ 15,\ 35,\ 50\,\mathrm{mg/L}$)

Enfin, je compare ce modèle étendu à des expériences menées avant le début de ma thèse avec des solutions micellaires de SDS auxquelles du dodécanol est ajouté comme co-surfactant. Ces dernières ont permis de tracer expérimentalement les courbes des charges et d'effectuer la comparaison avec le modèle. Un bon accord quantitatif est trouvé si on ajuste sur la quantité de dodécanol ajoutée plutôt que de rentrer la valeur nominale des solutions. Cela laisse supposer que les impuretés ont un rôle non-négligeable, et que les différentes variables physico-chimiques les caractérisant sont mal connues. Le modèle et ses résultats ont fait l'objet d'une publication dans *Soft Matter* [6] en 2022.

Le Chapitre 2 porte sur une tension de ligne dans les films de savon comportant des hétérogénéités d'épaisseurs. J'y établis en premier lieu l'expression d'un tenseur des contraintes capillaire 2D pour un élément de film comprenant un gradient d'épaisseur.

Grâce à ce dernier, il est possible d'effectuer un bilan des forces dans une zone séparant deux régions du film de savon qui ont des épaisseurs différentes. De par l'anisotropie des forces en jeu, on montre qu'un excès de contrainte est stocké dans cette zone de transition d'une épaisseur à l'autre. En prenant la limite d'un largeur de transition nulle, on construit ainsi un contour contenu dans le plan du film de savon le long duquel une tension de ligne est présente. Cette dernière pourrait être impliquée dans les écoulements dans le plan des films de savon dès lors que ceux-ci sont d'épaisseur non-uniforme, et il devient donc intéressant de la quantifier.

La suite du chapitre porte sur un montage expérimental où cette tension de ligne est mise en évidence. Il s'agit d'un film de savon à l'horizontale que l'on crée fin ($\sim 200\,\mathrm{nm}$) sur un cadre rectangulaire déformable au rapport d'aspect initial très allongé. En étendant le rectangle brusquement en largeur, on extrait du film épais ($\sim 10\,\mu\mathrm{m}$) des ménisques du cadre vers le plan du film pré-existant. On crée ainsi une situation où un film de savon possède deux régions

d'épaisseurs différentes, et l'arène de film fin initialement allongée relaxe vers une forme de cercle sous l'effet de la tension de ligne à sa frontière.

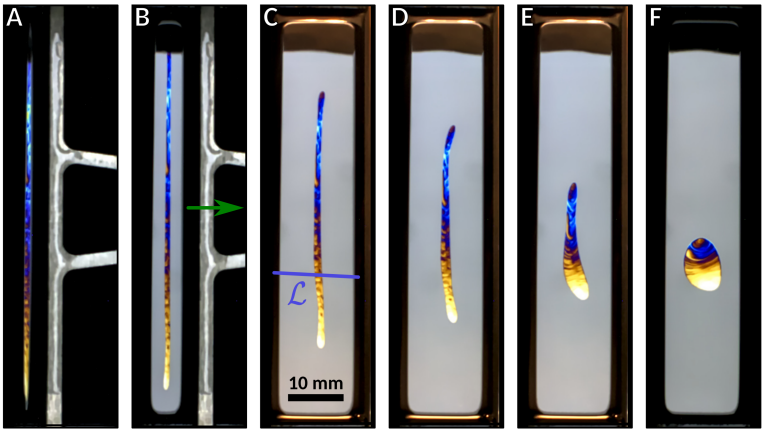

Figure 2: Timelapse de l'expérience de relaxation d'un patch de film fin (coloré) au sein d'un film plus épais (gris). Une tension de ligne T est présente le long du contour séparant les deux régions.

La tension de ligne est mesurée grâce à une caméra spectrale qui donne accès au profil d'épaisseur le long d'un segment perpendiculaire à la ligne de tension. En intégrant les gradients des profils d'épaisseurs, on obtient une mesure à 30% de la tension de ligne qui est de l'ordre de $T \sim 10^{10}\mathrm{N}$.

Afin de valider cette mesure, nous avons modélisé les écoulements, dont la tension de ligne est la force motrice. Connaissant la force de friction opposée à cette dernière, la friction sur l'air au-dessus et au-dessous du film, nous regardons la vitesse à laquelle l'arène relaxe vers un cercle. Un accord quantitatif entre mobilité prédite et mesurée valident notre mesure de la force motrice, et donc de la valeur de tension de ligne trouvée.

Le Chapitre 3 détaille la réponse expérimentale à la problématique principale de ma thèse. J'y rappelle d'abord la situation physique: nous nous intéressons à un système comportant trois films de savon reliés entre eux par un ménisque libre, où on impose des écoulements bouchons loin de ce dernier.

Un modèle décrivant le champ de vitesse dans les films, près du ménisque, a été développé avant le début de ma thèse par Bussonnière & Cantat [4]. Ses principaux éléments sont rappelés: des écoulements bouchon (sans cisaillement) sont imposés loin du ménisque, mais la présence de points d'arrêts aux interfaces dus à la symétrie de déformation impliquent l'existence de zones cisaillées au voisinage du ménisque. Dans ces zones, un cisaillement simple est attendu, dont la pente et la longueur sur laquelle il se développe dépendent directement de variables physico-chimiques et de la capacité du ménisque à échanger des surfactants avec les films. En effet, les points d'arrêt imposant des destructions/créations d'interface, connaître ces flux d'échange détermine la contrainte de Marangoni le long des films, et donc les cisaillements qu'ils subissent.

Le challenge expérimental qui se pose alors est de pouvoir mesurer simultanément ces quantités d'interface L_{in} et L_{out}. Cela est rendu possible par un montage commencé avant le début

de ma thèse et complété pour répondre à cette exigence. Je détaille donc dans une section l'ensemble de caméras utilisées pour permettre cette mesure: Trois caméras en fluorescence, une regardant le film comprimé, une sur un film étiré, une sur le côté du ménisque, et trois caméras spectrales regardant les profils d'épaisseur de chaque film. A cela s'ajoute un montage laser pour le photoblanchiement de l'agent fluorescent placé dans nos solutions pour pouvoir créer des traceurs passifs dans les films. Je détaille ensuite le protocole expérimental (vitesses des moteurs, temps de préparation, de déformation des films etc...). Une autre section décrit les traitements numériques relatifs à chaque caméra ainsi que les tracking de taille et position du ménisque, des films extraits lors des déformations et des points photoblanchis.

Avec ces informations, une nouvelle section décrit comment nous remontons aux quantités d'interface échangées et à la différence de tension entre les films. Cette dernière est trouvée principalement grâce à la position du ménisque, qui est une information qui reste délicate à trouver étant donnée la présence de glissements aux temps initiaux des déformations imposées. Ensuite, pour estimer les quantités d'interface L_{in} et L_{out}, l'information la plus délicate à trouver est l'état de compression des films. En effet, les longueurs recherchées sont proportionnelles aux quantités de surfactant qu'elles portent, et il faut donc corriger les longueurs directement mesurées par des facteurs de déformation ϵ estimés pour chaque film (étiré ou comprimé). Cela se fait en estimant pour chaque film la différence de longueur par rapport au cas initial, avec quelques subtilités quant à localiser précisément un système fermé pour chacun d'entre eux.

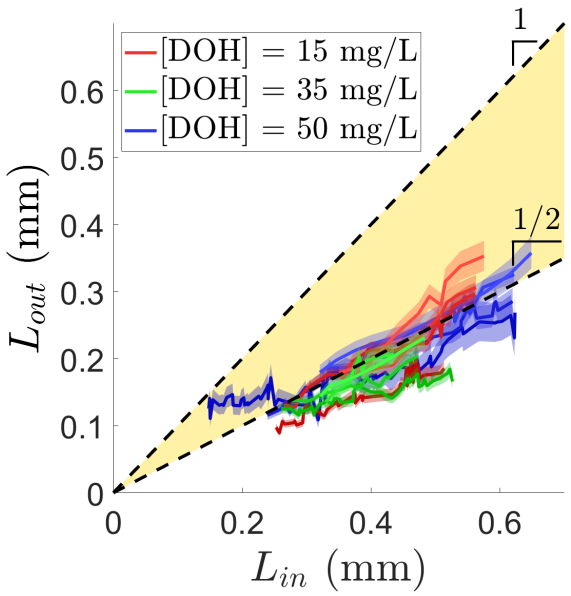

Figure 3: Quantités d'interface échangées mesurées simultanément. Le facteur 1/2 correspond au cas de l'absence d'échanges entre le ménisque et les films.

Une fois que ces déformations sont connues, L_{in} et L_{out} le sont également. Il apparaît alors clairement que pour toute les gammes de vitesses de déformations et de concentration en dodécanol utilisées ($V = 10 - 50\,\mathrm{mm/s}$, $[DOH] = 15 - 50\,\mathrm{mg/L}$), le cas $L_{out} = \frac{1}{2}L_{in}$ correspondant à l'absence d'échanges ménisque-film est atteint. Cela suggère donc que pour des gammes de taux de déformation autour de $\dot{\gamma} = 1 - 10\,\mathrm{Hz}$ et de chimies similaires (un ordre

de grandeur d'élasticité de film balayé avec le dodécanol), l'hypothèse de nullité pour ce flux peut être faite, ouvrant la voie pour clore le modèle théorique qui prédit la viscosité effective des mousses liquides élémentaires.

Enfin et avant de conclure, j'expose également dans ma thèse comment cette expérience de déformation de mousses liquides élémentaires permet de retrouver les élasticités de film définies et mesurées dans le Chapitre 1, et montre l'accord entre les deux mesures. D'autres déformations sont également montrées, et servent à discuter les différence attendues pour d'autres régimes et symétries, ou la place des recirculations gravitaires dans les mécanismes d'échange.

En conclusion, je récapitule ces différents chapitres et discute les développements expérimentaux et théoriques attendues après ces travaux.

Contents

0 Introduction

Here is a liquid foam

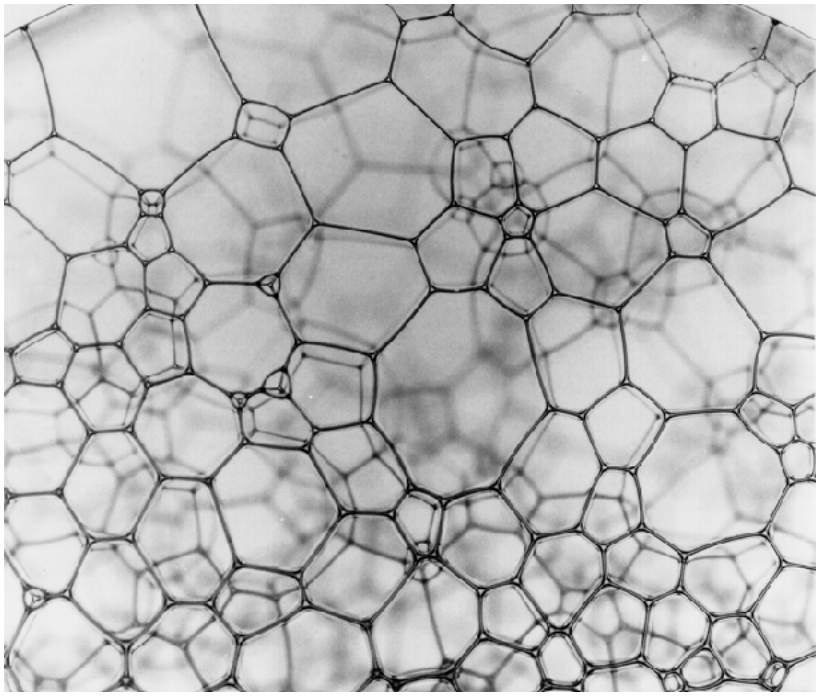

Figure 1: A dry liquid foam. Credits to S. Cohen-Addad, R.M. Guillermic & A. Saint-Jalmes [7].

What we see is a network of flat liquid films separating faceted bubbles. This is essentially a close look at what is in a sink while doing the dishes, or what we hold in our hands while shampooing! And we all know the recipe: a **liquid**, water most of the time, in which we add a

surfactant, soap most of the time, and some **mechanical work** to incorporate some **air** into the liquid. This creates a suspension of gas in a liquid, as we are accustomed to in everyday life, whether it is for washing, cooking, or simply enjoying the view of bubbles.

For an engineer, predicting the overall mechanical properties of these structures is a complex problem — whether it involves guiding their flow from point A to B... or preventing their formation in the first place.

Let us first have an even closer look, zooming on one single film with Fig.2**A**.

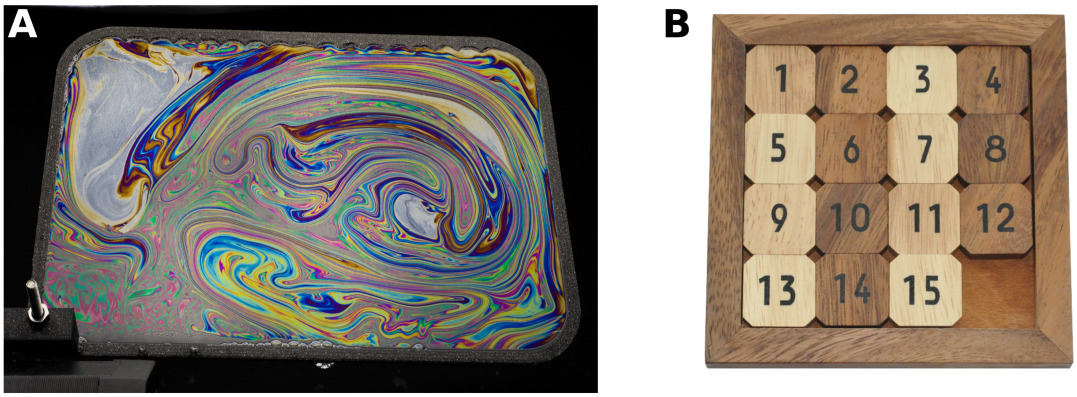

Figure 2: **A:** single flat foam film on a supporting frame. The interference colours correspond each to a thickness of film in the range $\sim 200 - 800$nm. Thicker pieces appear grey, thinner appear black. Credits to Eric Sorensen[2]. **B:** At the typical time scale of a foam film lifetime, each tiny coloured patch mentally cut out of it can be seen as a closed system which is advected in the plane of the film. Describing the in-plane motions of a foam film is a sliding puzzle game!

This is a flat film of liquid supported by a solid rectangular frame. The thickness of liquid varies from a few hundreds of nanometers to a few microns, around one hundred times thinner than a human hair!

Also, what remains hidden in the picture is the meniscus, which is a curved liquid beading at the edges present either on the supporting solid frame for our single film, or at the junctions between the films in the liquid foam. What we can see on the other hand are the heterogeneities of thickness in the film itself, evidenced by the (delightfully) colourful patterns at the surface. All of these factors contribute to the inherent complexity of this system even at this scale.

A first important piece of knowledge for instance, is that if we track by eye a tiny piece of film in the coloured patterns, it is a closed system which does not exchange any matter with its neighbours. This is true on the typical time scales $\sim 1 - 10\,\mathrm{s}$ at which we witness these colours moving, even if the said patch of film runs through the whole film!

As a child, I saw bright and wiggling colours in my bath. As an undergrad hydrodynamicist, I thought it was about the inner flows of a fluid sandwich made of two liquid-gas interfaces. As

[2]A beautiful zoology of foam films by Eric Sorensen at http://esorensen.com/soap-film-photography/. Many thanks to him.

a Ph.D student, I see now that it is all about a sliding puzzle game with patches of foam films (Fig.2**B**). A puzzle game with many mysteries yet to be solved: What forces set the pieces of film in motion within their own plane? How does a patch of film behave close to the meniscus? Can neighbouring films exchange patches if we deform them? With whom do they exchange? With the meniscus or with other films?

Part of these questions have had their answers in the literature, but an even bigger part is still open!

This thesis is about the adventure of such a 2D patch of foam film, a piece of a sliding puzzle: We are going to apply forces on it, advect it, stretch it and even try to shear it in its own plane. In the end, it will be allowed to deliver the surfactants it carries from one film to another in a foam, thus representing a transport mechanism relevant for foam rheology (Fig.3).

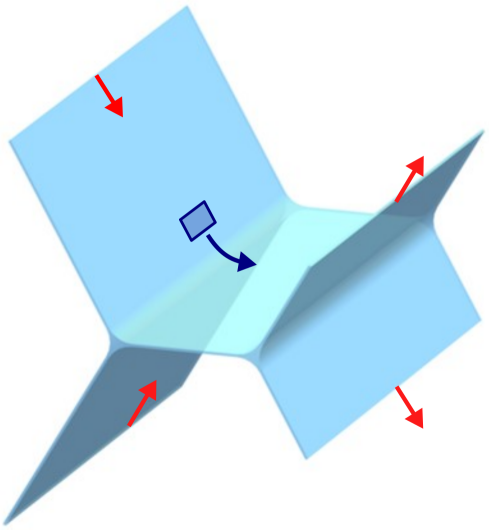

Figure 3: A local scale of a liquid foam such as shown above. Deforming the films (red) sets in motion patches of film. Some of them will even leave their plane (dark blue), thus representing a surfactant transport mechanism. These exchanges are of the utmost importance for the sake of describing the flows in the system.

0.1 The fluid dynamics around a surfactant-laden interface

As stated earlier in the very basic description of a bubble or a foam film, we are dealing with a very thin gas-liquid-gas sandwich. The major ingredient to add in order to stabilise this structure is the presence of surfactant molecules at the interface. But how do they organise for one interface first? What tools do we need to properly describe the features of an interface containing surfactants?

0.1.1 Surfactants

First, let us define what a surfactant is. A very usual example given at school is soap, often with the simplified chemical representation of a polar round head with an elongated non-polar carbon tail. Heads like water which is polar, tails prefer air which is non-polar. They ease the formation of bubbles and liquid foams by going at the liquid-air interfaces and lowering **surface tension, denoted** γ, which is usually presented as "the energy per unit area" it takes to create some interface.

Usual species of surfactants encountered in daily life can have many different origins. A lot of proteins are efficient surfactants: dairy and egg proteins are rather good examples, as both milk and beaten eggs foam well. Surfactants in cleaning agents also have many different origins, from the traditional *savon de Marseille* made with oleic acid from olive oil to "sulfates" (or SAS for secondary alkanesulfonates) used in shampoos and dishwashing liquids, which are petroleum derivatives.

In research, quite a wide range of surfactants is also utilised: TERGITOL's, Triton X-100, the C_nTAB family (for TrimethylAmmonium Bromide, exist with carbon chains from $n = 10$ to 16) and the sodium sulfate families. In the frame of this thesis work, we will focus on a surfactant from this last family, maybe the most widely used in soft-matter: **SDS for Sodium Dodecyl Sulfate**. Its structure is represented in Fig.4A. It is an anionic surfactant synthesised from **dodecanol (hereafter DOH)** shown in Fig.4B.

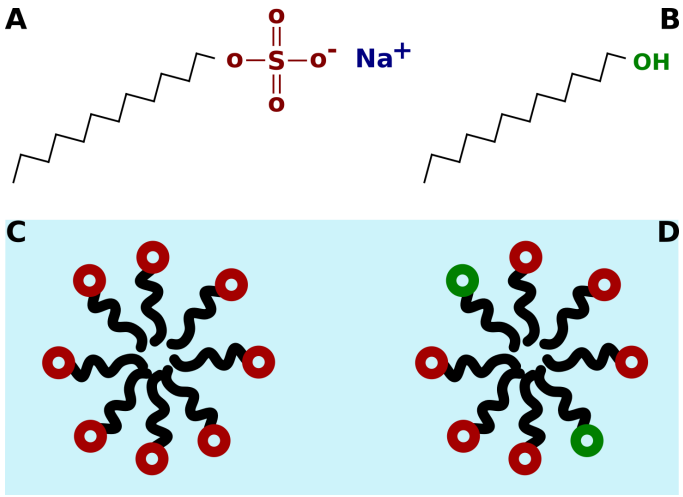

Figure 4: Structure of the two surfactants used in the frame of our work: **A:** SDS (for Sodium Dodecyl Sulfate) is a very soluble anionic surfactant (forms micelles in water **C**) and **B:** DOH for Dodecanol (poorly soluble, is the electrolysis product of SDS, hides in SDS micelles **D**)

SDS is a very soluble surfactant in water thanks to its very polar head. When its concentration reaches a critical value called Critical Micellar Concentration $CMC = 8.1\,\mathrm{mmol/L}$, SDS molecules start forming spherical structures called micelles, of which a schematic view is shown in Fig.4C and which represent an actual new phase in the system. Thus, above the CMC, the monomeric concentration of SDS in water remains capped at $CMC = 8.1\,\mathrm{mmol/L}$ and the

molecules in excess form micelles. On the other hand, DOH is a poorly soluble surfactant, having a solubility in pure water of $s = 2.2 \times 10^{-5}\mathrm{mol/L}$. When solubilised in a micellar SDS solution however, DOH can take refuge in the micelles, as shown in Fig.4D, and its overall solubility can go up to $s \sim 10^{-3}\mathrm{mol/L}$.

As for this choice of surfactant, it is very important to note that a tiny amount of DOH is still present in commercial SDS powders. The manufacturer only gives the global purity which is $> 99\%$. Later estimations made in the frame of our work (*cf.* chapter 1 subsection 1.2.1) tend to show that DOH represents approximately $\sim 0.1 - 0.2\%$ of the SDS-DOH population. It is a crucial factor as these tiny amounts of DOH drastically change the properties of the foam films and thus represent a control parameter in the following when we will be adding DOH ourselves to the solutions.

0.1.2 Definitions and generalities about interfaces and surface tension γ

> God made the bulk; surfaces were invented by the devil
>
> Wolfgang Pauli

Surface tension γ defined as an energy

Now that we have defined what our surfactants are and how they organise in the bulk liquid, which is always water in the frame of this work, let us see what happens when our solutions are put in contact with a gas interface, which is always air here. Thus, a first naive/schematic view of such an interface is given by Fig.5A, which can be imagined with or without the surfactants covering it: a discrete jump from one phase to the other, a 2D object which can possibly be populated by surfactants.

Most importantly, this description is associated with the definition of a central physical quantity that is the surface tension γ, first introduced by Gibbs [8, 9] and classically defined as the energy per unit area required to create some interface:

$$\gamma = \left.\frac{\partial F}{\partial A}\right|_{T,V,N} \tag{1}$$

Where F is the free energy, to be switched with any other thermodynamic potential depending on the variables of the problem (*e.g.* T,V,N the entropy, volume and quantity of matter), and A the interface area. The canonical molecular interpretation of this energy cost is to imagine a single molecule near the discrete interface and how the attractive interactions acting on it vanish in the direction of the interface, as air is very dilute (or similarly how they diminish in this direction for liquid-liquid interfaces). This results in an energy frustration of any molecule at the surface, meaning there is an energy cost per unit area to create the interface.

What is hidden in an interface?

However, the molecular reality is in fact more complicated than that. How does it make sense to speak of distance from the interface for a single molecule when these molecules define what the interface is? Part of the answer can be found if we dare opening the Pandora box of "what is hidden in an interface in a 3D world?". Let us do so gently, opening it ajar only, just to be sure at least of the sizes we are dealing with.

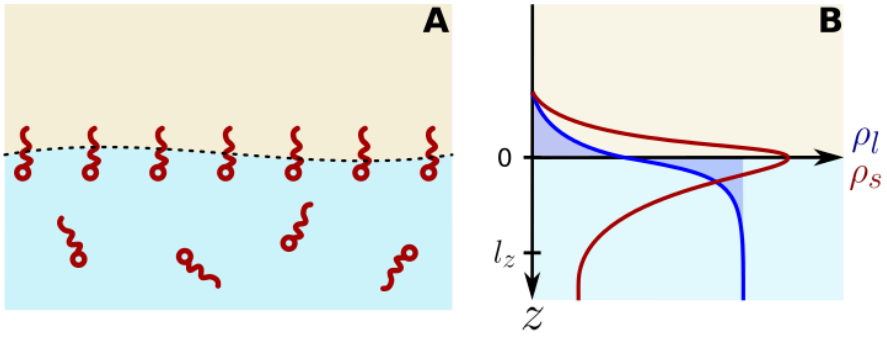

Figure 5: A liquid-gas interface wide open. **A:** Schematic view as a 2D object. **B:** Schematic view of the real 3D world as we open the interface. The typical thickness over which we jump from one phase to the other is of the order of $\sim 3-5\ r_M$ molecular sizes. ρ_l, ρ_g and ρ_s are respectively normalised densities of liquid, gas and surfactants.

Pauli warned us already: these are tricky objects to think about and describe. Let us have a closer look. In Fig.5B, in the case where there are no surfactants (meaning we temporarily forget about the red curve), the density of water molecules varies from a constant value, which is the bulk value, to zero over a width $\sim 1-10$ nm which is the size of several water molecules. This remains much thinner than regular foam films as we recall their typical thickness $h \sim 1\,\mu$m. The interface itself $z=0$ is here defined as the origin of a step function jumping from $\rho=0$ to $\rho_{l,bulk}$ that makes the two grey excess areas have equal surfaces.

What is surface tension in this 3D description? This is a matter of molecular dynamics: we would need to describe the potential of interaction between the molecules, draw the profile of density of energy of interactions across the interface and integrate it along z. The excess of energy compared with bulk liquid would be γ. We won't risk writing it in math mode though.

Now let us consider surfactants. We add the red curve to Fig.5B alongside the blue one. In the vicinity of $z=0$, the surfactants are much more concentrated. When we will get back to a 2D description, this local excess of molecules will be called surface excess (meant by comparison to the bulk value $\rho_{s,bulk}$). The existence of a surface excess for a species is the definition of what we have called so far a surfactant.

NB 1: This definition of "surfactant" is canonical in physical chemistry. For other communities in chemistry, a species also need to be soluble enough to form micelles in order to be called surfactant, and for example dodecanol would not be called surfactant, but rather "co-surfactant" as it relies on SDS to ensure its solubility. For hydrodynamicists like us, a surfactant would be anything changing our boundary conditions at the interface, which is more in line with the definition of the physical chemists.

The contribution of the surface excess of surfactant to the aforementioned energy integral of γ is negative, and thus adding surfactants results in a lower surface tension.

NB 2: This decrease of γ is very often proposed as an explanation for the foaming properties of soapy solutions. "Creating water-air interfaces costs less, thus allowing foams to exist". **This is utterly wrong.** A lot of pure liquids with surface tensions close to soapy solutions such as regular oils do not foam at all! Allowing a foam film to exist is not about how much it costs to create it, but rather giving its surface tension a law of evolution $\gamma(\epsilon, \dot{\epsilon})$ under a certain deformation of the interface ϵ to resist gravity and capillary forces. Describing these laws is a big part of this thesis work, as we will later see.

Adding a surfactant also raises the question of the evolution of the typical width l_z where we start deviating from the bulk properties, and to see to what extent the interface remains thin enough to be considered 2D. In our specific case of an ionic surfactant such as SDS, the typical width of the interface is the Debye length λ_s as predicted and experimentally shown by Bergeron *et al.* [10, 11] with DLVO theory [12, 13]. We can write it and estimate it in our case using our typical bulk concentration of surfactant (which is lower than the concentration in the interface):

$$l_z \sim \lambda_s = \sqrt{\frac{\epsilon_0 \epsilon_r k_B T}{\rho_s \mathcal{N}_A z_s^2 e^2}} \sim 10\,\mathrm{nm} \tag{2}$$

Where $\epsilon_0 \epsilon_r = 6.9 \times 10^{-10}\ \mathrm{F\,m^{-1}}$ is the electric permittivity of water, $k_B T = 4.1 \times 10^{-21}\ \mathrm{J}$ is the thermal energy, $e = 1.6 \times 10^{-19}\ \mathrm{C}$ is the elementary charge, $z_s = 1$ is the ionic valence of SDS, $\mathcal{N}_A = 6.64 \times 10^{23}\ \mathrm{mol^{-1}}$ is the Avogadro constant and $\rho_s > \rho_{s,bulk} = 1\ \mathrm{mol/m^3}$ is an order of magnitude for the concentration of SDS.

This is the order of magnitude of the range at which our interface can interact. Thus, this allows us to distinguish what is called a black film (so thin that it appears black), the world of physical chemists with $h < 100\,\mathrm{nm}$, from regular "thick" films, our world as hydrodynamicists with $h > 100\,\mathrm{nm}$. Below this limit, with black films, an important ingredient to add is disjoining pressure, a key physical quantity to study the stability of these systems which is directly linked to the ageing of liquid foams [14–16]. **Above this limit $h > 100\,\mathrm{nm}$, which will always be the case from now on**, we are allowed to close the box of the 3D interface and get back to our surface tension γ defined properly along a 2D interface.

Surface tension γ as a force per unit length and how to measure it

All these clarifications about interfaces being made, we can have a look at what happens depending on their geometries. In fact, as we implied earlier, our interfaces are going to be curved as the foam films have heterogeneous thicknesses and are connected to menisci at the edges. This is where surface tension comes into play, but rather as a force per unit length this time. The beauty is that although it is defined only in the 2D interface, its contributions are both on the normal and tangential constraints of the surface!

The stress at the interface can be written (neglecting surface viscosities for now):

$$\overline{\overline{\boldsymbol{\sigma}}}.\boldsymbol{n} = \boldsymbol{\nabla}_s \gamma + \kappa\gamma\ \boldsymbol{n} \tag{3}$$

Where $\overline{\overline{\boldsymbol{\sigma}}}$ is the stress tensor in the liquid, $\kappa = \kappa_x + \kappa_y$ is the local mean curvature, $\boldsymbol{n}$ is the normal vector of the interface (oriented toward the gas) and the s indices account either for the evaluation of quantities at the interface or in the local basis of the interface. The first term on the right hand side is the Marangoni stress, that is the gradient of surface tension in the local basis of the interface. The second term is a normal force to the interface which is related to the curvature of the surface.

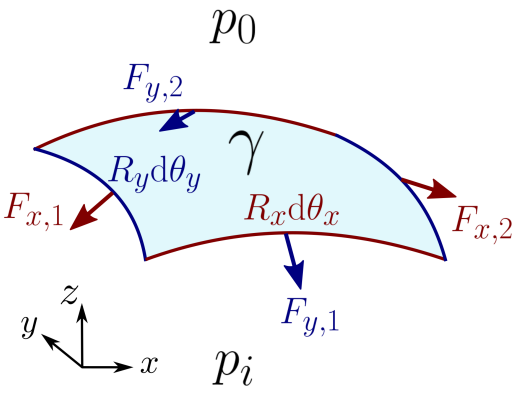

Figure 6: Jump of pressure $\Delta p = p_i - p_0$ across a curved interface subject to surface tension γ. R_x and R_y are the local radii of curvature along both axis x and y. $d\theta_x$ and $d\theta_y$ are the angular apertures of the interface element along x and y.

For an interface at equilibrium, the Marangoni stress disappears on the right hand-side of eq.3 and on the left hand-side the normal stress is only balanced by the difference of pressure between the two fluids:

$$(\overline{\overline{\boldsymbol{\sigma}}}.\boldsymbol{n})_{eq} = \kappa\gamma\boldsymbol{n} = \Delta p\boldsymbol{n} \tag{4}$$

Where $\Delta p = p_{gas} - p_{liq}$ is called the Laplace pressure jump. In Fig.6, we give a more geometrical view of the different forces acting along the edges of an element of interface. R_x and R_y are the radii of curvature along the two directions of the interface and $d\theta_x$, $d\theta_y$ are the angular apertures of the element along the same axis. The norms of the elementary forces can directly be written: $F_{x,1} = F_{x,2} = \gamma R_y d\theta_y$ and $F_{y,1} = F_{y,2} = \gamma R_x d\theta_x$. By projecting all the forces in the normal direction of the interface and writing the balance, the difference of pressure compensating for the curvature is given by the Laplace law:

$$\Delta p = \gamma\Big(\frac{1}{R_x} + \frac{1}{R_y}\Big) \tag{5}$$

Note that for a spherical interface, both radii of curvature are equal and we have a factor 2: $\Delta p = \frac{2\gamma}{R}$.

This pressure jump is an important ingredient as many experimental measurement methods for γ rely on a Laplace pressure measurement. In Fig.7, we display an overview of six different measurement methods for surface tension [17]:

- **Wilhelmy plate:** Relies on a direct measurement of the vertical component of the capillary force $F_{cap} = 2\gamma l \cos\theta_c$. The main difficulties are to know θ_c accurately and to wet the plate properly.

- **Maximum bubble pressure:** The goal is to blow a bubble at the tip of a capillary by imposing an air flow rate and to measure the pressure in the gas plug. At earlier times when less than half a sphere is out, the radius at the end of the gas plug decreases until a hemispherical bubble is created of radius R the radius of the capillary. After this time, as more air comes in, the radius of the bubble increases until the bubble detaches from the capillary. A minimum of radius is attained with the hemispherical bubble, and thus a maximum of pressure, which is measured. The Laplace law gives γ as both R and Δp are known.
- **Spinning drop:** An elongated plug of air is entrapped in the liquid in a horizontal spinning cylinder. The evolution of the length of the plug is a balance between the centrifugal forces applied on the bubble and its surface tension. Writing both energies, we have the relationship: $\gamma = \frac{\rho_l \omega^2}{4} R^3$ with ρ_l the liquid density and ω the angular velocity. By monitoring R, a precise measurement of γ can be done. This method is particularly useful for low surface tensions and is also often used with two immiscible liquids, replacing the fluid density by the difference of densities in the relationship above.
- **Du Noüy ring:** This method is very close to the Wilhelmy plate except the force is exerted on the interior and exterior of a circular ring of radius R. The extracted film takes shape of a catenoid, and a precise tedious calculation yields a relationship between the measured force and surface tension, knowing the geometry of the ring.
- **Capillary rise:** By dipping a cylindrical capillary of known interior radius, we see the rise of a liquid column above the surface of the bath which reaches an equilibrium quite rapidly. This is the historical experiment of Jurin, and a very academic example to highlight the presence of surface tension. The vertical liquid column balances the pressure drop due to the curvature of the wetting meniscus in the capillary. Knowing the interior radius of the capillary r_c, the height h and density ρ of the liquid column and the wetting angle θ of the liquid, it is possible to have a measurement of surface tension by writing the balance: $\rho g h = 2\gamma \cos\theta / r_c$. This method is unreliable in this form, but can be adapted for porous media and is well known in soil physics [18]
- **Pendant drop:** This method consists of creating a drop in air (or another liquid for liquid-liquid measurements) attached to a capillary of known geometry. The volume injected in the drop and the density of the liquid are known, and the profile of the drop is measured by a camera on the side. Fitting the profile, it is possible to determine the wetting angle precisely and by making the force balance with the weight it is possible to determine the surface tension. This is a very reliable method for a wide range of liquids. Besides, it enables dynamic measurements by controlling the amount of liquid pumped in/out of the drop, probing the surface rheology of the drop interface.

0.1.3 Coupling the bulk to the interface

For a single interface

As suggested earlier, the surface tension is a function of the surface excesses of the surfactant species dwelling at the interface. Let us give the notation Γ_i for the surface excess of a species

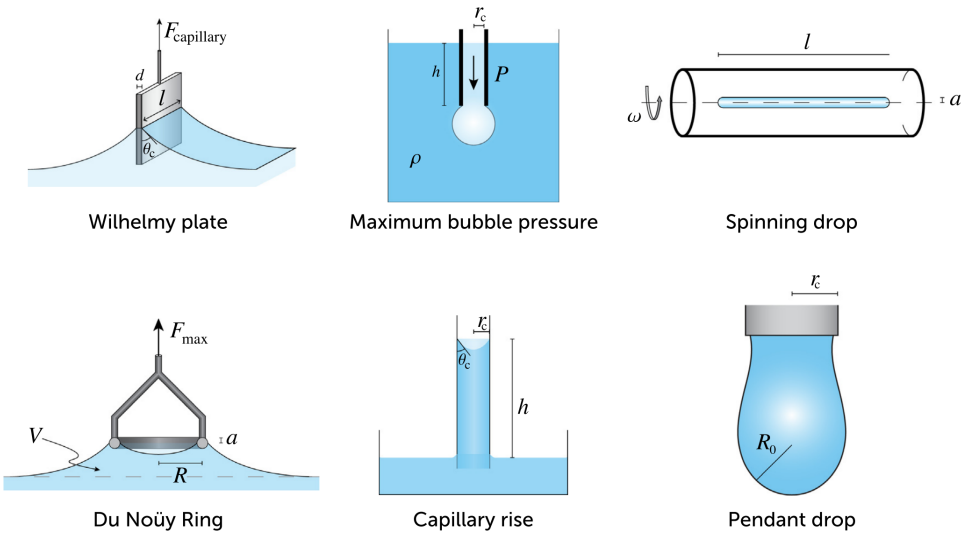

Figure 7: Various experimental techniques commonly used to characterise surface tension. Credits to Berry *et al.* [17].

i (usually expressed in $\mathrm{mol/m^2}$). Surface tension can be written as an unambiguous function of Γ_i using the thermodynamic identity (later detailed in chapter 1):

$$\mathrm{d}\gamma = -\sum_i \Gamma_i \mathrm{d}\mu_i \tag{6}$$

Where μ_i are the chemical potentials of the different species.

Thus, our problem is now to describe the evolution of these Γ_i as the population at the interface is coupled through diffusion to the population c_i in the bulk (the concentration of species i in $\mathrm{mol/m^3}$). **Note that for now we speak of an infinite bulk, thus not limiting the depth at which we probe it by diffusion**. This coupling is rather difficult to establish though, as it depends on the evolution of the area of the interface, the time of diffusion, of convection, the competition with other species *etc*... resulting in a complex function $\Gamma_i = f(c_i, A, \Gamma_j, t, ...)$ which is hard to describe in a general case. Even for a single species on an interface at rest in contact with an infinite bulk, the proper description of the diffusion problem is not trivial, as suggests the work of Ward, Tordai [19].

If we now want to capture the physics of these processes with scaling laws, we need to define several quantities. First the diffusion coefficient D_i $(\mathrm{m^2/s})$ giving the time τ for a species i to diffuse through a width l by: $\tau = l^2/D_i$. Second, what we will call the reservoir length $h_{\Gamma,i} = \Gamma_i/c_i$ which is a length giving an estimate of how deep we need to go in the bulk to gather enough surfactants to populate the interface. For surfactant molecules, this length is actually a good indicator of their solubility: soluble surfactants have a big population in the bulk, and we do not need to go "that far" to populate the interface ($h_\Gamma \longrightarrow 0$), insoluble surfactants are all the interface, and are barely present in the bulk ($h_\Gamma \longrightarrow \infty$).

These two limits, with SDS closer to the soluble limit and DOH closer to the insoluble limit, change drastically the physics of the interface if we want to deform it. This is well illustrated in

the Fig.8 from Manikantan *et al.* [20]. For a pure liquid (case **A**), the creation of an amount ΔA of interface has an energy cost given by the definition $\Delta F = \gamma_0 \Delta A$. For a soluble surfactant (case **B**), creating the same amount of interface requires to bring surfactants from the bulk to the interface, which is ensured by the vast amounts of surfactants present there, and the cost is $\Delta F = \gamma_{eq} \Delta A$ with γ_{eq} a surface tension of equilibrium for a given population c of surfactant in the bulk. For a perfectly insoluble surfactant (case **C**), the population at the interface is fixed and no exchange with the bulk is authorised, meaning that the surface tension γ varies as the interface is deformed leading to a complex energy contribution $\Delta F = \int \gamma(\Gamma) dA$ (**NB:** We took the example of the creation of an interface, meaning a deformation in extension of it, but the same reasoning goes for a compression, a destruction of interface requiring to evacuate surfactants towards the bulk).

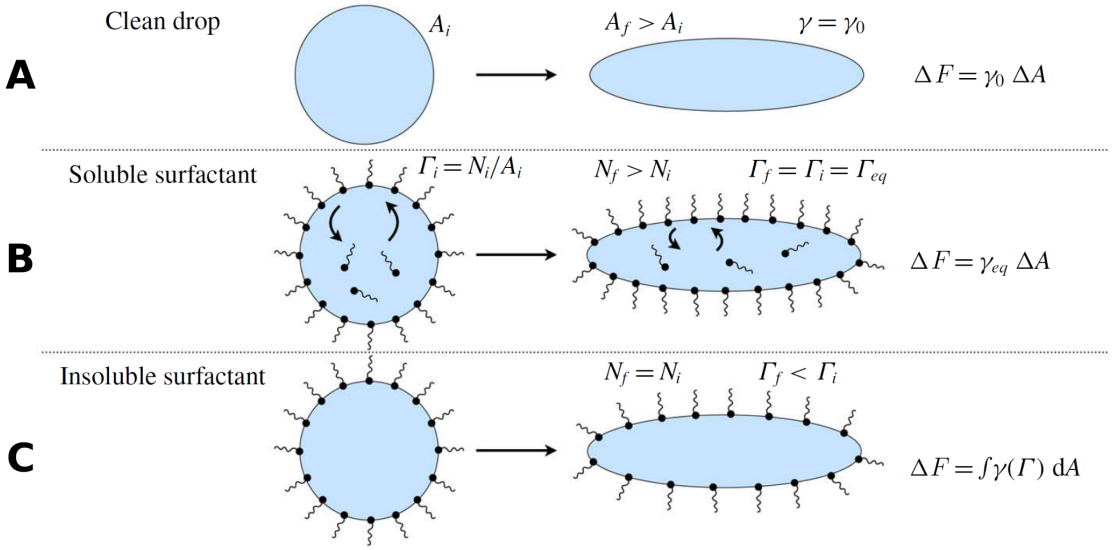

Figure 8: Energy cost of the creation of interface in the case of **A:** Pure liquid **B:** Soluble surfactants **C:** Insoluble surfactants. Credits to Manikantan *et al.* [20].

Any surfactant is between these two limits. Besides, even in the case of an infinite bulk, these limits are time dependent as it depends on the time it takes for the exchanges of surfactant to take place. In theory, any interface deformed fast enough can be considered to be loaded with insoluble surfactants. For regular surfactants such as SDS or DOH, which have approximately the same molecular sizes $R_{hydro} \sim 1\,\mathrm{nm}$, the diffusion coefficients can be estimated as:

$$D = \frac{k_B T}{6\pi\eta R_{hydro}} \sim 10^{-10}\ \mathrm{m^2/s} \tag{7}$$

Where $k_B T = 4.1 \times 10^{-21}$ J is the thermal energy, $\eta = 10^{-3}\ \mathrm{Pa \cdot s}$ is the dynamic viscosity of water and R_{hydro} the aforementioned hydrodynamic radius of the molecule. With such a diffusion coefficient, probing one millimetre takes approximately $\tau_{mm} \sim 10^4$ s and one micron $\tau_{\mu m} \sim 10^{-2}$ s, for examples. Below these times, which depend on the depth of depletion/evacuation, we cannot consider the interface to be at equilibrium, even though the surfactants are very soluble.

Furthermore, another ingredient very common with surfactant and present in our case is the presence of micelles. They fix the monomeric concentration of surfactants at the CMC, which is an important change in the diffusion field. In our specific case of SDS in micellar regime with DOH, it also represents a new time of diffusion in the system, as bulk-DOH is mainly stored in the micelles.

During the beginning of my Ph.D, a campaign of pendant drop measurements was performed with our foaming solutions in order to precisely know the equilibrium surface tensions for all our SDS/DOH mixtures. The results are shown in Fig.9. To fix ideas, the surface tension of pure water at $T = 20\,^{\circ}\mathrm{C}$ is $\gamma_0 = 72.8\,\mathrm{mN/m}$.

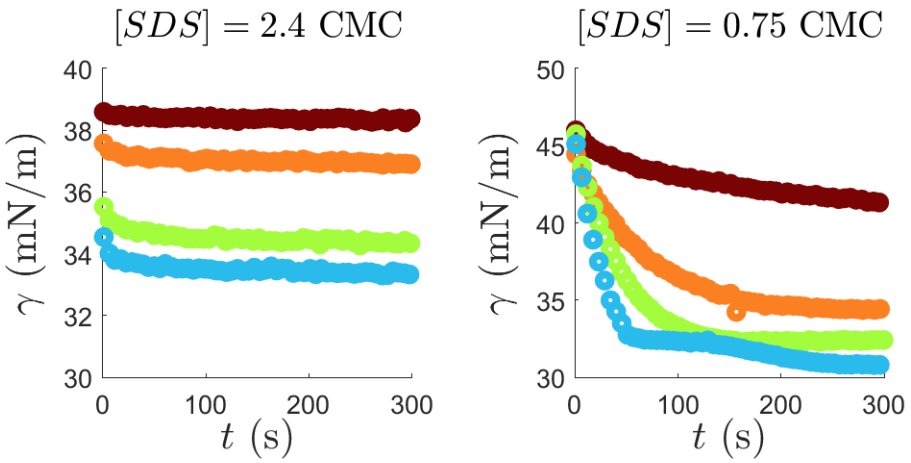

Figure 9: Surface tension of SDS/DOH mixtures measured by the pendant drop method. **Left:** Micellar regime $[SDS] = 2.4\ CMC$ for different concentration in DOH, increasing from top to bottom: 0 (red), 15 mg/L (orange), 30 mg/L (green), 50 mg/L (cyan). **Right:** Sub-micellar regime $[SDS] = 0.75\ CMC$ for different concentration in DOH, increasing from top to bottom: 0 (red), 5 mg/L (orange), 10 mg/L (green), 20 mg/L (cyan).

It has first to be noted that this method was performed at constant volume for the drop, thus injecting continuously liquid to compensate for the loss by evaporation. This may tend to concentrate the bulk in surfactant as time goes by. In the sub-micellar regime (Fig.9 Right), the equilibrium is essentially not attained. Whether or not DOH is present, the interface requires to probe deep in the drop to stabilise its population. For a drop of size $r \sim 1\,\mathrm{mm}$, we computed that it can go up to waiting for $\tau \sim 10^4\mathrm{s}$ which is not incompatible. Note that at a high concentration of $[DOH] = 20\,\mathrm{mg/L}$, we start to see what appears to be a phase transition in the form of an angular point for $\gamma(t)$. This could be related to the formation of highly concentrated regions in dodecanol at the surface (see Lu *et al.* [21], Fainerman *et al.* [22]).

In the micellar regime, surface tension stabilises over a few tens of seconds, as SDS is more concentrated overall. The remaining changes in surface tension are due to DOH and impurities, which are expected to be stored in the micelles in the bulk, enhancing their effective solubility. In the following, for most of our solutions, we work at at least twice the CMC in SDS where a γ_{eq} is very well defined.

All the parameters at stake here, micelle concentration, fraction of insoluble surfactants in

the micelles, reservoir lengths, diffusion distances, are all interdependent and represent a complex coupling between bulk and interface.

However, we have to bear in mind that all these interdependencies we just highlighted were meant in the case where our interface is in contact with an infinite homogeneous bulk. Thus we anticipate that because of the specific geometry of foam films, some of the exchange mechanisms will be blocked, and we will later see how it plays a role in the problem.

Now that we know more about the story and dependencies of γ, we need to build a proper constitutive law for the rheology of our interface, which involves other ingredients besides γ: surface viscosities.

0.1.4 Constitutive equation and 2D stress tensor $\overline{\overline{\sigma}}_s$

Let us provide our interface with a constitutive equation for a proper 2D stress tensor. It must take into account surface tension γ as well as what is called intrinsic viscosities η_s and κ_s. This description is known as a Boussinesq-Scriven model for the interface [23, 24], which has been thoroughly described by Lopez *et al.* [25] and Manikantan *et al.* [20]. In Appendix 1, we also address the construction of this tensor and the momentum conservation associated to it. It can be written:

$$\overline{\overline{\boldsymbol{\sigma}}}_s = \Big(\gamma + (\kappa_s - \eta_s)\boldsymbol{\nabla}_s \cdot \boldsymbol{v}_s\Big)\overline{\overline{\boldsymbol{I}}}_s + \eta_s\Big(\overline{\overline{\boldsymbol{\nabla}}}_s\boldsymbol{v}_s + {}^t\,\overline{\overline{\boldsymbol{\nabla}}}_s\boldsymbol{v}_s\Big) \tag{8}$$

Where γ is the surface tension, $\boldsymbol{v}_s$ the velocity at the interface, η_s the intrinsic surface shear viscosity, κ_s the intrisinc dilatational viscosity, $\boldsymbol{\nabla}_s$ the nabla operator in the basis of the interface, and $\overline{\overline{\boldsymbol{I}}}_s$ is the identity tensor in the same basis.

NB: we do not add any shear elastic response for the interface. With proteins or gels forming structures at the interface, this is a relevant ingredient though (see for example [26, 27]).

This constitutive equation is a complete 2D analogue of a 3D viscous compressible fluid. We can now write the stress balance for the interface:

$$\boldsymbol{0} = \boldsymbol{f}_{ext} + \boldsymbol{\nabla}_s \cdot \overline{\overline{\boldsymbol{\sigma}}}_s \tag{9}$$

Where $\boldsymbol{f}_{ext}$ are the exterior forces applied to the interface (such as friction with the bulk liquid and bulk gas for instance) and will be treated more thoroughly in chapter 1. If we develop the term with the stress tensor, which is done in detail in Appendix 1, the projection in the plane of the interface is [28–30]:

$$\boldsymbol{0} = \boldsymbol{f}_{ext,s} + \boldsymbol{\nabla}_s\gamma + \kappa_s\boldsymbol{\nabla}_s(\boldsymbol{\nabla}_s \cdot \boldsymbol{v}_s) + \eta_s\boldsymbol{\Delta}_s\boldsymbol{v}_s \tag{10}$$

Where $\boldsymbol{f}_{ext,s}$ is now the projection of the exterior forces in the plane of the interface. This expression eq.10 will be made explicit when needed only in the simple case of a quasi-plane interface.

Let us now focus on the second term of the right-hand side $\boldsymbol{\nabla}_s\gamma$, which is the Marangoni stress at the interface. This is actually where a lot of the physical richness lies in this equation, and we need to treat it carefully. All variations of surface tension ultimately have one origin in

the frame of our problem class: a variation of surface excess of surfactants Γ. The link between these variations is called the Marangoni modulus E_M [20, 28, 31] defined as:

$$E_M = -\Gamma \frac{\mathrm{d}\gamma}{\mathrm{d}\Gamma} \tag{11}$$

This is a thermodynamic quantity which can be computed using eq.6 and of which a model will be proposed for foam films throughout chapter 1.

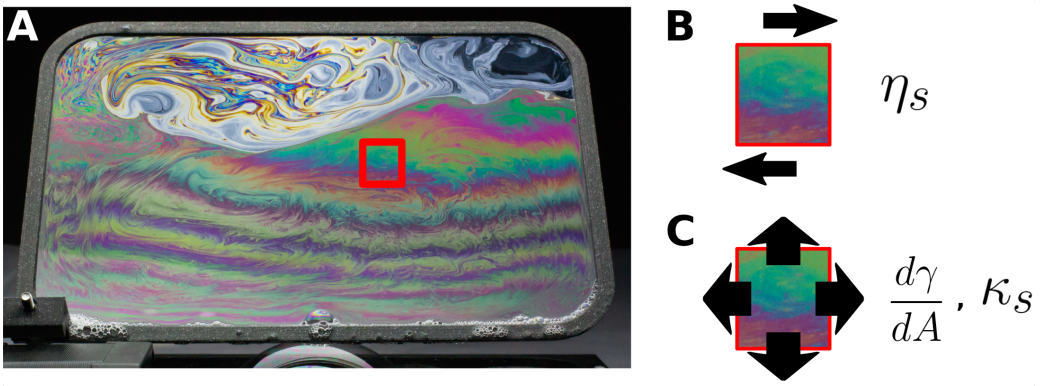

Figure 10: Ingredients for the interfacial rheology of a surfactant-laden interface: **A:** Let us look at the interface of a piece of film, and see the ingredients of the constitutive law (Credits to Eric Sorensen[4]). **B:** The interface element has a purely viscous response to shear, with a surface shear viscosity η_s. **C:** Under stretch, the film has both an intrinsinc viscous response (with κ_s the dilatational surface viscosity) and a response of surface tension $\frac{\mathrm{d}\gamma}{\mathrm{d}A}$ that includes an elastic part and an extrinsic viscous contribution. **NB:** For the sake of representation, here we take a piece of film big enough to encompass quite a large thickness variation. This has to be avoided in practice and a typical local scale in the following will be chosen below these scales. Also,we need to bear in mind that we use a foam film to illustrate the ingredients of a constitutive law which is valid in the more general case of a single interface in contact with a bulk of infinite size.

When a piece of interface A is deformed, its surface excess of surfactants $\Gamma = f(A)$ may vary. This also leads to a variation of surface tension with the area $\frac{d\gamma}{dA}$ which is taken into account in the $\boldsymbol{\nabla}_s\gamma$ term. Fig.10 summarises all the different contributions to the rheology of the interface, both under shear or dilation.

Notably, we can look at two limits. With insoluble surfactants, the population N at the interface is constant, leading to a linearly varying $\Gamma = N/A$ with $\mathrm{d}\Gamma = -N\mathrm{d}A/A^2$. With soluble surfactants, the bulk population compensates for the change in Γ during/after the deformation, leading to no change in surface excess and thus no change in surface tension. Thus, this is also a matter of how fast the deformation occurs, as soluble surfactants need time to restore their population through diffusion. This could be summarised by "any surfactant is insoluble for fast enough deformations of the interface".

[4] http://esorensen.com/soap-film-photography/

In the purely insoluble regime, the variations of γ are a conservative contribution and the deformed interface reacts with an elastic behaviour of **surface elasticity** $E_M = A\frac{d\gamma}{dA}\Big|_{insoluble}$. In the soluble regime, deforming the interface leads to a variation of surface tension $\frac{d\gamma}{dA} = f(\dot{\epsilon})$ depending on the deformation rate, which is the signature of a net loss of energy, *i.e.* an **extrinsic dilatational surface viscosity**.

This latter is not to be confused with the intrinsic viscosities η_s and κ_s which are features of the interface itself. The extrinsic dilatational viscosity originates from the bulk, whose role as a surfactant reservoir is to smooth out the surface variations of surfactant population by adsorption/desorption.

Having an experimental access to all these quantities is also very hard, and subject to a vast and perilous literature [32–36]!

Using a Langmuir-Blodgett apparatus (a quite ancient method [37, 38] which has had a century of technological improvements) can be relevant for specific cases such as the Marangoni modulus of very insoluble surfactants deposited from the gas phase [32], or complex molecules such as proteins or polymers which have very long diffusion dynamics (*e.g.* Renault *et al.* [39]). However, measuring the surface intrinsic viscosities with this apparatus poses first the problem of an unfortunate coupling between shear and compression because of the 1D stretching, and second a coupling with the extrinsic viscosity. In a classical Langmuir configuration, we end up measuring an effective viscosity which is a combination $\eta_{s,eff} = \eta_s + \kappa_s + E_M\tau$, with τ a typical time of adsorption/desorption [20].

Last but not least, the surface viscosity of a wide range of surfactants, notably soluble surfactants, are now known to be poorly measured, as bulk friction with the gas or liquid have been overlooked. This is the observation made by Zell *et al.* [36], who set an upper bound for the surface shear viscosity of soluble surfactants $\eta_{s,max} = 4 \times 10^{-9}\ \mathrm{Pa\,m\,s}$ which is below or of the order of the majority of measurements found in the literature.

We have encountered this problem of bulk friction in the frame of this work as well, and this will be subject to extensive discussions and modelling in chapter 2.

0.2 2D hydrodynamics and rheology of a foam film

Now that we have provided a proper rheological description of a single interface, let us look at the particular case this thesis work is all about: foam films. These systems are peculiar because of the extreme aspect ratios between the thickness separating two interfaces ($h \sim 10^{-6}\mathrm{m}$) and the typical length scales in the tangential directions to the interfaces ($\ell \sim 10^{-4} - 10^{-2}\mathrm{m}$). This has a lot of consequences on the viscoelastic response of the interfaces under deformation, as the total quantity of surfactants present at the interfaces can easily be of the order of/much greater than the quantities contained in the thin bulk separating them.

0.2.1 Foam films only have plug flows far from the meniscus

A first important piece of knowledge about foam films is that their Poiseuille flows due to local pressure gradients are very slow. The direct consequence is the uniformity of the velocity field

along the thickness of the film: a plug flow. Thus, a moving piece of interface carries its bulk all along its way! This is the sliding puzzle dynamics.

Let us put some numbers on the Poiseuille component of the flow. Using the geometry of Fig.11 for an element of film, we get the typical difference of pressure: $\Delta p \sim \gamma_0 h/\ell^2$. This leads to the typical Poiseuille velocity v_p between the interfaces:

$$v_p \sim \frac{h^2 \Delta p}{\eta \ell} \sim \frac{\gamma_0 h^3}{\eta l^3} \sim 10\,\mu\mathrm{m/s} \tag{12}$$

Where $\eta \sim 10^{-3}\mathrm{Pa}\cdot\mathrm{s}$ is the viscosity of water and $\gamma_0 \sim 10^{-2}\mathrm{N/m}$ the equilibrium surface tension of the foamy solution. **This velocity will be small compared to any other velocity seen in our foam films. Only block movements of both interfaces and the bulk they sandwich are enabled. This notably allows the existence of localised gradients of thickness in the film for times much longer than our typical time of experiments** $\tau_{def} \sim 1\,\mathrm{s}$**.**

0.2.2 Thin bulk means fast chemical equilibrium

Following up on the constitutive law for one interface eq.8, and the stress balance attached to it, what we need is an equation for γ in order to get a proper set of 2D Navier-Stokes equations. However, we just saw in subsection 0.1.4 that the coupling with an infinite bulk makes it very difficult to describe. To further advance, **we need to start not speaking of one single interface anymore, but rather look at our specific case of foam films where the bulk is thin enough for its surfactant reservoir to display finite size effects.**

As mentioned in subsection 0.1.4, the surface tension of a deformed interface is a function of time tending towards an equilibrium value imposed by the chemical equilibrium with the bulk. Let us have a look at the typical times of exchanges in a foam film. The geometry is shown in Fig.11.

Here, the thickness of the foam film $h \sim 1\,\mu\mathrm{m}$ imposes a confinement in the vertical direction. Also, we anticipate that the dynamics we will be looking at take place at the order of $\tau_{def} \sim 1\,\mathrm{s}$, and that all typical sizes in the tangential directions of film will be greater than/of the order of $\ell \sim 100\,\mu\mathrm{m}$.

Given these orders of magnitude, it is now possible to compute the time it takes for the interface to equilibrate with the bulk. In the case of a fresh interface in contact with a bulk very limited in depth, the main adsorption mechanism for times $t < \tau_{def}$ is diffusion [22, 40]. In this case, the time it takes for the chemical equilibrium to be established is $\tau_{d,\perp} = h^2/D \sim 10^{-2}$ s with $D \sim 10^{-10}$ m^2/s from eq.7. This time is much lower than the typical time of deformation, and **we thus consider the chemical equilibrium between the bulk and the interfaces to be instantaneous**.

In the tangential direction, all typical sizes are greater than $100\,\mu\mathrm{m}$ meaning that the transport by diffusion is here a matter of $\tau_{d,\parallel} = \ell^2/D \sim 10^2$ s. Also, we need to evaluate the bulk advection transport due to the Poiseuille flows computed in subsection 0.2.1 with its velocity $v_p \sim 10\,\mu\mathrm{m/s}$ and thus to a typical time of transport over ℓ:

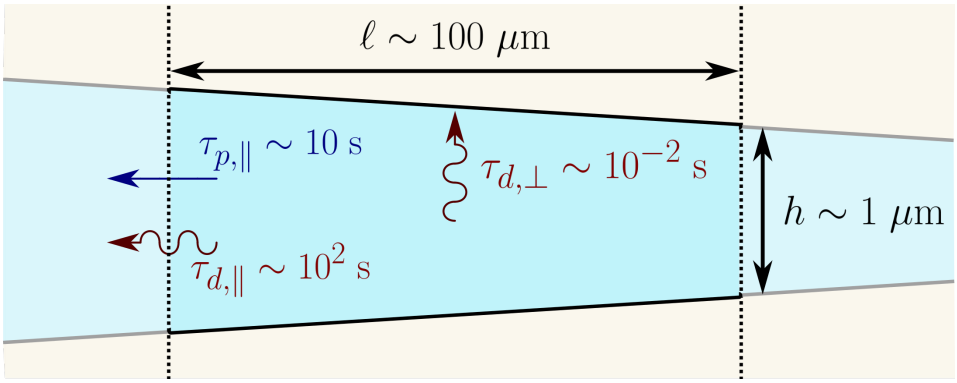

Figure 11: Side view of an elementary piece of film (a slab of the sliding puzzle game). For typical dimensions $\ell \sim 100\,\mu$m in the tangential directions of the film, the typical times of transport by diffusion and Poiseuille flow $\tau_{d,\parallel}$ and $\tau_{p,\parallel}$ are long compared to the time of dynamics $\tau_{def} \sim 1$ s, whereas in the normal direction, the thickness $h \sim 1\,\mu$m make diffusion be almost instantaneous with $\tau_{d,\perp} \sim 10^{-2}$ s.

$$\tau_{p,\parallel} \sim \frac{\ell}{v_p} \sim 10\,\mathrm{s} \tag{13}$$

Meaning that we have in both cases $\tau_{p,\parallel}, \tau_{d,\parallel} \gg \tau_{def}$ **and we can consider the film element to be a closed system with respect to surfactant conservation far enough from the meniscus** (where the thickness rapidly increases).

0.2.3 First model for film elasticity and its physical origin

Let us consider a piece of film of the same dimensions as described in Fig.11 with a single surfactant in the micellar regime (we discuss qualitatively the case of micellar SDS/DOH mixtures at the end of this subsection and quantitatively with the full chapter 1 dedicated to it). As demonstrated earlier in subsection 0.2.2, it can be considered as a closed system whose interfaces are at equilibrium with the bulk for deformations in the typical time range $\tau \sim 10^{-2} - 10\,\mathrm{s}$. This piece of bulk at rest is shown in Fig.12 Left, where the surface excess of surfactants $\Gamma = \Gamma_{eq}$ and the bulk concentration $c = c_{eq}$ are at equilibrium.

We want to impose a deformation ϵ in the direction tangential to the film, meaning the lengths in this direction become $L_\parallel = L_{\parallel,0}(1+\epsilon)$ and in the direction normal to the film $L_\perp = L_{\perp,0}/(1+\epsilon)$. The deformation remains of the order of $\epsilon = 1$ at most. Here we implicitly use a 2D model invariant by translation in the direction normal to the plane of the figure.

When we impose the deformation, the piece of film is stretched, and both areas A_0 of the interfaces are extended by the same factor $A = A_0(1+\epsilon)$. Their surface excesses Γ remain the same for both interfaces at all times. Volume is conserved $V = Ah = A_0 h_0$ imposing $h = h_0/(1+\epsilon)$. This leads to the conservation of the total population of surfactants:

$$2\Gamma_{eq} A_0 + c_{eq} A_0 h_0 = 2\Gamma A + cAh \tag{14}$$

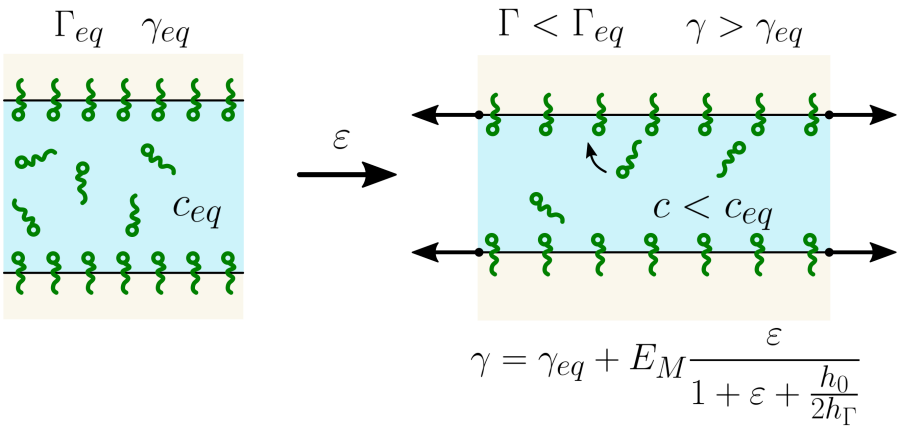

Figure 12: Elastic response of a single surfactant in the sub-micellar regime due to finite size effects of the bulk. Stretching a piece of film by a factor $(1+\epsilon)$ leads an increase of the area, thus diluting the surface excess Γ_{eq} of surfactants present at the interface. This dilution is compensated by the population present in the bulk, as the equilibrium is instantaneous given the small thickness of a foam film (*cf.* subsection 0.2.2). Because of the tiny volume, the bulk population of surfactants c_{eq} undergoes a significant drop, down to a value $c < c_{eq}$, thus balancing a decreased population $\Gamma < \Gamma_{eq}$ at the interface. This decrease of Γ leads to a reversible increase of surface tension $\gamma > \gamma_{eq}$. The same reasoning goes for a compression of the film $(\epsilon < 0)$.

We can now reintroduce the reservoir length $h_\Gamma = \Gamma/c$ which is considered here as a constant of the chemical equilibrium linking the surface and bulk populations of surfactants (this is the simplest model for the chemical equilibrium, and it already captures the physical origin of foam film elasticity, chapter 1 shows a more accurate one based on Langmuir isotherms). This allows us to rewrite the equilibrium as:

$$\Gamma\Big(1 + \epsilon + \frac{h_0}{2h_\Gamma}\Big) = \Gamma_0\Big(1 + \frac{h_0}{2h_\Gamma}\Big) \tag{15}$$

Thus, deforming the piece of foam film results in a change of both the concentration and the surface excess of surfactants if the term h_0/h_Γ remains of the same order of magnitude as $(1+\epsilon)$. That is if the film is thin enough for its bulk to be significantly depleted by a change of surface of the interfaces. With a change of surface excess, the surface tension of the interfaces $\gamma_{top/bot} = \gamma$ also changes at first order through the Marangoni elastic modulus defined by eq.11. Thus, a simplified expression for γ can be written:

$$\gamma = \gamma_{eq} + E_M \frac{\epsilon}{1 + \epsilon + \frac{h_0}{2h_\Gamma}} \tag{16}$$

This is the physical origin of foam film elasticity [8, 9], and it is not a dynamic process due to a sorption time, but a finite size effect of the bulk acting as a reservoir. This completely blocks the extrinsic dissipation originating from the bulk. Also, it has to be noted that this analytical expression relies on two bold approximations: that the surface excess is given by $\Gamma = ch_\Gamma$ and that γ varies linearly with Γ at first order.

Chapter 1 provides a more accurate model for film elasticity that I developed, taking into account the non-linear couplings between γ and Γ, and Γ and c, as well as the presence of micelles.

This elastic behaviour is thus conditioned by the reservoir length h_Γ which needs to be of the order of or greater than the typical thickness of the film $h_0 \sim 1\,\mu\mathrm{m}$. This is especially true for poorly soluble surfactants such as DOH where we estimate $h_{\Gamma,DOH} > 5\,\mu\mathrm{m}$ in Bussonnière *et al.* [4] based on the works of Fang *et al.* [41, 42]. Micellar SDS is much more concentrated in the bulk, and a first estimation using $\Gamma_{SDS} \sim 10^{-6}\ \mathrm{mol/m^2}$ [42], $c_{SDS} \sim 10\,\mathrm{mol/m^3}$ yields $h_{\Gamma,SDS} \sim 0.1\,\mu\mathrm{m}$ meaning the $h_0/2h_{\Gamma,SDS}$ term dominates and the elastic contribution of micellar SDS can be neglected *a priori*.

Also, this elasticity and the expression eq.16 for the surface tension remain valid as far as the piece of film can be considered to be a closed system at chemical equilibrium. That is at times $\tau \gg 10^{-2}\mathrm{s}$ long enough for the bulk-interface equilibrium to be reached, and $\tau \ll 10^{2}\mathrm{s}$ short enough for surfactant exchanges with neighbouring pieces of films to be neglected.

Lastly, the time evolution of γ due to the dissipation intrinsic to the interface is discarded here (*i.e.* the response of γ to $\dot{\epsilon}$ through η_s and κ_s). In the range of attainable strain rates $\dot{\epsilon}$, E_M dominates [4].

0.2.4 Far from the meniscus, film tension is uniform

Now that we have clarified the physical origin of foam film elasticity, we need to look at the tension balance in the film in order to describe the mechanics of not only a piece of film (size $\ell \sim 100\,\mu\mathrm{m}$), but of the foam film as a whole (size $L \sim 1\,\mathrm{cm}$). To do so, let us introduce the film tension σ^f, which is the total action of a piece of film (black dotted rectangle in Fig.13) on its neighbour. **This σ^f includes the capillary stress in the bulk, as well as the surface tension of both interfaces (and the surface elastic and viscous contributions this latter contains)**. At rest and for symmetric flat interfaces, we simply have $\sigma^f_{eq} = 2\gamma_{eq}$.

We also define a 2D model for a foam film of length L, of local coordinates (s, ζ) as shown in Fig.13, and invariant by translation along the third axis normal to the figure. The velocity in the liquid bulk is written $\boldsymbol{v} = u\ \boldsymbol{e}_s + w\ \boldsymbol{e}_\zeta$ and the thickness of the film $h(s)$ depends on the local abscissa s in the general case.

We start by writing the conservation of momentum projected along the s direction for a piece of film whose boundaries are set between the local abscissa s and $s + \mathrm{d}s$ and with ordinates ζ so that they include both interfaces (black dotted rectangle in Fig.13). It can be expressed as an integral over the liquid bulk $\zeta \in [0, h]$:

$$\int_0^h \rho\Big(\frac{\partial u}{\partial t} + u\frac{\partial u}{\partial s} + w\frac{\partial u}{\partial \zeta}\Big)\mathrm{d}\zeta = \frac{\partial \sigma^f}{\partial s} + \rho g_s h + f_g \tag{17}$$

Where g_s is gravity projected along s, f_g is the friction of the piece of film with the gas phase.

Expressing the conservation of volume with the invariance by translation along the normal to $Os\zeta$, we have $\frac{\partial w}{\partial \zeta} = -\frac{\partial u}{\partial s}$ and after a few integrations in eq.17:

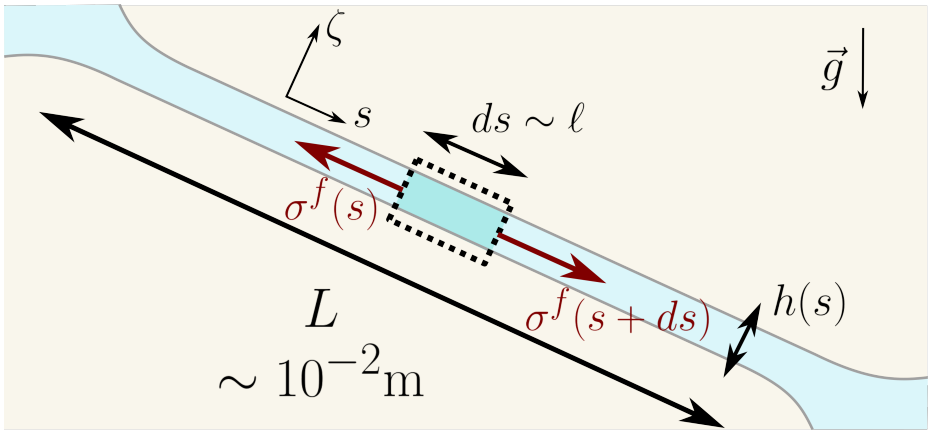

Figure 13: Force balance on a film element of Fig.11 (a slab of the sliding puzzle, in case the reader had forgotten our beloved analogy). A typical length for a foam film is given $L \sim 10^{-2}$ m (which is among the longest lengths of film encountered with real macroscopic liquid foams).

$$\rho\Big(\frac{\partial(h\langle u\rangle)}{\partial t} + \frac{\partial(h\langle u^2\rangle)}{\partial s}\Big) = \frac{\partial \sigma^f}{\partial s} + \rho g_s h + f_g \tag{18}$$

Where the brackets stand for the mean value over $\zeta \in [0, h]$.

This is where we need to put some orders of magnitude to further advance and estimate each term. To do so, we take the typical scales:

- $\tau_{def} \sim 1\,\mathrm{s}$ the typical time scale
- $L \sim 10^{-2}$ m the typical length scale along s, yielding $U \sim \frac{L}{\tau_{def}} \sim 10^{-2}$ m/s
- $h \sim 10^{-6}$ m the typical length scale along ζ
- $\rho = 10^3$ kg/m^3 the bulk density (water in most cases, including ours)
- $g_s \sim 10\,\mathrm{m/s^2}$ the projected gravity

Inertial terms scale both as $\frac{\rho h}{\tau_{def}^2} \sim 10^{-5}$ Pa and weight scales as $\rho g_s h \sim 10^{-2}$ Pa.

The air friction scales as $f_g \sim \eta_g \frac{U}{\delta}$, where $\eta_g \sim 10^{-5}$ Pa s is the gas viscosity and δ is a Blasius length over which momentum diffuses in the neighbouring gas. We estimate $\delta \sim \sqrt{\frac{\eta_g \tau_{def}}{\rho_g}} \sim 10^{-3}$ m with $\rho_g = 1\,\mathrm{kg/m^3}$ the air density and we get $f_g \sim 10^{-4}$ Pa.

The gradient of film tension is estimated by estimating the value of the film elasticity $E_f \simeq 2E_M$, which is of the order of $E_f \sim 10^{-2}\,\mathrm{N\,m^{-1}}$ [4, 6], yielding the scaling $\frac{\partial \sigma^f}{\partial s} \sim \frac{E_f \epsilon}{L} \sim 1\,\mathrm{Pa}$ with $\epsilon \sim 1$ which is very large compared to any other term. Note that this can be seen as a lower estimate, as the intrinsic viscosities of the interfaces or the capillary stress may also contribute to film tension (we will later see that they do not far from the edges of the foam film).

We can thus conclude that for a typical deformation of more than $\epsilon_{min} = 10^{-2}$, no other force can balance the tension gradient, and thus **film tension σ^f is uniform in a foam film, far from its edges**. This is the limit of high elasticities, which will essentially be always valid in the frame of our study, as well as for a very wide range of foams.

However, it has to be noted that in other situations, gravity can be important [43], or inertia for film rupture [44–46].

0.2.5 The incompressible interface limit

Since Mysels, Frankel and Shinoda [47–49] and the first actual measurements of foam film elasticities E_f by Prins *et al.* [5,50], a first key observation is that foam films are hard to stretch. This means that the cost E_f to pay is high.

Most of the time, we assume incompressible interfaces, meaning we close the problem imposing:

$$\boldsymbol{\nabla}_s \cdot \boldsymbol{v}_s = 0 \tag{19}$$

This is a robust assumption for a wide range of problems [51–53] which we will later use in chapter 2. This hypothesis only finds its limits when the films are stretched or compressed by imposing a significant change of area as we will later see in chapters 1 and 3. In Appendix 2, we propose a general framework for compressible interfaces in the limit of high elasticities.

0.3 Flows in foam films at a junction with a meniscus

Since the beginning of this manuscript, I have been carrying the metaphor of the sliding puzzle for a foam film to establish the idea that pieces of films are advected patches interacting with one another not through bulk Poiseuille flows, but rather with their surface rheology. This is a faithful representation up to a certain extent, and this section proposes to see the situations where it is not anymore. That happens notably for times much longer than our typical $\tau_{def} \sim 1\,\mathrm{s}$, or at the edges of a foam film where it is put in contact with a meniscus. The typical dimensions for a meniscus (and its radius of curvature) is of the order of $r_m \sim 100\,\mu\mathrm{m}$, which is two orders of magnitude above the typical thickness of a film!

All the following subsections correspond each to a phenomenon which will be observed in my experiments. Some of them are used to our advantage (Frankel film extraction), others hinder my measurements (Marginal regeneration, Rayleigh-Taylor instability...). And all need a proper description.

0.3.1 Lubrication equations in a foam film

We aim here at establishing a general set of equations for the thickness profile of two symmetrical incompressible interfaces set in motion. In the bulk of a foam film, the liquid flow is governed by the Stokes equations:

$$\begin{cases} \eta\ \boldsymbol{\Delta v} - \boldsymbol{\nabla} p = \mathbf{0} \\ \boldsymbol{\nabla} \cdot \boldsymbol{v} = 0 \end{cases} \tag{20}$$

Where η is the bulk viscosity and p the pressure in the liquid.

Given the geometry of millimetric/centimetric foam films (the same aspect ratio as if a paper sheet was 10 to 100 times thinner), the bulk flows are described using the lubrication equations. We will use the notations of Fig.14, with the Oxz plane being the medium plane of the foam film, and $y = h(x)$ the ordinate locating the position of the interface. For now we consider the 2D problem of two symmetrical incompressible interfaces. They are described by any semi-thickness field $h(x)$ varying slowly enough to remain in the frame of the lubrication approximation, and with an imposed velocity $v_x(x, h(x)) = U$ which is uniform along the interface as this latter is incompressible.

The lubrication equations can be written as follows (established in [54, 55]):

$$\begin{cases} \eta \partial_{yy} v_x - \partial_x p = 0 \\ \partial_y p = 0 \\ \partial_x v_x = -\partial_y v_y \\ v_x(x, h(x)) = U \end{cases} \tag{21}$$

Where lines 3 and 4 are respectively the conservation of volume and of the area of interface. The pressure field is only depending on x, and as the curvature of the interfaces remains small, we can write p as the Laplace pressure jump: $p = \gamma_0 \partial_{xx} h$, where γ_0 is the surface tension of the interfaces. Given the independence of the pressure gradient with y, the boundary condition $v_x(x, h(x)) = U$ and the geometry of the problem, the velocity field can be integrated as:

$$v_x(x, y) = U + \frac{1}{2}\frac{\gamma_0}{\eta} \partial_{xxx} h\ (y^2 - h^2) = v_{ad} + v_{cap} \tag{22}$$

This velocity field can be integrated to get the flow rate:

$$Q = \int_{-h}^{h} v_x(x, y) \mathrm{d}y = 2Uh - \frac{2}{3}\frac{\gamma_0}{\eta} h^3 \partial_{xxx} h \tag{23}$$

Whose conservation law (line 3 of eq.21) yields the equation for h:

$$\partial_t h + U \partial_x h - \frac{1}{3}\frac{\gamma_0}{\eta} \partial_x (h^3 \partial_{xxx} h) = 0 \tag{24}$$

This is the generic equation for the evolution of a profile $h(x, t)$ given the velocity U which can be a function of time, negative or positive, but must remain uniform at the interfaces because of the surface incompressiblity condition.

This equation opens up pathways to the solutions of problems where bulk transport in foam films matter. This happens for instance near the edges of a foam film, where the flat film is connected to a meniscus, and we propose to see two examples in the following: the Frankel problem and the Aradian problem.

0.3.2 Steady state film extraction: the Frankel problem

To close the problem of eq.24, we either need to get an initial profile for $h(x, t = 0)$ or to look at its steady solutions, as well as getting more spatial conditions for h.

Here, we look at the problem of a steady film extraction from a meniscus as shown in Fig.14. It is called the Frankel's problem and has been extensively studied, both experimentally and theoretically [47, 51, 52, 56]. We take the steady state of eq.24 where we impose a given U **chosen positive along** $+x$ **for now**, and a limit of constant curvature $\partial_{xx}h \to 1/r_m$ when $x \to -\infty$ in the meniscus.

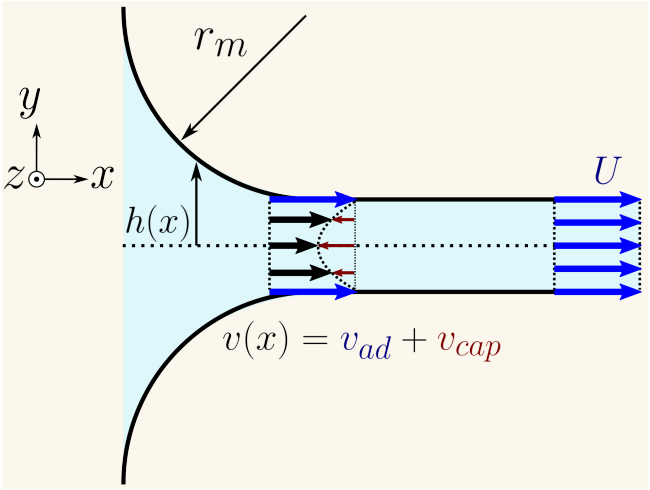

Figure 14: Notations for the Frankel problem. A flat film is connected to a meniscus along the x axis. A steady plug flow U is imposed far from the meniscus, and this latter has a constant curvature $\partial_{xx}h = 1/r_m$ in $x \to -\infty$. The steady flow at the junction (called the dynamic meniscus) is the sum of an outward plug flow v_{ad} and an inward capillary flow v_{cap}.

The equations of the problem thus write:

$$\begin{cases} U\partial_x h - \frac{1}{3}\frac{\gamma_0}{\eta}\partial_x(h^3\partial_{xxx}h) = 0 \\ \partial_{xx}h(x \to -\infty) = 1/r_m \\ v_x(x \to +\infty, y) = U \end{cases} \tag{25}$$

Which can be solved either numerically or with scaling laws. Let us proceed with the latter. As we impose a constant velocity far from the meniscus, mass conservation imposes the existence of the limit $h(x \to +\infty) = h_\infty$, giving us a typical scale for h of which we want to make the scaling explicit.

The meniscus imposes $\partial_{xx}h = 1/r_m$, meaning the typical scale ℓ_x over which h varies is given by $\ell_x \sim \sqrt{h_\infty r_m}$. By injecting this in eq.25 (line 1), it comes:

$$h_\infty \sim r_m Ca^{2/3} \tag{26}$$

Where $Ca = \frac{\eta U}{\gamma_0}$ is a capillary number comparing viscous and interfacial forces. Numerical calculations give the prefactor which is $\simeq 1.34$.

This law means that the faster a foam film is extracted from a meniscus, the thicker are the newly created pieces of film with a power law $2/3$ with the velocity of extraction. In practice when it comes to stretching a foam film at a given velocity, it is qualitatively very useful, as it allows us to extract films quite uniform in thickness in a very repeatable way. **This is what we will call a Frankel film, and we will have an extensive use of this name.**

Also, it has to be noted that although the interface is kept incompressible, it is subject to a difference of surface tension $\Delta\gamma^{out}$ between the meniscus and the flat film. This is no contradiction, but the fact that the incompressible limit is equivalent to taking $E_f \to \infty$ and the deformation $\epsilon \to 0$ with their product being constant and equals to the difference of tension $\Delta\gamma^{out} \sim E_f\epsilon$. It can be numerically computed and is [48]:

$$\Delta\gamma^{out} = 3.84\gamma_0\ Ca^{2/3} \tag{27}$$

The main use of the Frankel's problem we make in practice is when we stretch a foam film. Initially, the foam film is of thickness h_{init} and is linked to a meniscus. Stretching it means imposing a plug flow in the initial film, because of the arguments developed in subsection 0.2.1. **The steady response of the system described by the Frankel's law leads to the situation shown in Fig.15: some film is extracted at the same steady velocity U than the preexisting film, but with a thickness h_∞ set by the law 26.** Both films exist in the same plane, with a thickness jump between them. This thickness heterogeneity is stable, and would tend to smooth out at much longer times $\tau \gg 1\,\mathrm{s}$ with a dynamics given in [57]. **Thus, the frontier between the two films is a material point whose tracking will be useful many times in this manuscript. Also, in practice, even for small imposed velocities, the Frankel films are generally thicker than the preexisting films.**

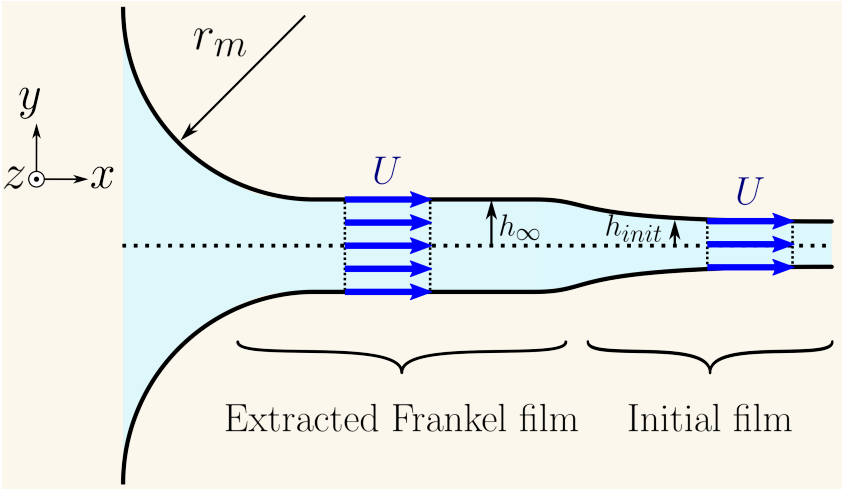

Figure 15: Extraction of a Frankel film at a steady velocity U. In the general case, the preexisting flat film set in motion has a thickness $h_{init} \neq h_\infty$. In practice, we often have $h_\infty > h_{init}$.

Now a complete other range of problems: what about taking a negative value for U? The problem is actually solved in a completely different way, as h_∞ has to be provided besides U,

and is not a mere consequence of the balance between viscous and capillary forces. The resulting tension in this case writes [48]:

$$\Delta\gamma^{in} = \gamma_0 \ (3Ca)^{2/3} \left(2.55\alpha^{1/3} - 2.68\right) \tag{28}$$

Where $\alpha = (h\infty/r_m) \ (3Ca)^{-2/3}$.

This is an important result. Tension has a unique value in the film (as seen in subsection 0.2.4), and a unique value in the meniscus. The gap between these two values can be filled either by a $\Delta\gamma^{in}$ or a $\Delta\gamma^{out}$ with respectively a negative or positive U and for different thicknesses h_∞ (the nullity of U is no practical case when a film is being deformed). This leads to an instability which spontaneously breaks the symmetry along the dimension parallel to the meniscus: this is called marginal regeneration, and we will describe it later in subsection 0.3.4.

Important remark: The problem of taking into account the visco-elasticity of the interfaces (meaning we have $U(x)$ no longer uniform) is quite a recent theoretical advance, and can be found in Seiwert *et al.* [51, 52].

0.3.3 Capillary suction near the meniscus: Aradian's marginal pinching

Let us look now at the instationary problem of a flat film at rest ($U = 0$) put into contact with the meniscus. We will call this problem the Aradian problem [58]. It has the same configuration as previously, but now we keep the time varying term of eq.24 and discard the convection term:

$$\begin{cases} \partial_t h - \frac{1}{3}\frac{\gamma_0}{\eta}\partial_x(h^3\partial_{xxx}h) = 0 \\ \partial_{xx}h(x \to -\infty) = 1/r_m \\ v_x(x \to +\infty, y) = 0 \\ h(x \to +\infty) = h_\infty \end{cases} \tag{29}$$

It describes what happens to a film at rest when put into contact with a meniscus. As the film is flat (at air pressure) and the meniscus is curved with a negative pressure, the meniscus sucks back fluid from the film, which is what has already been called **capillary drainage** in this manuscript. However, the film does not drain uniformly along x, and we rather see the formation of a depleted zone near the meniscus whose geometry includes different lengths, as shown in Fig.16.

The main problem leading to such a multiplicity of lengths is that although the draining Poiseuille flow develops over a large length W, the majority of the gradient of curvature $\partial_{xxx}h$ linking the meniscus to the flat film, and which is the main driving force, develops over a very localised zone w. All that means the problem needs a careful handling, and a mathematical treatment which involves an asymptotic matching between the two scales. If we now want to find the main results using scaling laws, we also need to do it carefully, by considering the following:

- h_∞ and W are the typical scales for large x. h_∞ is a given parameter from the initial conditions, W is a variable of which we seek the scaling. They are linked by the conservation of flow rate (line 1 of eq.29), leading to: $W \sim h_\infty\left(\frac{\gamma}{\eta h_\infty}\right)^{1/4} t^{1/4}$.

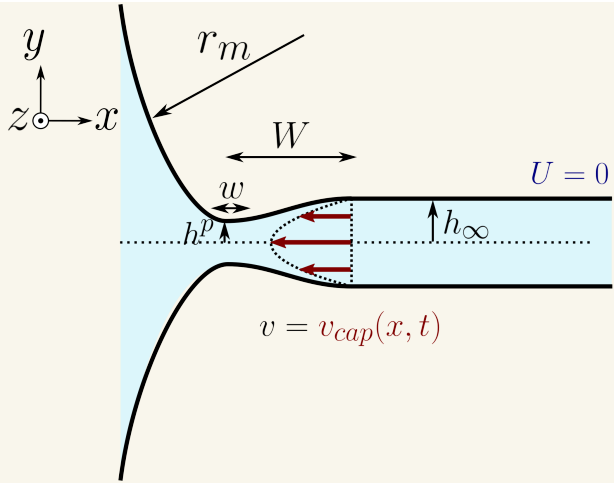

Figure 16: Notations for the Aradian problem. A flat film of thickness h_∞ is connected in $x \to -\infty$ to a meniscus of constant curvature $\partial_{xx}h = 1/r_m$. The flat film is immobile in $x \to +\infty$ and we look now at the unsteady problem of the time evolution of the film at the junction. Because of capillary suction acting alone, the initial flat film locally thins out with a non-trivial multi-scale dynamics.

- h^p and w are the typical scales for small x around the position of minimal $h \sim h^p$. Both of them are sought variables, linked by the curvature condition of the meniscus (line 2 of eq.29), leading to: $h^p/w^2 \sim 1/r_m$.
- The matched asymptotic expansion linking the two scales, developed in [58], imposes to match the slopes so that: $h^p/w \sim h_\infty/W$.

We thus have three equations for three variables of which we write the scalings:

$$\begin{cases} W \sim h_\infty \left(\frac{\gamma}{\eta h_\infty}\right)^{1/4} t^{1/4} \\ w \sim r_m \left(\frac{\gamma}{\eta h_\infty}\right)^{-1/4} t^{-1/4} \\ h^p \sim r_m \left(\frac{\gamma}{\eta h_\infty}\right)^{-1/2} t^{-1/2} \end{cases} \tag{30}$$

These scalings reveal a complex dynamics (whose complete calculation is full of subtleties) which is at the origin of the dimple observed in thin film balance or AFM experiments [59–62].

This process is directly linked to the ability of the interface to create tension gradients. If we remove this from the interface, theoretical arguments show that no pinching occurs [63].

0.3.4 Marginal regeneration

Marginal regeneration is a phenomenon occurring at the junction between a foam film and its bordering menisci where we observe simultaneously thin patches of film going out of the meniscus and thicker ones going in the meniscus through channels separating the thin patches. It has been first observed and named by Mysels *et. al* [47] in 1959. It appears spontaneously in vertical foam films where it was first observed, in which gravity set patches of film in motion, producing

mushroom-shaped contrasts of colours in foam films and bubbles with the right lighting (the coupling between gravity and the thickness of foam films and the existence of a Raleigh-Taylor-like instability is discussed in subsection 0.3.5). Since then, it has been mostly studied in vertical situations [46, 64, 65].

However, it is actually best observed with horizontal foam films undergoing a uni-axial compression, as illustrated in Fig.17. This is an experiment conducted by Trégouët *et al.* [66]. Pictures **A**-**D** are a timelaspe of a deformed foam film with marginal regeneration seen with fluorescence imaging (the brighter the thicker).

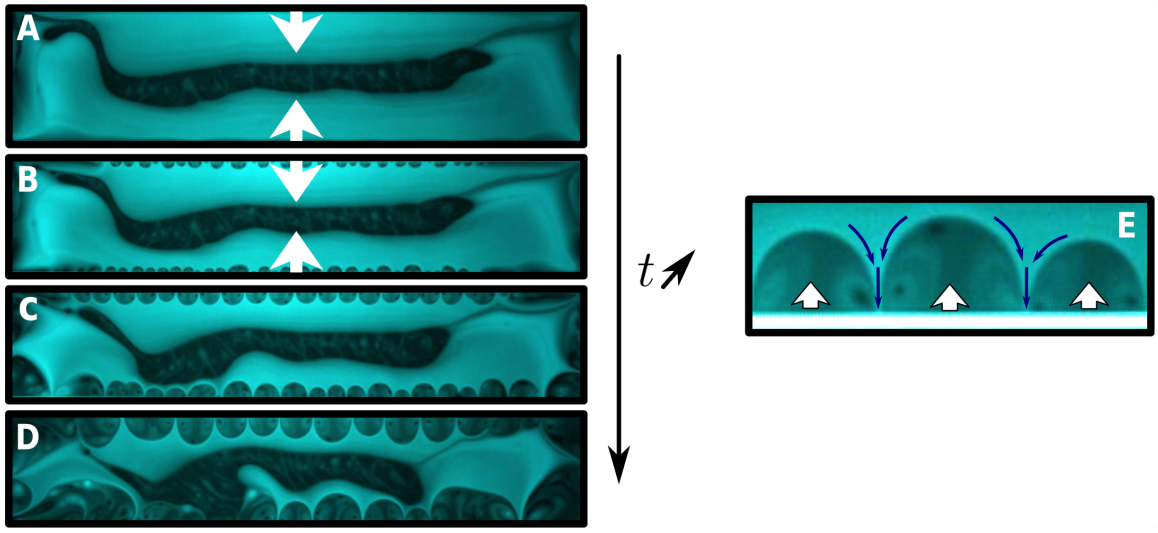

Figure 17: Foam film undergoing an initial uniaxial compression (scale of the film: 6.5 cm large in the horizontal dimension) with a growing marginal regeneration instability (times from A to D: $t = 0,\ 2,\ 4,\ 7$s). The film is observed under fluorescence imaging (the brighter the thicker): **A-B:** The film is being compressed (white arrows) and small semicircular patches of thin film starts going out. **C-D:** Ripening of the patches, as they grow by more thin film extraction and coalescence of adjacent patches. **E:** Zoom at a local scale of **D**, white upward arrows bordering the meniscus (white horizontal fringe at the bottom) are the direction of thin film extraction. Blue downward arrows are for the ingoing thick patches channelled between the thin patches.

A and **B** show the film being compressed, thus forcing either the contraction of the foam film, or the evacuation of patches of film toward the edges at the menisci. Because film elasticity E_f is high (*cf.* subsection 0.2.4), the drop in tension is significant enough to ensure that the foam film does not withstand the whole compression with a global thickening of the pre-existing film, but rather by evacuating some film toward the menisci.

In pictures **B**-**D**, we see the formation of circular thin patches at the edges perpendicular to the axis of deformation. As time goes by, they grow and even coalesce.

Picture **E** is a zoom at one of these edges: it shows how some thick film goes in the meniscus (which is the white fringe at the bottom) following the blue arrows, and how some thin film goes out of it following the white arrows. The thick ingoing film is the film pre-existing the

deformation, prepared like so before the experiment, imposing a h_{thick} to the system. The thin film goes out of the meniscus spontaneously with their own thickness and velocity.

It is puzzling to see this spontaneous symmetry breaking along the pushed menisci, all the more when it involves the extraction of patches of film in the plane of an already-compressed foam film. This weird behaviour can be rationalised by considering the Frankel's problem**s** identifiable in this situation. In fact, in subsection 0.3.2, we describe the 2D problem of an advected flat foam film connected to a meniscus depending on a virtually imposed velocity U, which can be either positive (outgoing film) or negative (ingoing film). Two points must be raised with respect to the experiment of Fig.17: the Frankel's model is 2D, supposing an invariance by translation along the meniscus, while in practice we cannot impose U but rather a difference of tension $\Delta\gamma$ with the menisci by compressing the film.

Thus, the advection velocity toward the menisci is actually an experimentally free parameter that has to adapt to the imposed tension $\Delta\gamma$ (which must be uniform in the film *cf.* 0.2.4), and it can do it in multiple ways, possibly choosing different ones for different positions along the meniscus! As long as the area conservation is preserved.

Depending on the sign of U, the tension admits two different expressions: eq.27 $\Delta\gamma^{out}$ for positive U (extraction of film), eq.28 $\Delta\gamma^{in}$ for negative U (evacuation of film). The two tensions can have the same values for different velocities U and thicknesses h_∞ and it is possible to find a working point where $\Delta\gamma^{out}(U^{out}) = \Delta\gamma^{in}(U^{in}, h_\infty^{in}) = \Delta\gamma$ (Note that here h_∞^{out} is completely determined by U^{out}, and $h_\infty^{in} = h_{thick}$ depends on the initial film undergoing compression).

However, the existence of this working point is obviously not the whole story, as the thin patches develop with regular patterns: semicircular growing shapes that coalesce as they get closer to one another. The initialisation of this dynamics is still a work in progress, a solid lead being to start from an Aradian's marginal pinching profile (see subsection 0.3.3) invariant by translation along the meniscus, which is unstable and destabilises with the forcing imposed by the compression. The ripening dynamics of these patches on the other hand is already well understood, as the width of the thin patches, the width of the thick film channels and the ingoing/outgoing velocities must obey surface conservation and the uniformity of film tension at all times. This last point is developed in [66].

Finally, and to motivate why I elaborate so much about marginal regeneration, I have to say that later on this instability will be quite a recurrent limiting factor for my measurements. In fact, it eventually always appears whenever a film is being compressed. The whole chapter 3, that is the core of the experimental work of my thesis, is about how deformed foam films can relax by exchanging pieces of interface through their meniscus. In this regard, marginal regeneration will be close to my worst enemy as it breaks the main translational symmetry our models rely on. Thus, the general goal from now on is to keep the experimental conditions so that we work before the initialisation of this instability (by trial and error mostly).

Important Remark: The semicircular shape of the thin patches is the signature that a line tension exists at the border with the thicker film. Chapter 2 is dedicated to this line tension, of which a theoretical description and a measurement are detailed.

0.3.5 Rayleigh-Taylor-like instability with thickness heterogeneities and gravity

When marginal regeneration was first described [47], the thin patches were observed not as growing semicircular patterns near the border (where they are produced as discussed in subsection 0.3.4), but rather as rising mushroom-shaped pieces of film. This is not a feature of marginal regeneration itself, although it is often what comes to mind when we use this term, but of the in-plane rearrangements of the patches of film depending on their thickness in order to minimise the gravity potential energy of the foam film.

The mushroom shapes are in fact a feature of a Rayleigh-Taylor-like instability happening at the border between a thick piece of film that is on top of a thinner one. This instability is well known in the context of thin patches moving up in a film, and contributing to drainage [46, 67] but is easier to quantify with a more controlled initial thickness distribution. Such a controlled experiment from Shabalina *et al.* [68] is represented in Fig.18 **A**-**D**, showing such patterns. A foam film is stretched from top to bottom (the white arrows indicate the position of the moving bottom of the film). What we see in the coloured film is that the thin patches produced by marginal regeneration before the stretching rise to the top (*e.g.* with **C**, the yellow mushrooms are thinner than the purple film in which they rise, the latter being thinner than the grey Frankel films extracted at the top and bottom edges). In the same way, the thick grey film at the top in **D** (highlighted by the red rectangle) starts destabilising with an identifiable wavelength.

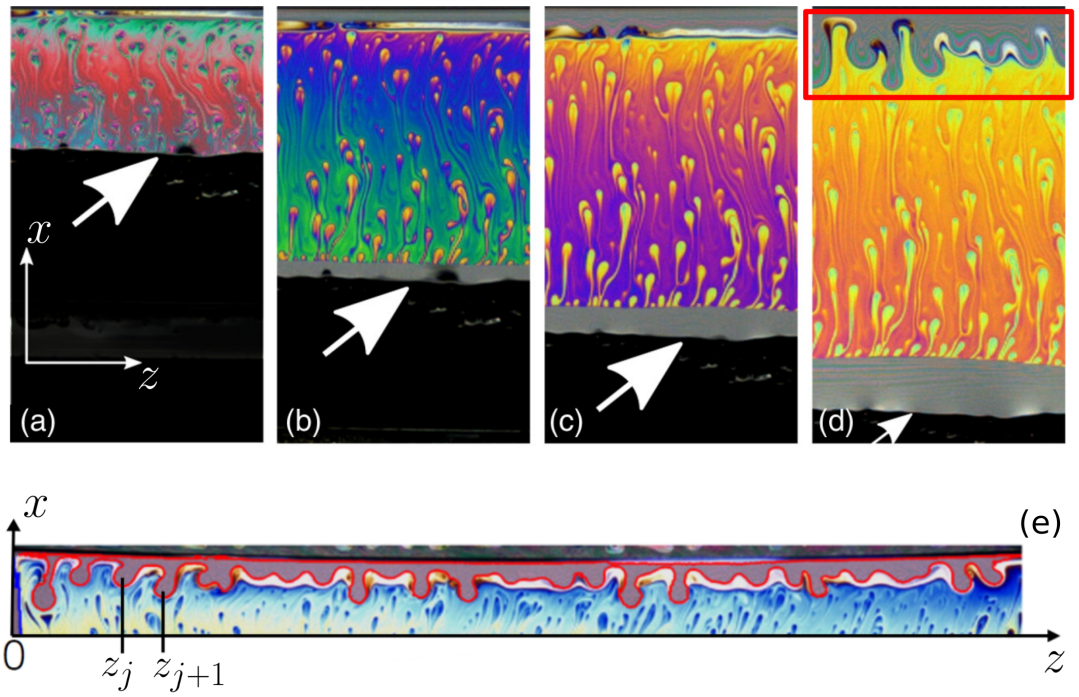

Figure 18: Stretching of a vertical film (width of (a)-(d): 10.3 mm). A 2D Rayleigh-Taylor instability occurs where thicker films are on top of thinner ones. The white arrows show the bottom of the film being stretched from **(a)** to **(d)** (resp. (a) 0 ms, (b) 67 ms, (c) 83 ms and (d) 167 ms

This instability can really be thought as a 2D analogue of the 3D Rayleigh-Taylor instability, swapping fluid density ρ for thickness of film h, pressure p for film tension σ, and bulk viscosity η for η_s a surface shear viscosity. One more exotic ingredient to add which has already been introduced in subsection 0.3.4 is the line tension T existing at the border between the two films because of the thickness jump (a full theoretical description followed by an experimental measurement is developed in chapter 2). Here, it holds the same role as surface tension in the 3D instability, as it tends to hinder the existence of the small spatial wavelengths for the border.

A linear stability analysis can give the spatial wavelength λ_c maximising the growth rate n of the instability. The latter is dominated by inertia at low λ and by viscous forces at high ones:

$$\begin{cases} n_{\mu_s} \sim \lambda \\ n_{in} \sim \lambda^{-1/2} \end{cases} \tag{31}$$

These two limits imply the existence of an optimal growth rate n_c at a given critical λ_c that can be computed with the full calculation of the linear stability analysis and which is in quantitative agreement with the wavelength measured in Fig.18(e).

This instability occurs quite rapidly at our typical time scale $\tau_{def} \sim 1\,\mathrm{s}$ (*cf.* time scales Fig.18), meaning that stretching a vertical film can be a problem depending on where we are looking at. As a Frankel film is most of the time thicker than the stretched film pulling it out of the meniscus, **it will not be possible to measure properly the outgoing quantities of films at a meniscus located on top of a vertical stretched film**. This will be another limitation for our experiments later on.

0.3.6 Evaporation

Speaking of important flows for the sake of describing our experiments, we need not to forget the influence of evaporation, which tends to uniformly thin out our foam films. As unconditioned air is never at water saturation, it remains a mechanism of great importance. The experimental work of the present thesis is taking place in this context.

In the literature, the dynamics of evaporation-induced ruptures are well rationalised for a single film [67, 69], yielding the order of magnitude for the thinning of $\sim 20\,\mathrm{nm/s}$ in normal conditions of temperature and average humidity ($\mathrm{rH} \sim 30-70\%$). However, the exact mechanism triggering the rupture of the thinned film is still only conjectured to be a fast local loss of mass in the film due to evaporation becoming important compared to film drainage. This is supposed to take place in a short amount of time which depends on the relative humidity.

With regard to our foam films, evaporation is important in the sense that their lifespan was seen to be highly dependent on the relative humidity, which was kept at a minimum threshold of $\mathrm{rH} = 55\%$ using an air humidifier. Living in Brittany also helped out.

0.4 Elementary liquid foams

Now that we have discussed what happens with a foam film and what occurs when we connect it to a meniscus, we will take a bottom-up approach towards liquid foams by looking at one scale

above: elementary liquid foams. These are arrangements of several foam films connected by menisci, defining a mesoscopic scale between the individual film and the liquid foam. **Chapters 1 and 3 concern this scale.** Thus, our goal is now to look at the hydrodynamics of these systems by probing their mechanical response around their equilibrium state.

All the following subsections constitute a state of the art for elementary liquid foams. **Notably, I detail them in a chronological way, so that it is possible to see how the hypotheses made on the surfactant exchanges in the system have gotten more and more refined over the last 20 years. The following papers represent important milestones for the problem we address in chapter 3.**

0.4.1 Plateau's laws: the local equilibrium state for the shape of liquid foams

Dry liquid foams are by no means at thermodynamic equilibrium. In fact, if we wait long enough, evaporation, gravity or capillary drainage will force rearrangements to occur. However, for intermediate times, the local structures they adopt obey several rules dictated by a local mechanical equilibrium. These are the Plateau's laws, stated by Joseph Plateau in 1873 [70] and demonstrated by Almgren & Taylor in 1976 [71]:

- Foam films have a uniform mean curvature, meaning the gas volumes they separate have each a uniform pressure given by Laplace's law (eq.5).
- Menisci are where three foam films intersect, and they do so with an angle of $120\ ^o$ which minimises the resulting interface.
- Vertices are where three bubbles meet, or equivalently where four menisci intersect. They do so with a tetrahedral symmetry, with angles of $109.47\ ^o$.

These laws hold as long as we keep the foam as ideal as possible, that is very dry, at a global mechanical equilibrium, with a uniform surface tension. In the following most of the dynamics we will be looking at are variations around this mechanical equilibrium state with respect to normal motions of the film. These variations are small, and usually are deviations of the order of $1\ ^o$ around the $120\ ^o$ of the second law.

Lastly, mechanically stressing an elementary foam out of the Plateau's law induces some dissipation, as it relaxes back to another state also prescribed by these laws [72,73]. Rationalising and predicting this is what requires the biggest efforts from our community, and what represents a pathway towards better rationalising the effective viscosities of liquid foams.

0.4.2 T1 events and the Durand-Stone experiment

If a liquid foam respecting Plateau's law undergoes shear or compression at a global scale, bubbles are rearranging at the local scale. This is the scale of elementary liquid foams. Notably, a singular event at this scale is what is called a *T1 event* [74–77] of which an illustration is shown in Fig.19. It consists of a local change of rules for the neighbourhood of bubbles, which are prescribed by the Plateau's laws again. For a 2D monodisperse hexagonal foam, it is a displacement of one

line of bubbles with respect to another one with an amplitude of one bubble. This results in the full compression of the central film of an elementary assembly of five films (represented in red in Fig.19), the temporary merging of the two menisci at its edges, and the stretching of a new film separating the two new bubble neighbours (in yellow). This is the most elementary event of rearrangement involving the merging and splitting of entire menisci (**NB:** *T2 events* also exist, consisting of a bubble disappearing and creating a vertex).

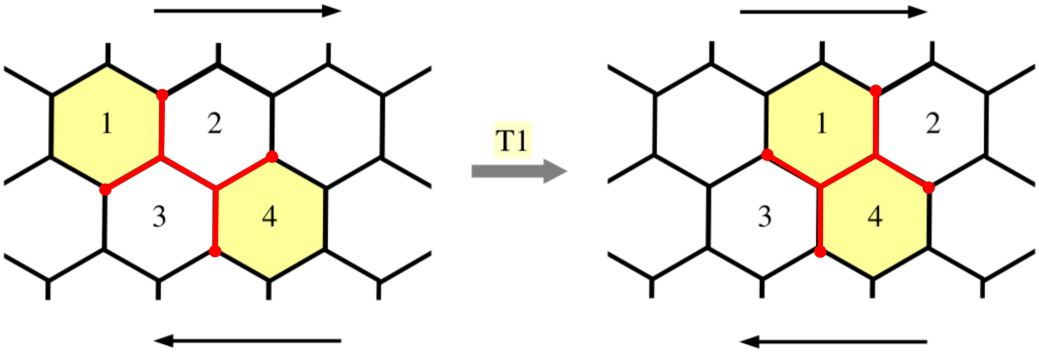

Figure 19: T1 rearrangement in a 2D foam. Credits to Titta *et al.* [3]

Thus, both the starting and ending points of this T1 process represent a local minimum of energy for the system, respecting Plateau's laws. The goal now is to probe how to pass from one state to another, and if we can get some rheological information about the foam films by doing so. The idea is that the dynamics takes place in two steps: first we load elastically the system by compressing the central film until it disappears, putting the system in the unstable configuration of four films connected by one meniscus. At this point, we stop adding work to the system, which relaxes on its own towards a similar configuration as its initial state, at a lower energy. Quantifying the time of this relaxation was the missing key to get a proper loss modulus for the system.

This has been done by Durand *et al.* [1] in 2006 by looking with a high speed camera at a 2D liquid foam inducing rearrangements by pumping air against it. The notations are shown in Fig.20.

I will detail their approach a bit, as it is full of problems and ideas we will later face again for our own experiments and models.

They look at the dynamics of relaxation of $x_B(t)$, writing the force balance at both menisci:

$$2\gamma_{sides}(t)\cos\alpha(t) - \gamma_{central}(t) - (\mu_s + \kappa_s)\left.\frac{\partial U}{\partial x}\right|_{x=x_B} = 0 \tag{32}$$

Where γ_{sides} is the surface tension of the four films at the edges, $\gamma_{central}$ the surface tension of the central film and U is the interface velocity in the central film. The third term combines both the shear and dilatational viscous constributions of the interfaces, which take this form in this 1D model. To further advance, the authors have to make a few important assumptions:

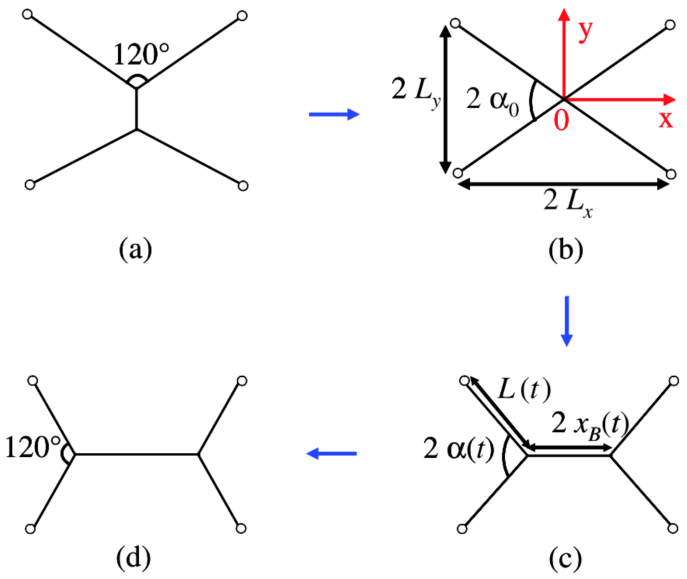

Figure 20: Notations used by the authors to describe the T1 experiment. Credits to Durand *et al.* [1]

- Bulk viscosities (air and liquid frictions) were discarded right off.
- Surface tension responds to deformation with its Marangoni modulus E_M (eqs. 11). It means we suppose here that we are in the insoluble limit.
- The four vertical films on the sides will be supposed at rest at all times, meaning the we impose $\gamma_{sides}(t) = \gamma_{eq}$. That means that we virtually fix the surface tension somewhere in the system so that the side films get rid of as many interface as they need as $L(t)$ decreases to enforce this condition. It thus also sets the interface velocity U at $x = x_B$. This is a bold guess, but a necessary one here, which seems reasonable as the central film is the one undergoing the biggest deformation in the process. However, it is artificial, and the next models will not make this assumption (including the one used in chapter 3 detailed in 0.4.5), and the experiments will show that it could not be made.

Solving the problem like so, they end up with two quantities both deductible from $x_B(t)$ and $\dot{x}_B(t)$ linked by an affine relationship whose coefficients give E_M and $\mu_s + \kappa_s$. They thus make an estimate of both the surface elasticity and viscosities for SDS solutions and a mixture of polymer and proteins (bovine serum albumine and propylene glycol alginate):

$$\begin{cases} E_{M,SDS} = 32 \pm 8\,\mathrm{mN/m}\ ;\ (\mu_s + \kappa_s)|_{SDS} = 1.3 \pm 0.7\,\mathrm{mPa \cdot m \cdot s} \\ E_{M,mix} = 65 \pm 12\,\mathrm{mN/m}\ ;\ (\mu_s + \kappa_s)|_{mix} = 31 \pm 12\,\mathrm{mPa \cdot m \cdot s} \end{cases} \tag{33}$$

These first measurements of the Marangoni modulus and the surface viscosities is a valuable lesson. They all are very high values compared to the existing literature at the time, and to more recent measurements [6, 36, 78].

Notably, more recent and refined models do not make the assumption $\gamma_{sides}(t) = \gamma_{eq}$ for the vertical films. This sets artificially the quantity of interface exchanged by them towards the central film. **This raises a problem however: the two interfaces of each vertical film do not undergo the same dynamics at all. In fact, as seen in Fig.20, the top and bottom interfaces are free to slide from the vertical films to the central film, but the right and left interfaces have a stopping point at the menisci by symmetry.** Although it is taken into account that each vertical film feeds the central film with only half the quantity of interface it gives up, the lost half is implicitly completely ditched into the bulk of the meniscus if we want to ensure that the tensions in the vertical films remain the same. This is a hidden hypothesis whose validation/invalidation is at the core of the main chapter of this thesis, chapter 3.

0.4.3 Axisymmetric elementary liquid foam under small deformation: the Besson-Debrégeas experiment

The experiment by Besson *et al.* [78] described in this subsection examines a configuration similar to the previously observed T1, but in an axisymmetric geometry. Unlike in Durand *et al.* [1], where the setup solely allows us to explore the dynamics between two static states, we have here the ability to control the deformation of the central film, compression or stretching, by observing an oscillatory regime.

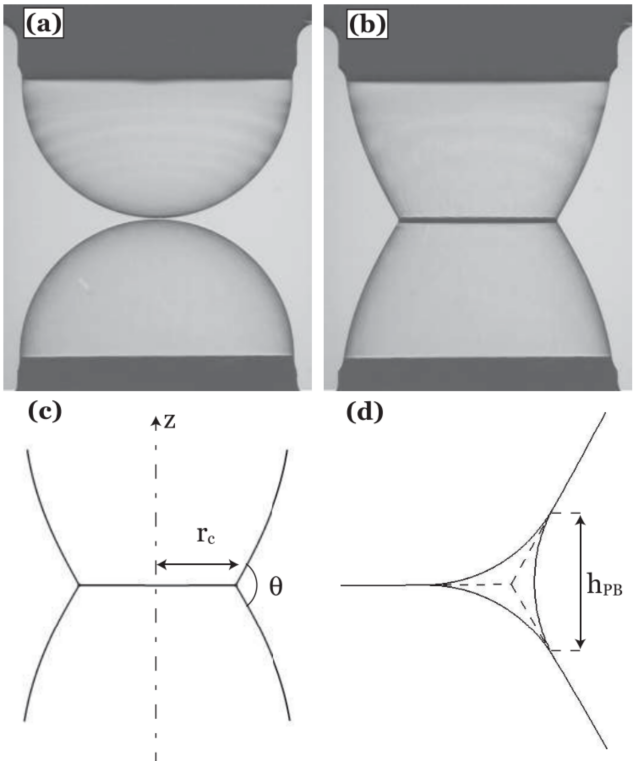

Figure 21: Besson-Debrégeas experimental setup: **(a)** Two identical bubbles being slowly brought into contact. **(b)** The contact is made and the radius of the flat film rises. **(c-d)** Notations used to describe the geometry of the problem. Credits to Besson *et al.* [78]

In this configuration and in the theoretical model developed with it, different time regimes exist where the surface tensions of the vertical films are now not artificially kept equal to the equilibrium value but are rather time varying variables, which are decoupled between the outer and inner interfaces. This is a very important point as it allows to take into account regimes where we expect interfaces of the same foam film to have a relative motion, meaning there is a bulk shear to take into account for the effective loss modulus of the elementary foam! **This will be a key ingredient for this thesis work, as this paper from Besson *et al.* [78] is the first to consider a refined model for the surfactant exchanges between the three different interfaces neighbouring a meniscus, unveiling the existence of dissipative phenomena in elementary liquid foams that are not due to the surface rheology of single interfaces alone.** Also, this paper brings novelty in terms of experimental access to these differences of tensions, by measuring the angle deviation from the Plateau's law.

To achieve this, the authors create two bubbles with the same diameters of $2R = 7\,\mathrm{mm}$, facing each other, and mobile along a common vertical axis. This configuration is depicted in Fig.21. The pressure in the bubbles is determined by the Laplace's law, and they gradually bring them into contact. As a result, they create a contact zone, a third flat film connected to the two bubbles by a circular meniscus (see Fig.21B). Since the pressures of the bubbles remain the same and identical, Laplace's law dictates that the surfaces of revolution for each bubble have principal curvatures that satisfy $\kappa_1 + \kappa_2 = 2/R$, and the central film between them must be flat.

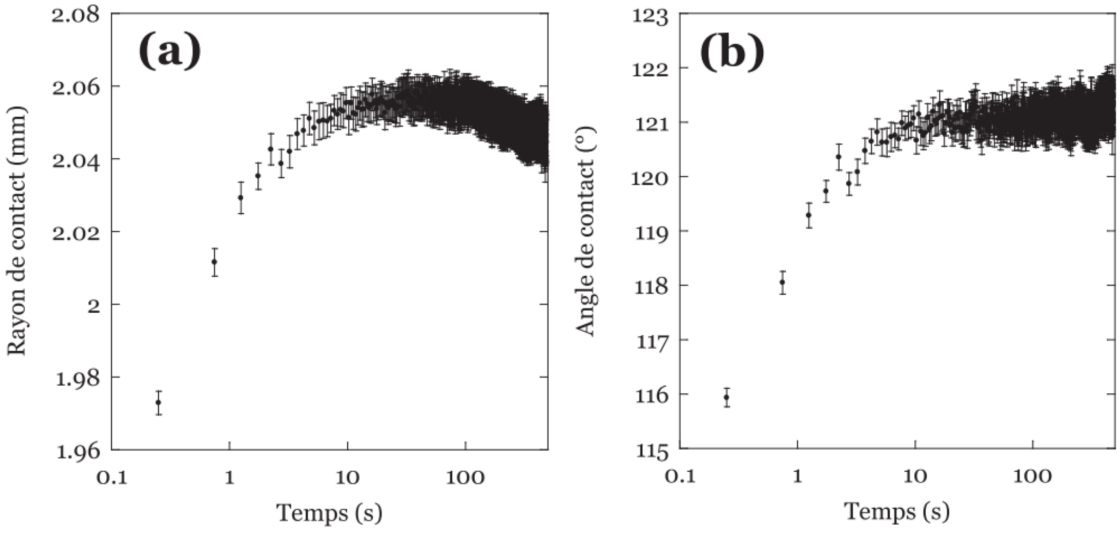

Figure 22: **(a)** Contact radius $r_c(t)$ as a function of time for a typical experiment. **(b)** Contact angle $\theta(t)$ as a function of time. Credits to Besson *et al.* [78] (Pardon their french for the axis names)

Once the contact is made, the system undergoes rapid changes, akin to a T1 relaxation with a contact radius r_c for the central film growing over time, and the outer contact angle θ opening up. Fig.22 illustrates a typical experiment. After approximately $10\,\mathrm{s}$, they reach mechanical equilibrium: θ plateaus, and r_c reaches its maximum before decreasing at longer times because of bubble ageing through gas escaping due to the inner overpressure. This typical time scale

is governed by surface rheology, surfactant exchanges through the meniscus, and possibly other damping forces (inertia, air friction).

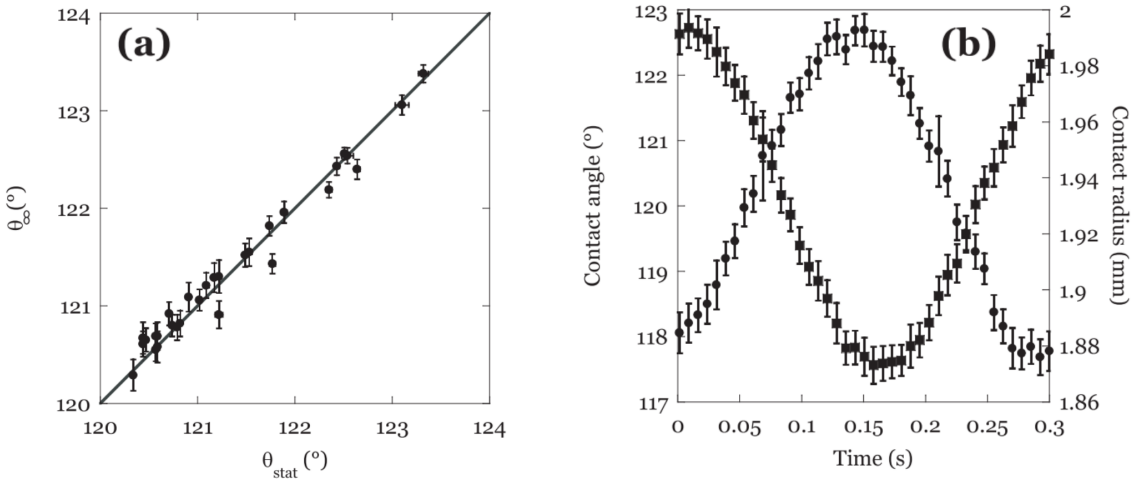

Figure 23: Static and dynamic measurements: **(a)** Experimental static angle θ_∞ plotted against the static angle θ_{stat} predicted by the decorated meniscus model of Fortes *et al.* [79]. Credits to Besson *et al.* [78]

The transient regimes towards mechanical equilibrium shown in Fig.22 are not the main objects of study of this paper however, as they are mainly used to define the static state around which the system will be dynamically probed. To achieve this, the bubbles are brought closer together and moved apart, varying the pulsation $\omega \in [10^{-1}, 10^2]$ rad/s while keeping the amplitude constant. This makes r_c and θ vary as:

$$\begin{cases} r_c(t) = r_{c,0} + \Delta r_c(\omega)\cos(\omega t) \\ \theta(t) = \theta_0 + \Delta\theta(\omega)\cos(\omega t \phi(\omega)) \end{cases} \tag{34}$$

Where the equilibrium angle $\theta_0(t)$ depends on time in all generality as $r_c(t)$ varies. A typical measurement is shown in Fig.23. The phase shift between the two signals allows us to define the elastic and loss moduli $A^* = A'(\omega) + iA''(\omega)$:

$$\begin{cases} A'(\omega) = -\frac{\Delta\theta}{\Delta r_c} r_{c,0}\cos(\phi(\omega)) \\ A''(\omega) = -\frac{\Delta\theta}{\Delta r_c} r_{c,0}\sin(\phi(\omega)) \end{cases} \tag{35}$$

Which are plotted in Fig.24(b). It is very important to note that these are **not** the moduli associated with the elasticity and viscosities of a single film! In order to estimate the latter, the authors also perform experiments on a single bubble which undergoes sinusoidal volume variation using half of their setup. In a similar way as previously, the phase shift between the recorded bubble volume and the measured inner pressure allows the authors to define an interface dilatational modulus $E^*(\omega) = E'(\omega) + iE''(\omega)$. They link this modulus to the evolution of the surface tension of a single interface undergoing a deformation ΔS of its initial surface S_0 as:

$$\gamma(t) = \gamma_0 + E'(\omega)\frac{\Delta S}{S_0}\cos(\omega t) + E''(\omega)\frac{\Delta S}{S_0}\sin(\omega t) \tag{36}$$

In this configuration E'' is the signature of the intrinsic and extrinsic viscosities of a single interface deformed with a spherical dilation. E' and E'' are plotted in Fig.24(a). The goal is now to link the modulus of the elementary foam A^* to the dilatational modulus of a single interface E^*. Both of them differ because of in-plane exchanges of interface at the meniscus, from one film to another. **This difference is what makes the rheology of elementary liquid foams a bridge between the surface rheology of single foam films and the rheology of liquid foams, the former being not sufficient to describe the latter.**

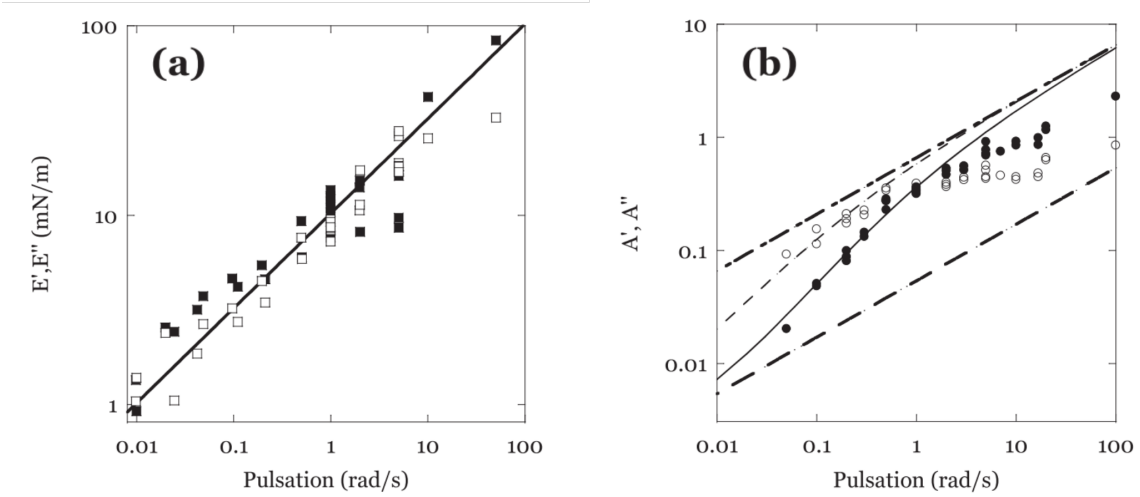

Figure 24: **(a)** Dilatational moduli of a single interface as function the pulsation. Closed squares for the elastic modulus E', open squares for the viscous modulus E''. The line is a model by Lucassen [80]. **(b)** Elastic and loss moduli of the elementary liquid foam. Closed circles for A', open circles for A''. Credits to Besson *et al.* [78]

The authors thus develop a model based on the conservation of surfactants of the three different interfaces present in the system denoted 1, 2 and 3 and represented in Fig.25. The key ingredient here is the flux J_s, which takes into account the surfactant exchanges between the films, which is coupled to the transverse exchanges J_v between the two interfaces of a same film. They can be expressed as:

$$\begin{cases} J_s = D_s \frac{\Gamma_2 - \Gamma_3}{L} 2\pi r_c \\ J_v = S\frac{\mathrm{d}\Gamma}{\mathrm{d}t}\left(1 - \frac{E_0}{E^*}\right) \end{cases} \tag{37}$$

Where L is an unpredicted typical length over which the gradient of surface excess between Γ_2 and Γ_3 is developed, D_s a surface diffusion coefficient and E_0 the Marangoni modulus of the interfaces (*i.e.* the surface elasticity of the interface in the insoluble limit, see eq.11).

NB: Durand *et al.* [1] also have this J_s with their model where it is a slave parameter $\Gamma_{eq} \times U$ ensuring $\Gamma_2(t) = \Gamma_{eq}$. With Besson *et al.* [78] both J_s and Γ_2 are allowed to vary, and the fate of the surfactants of S_1 is also taken into account through J_{v_1}.

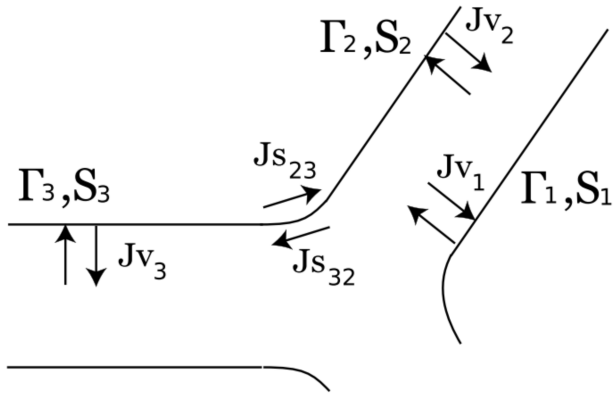

Figure 25: Notations used by the authors for the three interfaces in the problem. Credits to Besson *et al.* [78]

The next step is thus to write the surfactant conservation for the three interfaces and to relate it to the expression of the surface tension, which is linked to the change of surfaces through eq.36. This yields the three variations $\Delta\gamma_i(\omega)$, giving access to the variations of angle with:

$$\Delta\theta = \frac{1}{\sqrt{3}\gamma_0}(\Delta\gamma_1 + \Delta\gamma_2 - 2\Delta\gamma_3) \tag{38}$$

This allows to finally write the expression of the modulus A^* as defined by eq.35:

$$A^* = \frac{2E^*}{\sqrt{3}\pi\gamma_0}\Big(\frac{iE_0\omega\tau}{E^* + iE_0\omega\tau}\frac{4R^2}{2R^2 - r_{c,0}^2} + \frac{E^*}{E^* + iE_0\omega\tau}\frac{r_{c,0}^2}{2R^2 - r_{c,0}^2}\Big) \tag{39}$$

Where $\tau = \left(2\pi\frac{r_{c,0}}{L}D_s\frac{S_{2,0}+S_{3,0}}{S_{2,0}S_{3,0}}\right)^{-1}$ is a typical time of equilibrium through surface diffusion between interfaces 2 and 3 (mind the missing factor $1/\pi$ in the eq.25 of the original paper [78]).

This typical time sets two different regimes for A^*: $\omega\tau \ll 1$ where interfaces 2 and 3 are at equilibrium and their total surface $S_2 + S_3$ is conserved so that only S_1 undergoes the compression/stretching cycles; $\omega\tau \gg 1$ the three interfaces withstand the compression/stretching cycles independently from one another. These two limits are plotted in Fig.24(b) as the bottom dashed line ($\omega\tau \ll 1$) and the top dash-dotted line ($\omega\tau \gg 1$). Two fits with the full equation 39 are also plotted, fitting with $\tau = 3 \times 10^{-4}$ s. There is a quantitative match at low frequencies, whereas it starts deviating for frequencies higher than $\omega > 1\,\mathrm{rad/s}$.

This paper concentrates most of the ideas at the foundation of the main contribution of this thesis, that is presented in chapter 3. As developed at the end of the last subsection 0.4.2, the main problem we face when we build a rheological model for an elementary foam, that is here three interfaces around a meniscus, is solving properly the surfactant exchanges occuring between the interfaces, the film bulks, and the meniscus bulk. Both papers from Durand *et al.* [1] and Besson *et al.* [78] make two completely different assumptions regarding the role of the meniscus: the former authors implicitly use it to get rid of an excess of surfactants to enforce their equilibrium condition for the side films, the latter do not write any surfactant transfers towards/from it, artificially blocking bulk surfactant diffusion from this region.

To focus on Besson's paper again, where the description of the surfactant field is more exhaustive, a few points can be raised:

- The model is geometry dependent, and it does not describe the local flow fields in the films and the meniscus, meaning it is hard to predict the robustness of it if R is taken much bigger or much shorter.
- The amplitude of the mechanical solicitations is small, with deformation of the order of $\epsilon \sim 5 \times 10^{-2}$, allowing the authors to neglect the potential exchanges of interface with the two bubble supports. For bigger amplitudes of deformation, which locally exist in a macroscopic foam even for small global deformations (during a T1 event for instance), this assumption cannot be made.
- The *ad hoc* time τ hides the variables L, which is unpredicted, making the problem free of the local detail (*i.e.* the flow field and the surfactant field in the vicinity of the meniscus). However, if L starts being of the order of R for instance, it adds some geometry-dependence to the problem. Besides, L might very well be a function of the pulsation $L(\omega)$ in all generality, making it a possible candidate to explain the high frequency discrepancy observed by the authors.

All these pieces of evidence tend to show there is a need for a local model of the flow and surfactant fields near the meniscus. Notably, the length L added by the authors would require a proper description, which is provided by Bussonnière *et al.* [4] and detailed a bit later in 0.4.5.

0.4.4 Recent numerical advances

Simulating elementary foams is a numerical challenge on its own, as it requires to predict flow and surfactant fields in menisci and foam films, whose geometries evolve in time and which have very different aspect ratios. Titta *et al.* [3] (2018) have performed an exhaustive simulation of an elementary foam-like configuration illustrated in Fig.26, undergoing a global shear imposed by setting the relative velocity U of the two supporting plates. The aspect ratio of the simulation is the one shown in the figure.

The bulk flow is described using the momentum conservation:

$$\boldsymbol{\nabla} \cdot \boldsymbol{u} = 0 \tag{40}$$

$$\rho\Big(\frac{\partial \boldsymbol{u}}{\partial t} + (\boldsymbol{u} \cdot \boldsymbol{\nabla})\boldsymbol{u}\Big) = \boldsymbol{\nabla} \cdot \overline{\overline{\boldsymbol{\sigma}}} + \gamma\ \kappa\ \delta_\Gamma \boldsymbol{n} + (\boldsymbol{\nabla}_s \gamma)\delta_\Gamma \tag{41}$$

Where $\boldsymbol{u}$ is the velocity, $\overline{\overline{\boldsymbol{\sigma}}} = -p\overline{\overline{\boldsymbol{I}}} + \eta(\overline{\overline{\boldsymbol{\nabla}}}\boldsymbol{u} + {}^t\overline{\overline{\boldsymbol{\nabla}}}\boldsymbol{u})$ is the bulk stress tensor, γ is the surface tension, κ the local curvature of the interface, $\boldsymbol{\nabla}_s$ the del operator projected on the interface, which has a normal vector $\boldsymbol{n}$ and is localised by the Dirac function δ_Γ. The first term on the right-hand side accounts for the bulk stress, the second term for the Laplace pressure jump at the interface and the third one for the Marangoni stress at the interface.

That accounts for the flow field, which is directly dependent of γ of which we need a law to close the problem. This is solved by giving a conservation law for surfactants (*i.e.* for bulk

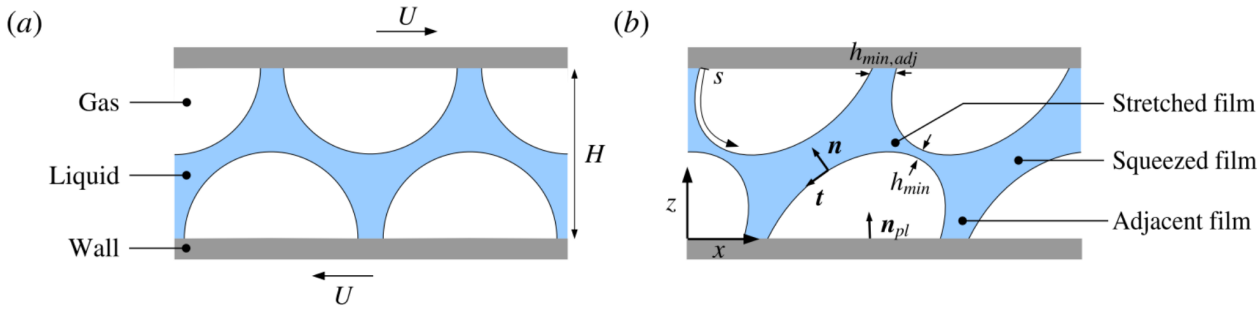

Figure 26: Notations and geometry of the elementary foam studied in [3] (faithful aspect ratios). **(a)** Initial state of the foam at the beginning of the simple shear (of imposed strain rate $\dot{\epsilon} = U/H$). **(b)** The elementary foam under shear between two T1 events. Credits to Titta *et al.* [3]

concentration c and surface concentration Γ), associated with an isotherm model giving the relation $\gamma = f(\Gamma)$. The bulk and surface conservations of surfactants, as well as the Langmuir isotherm chosen for the simulation write:

$$\frac{\partial c}{\partial t} + \boldsymbol{\nabla} \cdot (\boldsymbol{u}c) = D_c \Delta c \tag{42}$$

$$\frac{\partial \Gamma}{\partial t} + \boldsymbol{\nabla}_s \cdot (\boldsymbol{u}\Gamma) = D_\Gamma \Delta \Gamma + j \tag{43}$$

$$\gamma = \gamma_0 + RT\Gamma_\infty \ln\left(1 - \frac{\Gamma}{\Gamma_\infty}\right) \tag{44}$$

Where D_c and D_Γ are the bulk and surface diffusion coefficients for the surfactant, j is a surfactant flux from the bulk given by the Langmuir isotherm, RT is the molar thermal energy and Γ_∞ a saturating surface excess. I will elaborate more on the Langmuir isotherm model later in chapter 1.

These equations are solved given the initial geometry shown in Fig.26(a) and using a level-set function locating the interface over time (adding one more numerical transport law to the physical problem). This gives access to the force exerted by the fluid on the plates (Fig.27(a)) in a transient regime and in steady state. Thus, the authors are allowed to compute the initial elastic loading of the system followed by force oscillations. Past the transient regime, it is possible to compute the dissipated power of both the bulk and of the interface, and to see how the injected power is shared between both contributions (Fig.27(b)).

In Fig.27(a), the black line is the sum of all the forces exerted on the plate as a function of time when the velocity U is turned on (orange the capillary forces, red the viscous forces in the liquid, blue in the air). After a transient regime, the oscillations correspond to a series of T1 events occurring in the system. The dissipated energy during this process is computed and plotted in Fig.27(b). The squares correspond to the injected energy of a cycle, which is totally dissipated over one period of oscillations, either by viscous bulk forces (red circles) or surface dissipation (the difference between the two). The latter contribution is due here to the sole

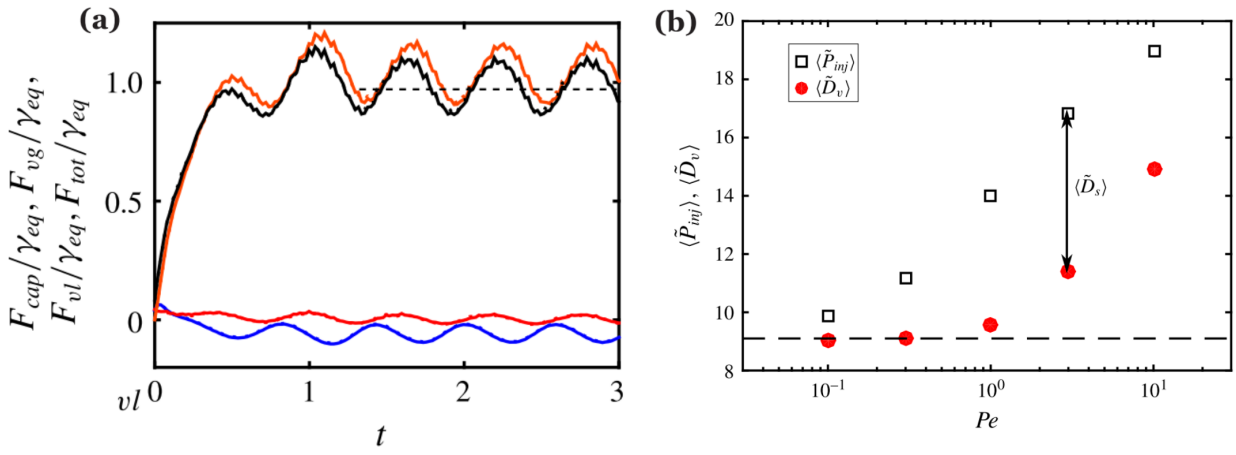

Figure 27: **(a)** Forces applied by the foam on the plates, Black is the sum of all the others: orange are the capillary forces, red to viscous forces in the liquid and blue to viscous forces in the gas. **(b)** Time-averaged injected (black) and dissipated (red) powers over a cycle. Credits to Titta *et al.* [3]

extrinsic viscosity of the interfaces, as no dilatational or shear viscosities have been added to the surface rheology. The abscissa is the Péclet number of the system, which is defined as:

$$Pe = \frac{UH}{D_c} = \frac{UH}{D_\Gamma} \tag{45}$$

Whose second equality is a hypothesis of the authors.

What we see is that as the velocity of the mechanical solicitation increases, the contribution of the interface for the dissipation increases until it Plateaus. This means that the ratio $\langle\tilde{D}_s\rangle/\langle\tilde{D}_v\rangle$ peaks at around $Pe \simeq 1$, where the extrinsic viscosity yields its maximal dissipation. This is not intuitive, but already predicted by a model from Lucassen *et al.* [81].

This is the state of the art in terms of numerics for a local description. The problem of dealing with the real aspect ratio of the films and menisci is still a problem today, but these toy 2D foam models seem to already capture a lot of the mechanical response of the elementary liquid foams. In that respect, numerical models for foams and foam films with more complex structures are fed with unphysical local models [82, 83]. Also, building the bridge towards a full model for macroscopic liquid foam rheology is a whole field of research, on which I will not elaborate. Efforts from our community in this direction have been made in particular by Besson *et al.* [2] and Denkov *et al.* [84], as well as in Cohen-Addad's and Höhler's groups [85–87].

0.4.5 Rheology of an elementary liquid foam: state of the art in Isabelle Cantat's group at the beginning of my Ph.D

Adrien Bussonnière, Emmanuel Schaub and Isabelle Cantat developed an experimental setup [4] allowing the large deformation of an elementary liquid foam which resembles the Besson-Debrégeas setup [78] but with an invariance by translation symmetry instead of the axisymmetry.

This foam is shown schematically in Fig.28**(a)**. It is $4.2\,\mathrm{cm}$ wide in the z direction, and the four edges parallel to z are mobile edges imposing a deformation at the four peripheral films.

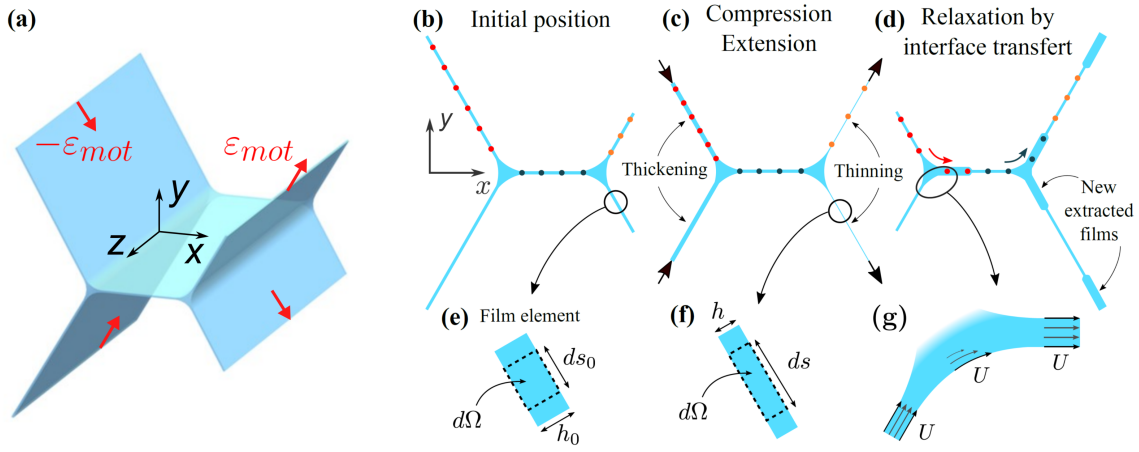

Figure 28: Deformation of an elementary liquid foam with 5 films. **(a)** The mobile sides are the four external edges of the vertical films, they impose deformations $\pm\epsilon_{mot}$ of opposite signs on the right/left sides. **(b-d)** Schematic view of the time evolution of the films throughout the deformation, where the coloured dots are elementary material systems at the interface which are followed along their trajectories: compressed films thicken and give up interface to the central film, stretched films thin out and extract interface from the central film. **(e-f)** Local view of the compression/stretching of the films. **(g)** Local view of the flow fields responsible for the interface exchanges, that is plug flows far from the menisci and local shears near them. Credits to Adrien Bussonnière *et al.* [4].

Doing so results in the scenario detailed in Fig.28**(b-d)**: The coloured dots represent elementary material systems at the interface which are followed along their trajectories, thus illustrating film compression/extension as well as interface transfers from one film to the other. Compressed films thicken and relax through giving up some interface, while the stretched films get thinner and accept some new extracted film in their plane.

Under deformation, this system remains invariant by translation along z for a time long enough (this is later discussed in chapter 3) to allow us to define everything in terms of 2D deformations in each films. Thus, each film undergoes a certain deformation ϵ which is defined using the notations in Fig.28**(e-f)** as $\epsilon = ds/ds_0 - 1 = h_0/h - 1$ which is uniform in the film because of the uniformity of tension far from a meniscus, as discussed in subsection 0.2.4. These deformations are defined for each film by looking at the pieces of films already present in the plane before the deformation (when their size ds_0 is defined). Because of the interface transfers, these deformations are thus distinguishable from the imposed deformations $\epsilon_{mot} = L_m/L_m(t=0) - 1$, which are defined for each motor with the distance L_m between the motor and the rest positions of the neighbouring free meniscus.

On the other hand, it is possible to get a measurement of the difference of tensions $\Delta\sigma$ between the deformed films based on the same principle as in the Besson-Debrégeas experiment [78], that is by looking at the angles around the menisci and their deviations from the Plateau's laws. The

principle of this measurement is more detailed in chapter 3. Thus, by monitoring the difference of tensions $\Delta\sigma$ between the films, the deformations ϵ of the films, and knowing the imposed deformations ϵ_{mot} to the system, we are able to draw the graphs of Fig.29.

In **A**, blue is the global deformation imposed to the whole elementary foam, and we show here a ramp experiment imposed in $0.1\,\mathrm{s}$, thus corresponding to a strain rate of $10\,\mathrm{Hz}$. Red is the response of the system with a difference of tension $\Delta\sigma$ normalised by the equilibrium tension σ_0 known with our pendant drop campaign. **This response is that of a Maxwell fluid: elastic at shorter times, viscous at longer times.**

In **B**, we still plot the difference of tension $\Delta\sigma$, but this time against the deformation ϵ measured in the films. The blue curve is obtained during the ramp of deformation, and the purple one is obtained during the relaxation process. The collapse of both curves means that the viscous dissipation is not located in the pieces of film far from the meniscus, which react as non-linear springs. This elastic behaviour is well understood and characterised, and is the topic of chapter 1 where measurements are rationalised with a thermochemical model.

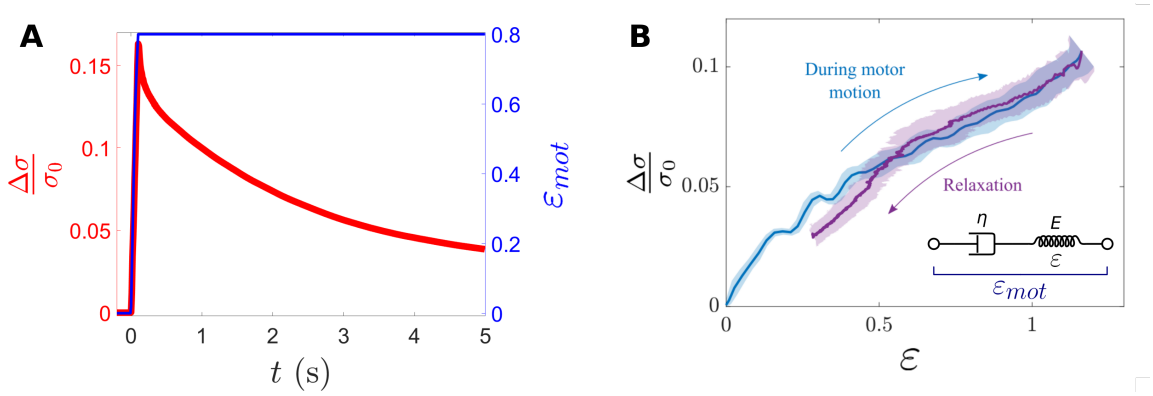

Figure 29: Rheological curves of an elementary liquid foam. **A** Blue: ramp of deformation imposed by the motors; Red: response of the system in terms of difference of tension between the stretched and compressed films. It is the response of a Maxwell fluid. **B** Stress-strain curve of the system computing the deformation ϵ of the films (*i.e.* far from the meniscus), we have a non-linear elastic response from the spring component of our Maxwell fluid.

The more mysterious part of this dynamics is the relaxation through viscous dissipation. If not for the compressed/stretched films, where is it located? How can we describe it? This is what Bussonnière *et al.* [4] addressed in a paper published right at the beginning of my thesis work: the viscous dissipation is expected to be located in a very localised zone at the junction with the menisci, in the form of a simple shear flow in the thickness of the films. Its existence is driven by a coupling with a difference of Marangoni stresses between both interfaces, arising as the moving interfaces meet at the meniscus.

These interfaces must be supplied in/get rid of surfactants as they are deformed, and the exchange mechanisms between the interfaces and with the meniscus were left in the model with adjustment parameters. The aim of chapter 3, is about quantifying those exchanges in order to close the model. We will do so by looking at an even more elementary liquid foams: 3 films connected by a single free meniscus.

In the three articles we discussed [1, 4, 78], the amount of surfactant flowing from one film to its neighbour is a crucial parameter, unknown and required to close the model. In the three cases, it is used as an adjustable parameter.

The prediction of this surfactant transfer is made difficult because the role of the meniscus in the process is an open question : does it play, or not, a role of surfactant reservoir for the adjacent films ?

The main result of chapter 3 will be a direct measure of this transfer, leading to the conclusion that the meniscus does not provide or absorb surfactant during the process.

0.5 Spontaneous evolution of foams and films : some other physical processes

0.5.1 Normal motion of the films

When it comes to compare the physics this manuscript is about to macroscopic foam and single bubble physics, it is worth keeping in mind that a first line we draw here is that we do not address the problem of normal motions of foam films. This is because the shape of our elementary foam is always very close to its equilibrium shape. The normal motions are much better known than the tangential ones addressed in this manuscript, but important questions are still investigated.

For instance, these motions are especially important in liquid foams to explain their acoustics [88], as the speed of sound can be resolved only taking into account the normal oscillations to the films. They also are important in the case of film burst, where the film actually retracts with a violent normal flapping motion [89] ! This last peculiar dynamics could even be relevant for the matter of salt microparticles projection from the sea to the atmosphere, which is important for cloud formation.

Back to rheology, unless the strain rate becomes too high [90], the structure stays close to its equilibrium shape most of the time, as in our setup. Just after T1 however, the shape is far from equilibrium and fast normal motions are observed, which can not be reproduced with our set-up.

0.5.2 Gravity drainage

Both elementary and disordered macroscopic liquid foams undergo drainage at longer times. That includes gravity drainage, which makes the liquid fraction increase at the bottom of the foam (or equivalently makes the bottom films thicker in elementary foams), as well as capillary drainage (*cf.* 0.3.3) responsible for the thinning of foam films near their edges.

Gravity drainage leads to a very heterogeneous ageing, as shown in Fig.30, with thinner films, bigger bubbles on top and thicker films, smaller bubbles at the bottom. This can make the global mechanical properties difficult to predict, and the rheology hard to characterise as it becomes time-dependent. In the frame of this manuscript, with the elementary liquid foams we study here, gravity can also become a problem as it leads to thicker films at the bottom compared to the top ones and induces flows in the meniscus which are not horizontal. However, the time scales

we address are shorter than the typical time scale of the gravitational drainage, thus allowing us to neglect its influence.

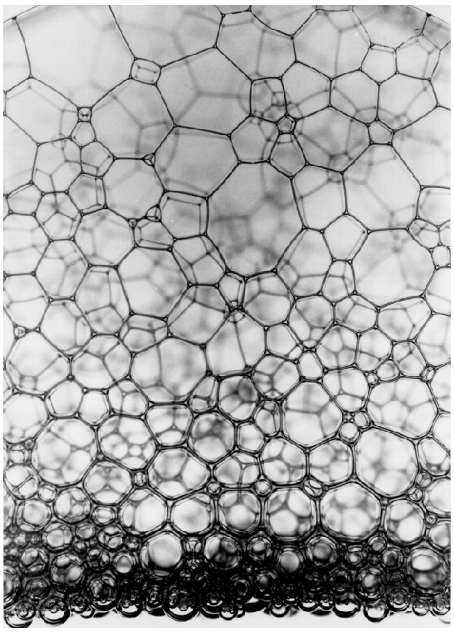

Figure 30: A liquid foam ageing through gravity drainage. Top is dry, bottom is wet. Credits to S. Cohen-Addad, R.M. Guillermic & A. Saint-Jalmes [7].

0.5.3 Coarsening of liquid foams

In the frame of foam physics, coarsening is how the foam tends to have a decreasing number of bubbles over time, and an increasing mean size for them. This is due to two main mechanisms: film rupture, leading to the destruction of two bubbles and the creation of a bigger one, and Ostwald ripening, when small bubbles with bigger pressures empty themselves in larger ones through gas diffusion across foam films. Our elementary foam has bubbles opened to the atmosphere, and we consider only cases without ruptures. So these ageing processes do not occur in our situation.

Film ruptures occur mainly due to the drainage mechanisms discussed before. These events lead to bubble rearrangements as the menisci supporting broken films move to a new equilibrium position, and often cause T1 events in their vicinity. Thus, even without exterior solicitations, the study of elastic and dissipative phenomena at stake in the deformation of elementary foams is still relevant.

The same goes for Ostwald ripening, as a change of bubble size can trigger a T1 event. Moreover, a recent study from A.Saint-Jalmes & C.Trégouët [91] has shown that a steady shear slows down the ageing process. The reason behind it was found to be the constant extraction of Frankel films (*cf.* subsection 0.3.2) out of the menisci, counterbalancing drainage by renewing foam films with thick pieces. Thicker films means slower gas diffusion, and thus slower Ostwald ripening. Here again, the evolution of film thickness induced by bubble deformation, which is at the core of our study, plays an important role.

0.5.4 Link to liquid foams in the industry and daily life

This thesis work is about a very simple chemistry in the eye of an engineer. Yet, a mixture of two species, SDS and DOH (or even three as fluorescein counts as salt *cf.* chapter 1) is already a complex problem for hydrodynamicists. In fact, SDS as a soluble surfactant allows the existence of our foam, while DOH as a poorly soluble one changes drastically the elasticity of the films. The boundary conditions for our flow describing this chemical reality are full of subtleties already.

Then, what to think of scaling up this work not only for macroscopic foams, but rather actual foams used in the industry or encountered in daily life? This is where we must be even more cautious in our approach.

Scaling up our elementary foams: Part of the physics is captured

The use of the physics behind liquid foams in the industry is kept at the scale of classical rheology and correlations between the surface properties (Marangoni modulus, surface shear viscosity...) and the effective properties of the macroscopic materials. From there, a wide variety of behaviours exists and the scale of the elementary foam is relevant for part of it.

As discussed earlier, viscoelastic response of dry foams can be already recovered in elementary foams, but it has to be noted that real foams also show many other properties not captured/not rationalised at our local scale: plasticity due to film rupture under shear or repositioning at the edges of the foam, thixiotropy as the foam ages... Most of these phenomena depend either on bubble size, liquid fraction, or ageing time. Our elementary foams model huge centimetric bubbles, so that all the typical length scales are decoupled. This serves the physics best, but also mean that we will not be able to probe directly all these coupled dynamics depending on the bubble size or the liquid fraction.

More complex chemistries: even more physical ingredients

The simplest surfactants used broadly in industries such as cosmetics, detergent or food industries are quite close to SDS and are grouped under the name "sulfates". They are produced using byproducts of the oil industry, hence their abundance, and are mixes of molecules with a skeleton ranging from 8 to 16 carbon atoms with a sulfate group located on a random carbon. SDS (of which the structure is recalled in Fig.4) is actually a model surfactant for these systems.

Sulfates are used for daily life applications as a foaming agent (dishwashing liquid, shampoo...), as well as in many industries. Half the global production of surfactants (including sulfates) goes to the mining industry for what is called froth flotation, in which valuable minerals are separated from the rest by being put into contact with foams. This separating process relies on the difference of wetting properties of the materials, and foam are used to exacerbate this differentiation.

For other industries, such as the dairy industry for instance, uncontrolled foaming is a huge problem. Due to the potentially very high air fraction of these materials (up to 99%), piping foamy liquids can represent a loss of energy and storage volume.

In all these cases, the effect of chemistry is already well rationalised, and these industries have many foaming/anti-foaming agents for a wide range of situations. However, some of these

chemical species endow liquid foams with other physical ingredients which are still to be better described by physicists!

For example, foam films can become very stiff when made out of protein solutions or gels, as the molecules can go at the interface where they react and form 2D networks. This has been observed with bovine serum albumine (BSA) for instance [92]. This leads to enhanced stability, possibly greater film elasticity... and even the existence of surface shear elasticity [26]!

Another remarkable fact when using such larger molecules is their much bigger diffusion times. This is expected to play a major role at the local scale of elementary foams already, as the adsorption/desorption dynamics sets the shear flow described in chapter 3, thus controlling the mechanical dissipation of the foam.

Knowing all these open questions surrounding surface rheology, elementary and macroscopic foams, how they relate, how different they are, let us now take a step back. Back to our local scale. Back to a simpler chemistry.

Plan

What follows is the main body of this manuscript, my thesis work.

Chapter 1 is about the elastic response of an elementary liquid foam and how to predict it with a thermochemical model I developed and solved numerically.

Chapter 2 is about a novel measurement of a line tension caused by the presence of thickness heterogeneities in a foam film. I present there the experiments I supervised and the theoretical model I used to describe the in-plane motions in the film in order to validate our force measurement.

Chapter 3 is the core experimental work of my thesis. I first elaborate on the state of the art by presenting the model describing the flow fields in an elementary liquid foam. This model raises a question: does a patch of interface exchange any surfactants with the meniscus when it goes from one film to another ? I answered this question experimentally and present the results in this chapter.

1

Elasticity of a single foam film and how to measure it

In subsection 0.2.3, we introduce the notion of film elasticity, which is directly linked to the Marangoni modulus of the interfaces sandwiching the bulk. This elastic behaviour arises from a finite size reservoir-effect of the bulk in the peculiar geometry of a foam film.

In this chapter I show the thermochemical model I developed to predict the elasticity of foam films, made of a mixture of SDS and dodecanol, which I will use in the whole manuscript. The originality of this work is to address the non linear regime, due to geometrical and physico-chemical effects. My theoretical results are confronted to the experimental data obtained by Raphaël Poryles and Adrien Bussonnière at the IPR before my arrival. These results are published in *Soft Matter* [6].

1.1 Surface and film elasticity measurements in the literature

1.1.1 SDS/DOH mixtures: a few more comments

The classical methods for measuring surface tension presented in subsection 0.1.2 are key characterisation methods both in the academic and industrial worlds, and have yielded a vast literature for SDS/DOH alone. We made our own measurements for the equilibrium surface tensions of our SDS/DOH mixtures, which we presented in Fig.9. The main interest of this surfactant combination is that it allows to tune quite finely the surface rheology of the foam films with tiny amounts of DOH, hence allowing us to explore a lot of different regimes.

Interestingly, SDS is a common surfactant, making it a popular troublemaker! It is well known to host DOH traces, as it is its hydrolysis product, and to be difficult to purify through recrystallisation. Both the amount of theses traces in commercial SDS and the kinetics of the hydrolysis reaction have been discussed, from the 80's until quite recently [93, 94]. Besides, as DOH tends to hide in SDS micelles, new parameters appear when trying to solve the thermochemical problem of quantifying population of DOH at the interface. This will be taken into account in our thermochemical model for the mechanical response of foam films made with SDS/DOH mixtures, and will even allow us to estimate the amount of impurities.

Also, the critical micellar concentration of SDS is a sensible parameter, as it varies with temperature, pH, the presence of other ionic species, varying from $5 - 10\,\mathrm{mmol/L}$ [5, 41, 95–97] with a convergence towards the value of $CMC = 8.1\,\mathrm{mmol/L}$ in normal conditions of temperature and pH [98]. This value is the one we retain in the following.

1.1.2 Film elasticity and model in the submicellar regime: the Prins experiment

As an introduction to this chapter, we present a historical experiment and model developed by Prins *et al.* [5] in 1967 where the elastic response of a foam film is probed with an ingenious system. The main problem when it comes to deform foam films are the tiny forces at play, making the system easy to break under disproportionate solicitations. In fact a first order of magnitude for a deformation $\epsilon = 1$ (*i.e.* an extension of 100%) is $F \sim E_f W \sim 10^{-5}$ N for $E_f \sim 1\,\mathrm{mN/m}$ and a typical width of film $W \sim 1\,\mathrm{cm}$.

Thus, the *tour de force* introduced by Prins *et al.* which has become a general idea in this context, is to counteract these tiny tension forces with... the tension of another foam film. The authors have designed the experimental setup illustrated in Fig.1.1 (Left) where they create a vertical film out of a bath of soapy solution. They monitor the vertical thickness profile of the film using monochromatic light interferences, with a sodium lamp seen in reflection on the film. Once the initial film is formed, they stretch it vertically a second time, drawing out a Frankel film in the plane of the preexisting film. The thickness of this new film is also measured as well as the evolution of the profile of the preexisting one. The former allows them to deduce the weight imposed at the bottom of the preexisting film, that is the driving force of the deformation, and

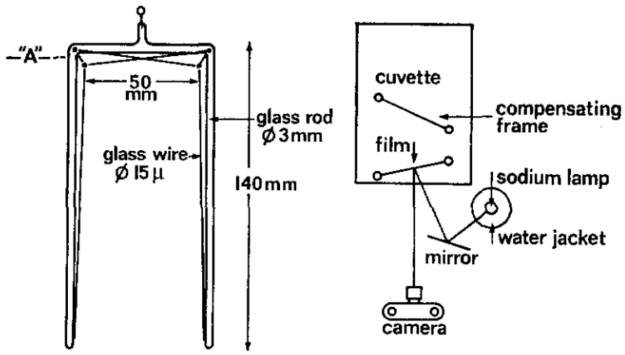

TABLE I

ELASTICITY OF FILMS DRAWN FROM SOLUTIONS OF SODIUM DODECYL SULFATE (c.m.c. 5×10^{-6} moles.cm.$^{-3}$)

Thickness (*micron units*)	Concentration (*moles.cm*$^{-3}$)	
	4.10^{-6}	15.10^{-6}
0.452		2.3 ± 0.4
0.678	58	1.7 ± 0.2
0.904	47 ± 3	1.3 ± 0.10
1.130	38 ± 1	1.18 ± 0.06
1.356	36 ± 3	1.07 ± 0.05
1.582	33 ± 2	1.00 ± 0.04
1.808	31 ± 2	0.94 ± 0.07
2.034	28 ± 1	0.91 ± 0.04
2.260	27 ± 1	0.89 ± 0.07

Figure 1.1: **Left:** Schematic view of the experimental setup. **Right:** Computed film elasticities for SDS solutions in sub-micellar (middle column) and micellar (right column) regimes.

the latter allows them to compute the deformation of the film, as it gets thinner to compensate for the extension of its area.

Knowing the factor ϵ of deformation, so that the area of the preexisting film is $A = A_0(1+\epsilon)$ and its thickness profile $h = h_0/(1+\epsilon)$, where the 0 indices account for the initial values, the authors define the film elasticity:

$$E_f = \frac{\mathrm{d}\sigma^f}{\mathrm{d}\ln A} \tag{1.1}$$

This definition coincides with the definition we will use later on in this chapter. Also we must notice that for a vertical film, the variation of film tension $\mathrm{d}\sigma^f$ must balance at each altitude the weight of the pieces of film below it. This last point means that careful integration of the thickness profile must be performed, as well as a lot of experimental precautions. For instance the necessary presence of a balancing twin frame, with its own foam film, that plunges into the bath as the main frame is drawn out to keep constant the total area of interface present at the surface of the bath.

Also, because the initial film is let to drain for a short while, its thickness distribution is at mechanical equilibrium, meaning that the thinner parts are on top of the thicker ones. By monitoring the different $\epsilon(z)$ with the interferences, and integrating the thickness profiles to yield the $\mathrm{d}\sigma^f(z)$ it is possible to measure different elasticities in the same film for different thicknesses, as we expect $E_f = f(h)$ to be a function of the thickness of the film.

This allow the authors to compute E_f for a wide range of thicknesses and chemistries. Regarding SDS/DOH mixtures, the authors first report the Table I of Fig.1.1 (Right) for SDS "alone" at two concentrations corresponding respectively to $0.62\ CMC$ and $1.85\ CMC$ of SDS. For the same thicknesses (the values of the measurable thicknesses are fixed by the wavelength used) a factor 20 is observed between the submicellar and micellar regimes! For a given concentration of SDS, the elasticity of the film decreases with the thickness, with a factor $1/2$ for a film 5 times thicker.

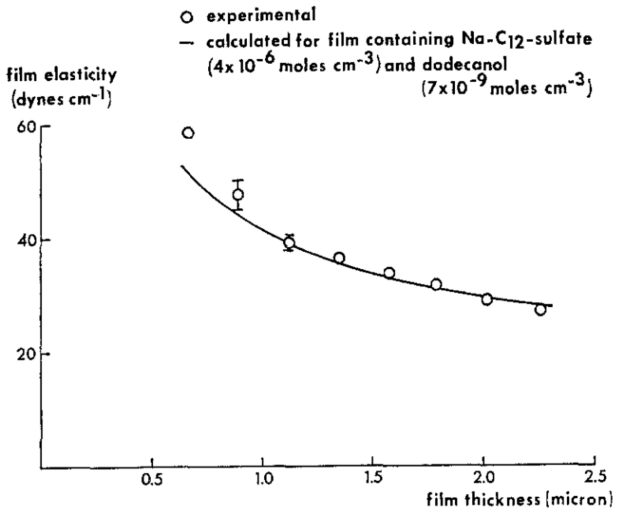

Figure 1.2: Film elasticity as a function of film thickness in the sub-micellar regime. The solid line is a fit by adding a concentration of dodecanol supposedly taking into account the impurities of SDS.

The authors also describe a model for submicellar mixtures giving access to a full expression for the film elasticity. It is based on a Langmuir isotherm model of adsorption/desorption (which is presented in details in section 1.2) combined to mass conservation which allows them to get an analytical formula for E_f. This expression depends on the thickness h_0 of the film and the adsorption/desorption coefficients for SDS/DOH, which are known thanks to prior Langmuir trough experiments. This model fits the data of Fig.1.2, that is the submicellar column of Table I of Fig.1.1... if a virtual small quantity of dodecanol is added besides SDS, which is here to take into account the impurities present in commercial SDS.

However, this model is not adaptable to the micellar regime in an analytic form, as it would mean taking into account another phase, the micellar phase, which hosts and exchanges both SDS/DOH with the bulk monomeric phase. This is where the numerics of nowadays can help, and we will see in section 1.2 how we implement this to our own experiments to predict the strain-stress curves, both below and above the CMC, and for large deformations in the non-linear regime.

1.2 Thermochemical models for foam film elasticities

Prins *et al.* developed an analytical model for submicellar solutions (with a single surfactant or a mixture), which we will extend to the micellar regime with numerical tools.

The assumptions of our model are (most of them being those of Prins *et al.* [5]):

- Surface tension is uniform in the foam film, and both its interfaces have the same value (*cf.* subsection 0.2.4).
- Chemical equilibrium is reached instantaneously whenever a deformation is applied (*cf.* subsection 0.2.2).

- The piece of film we consider is a closed system (*cf.* subsection 0.2.2): volume is conserved and the total quantities of surfactants (SDS and DOH) contained in the interfaces and the bulk are conserved.
- The bulk monomeric concentration of SDS is capped $c_s^m = CMC$ whenever a micellar phase exists.
- Dodecanol population in the bulk is shared between a monomeric population, and a micellar concentration proportional to the concentration of micellar SDS.
- The chemical equilibrium between the bulk and the interfaces is modelled with Langmuir isotherms and concerns the bulk monomeric concentrations of sufactants only.
- SDS is an anionic surfactant, each molecule comes with a sodium counterion Na^+ whose populations will likewise be shared between the bulk, the micelles and the interface.

This is the overview of our model, which will be solved numerically in the end. Let us now write down the proper system of equations.

1.2.1 Our model for SDS/DOH mixtures

Adsorption laws

We start by writing the population shares of SDS and DOH in the bulk. The former has a surface excess Γ_s and a total bulk concentration $c_s = c_s^m + c_s^M$ shared between monomers c_s^m and micelles c_s^M so that:

$$c_s^m = c_s \quad \text{if} \quad c_s < CMC \quad \text{and} \quad c_s^m = CMC \quad \text{otherwise.} \tag{1.2}$$

The total DOH population has a surface excess Γ_d and a bulk population $c_d = c_d^m + c_d^M$ that is shared between a monomeric population c_d^m and a micellar population c_d^M. As micelles are composed of SDS for an overwhelming majority, we consider that the micellar population of DOH is simply given by a law of mass action $c_d^M = K c_d^m c_s^M$ writing:

$$c_d = c_d^m (1 + K c_s^M) \tag{1.3}$$

Also, the sodium counterion population must be taken into account, as bringing a molecule of SDS at the interface means bringing a counterion along with it to ensure the electroneutrality of the interface. This comes with consequences for the statistical presence of SDS at the interface. Thus, let us denote $\Gamma_n = \Gamma_s$ the surface excess of Na^+, $c_n^m = c_s^m$ its bulk concentration for the monomeric SDS phase, and $c_n^M = c_s^M$ its bulk concentration associated with the SDS micellar phase.

The chemical equilibria between the interface, the bulk monomeric phase and the bulk micellar phase are written using a Langmuir isotherm model. This model considers: ***(i)*** that the interface is a set of fixation sites of maximum surface excess Γ_∞, ***(ii)*** that the probability of desorption of a species i is proportional to its surface excess Γ_i, ***(iii)*** that its probability of adsorption is proportional to its bulk monomeric concentration c_i^m and to the number of vacant sites $\Gamma_\infty - \sum_k \Gamma_k$. This can be written in terms of flux for any species $i = \{s, d, n\}$:

$$j_i^- = k_i^- \Gamma_i \tag{1.4}$$
$$j_i^+ = k_i^+ c_i^m \Big(\Gamma_\infty - \sum_k \Gamma_k\Big) \tag{1.5}$$

Writing the chemical equilibrium in this case means equating $j_i^- = j_i^+$ for the three populations of SDS, DOH and sodium ions. We define $K_i = k_i^+/k_i^-$ for each species, and solving these three equations yields the surface excesses:

$$\Gamma_d = \Gamma_\infty \frac{K_d c_d^m}{1 + 2K_s c_s^m + K_d c_d^m} \tag{1.6}$$
$$\Gamma_s = \Gamma_n = \Gamma_\infty \frac{K_s c_s^m}{1 + 2K_s c_s^m + K_d c_d^m} \tag{1.7}$$

Note that the factor 2 at the denominators is the result of the electroneutrality imposed to the interface. This has an entropic cost for a counterion to be brought at the interface along with an SDS molecule.

Mass conservations

As we assume that each piece of deformed film of volume $V = hS$ is a closed system, and that the tension is uniform in the film (meaning the populations of surfactants are uniform), we can write the same law for both SDS and DOH: $2\Gamma_i S + c_i h S = \mathrm{cst}$, with $i = \{s, d\}$. Also, the deformation of this piece of film can be written as $\epsilon = S/S_0 - 1$ with S_0 its initial surface. As the volume is preserved, we thus have $S = S_0(1+\epsilon)$ and $h = h_0/(1+\epsilon)$ for respectively the surface and thickness of film. Casting this into the conservations of SDS and DOH yields:

$$2\Gamma_d(1+\epsilon) + c_d h_0 = 2\Gamma_{d,0} + c_{d,0} h_0 \tag{1.8}$$
$$2\Gamma_s(1+\epsilon) + c_s h_0 = 2\Gamma_{s,0} + c_{s,0} h_0 \tag{1.9}$$

These conservation laws, when fed with a given deformation ϵ and initial conditions $(c_{s,0}, c_{d,0}, h_0)$, are a set of equations which become implicit in the case of the micellar regime, as the total bulk concentrations c_s and c_d are actually each the sum of two variables: a monomeric and a micellar concentration. This is why this model becomes analytically intractable in the micellar regime. For an analytical resolution in the submicellar regime, see Prins *et al.* [5].

Thermodynamic identity

We need now to link surface tension to the surface excesses of all the species, in order to couple it with the mass conservation equations. Thus, we first write formally the evolution of surface tension with respect to the chemical potentials of all the surface active species. We do so by expressing the variation of internal energy $\mathrm{d}U$ for a piece of film, that is the first fundamental thermodynamic relation:

$$\mathrm{d}U = -p\mathrm{d}V + T\mathrm{d}\mathcal{S} + \sum_k \mu_k \mathrm{d}N_k + \gamma \mathrm{d}S \tag{1.10}$$

Where p is the pressure in the film, V the volume of the piece of film, T the temperature, $\mathcal{S}$ the entropy, μ_k the chemical potential of each species $k = \{s, d, n\}$ at the interface, N_k their surface populations, γ the surface tension and S the surface of the piece of film.

On the other hand, as the internal energy $U(V, \mathcal{S}, N_k, S)$ is an extensive function of volume, entropy, surfactant populations and surface, the Euler's theorem for homogeneous functions writes $U = -Vp + \mathcal{S}T + \sum_k \mu_k N_k + \gamma S$, which be can differentiated:

$$\mathrm{d}U = -p\mathrm{d}V - V\mathrm{d}p + T\mathrm{d}\mathcal{S} + \mathcal{S}\mathrm{d}T + \sum_k (\mu_k \mathrm{d}N_k + N_k \mathrm{d}\mu_k) + \gamma \mathrm{d}S + S\mathrm{d}\gamma \tag{1.11}$$

This can now be equated with the fundamental thermodynamics identity and yields:

$$\mathrm{d}\gamma = h\mathrm{d}p - s dT - \sum_k \Gamma_k \mathrm{d}\mu_k \tag{1.12}$$

Where h is the thickness of the piece of film, s is its entropy per unit area and $\Gamma_k = N_k/S$ are the surface excesses which eventually appear here. As we are in normal conditions with constant pressure and temperature throughout the whole experiment, we can thus directly write the relation between surface tension and the chemical potentials of the surface active species:

$$\mathrm{d}\gamma = -\sum_k \Gamma_k \mathrm{d}\mu_k \tag{1.13}$$

Chemical equilibrium

A thermodynamic consequence of the instantaneous chemical equilibrium we impose in the piece of film is that the chemical potentials of the interface and the bulk must be equal. More precisely, for each species, the equality of the chemical potential between the interface, the bulk monomeric populations and the bulk micellar populations must be respected. These conditions are already enforced with all the equilibrium and adsorption laws written in subsection 1.2.1. What we need to write here besides all this is the form of the chemical potential of the monomeric phase:

$$\mu_{k,interface} = \mu_{k,bulk,mono} = \mu_{k,0} + RT\ln(c_k^m) \tag{1.14}$$

Meaning we can now express the surface tension variation as:

$$\mathrm{d}\gamma = -\sum_k RT\Gamma_k \mathrm{d}(\ln c_k^m) \tag{1.15}$$

This can be integrated using the expressions of the Γ_k's 1.6 and yields the full expression:

$$\gamma = \gamma_w - RT\Gamma_\infty \ln\left(1 + 2K_s c_s^m + K_d c_d^m\right) \tag{1.16}$$

Where $\gamma_w = 72.8\,\mathrm{mN/m}$ is the surface tension of pure water, or the glycerol/water mix free of any surfactant. This is the relation between the surface tension and the monomeric concentrations of SDS and DOH.

	Γ_∞ (mol/m^2)	K_s (m^3/mol)	K_d (m^3/mol)	K (m^3/mol)
van den Tempel *et al.* [31]	$2.5 - 5\ .10^{-6}$	5		
Prins *et al.* [5]	7.10^{-6}	0.38	233	
Joos *et al.* [95]	7.10^{-6} (from lit.)			
Vollhardt *et al.* [96]	14.10^{-6} (from data)	0.13	98	
Fang *et al.* [41]	6.10^{-6} (from lit.)	0.78 ou 0.48	1600	4.67 or 5.83
Vollhardt *et al.* [97]	$6.5\ 10^{-6}$	0.13 (from lit.)	98 (from lit.)	

Table 1.1: Table of the co-adsorption Langmuir parameters found in the literature, by chronological order. Most parameters are deduced by the authors from comparison with their experimental data, but some are taken from the previous articles ('from lit.') and some are not given in the paper but can be deduced from the data ('from data').

Numerical resolution and chemical parameters

Equation 1.16 giving $\gamma = f(c_s^m, c_d^m)$ is coupled to the mass conservations 1.8-1.9 we recall:

$$2\Gamma_d(1+\epsilon) + c_d h_0 = 2\Gamma_{d,0} + c_{d,0} h_0$$
$$2\Gamma_s(1+\epsilon) + c_s h_0 = 2\Gamma_{s,0} + c_{s,0} h_0$$

And the chemical equilibrium laws between the monomeric and micellar concentrations:

$$c_s^m = c_s \quad \text{if} \quad c_s < CMC \quad \text{and} \quad c_s^m = CMC \quad \text{otherwise.}$$
$$c_d = c_d^m(1 + K c_s^M)$$

This set of equations must be fed a deformation ϵ, initial concentrations $c_{s,0}$ and $c_{d,0}$, an initial thickness h_0 and the chemical parameters K, K_s, K_d, Γ_∞. Then, a numerical resolution can be performed to determine γ. It is related to the film tension σ^f defined in eq.0.2.4 by $\sigma^f = 2\gamma$.

This is done with a MATLAB code using symbolic computation to approach a solution where mass conservation laws are enforced as close as possible. Performing the minimisation starting with the trivial case $\epsilon = 0$ and increasing (resp. decreasing) gradually searching in the vicinity of the previous solution yields very good results and essentially no numerical error on the total solution $\sigma^f(\epsilon)$.

Regarding the chemical parameters, a wide literature gives access to them, although certain values took time to converge and some are still open to debate [5,31,40,41,95,97]. I report Table 1.1 extracted from our paper Poryles *et al.* [6], which summarises all the parameters we found. Notably, the set of parameters we retain for our numerical resolution is: $K = 4.67\,\mathrm{m}^3/\mathrm{mol}$, $K_s = 0.14\,\mathrm{m}^3/\mathrm{mol}$, $K_d = 98\,\mathrm{m}^3/\mathrm{mol}$ and $\Gamma_\infty = 6.5 \times 10^{-6}$ mol/m^2.

1.2.2 Numerical results

In Fig.1.3, we report our numerical resolution of the system of subsection 1.2.1, in micellar regime (**A**) and submicellar regime (**B**).

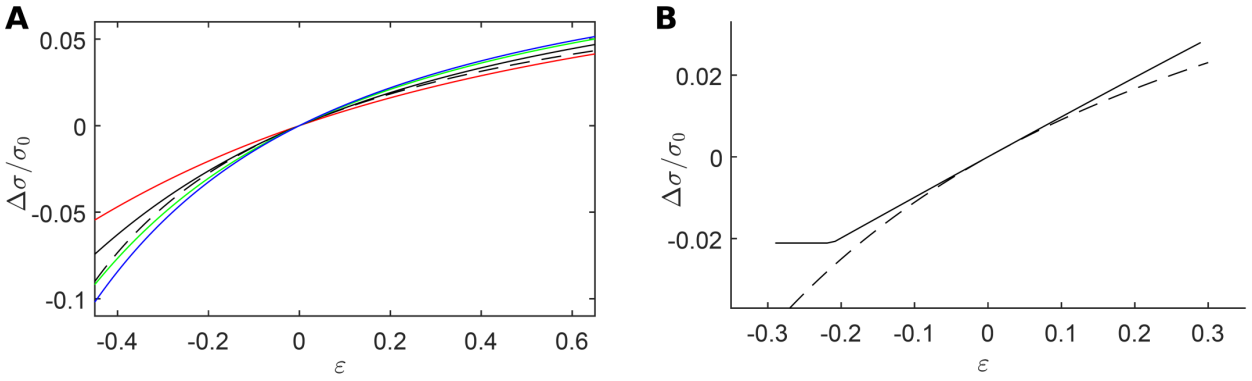

Figure 1.3: Numerical resolution of the strain-stress curves (centred and normalised with the equilibrium tension σ_0). **A:** with $c_s = 2.4\ CMC$ and $c_d = 153\,\mathrm{mg/L}$. The different colours account for different thickness of films h_0 (which is a parameter of the model) from blue to red: $h_0 = 0.3, 0.5, 1, 2\,\mu\mathrm{m}$. The black solid line, which is the full numerical resolution with $h = 1\,\mu\mathrm{m}$, is fitted with the black dotted line with a function $E_f \frac{\epsilon}{1+\epsilon}$ (fitting on E_f). **B:** without dodecanol with an SDS concentration $c_s = 0.9\ CMC$ close to the micellar regime. The solid line is the numerical resolution: for some negative threshold value of ϵ, the micellar regime is attained, and the contribution of SDS to film elasticity vanishes. The dashed line is the best fit with the same function $E_f \frac{\epsilon}{1+\epsilon}$ as previously.

Fig.1.3 **A** shows the strain-stress curves predictions for various thicknesses of film (solid lines) varying over an order of magnitude $h_0 = 0.3, 0.5, 1, 2\,\mu\mathrm{m}$. We define the film elasticity E_f as the slope in origin of these curves, and we see that varying h by an order of magnitude leads to a change in elasticity by a factor 2 at best. **Film elasticity is a slowly varying function of film thickness**.

As eq.16 already suggests despite its crude model, these curves are non-linear in ϵ, Also, we choose to fit our data with the following function:

$$\Delta\sigma = E_f \frac{\epsilon}{1+\epsilon} \tag{1.17}$$

Which defines a film elasticity E_f as its slope in origin.

Important Remark: This function is **NOT** an application of the model of subsection 0.2.3 with $h_\Gamma \gg h_0$ and $E_f = 2E_M$ which we will not risk identifying. It only captures the non-linearity of the curves and allows us to compare the relative stiffness of the different solutions.

The dashed lines in Fig.1.3 are fits with eq.1.17 for $h = 1\,\mu\mathrm{m}$. We see that they indeed capture the non-linearity, but there is also a small discrepancy at large ϵ. As we anticipate that the thicknesses of our films are varying around $h = 0.5 - 1.5\,\mu\mathrm{m}$ and are not always known, the

small discrepancy of the fit will remain under our error bars and eq.1.17 remains a solid tool to characterise our film elasticities.

Fig.1.3 **B** shows the stress-strain curve for a submicellar regime of SDS without dodecanol. In this regime, an interesting feature that we highlight is the passage from the submicellar to the micellar regime occurring for ϵ going below ~ -0.2. When the micellar regime is attained, the film elasticity completely vanishes, meaning that micellar SDS alone has no contribution to it. This can be rationalised by the fact that above the CMC, the bulk monomeric concentration of SDS is always the same, capped at the CMC. Thus, the surface population in equilibrium with this bulk concentration is the same whatever the ϵ, and γ is constant.

Important Remark 2: The other consequence is that the elasticity shown in Fig.1.3 **A** is due to the contribution of dodecanol ! In this latter case, the SDS concentration above the CMC still matters, as dodecanol is shared between the surface, the bulk and the SDS micelles.

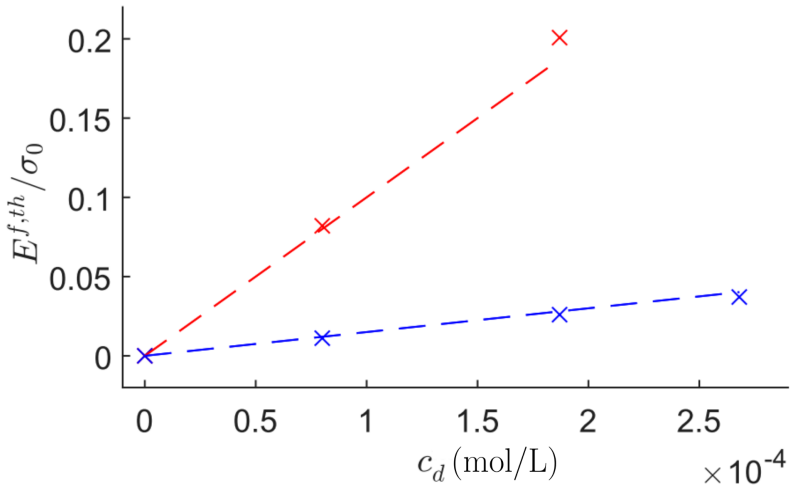

Figure 1.4: Film elasticities E_f fitted on our numerical model as a function of dodecanol concentration for: (red) $c_s = 1.2\ CMC$, (blue) $c_s = 2.4\ CMC$.

Back to the micellar regime, Fig.1.4 shows how E_f (computed through our fits on the numerical resolutions of stress-strain curves) depends on the dodecanol concentration c_d. **Dodecanol is expected to be the main parameter to tune the elasticity of our solutions, as a factor 2 on its concentration can lead to one order of magnitude on E_f !**

This is all the predictions we can make on these stress-strain curves, extending the pioneering work of Prins *et al.* [5] to micellar regimes of SDS/DOH mixtures. We shall now look at the experiments which have allowed us to measure those curves, and compare them to our model.

1.3 A foam film rheometer

The experimental values of the film elasticity we discuss below have been obtained by Raphaël Poryles, using a set up very similar to the set up I used during my PhD to obtain the experimental results of Chapter 3. Here the elementary foam has 5 films, whereas I used a 3 films set-up.

In this section, I briefly present the 5 films set-up, but the precise data analysis will not be discussed here, as it is not part of my work. **I will elaborate much more about both the technological aspects and the data processing in chapter 3 for this reason.**

1.3.1 Experimental setup

The experimental setup is about creating a deformable centimetric elementary foam as depicted in Fig.1.5 and presented more thoroughly by Bussonnière *et al.* [4]. It is composed of five films linked by two free menisci, embedding a central film of length $d_c = 6\,\mathrm{mm}$. The edges at min $z = 0$ and max $z = 42\,\mathrm{mm}$ are supported by a rigid metallic frame along which four motors are free to slide at imposed velocities U_m, supporting the four edges with the red velocity arrows. The rigid frame respects the 120^o of the rest angles between the films.

As it will be shown later, even during rather fast deformations, the angle between the films stay close to $120\ ^o$, as the relative tension variation remains small. In that context, a great advantage of this system is that the films are thus flat rectangles that stay in the same plane whatever the position of the motors. This makes the image acquisition much easier, which is at the origin of all our measurements.

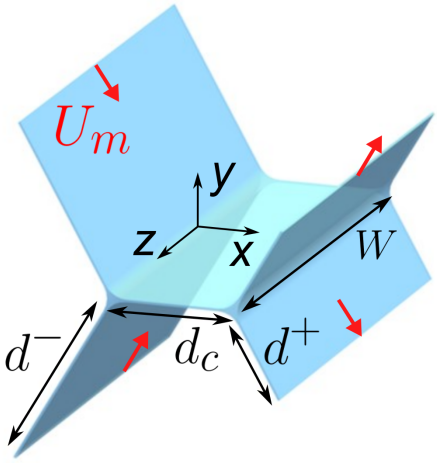

Figure 1.5: Notations and geometry for the elementary foam with 5 films used in this chapter.

This geometry is very close to that of the Besson & Debrégeas setup [78], with an invariance by translation along z instead of an axisymmetry. The gain here is that we have more degrees of freedom for the deformation of the elementary foam, as each motor can have its own velocity/displacement instructions, and also allows us to probe greater amplitudes of deformations ($\epsilon \sim 1$ here *vs.* $\epsilon \sim 0.05$ in the Besson & Debrégeas setup). The main shortcoming of our setup

however is that we will not be able to probe as wide of a range of deformation rates because of the camera resolution and the limitations of the motors (we will have $\dot{\epsilon} \sim 1 - 10\,\mathrm{Hz}$ *vs.* $\omega \sim 0.01 - 100\,\mathrm{rad/s}$).

The foam films are made by bathing the whole deformable frame in soapy solutions which are SDS/DOH aqueous mixtures with 15% of glycerol in volume and fluorescein (at $[Fluo] = 0.8\,\mathrm{g/L}$). This action is automatically performed in a repeatable way using a step-by-step motor rising a bath towards the frame.

The system is monitored from the top using fluorescence cameras with the relevant colour filter for fluorescein. This allows us to track the displacements of the menisci (which are saturated given their thicknesses $\sim 300\,\mu\mathrm{m}$ compared to the films $\sim 1 - 10\,\mu\mathrm{m}$).

The applied deformation has a top-down symmetry, compressing two sides, stretching the two others as depicted in Fig.1.6A. The situation is also symmetrical in amplitude, as the compressed films go from $d^-(0) = d_0 + A/2$ to $d^-(t_{end}) = d_0 - A/2$, the stretched films from $d^+(0) = d_0 - A/2$ to $d^+(t_{end}) = d_0 + A/2$. $d_0 = 12.2\,\mathrm{mm}$ and A varies in the range $[4, 14]$ mm. A first experimental observation is that the central film has a deformation ϵ that remains small ~ 0.1 compared to the other films ~ 1. This leads to consider that the central film remains at its equilibrium tension σ_0.

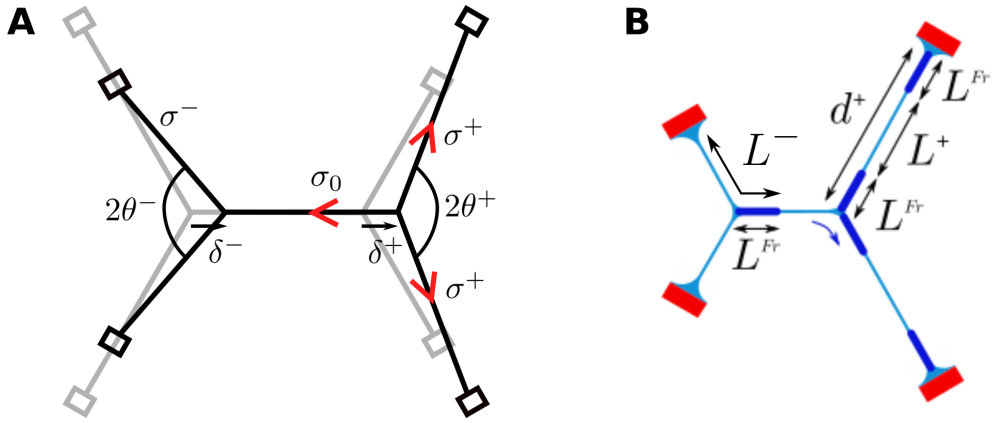

Figure 1.6: Notations for the stress and deformation measurements in the elementary foam. **A:** Compressing and stretching the films result in decreased/increased tensions that induce changes of angles between the films. **B:** Extraction/Withdrawal of lengths of films in the planes of the films must be taken into account to compute the actual deformations of the films.

Fig.1.6A also illustrates the stress measurement in the system. It is based on the same principle as in Besson *et al.* [78], that is a measure of the dynamics of the angles $\theta^{\pm}$, whose deviation from a static value (here given by the second Plateau's law $2\theta_0 = 120^o$) is directly linked to a difference of film tension between the three neighbouring films. Writing the tension balance projected on the horizontal direction at all times (neglecting inertia) gives:

$$\frac{\Delta\sigma^{\pm}}{\sigma_0} = \frac{\sigma^{\pm} - \sigma_0}{\sigma_0} = \frac{1}{2\cos\theta^{\pm}} - 1 \tag{1.18}$$

The angles $\theta^{\pm}$ can be deduced from the displacements $\delta^{\pm}$ of the menisci, and the known positions of the motors at all times. This gives experimental access to the dynamics of film tension.

On the other hand, in Fig.1.6B, we illustrate how the deformations ϵ are obtained. As discussed in 0.4.5 the film deformation can not be directly deduced from the motor and mensicus motion. Fortunately, we have a clear signature of the film creation at the boundary between the streched films and the meniscus : these new pieces of film obey the Frankel law discussed in subsection 0.3.2. They are much thicker (usually 10 times), and thus appear much brighter in the fluorescence images, than the film initially present on the frame, before the deformation. This allows to track these preexisting pieces of film and to define their deformations as:

$$\epsilon^{\pm}(t) = \frac{L^{\pm}(t)}{L^{\pm}(0)} - 1 \tag{1.19}$$

Where $L^{\pm}(0) = d_0 \mp A/2$ is the initial length of preexisting film, and $L^{\pm}(t) = d^{\pm} \mp 2L^{Fr}(t)$ is the current value estimated by taking into account the presence of Frankel films. The underlying assumption of these expressions is that the same quantity of film $L_{Fr}(t)$ (measured only in the central film) goes out/in of all the menisci. **This a rather bold assumption that is needed to further advance with these experiments. Notably, chapter 3, which is about a similar setup, aims at going beyond this approximation.**

1.3.2 Experimental results and comparison with the predictions

The two measures of $\Delta\sigma^{\pm}$ and $\epsilon^{\pm}$ give experimental access to stress-strain curves for the system. Both can be put in the same graph, as $\Delta\sigma^{+}, \epsilon^{+} > 0$ and $\Delta\sigma^{-}, \epsilon^{-} > 0$ are respectively the stress-strain curves in extension and in compression.

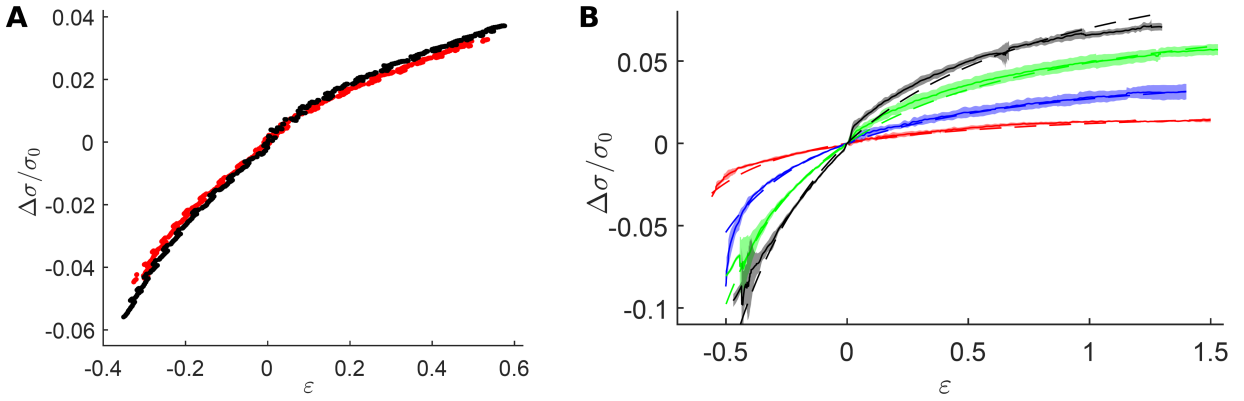

Figure 1.7: Stress strain curves: **A:** For a given chemistry ($c_s = 2.4\ CMC$ for SDS, $c_d = 35\,\mathrm{mg/L}$ for DOH) with different velocities of deformations (red $U_m = 5\,\mathrm{mm/s}$, black $U_m = 10\,\mathrm{mm/s}$). **B:** For different concentration of dodecanol with the same deformation $U_m = 10\,\mathrm{mm/s}$ and SDS concentration $c_s = 2.4\ CMC$ (from red to black: $c_d = 0, 15, 35, 50\,\mathrm{mg/L}$).

In Fig.1.7A, we show two typical curves for a micellar SDS/DOH mixture ($c_s = 2.4\ CMC$ for SDS, $c_d = 35\,\mathrm{mg/L}$ for DOH) for two different velocities of deformation $U_m = 5\,\mathrm{mm/s}$ (red)

and $U_m = 10\,\mathrm{mm/s}$ (black) at fixed $A = 6\,\mathrm{mm}$. Their superimposition is a piece of evidence that the contributions of the intrinsic/extrinsic viscosities of the interfaces can be neglected.

NB 1: The origin is a slightly angular point, this may be due to an initial repositioning of the films when we start the deformation, which is also encountered in chapter 3 and more thoroughly investigated in subsection 3.8.1.

In Fig.1.7B, we fix $U_m = 10\,\mathrm{mm/s}$ and the dodecanol concentration is varied in the range $c_d = 0, 15, 35, 50\,\mathrm{mg/L}$ from red to black (the green of Fig.1.7B corresponds to the black of Fig.1.7A). **We thus see that the more we add dodecanol (a poorly soluble surfactant), the stiffer the foam films get.** The full lines are the experimental data with errors remaining on average below $\sim 5\%$.

We have now given ourselves everything to draw these stress-strain curves for deformed foam films, let us compare them to the thermochemical model of section 1.2. Fig.1.8 is a reboot of Fig.1.3 with now the experimental data (open circles).

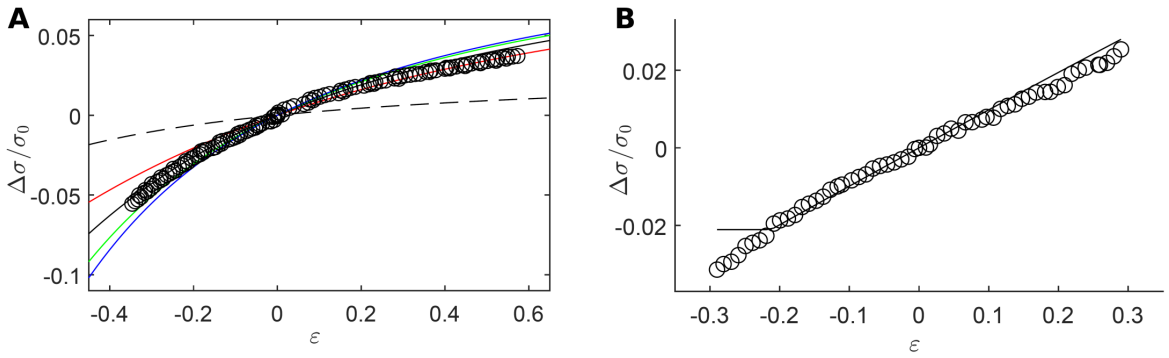

Figure 1.8: Predicted stress strain curves taken from Fig.1.3 with experimental data as the black circles: **A:** with $c_s = 2.4\ CMC$ and $c_d = 153\,\mathrm{mg/L}$. The different colours account for different thickness of films h_0 (which is a parameter of the model) from blue to red: $h_0 = 0.3, 0.5, 1, 2\,\mu\mathrm{m}$. **B:** without dodecanol with an SDS concentration $c_s = 0.9\ CMC$ close to the micellar regime. The solid line is the numerical resolution: for some negative threshold value of ϵ, the micellar regime is attained, and the contribution of SDS to film elasticity vanishes.

In the first case **A**, we have $c_s = 2.4\ CMC$ and $c_d^{nom} = 35\,\mathrm{mg/L}$ the nominal concentration in DOH. The black circles are the experimental data corresponding to the green curve of Fig.1.7B. We first tried to plot the numerical prediction using the nominal concentration of DOH c_d^{nom}, resulting in the black dotted line. The slope remained too small, even when we start sweeping realistic values for the film thickness which has been measured as $h_0 = (1.0 \pm 0.5)\ \mu\mathrm{m}$. We thus took the intermediate value $h_0 = 1\,\mu\mathrm{m}$ and fitted on an effective dodecanol concentration c_d^{fit}, with in mind to take into account the impurities present in the solution besides the nominal concentration of dodecanol added by us. The black solid line is the main fit with $h_0 = 1\,\mu\mathrm{m}$ and $c_d^{fit} = 153\,\mathrm{mg/L}$.

In the second case **B** with $c_{s,0} = 0.9\ CMC$, the circles are the experimental data, the solid line is our model, and the slope agreement is rather good without any fitting parameter. The

only physical ingredient we do not capture is the elasticity of the film as it is compressed enough for it to reach $c_s = CMC$ when the interfaces evacuate surfactants towards the bulk. As said above, in our model, without the presence of any other surfactants, the elastic contribution of SDS vanishes, which we do not observe experimentally. One reason might be what we suppose for our initial conditions (given by the foam films we extract from the bath), that is we have a piece of bulk with a total concentration $c_{s,0}$, which is the nominal concentration of surfactant added to the solution, sandwiched between two interfaces whose surfactant populations $\Gamma_{s,0}$ are at equilibrium with it. Given the short amount of time it takes to create these interfaces when they are extracted, we could expect them to tap into the already-isolated piece of bulk being extracted, thus lowering the initial concentration $c_{s,0} < c_s^{nom}$ below the nominal concentration. This problem of film extraction, and to what extent the initial extracted film shares the same concentrations than the bath, is still open to debate. This was discussed by de Gennes [43] in 2001, in which a model keeping mechanical and thermodynamic equilibrium instantaneous, even at the short time scales of a film pullout, can lead to predict unrealistic shapes for foam films.

Now, it is also possible to extract a film elasticity E_f out of the experimental data using the same fit of eq.1.17, just as we did with our numerical predictions. These fits are represented as the dotted lines in Fig.1.7B and describe well our experimental data as well.

1.3.3 Theoretical and experimental film elasticities

Experimental film elasticities are reported in Fig.1.9: **A** where SDS is at $c_s = 1.2\ CMC$ (red) and $c_s = 2.4\ CMC$ (blue, corresponds to the four curves of Fig.1.7B) and **B** where no dodecanol is added to the solution and c_s varies from $0.75\ CMC$ to $6\ CMC$ (the red and blue points match the points of **A** at $c_d^{nom} = 0$). The dotted lines in **A** are only guides to the eye. The denomination c_d^{nom} in **A** is the nominal concentration of dodecanol, that is the quantity effectively added to the solutions.

A first observation, without dodecanol on Fig.1.9**B**, is that film elasticity is a decreasing function of c_s. The extreme values tell us that an increase by a factor 10 in SDS concentration can yield a decrease by a factor 50 in film elasticity. This behaviour is not easy to rationalise, as a pure micellar SDS solution is expected to have a vanishing film elasticity under the assumption that the chemical equilibrium is met at all times. This very last point of chemical equilibrium hypothesis is not to be called into question again however, since if it was the problem, we would see a velocity dependency of our elasticity, which we do not. **As discussed earlier, SDS is known to come with residual dodecanol, and its micelles to host them in the bulk [42, 93], which is a first unwanted source of surface active impurities contributing to the elasticity as the main surfactant contribution vanishes.** Also, the exchanges of these impurities between the bulk and the micellar phase (more micelles means more soluble impurities) make the dependency of E_f with $c_s > CMC$ non trivial, even at fixed quantities of impurities, making it even harder to rationalise.

Also, when we start adding DOH ourselves (*cf.* Fig.1.9**A**), the elasticity of foam films increases quite rapidly, over an order of magnitude by adding up to $c_d^{nom} = 50\,\mathrm{mg/L} = 2.7 \times 10^{-4}\ \mathrm{mol/L}$ making it comparable to the elasticity of SDS in its submicellar regime. This increase in elasticity is all the more important as the SDS concentration is close to the CMC. This can be qualitatively rationalise by the fact that more micelles means a greater share of the population of DOH in the

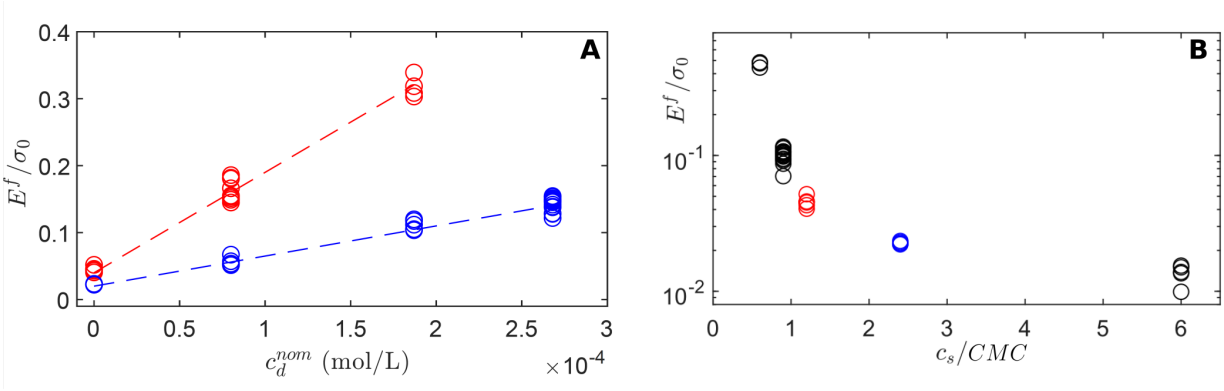

Figure 1.9: Film elasticities: **A:** as a function of the dodecanol concentration c_d (red $c_s = 1.2\ CMC$, blue $c_s = 2.4\ CMC$); **B:** as a function of SDS concentration without any added dodecanol.

micellar phase, making its equilibrium surface population variations lower when the interface is deformed.

Effective concentration of dodecanol

These fits over the dodecanol concentration can be repeated so that we match the films elasticities $E^{f,th} = E^{f,exp}$ measured earlier, and we estimate the effective dodecanol concentrations $c_d^{fit} = f(c_d^{nom})$ in Fig.1.10. In red we have the data for $c_s = 1.2\ CMC$, in blue $c_s = 2.4\ CMC$. The black dotted line is the first bisector, where the data would be in the case of a flawless model applied to ideal solutions.

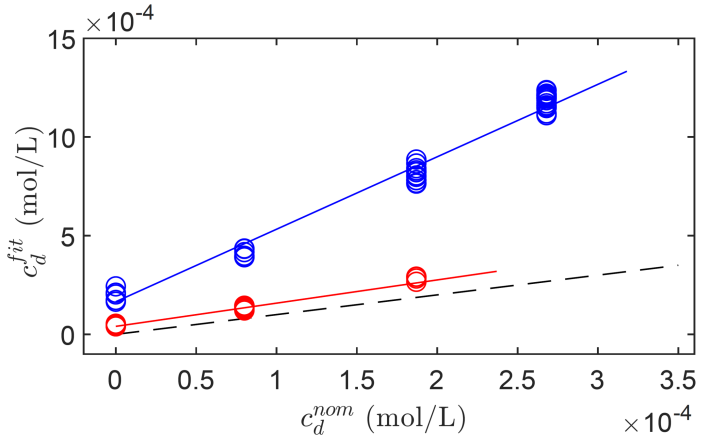

Figure 1.10: Fitted concentration of dodecanol c_d^{fit} as a function of the nominal concentration c_d^{nom} added to the solutions. Blue is with $c_s = 2.4\ CMC$, red is for $c_s = 1.2\ CMC$. The black dotted line is the function $y = x$.

The first observation is that the global quantity of dodecanol virtually added to the solution to get a quantitative match with the data increases with the concentration of SDS. This is expected, as more SDS means more impurities in the solution. However, the slopes are larger

than 1, with the red one, close to the CMC being almost 1 while the blue one is closer to 3. This is the signature that SDS impurities alone cannot explain the quantitative mismatch between our data and our model fed with the nominal concentrations of DOH. Seeing the dependency of this slope with the concentration of SDS, this might be a problem caused by a flawed value for K, the exchange coefficient between the micellar and monomeric bulk phases. Another possible explanation could be direct DOH exchanges between the SDS micelles and the interface.

1.4 Conclusions of Chapter 1

- Foam film elasticity is not a trivial concept: it is not about surfactant gradients or unsteady diffusion problems but rather finite size effects of the bulk for the sake of populating the interfaces.
- Back in 1967, Prins *et al.* [5] developed a theoretical model based on Langmuir isotherms taking into account the small thicknesses of the bulk and made predictions for the elasticities in the submicellar regime. They also conducted experiments which validated their model, stretching a vertical film and looking at its thickness profile.
- I extended the model to the micellar regime, which required a numerical resolution not available at the time of Prins. We fitted the model on experimental data made prior to my arrival, deforming a 5 films elementary foam allowing us to draw the stress-strain curves of foam films $\frac{\Delta\sigma}{\sigma_0} = f(\epsilon)$.
- Our thermochemical model captures the qualitative behaviour of these curves but fails to predict them quantitatively with the nominal concentrations of surfactants added to the solutions.
- The not-so-well-known kinetics of hydrolysis of SDS into dodecanol and the sensibility of film elasticity with insoluble impurities make it difficult to actually control and predict the stress-strain curves quantitatively. We fitted our model on an effective dodecanol concentration encompassing both the amount of dodecanol already present with SDS and the insoluble impurities present in the air.
- We managed to evaluate film elasticity E_f for quite a wide range of SDS and dodecanol concentrations. This will be useful later on while looking at the visco-elastic response of an elementary foam in chapter 3, in order to validate the elasticity measurements performed thereupon.

2

In-plane motions in a foam film: line tension and damping forces

Foam films display complex 2D motions in their own planes, which can be easily visualised when we look at the reflected dancing colours at their surface. Any child playing with bubbles can notice it! A closer look also reveals that these coloured patterns tend to adopt circular shapes. But what is the driving force at play here? How is it related to the colours? The short answer is: the different colours correspond to different film thicknesses, and the resulting thickness gradient corresponds to a driving force on the interfaces, due to its excess of energy compared to a flat film. Hence the coloured circular arrangement seen at the surface.

Also, the motions implied by these forces must be damped somehow, and we need to clarify the physical ingredients potentially at stake here: it may be due to the intrinsic surface shear viscosity η_s and/or bulk viscosities of both the gas and the liquid η_g or η_l. The competition between these ingredients, and more incredibly the existence of a surface viscosity in a certain range of situations, is still open to debate!

In this chapter, I will expose the work of our group around an experimental setup which allowed us to create and measure a line tension T in the plane of a single foam film, using its heterogeneities of thickness. By studying the relaxation of a patch of foam film, and knowing the damping mechanism at play, we were able to quantify and validate our force measurement of T. This setup was built a first time during the internship of Marion Berry (spring/summer 2021, supervised by Raphaël Poryles), from which a proof of concept and preliminary results were obtained, and a second time the year after for the internship of Gaëlle Audéoud (spring/summer 2022 supervised by me), from which the definitive experimental data were obtained. I made the data analysis and the theoretical model, under the supervision of Isabelle Cantat, and the results have been submitted to *Physical Review Letters* [99] (currently addressing minor revisions).

2.1 Capillary force and line tension in foam films

As we discussed in the Introduction, in-plane motions of foam films are only about plug flows for time scales up to tens of seconds (*cf.* 0.2.1), giving them a sliding puzzle-like dynamics. This has proven to be a crucial piece of information, as it enabled the development of a general theoretical framework for these motions in the form of 2D Navier-Stokes equations. This conception of foam films retraces back to the work of Mysels, Couder *et al.* [28,49], part of which being fairly recent.

These equations have since enabled to further advance in the description of these systems: measuring surface viscosities [1,36], studying gravity drainage and the convection in the plane of foam films [64,100], or even 2D turbulence phenomena [101]. A proper passage from a 3D to a 2D Stokes equation in the case of a foam film is derived and proposed in Appendix 4, along with its Green function.

In this section, we write our own equation of motion following the same path as these previous studies. The novelty is that we build a stress tensor for the fluid which takes into account thickness gradients in the film. Once we have this constitutive law and the corresponding equation of motion, we will focus on the particular case of a very localised thickness gradient, which will allow us to define a line tension T, and the 2D Stokes equation in which it is a source term.

All this preparatory theoretical work will help us describe the experiment of the next section where a line tension is brought to light by a "simple" relaxation phenomenon.

2.1.1 Building the capillary stress tensor for an elementary piece of film with a thickness gradient

We consider the piece of film represented in the Figure 2.1. It is limited by the two interfaces and by the vertical planes which intersect the plane $z = 0$ along the elementary lengths $d\xi$ and ds. The unit vector $\boldsymbol{n}$ is chosen along the steepest slope of the interface and the unit vector $\boldsymbol{t}$ is perpendicular to $\boldsymbol{n}$ (both in the (x, y) plane):

$$\boldsymbol{n} = (h_x, h_y, 0)/\sqrt{h_x^2 + h_y^2}\ , \quad \boldsymbol{t} = (h_y, -h_x, 0)/\sqrt{h_x^2 + h_y^2} \tag{2.1}$$

With the indices accounting for the derivatives along the specified coordinates of the cartesian basis $\mathcal{B}_0 = (\boldsymbol{e}_x, \boldsymbol{e}_y)$.

Our goal is now to build the 2D stress tensor for the film $\overline{\overline{\boldsymbol{\sigma}}}_{cap}$ by considering the forces exerted on the lateral faces. Note that the air pressure is taken as the pressure reference, so that no forces are exerted on the top and bottom interfaces. The norm of the thickness gradient is a small parameter in the problem, as classically used in the lubrication approximation. To build the film stress tensor, we anticipate that the forces exerted on the system are of order 2 in this parameter (as will be shown below), and we thus drop higher order terms. Also, we consider that both interfaces are subject to a surface tension $\gamma = \gamma_0 + \delta\gamma$ deviating from its equilibrium tension γ_0 by a second order term $\delta\gamma$.

Let us first consider the face 1 defined in Fig.2.1. It is a rectangle of area $dS_1 = 2hds$ of normal $\boldsymbol{n}$, and we denote $\boldsymbol{dF}_1 = \boldsymbol{dF}_{p,1} + \boldsymbol{dF}_{\gamma,1}$ the total force applied on the surface. The local pressure in the film is $P = -\gamma_0 \Delta h$, leading to the pressure force $\boldsymbol{dF}_{p,1} = -PdS_1\boldsymbol{n} = 2\gamma_0 h \Delta h ds \boldsymbol{n}$. Note

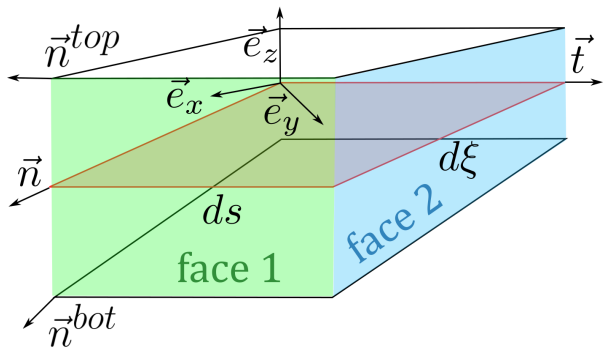

Figure 2.1: Notations for an elementary piece of foam film confined between two liquid-gas interfaces. The semi-thickness h of the foam film varies along ξ.

that here we discarded the second order term $\delta\gamma$ in the Laplace pressure as we anticipate it would yield a contribution of high order.

The forces induced by the surface tension at the top and bottom interfaces $\boldsymbol{dF}_{\gamma,1}$ need more precautions as the force orientations are slightly tilted with respect to $\boldsymbol{n}$ and differ between both interfaces. They are applied along the vectors:

$$\boldsymbol{n}^{top/bot} = \frac{\boldsymbol{n} \pm ||\boldsymbol{\nabla} h|| \boldsymbol{e}_z}{\sqrt{1 + ||\boldsymbol{\nabla} h||^2}} \tag{2.2}$$

Where by definition of our local frame $\mathcal{B}_e = (\boldsymbol{n}, \boldsymbol{t})$, we have $||\boldsymbol{\nabla} h|| = |\partial_\xi h|$. Thus, we write the forces:

$$\boldsymbol{dF}_{\gamma,1} = (\gamma_0 + \delta\gamma) ds \ (\boldsymbol{n}^{top} + \boldsymbol{n}^{bot}) = \Big(2\gamma_0 (1 - \frac{||\boldsymbol{\nabla} h||^2}{2}) + 2\delta\gamma\Big) ds \ \boldsymbol{n} \tag{2.3}$$

In which the two contributions along $\boldsymbol{e}_z$ compensate for each other, leading to this development at second order. We can now write the total force acting on face 1:

$$\boldsymbol{dF}_1 = 2\Big(\gamma_0 (1 - \frac{||\boldsymbol{\nabla} h||^2}{2} + h\Delta h) + \delta\gamma\Big) ds \ \boldsymbol{n} \tag{2.4}$$

We now look at face 2 of normal $\boldsymbol{t}$. In a similar way, we write the pressure force $\boldsymbol{dF}_{p,2} = -P dS_2 \boldsymbol{t} = 2\gamma_0 h \Delta h d\xi \boldsymbol{t}$ which is similar to face 1 at leading order despite the trapezoidal form of dS_2.

This time, the direction of the forces due to surface tension is horizontal along $\boldsymbol{t}$ on both interfaces. The subtlety here lies in the lengths over which are applied the surface tension at the top and bottom interfaces, and which are given by $dl_2 = d\xi(1 + ||\boldsymbol{\nabla} h||^2/2)$ at second order. This leads to the expression:

$$\boldsymbol{dF}_{\gamma,2} = 2(\gamma_0 + \delta\gamma) dl_2 \ \boldsymbol{t} = \Big(2\gamma_0 (1 + \frac{||\boldsymbol{\nabla} h||^2}{2}) + 2\delta\gamma\Big) d\xi \ \boldsymbol{t} \tag{2.5}$$

And we finally have the full expression of the force on face 2:

$$\boldsymbol{dF}_2 = 2\Big(\gamma_0(1+\frac{||\boldsymbol{\nabla} h||^2}{2}+h\Delta h)+\delta\gamma\Big)d\xi\ \boldsymbol{t} \tag{2.6}$$

The goal now is to finally write $\overline{\overline{\boldsymbol{\sigma}}}_{cap}$ whose general expression is given and developed:

$$\overline{\overline{\boldsymbol{\sigma}}}_{cap} = \begin{pmatrix} \frac{d\boldsymbol{F}_1}{ds}.\boldsymbol{n} & \frac{d\boldsymbol{F}_1}{ds}.\boldsymbol{t} \\ \frac{d\boldsymbol{F}_2}{d\xi}.\boldsymbol{n} & \frac{d\boldsymbol{F}_2}{d\xi}.\boldsymbol{t} \end{pmatrix}_{\mathcal{B}_e} = \gamma_0 \begin{pmatrix} -||\boldsymbol{\nabla} h||^2 & 0 \\ 0 & ||\boldsymbol{\nabla} h||^2 \end{pmatrix}_{\mathcal{B}_e} + 2\Big(\gamma_0(1+h\Delta h)+\delta\gamma\Big)\overline{\overline{\boldsymbol{I}}}_2 \tag{2.7}$$

Which can be more easily transcribed in the initial cartesian basis $\mathcal{B}_0 = (\boldsymbol{e}_x, \boldsymbol{e}_y)$ in the form $\overline{\overline{\boldsymbol{\sigma}}}_{cap} = \overline{\overline{\boldsymbol{\sigma}}}^{\,*}_{cap} + \sigma^f \overline{\overline{\boldsymbol{I}}}_2$, with $\sigma^f = 2\Big(\gamma_0(1+h\Delta h)+\delta\gamma\Big)$ and:

$$\overline{\overline{\boldsymbol{\sigma}}}^{\,*}_{cap} = -\gamma_0 \begin{pmatrix} \partial_x h^2 - \partial_y h^2 & 2\partial_x h\ \partial_y h \\ 2\partial_x h\ \partial_y h & \partial_y h^2 - \partial_x h^2 \end{pmatrix}_{\mathcal{B}_0} \tag{2.8}$$

This tensor $\overline{\overline{\boldsymbol{\sigma}}}_{cap}$ eq.2.7 accounts for all the capillary forces acting on a piece of foam film with a thickness gradient such as depicted in Fig.2.1. It takes into account both the pressure and surface tension forces projected in the plane of the film.

However, the specific case we want to further describe and study has only very localised regions where h varies. The experimental situation will be described in section 2.2: we create two adjacent regions of constant thicknesses (or varying very slowly spatially) where the variations of h are all contained at the border. This border is so thin compared to the dimensions of the two regions that we will aim at describing this zone as a 1D object subject to a line tension T defined and computed using $\overline{\overline{\boldsymbol{\sigma}}}_{cap}$.

2.1.2 Gradients of thickness localised in a very thin region: building a line tension T

The goal of this subsection is to consider the limit where **the thickness of the foam film varies in a very localised zone only, which we will call thickness jump zone hereafter.** We will approximate this thin zone to a closed contour $\mathcal{C}$, of any shape, across which we jump from a thickness h_1 to h_2. By expressing the capillary stress tensor $\overline{\overline{\boldsymbol{\sigma}}}_{cap}$ in this region, we can integrate the forces and exhibit the presence of a line tension T acting along $\mathcal{C}$.

We will focus on the force acting on a section line normal to $\mathcal{C}$, exerted by one side of the line on the other. The line tension T is defined as the excess of force applied by one side of the line on the other (Fig.2.2, the line is parallel to the thickness gradient) compared to the case where we would have a flat film with interfaces at the equilibrium surface tension γ_0. It can be expressed as (**note that we define T for a single interface whereas $\overline{\overline{\boldsymbol{\sigma}}}_{cap}$ has been already defined for two interfaces**) :

$$T = \int_{\xi_{min}}^{\xi_{max}} \boldsymbol{t}.(\frac{1}{2}\overline{\overline{\boldsymbol{\sigma}}}_{cap} - \gamma_0\overline{\overline{\boldsymbol{I}}}_2).\boldsymbol{t}\ d\xi \tag{2.9}$$

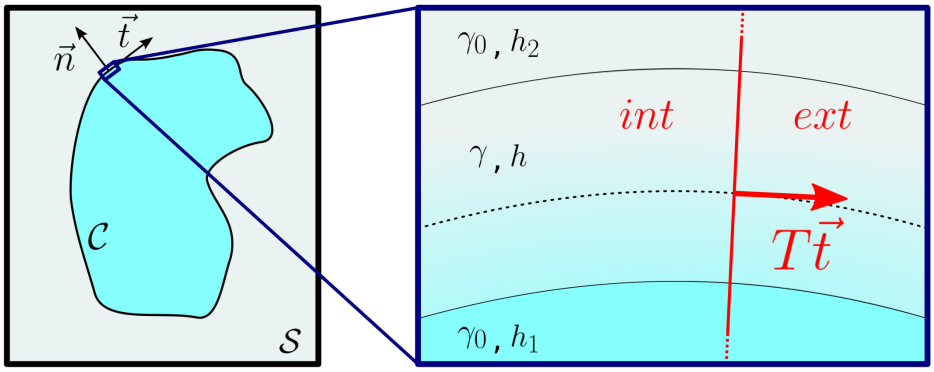

Figure 2.2: Contour $\mathcal{C}$ separating two zones of different thicknesses h_1 and h_2 at equilibrium surface tension γ_0. Line tension T is defined as the excess force applied by one side (ext) on the other (int) compared to a case where there is no change in h or γ along the line.

Where ξ_{min} and ξ_{max} are chosen outside of the transition region, so that the integral does not depend on their precise value. The computation of T needs to be carefully written, as not only the thickness varies along ξ, but also the surface tension $\gamma = \gamma_0 + \delta\gamma$.

Surface tension profile within the thickness jump zone

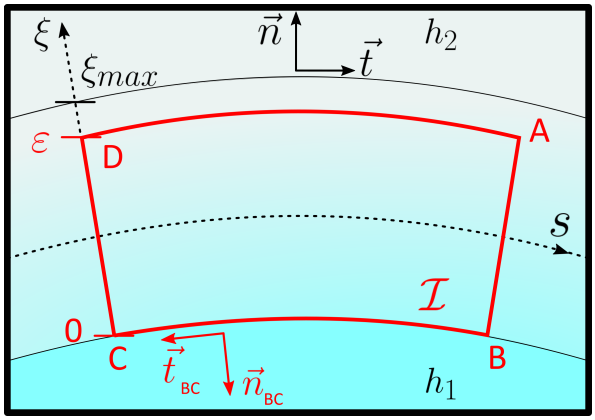

Figure 2.3: Notations for a contour $\mathcal{I}$ in the thickness jump zone symbolised by the colour gradient. By integrating the interface stress along this contour for any ε, we get an expression for the local tension $\gamma(\xi)$ in the thickness jump zone, enabling the computation of the line tension T.

In order to estimate $\delta\gamma$ in the thickness jump zone, we start by doing a force balance over a contour $\mathcal{I}$ defined in Fig.2.3. It follows the tangential direction of $\mathcal{C}$ and encompasses a range of ξ from $\xi_{min} = 0$ the edge of the inner side where $h = h_1$ to $\xi = \epsilon$ arbitrarily taken between 0 and $\xi = \xi_{max}$ the edge of the outer side where $h = h_2$. The choice of ξ_{max} is a practical problem which we address in the experimental section 2.3.4. Another important assumption is that the zone where $\boldsymbol{\nabla} h$ is not negligible is very localised. That means we assume that $\xi_{max}/R \ll 1$, the

width ξ_{max} over which h varies is much smaller than the radius of curvature R of contour $\mathcal{C}$. We will thus develop our force balance equation in orders of $\frac{\xi_{max}}{R}$.

Let us write this force balance acting on the closed contour $\mathcal{I}$:

$$\boldsymbol{F}_{\mathcal{I}} = \oint_{\mathcal{I}} \overline{\overline{\boldsymbol{\sigma}}}_{cap}.\boldsymbol{n}_{\mathcal{I}}\, d\mathcal{I} \tag{2.10}$$

Where $\boldsymbol{n}_{\mathcal{I}}$ is the local normal vector oriented outward to the contour $\mathcal{I}$ of which we show an example for the segment $[BC]$ in Fig.2.3 (not to be confused with $\boldsymbol{n}$, the local normal to $\mathcal{C}$). On the one hand, the integrals over $[AB]$ and $[CD]$ have constant local normal vectors $\boldsymbol{n}_{AB}$ and $\boldsymbol{n}_{CD}$ and a varying stress tensor $\overline{\overline{\boldsymbol{\sigma}}}_{cap}$ as the thickness h varies. On the other hand, $\overline{\overline{\boldsymbol{\sigma}}}_{cap}$ is constant over $[BC]$ and $[DA]$, but the local normal vectors $\boldsymbol{n}_{BC/DA}(s_{\mathcal{I}})$ will vary. Note that because we suppose that the local curvature $\kappa = 1/R$ of $\mathcal{C}$ varies slowly along the curvilinear abscissa, we approximate the Laplacian in the expression of $\overline{\overline{\boldsymbol{\sigma}}}_{cap}$ to $\Delta h = \partial_{\xi\xi} h$, and we get, using eq.2.7:

$$\begin{aligned}\frac{\boldsymbol{F}_{\mathcal{I}}}{\gamma_0} = &\Big[\boldsymbol{n}_{AB} + \boldsymbol{n}_{CD}\Big] \int_0^{\epsilon} \Big[(\partial_\xi h)^2 + 2h\partial_{\xi\xi} h + 2(1 + \frac{\delta\gamma}{\gamma_0})\Big] d\xi \\ &+ 2(1 + \frac{\delta\gamma(0)}{\gamma_0}) \int_B^C \boldsymbol{n}_{BC}(s_{\mathcal{I}}) ds_{\mathcal{I}} \\ &+ \Big[-(\partial_\xi h)^2\Big|_\epsilon + 2h\partial_{\xi\xi} h\Big|_\epsilon + 2(1 + \frac{\delta\gamma(\epsilon)}{\gamma_0})\Big] \int_D^A \boldsymbol{n}_{DA}(s_{\mathcal{I}}) ds_{\mathcal{I}}\end{aligned} \tag{2.11}$$

The first line accounts for the integral over $[AB]$ and $[CD]$, the second for $[BC]$ and the third for $[DA]$. Note that we use $\partial_\xi h = 0$ and $\partial_{\xi\xi} h = 0$ at $\xi = 0$ as the inner and outer region of $\mathcal{C}$ are defined so that $h = \mathrm{cst}$.

We now express the local vectors of $\mathcal{I}$, $\boldsymbol{n}_{AB}$ and $\boldsymbol{n}_{CD}$ in the local basis of $\mathcal{C}$ $(\boldsymbol{t},\boldsymbol{n})$ using the local curvature of $\mathcal{C}$ denoted $\kappa = 1/R$, and the length $[BC] = L$:

$$\begin{aligned}\boldsymbol{n}_{AB} &= \boldsymbol{t} - \frac{L}{2R}\boldsymbol{n} \\ \boldsymbol{n}_{CD} &= -\boldsymbol{t} - \frac{L}{2R}\boldsymbol{n}\end{aligned}$$

And the vector integrals over $[BC]$ and $[DA]$:

$$\begin{aligned}\int_B^C \boldsymbol{n}_{BC}(s_{\mathcal{I}}) ds_{\mathcal{I}} &= -L\boldsymbol{n} \\ \int_D^A \boldsymbol{n}_{DA}(s_{\mathcal{I}}) ds_{\mathcal{I}} &= +L(1 + \frac{\epsilon}{R})\boldsymbol{n}\end{aligned}$$

Furthermore, because the contour $\mathcal{C}$ is closed and the capillary forces diverge as $\xi_{max} \longrightarrow 0$, we neglect inertia and viscous forces and we have the nullity of $\boldsymbol{F}_{\mathcal{I}}$. Projecting eq.2.11 along $\boldsymbol{n}$, dividing by L, and setting $\delta\gamma(0) = 0$ (even if it mean redefining the reference of surface tension with an offset to the equilibrium value), we get:

$$0 = -\frac{1}{R}\int_0^{\epsilon}\Big[(\partial_\xi h)^2 + 2h\partial_{\xi\xi}h + 2\frac{\delta\gamma}{\gamma_0}\Big]d\xi \qquad (2.12)$$
$$+ (1+\frac{\epsilon}{R})\Big[-(\partial_\xi h)^2\Big|_\epsilon + 2h\partial_{\xi\xi}h\Big|_\epsilon + 2\frac{\delta\gamma(\epsilon)}{\gamma_0}\Big]$$

Out of the integral, two terms depending directly on h scale as $\mathcal{O}(\frac{h^2}{\epsilon^2})$ and are balanced by the field of surface tension $\frac{\delta\gamma(\epsilon)}{\gamma_0}$. We also notice the presence of terms of order $\mathcal{O}(\frac{h^2}{\epsilon R})$ which need to be balanced by $\frac{\delta\gamma(\epsilon)}{\gamma_0}$ as well. Writing with the $\nabla = \partial_\xi$ notation again, eq.2.12 leads to an expression of the field of surface tension:

$$\frac{\delta\gamma}{\gamma_0}(\epsilon) = \frac{1}{2}||\boldsymbol{\nabla} h(\epsilon)||^2 - h\Delta h(\epsilon) + \Gamma_{sup}(\epsilon) \qquad (2.13)$$

Where the first two terms are of lowest order $\mathcal{O}(\frac{h^2}{\epsilon^2})$ and where Γ_{sup} is the correction for the higher order $\mathcal{O}(\frac{h^2}{\epsilon R})$. The first two terms of the surface tension field are sufficient to advance and to finally define the line tension T, and a discussion about the higher order term $\Gamma_{sup} = \mathcal{O}(\frac{h^2}{\epsilon R})$ awaits the interested reader in subsection 2.1.3.

Final expression of T

We now have the expression $\delta\gamma(\epsilon)$ for the surface tension anywhere in the thickness jump $\epsilon \in [0, \xi_{max}]$. This is a key information as the general expression of T writes using the expression of $\overline{\overline{\boldsymbol{\sigma}}}_{cap}$ of eq.2.7:

$$T = \int_\xi \boldsymbol{t}.(\frac{1}{2}\overline{\overline{\boldsymbol{\sigma}}}_{cap} - \gamma_0\overline{\overline{\boldsymbol{I}}}_2).\boldsymbol{t}\ d\xi = \gamma_0\int_\xi \Big(\frac{1}{2}||\boldsymbol{\nabla} h||^2 + \frac{\delta\gamma}{\gamma_0} + h\Delta h\Big)d\xi \qquad (2.14)$$

Thanks to the expression of $\delta\gamma$ given by eq.2.13, the lowest order is simplified: the gradient term is completed and the laplacian term is cancelled, yielding:

$$\boxed{T = \gamma_0\int_{\xi_{min}}^{\xi_{max}} ||\boldsymbol{\nabla} h(\xi)||^2\ d\xi} \qquad (2.15)$$

This is the expression for the line tension acting along $\mathcal{C}$. Interestingly, this quantity is actually twice the excess of energy stored in the excess of area in the thickness jump zone. Another computation based on thermodynamics considerations and a discussion awaits the reader in subsection 2.1.3.

2.1.3 Important remarks

Line tension expression through virtual work considerations and factor 2 with the excess of energy per unit length of line

In subsection 2.1.2, we have found an expression of the line tension T, which is actually an excess of stress stored into the thickness jump. We found it by considering the mechanical equilibrium of a tilted patch of film at rest in this region. What is implied through the existence of this

mechanical equilibrium is that an element of film flattens out through capillary flows at times much longer than the time of our experiment. In this mean time, surface tension enforces surface conservation by being larger in the thickness jump. This is all due to this intrinsic feature of a surfactant-laden interface that is being able to create Marangoni stresses to resist capillary flows.

However, the expression of the excess of stress/line tension T can also be retrieved by considering the virtual work of the flat films neighbouring the thickness jump, which act as reservoirs of surface tension, both sides being set at reference tension $\gamma = \gamma_0$. These works must be computed under the constraints of conserved volume and area of interface.

Let us consider a portion of thickness jump, of initial width ξ_{max} (along y), length L (along x) (with respect to the notations of subsection 2.1.2), and initial thickness field h_0. $A^p = L\xi_{max}$ denotes the projected area of interface. We also consider that the thickness jump is in contact with a reservoir of surface tension set at γ_0. The portion of thickness jump is deformed, with its width becoming $\xi_{max} + d\xi_{max}$, its length $L + dL$ and its thickness field h. These variations verify $d\xi_{max}dL < 0$ as we impose the set of constraints: (i) $V = \int_{A^p} h dxdy = \text{cst}$ conserved volume, and (ii) $A = \int_{A^p}(1 + \frac{1}{2}||\boldsymbol{\nabla} h||^2)dxdy = \text{cst}$ conserved area of interface. We will denote $\delta\ell = \frac{1}{2}\int_0^{\xi_{max}} ||\boldsymbol{\nabla} h_0||^2 dy$ the excess of length stored in the thickness jump along the y axis in the initial state.

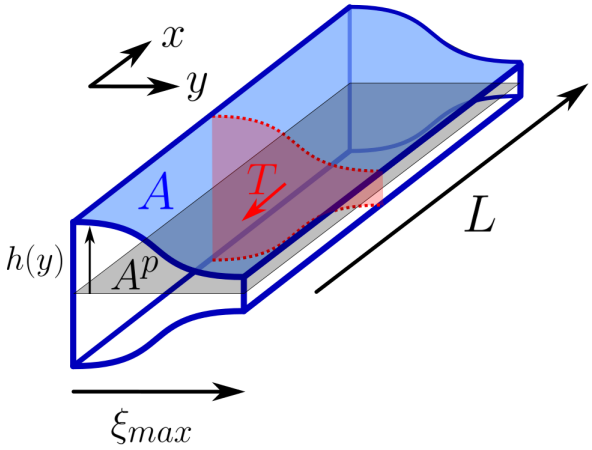

Figure 2.4: Notations for a segment L of thickness jump.

The work of the reservoir in this transformation must be zero, as there is no dissipative phenomenon at stake here, nor any internal energy variations as area is conserved. This writes:

$$\delta W^{res} = 0 = \gamma_0 dA^p + T dL \tag{2.16}$$

Where T is the line tension, defined for one interface, that is an excess of stress stored in the thickness jump. In order to determine T, we need to provide an expression for the variation of projected area A^p during the transformation. This variation is the consequence of imposing both volume and interface area conservations, meaning we work at constant distribution of thicknesses (the histograms of h_0 and h are the same). Thus, patches of film are redistributed in steeper regions during the transformation (for $dL > 0$, resp. flatter regions for $dL < 0$), and the projected area A^p changes.

These constraints impose a dilation along the y axis, and the relationship between the gradients of thickness writes:

$$\boldsymbol{\nabla} h = \boldsymbol{\nabla} h_0 \times \left(\frac{1}{1+\frac{d\xi_{max}}{\xi_{max}}}\right) \tag{2.17}$$

Area conservation can be written between both configurations:

$$L \times (\xi_{max} + \delta\ell) = (L + dL) \times \int_0^{\xi_{max}+d\xi_{max}} (1 + \frac{1}{2}||\boldsymbol{\nabla} h||^2) dy \tag{2.18}$$

Where a change of variable $y' = y/(1+\frac{d\xi_{max}}{\xi_{max}})$ can be applied in the integral of the left-hand side, as well as eq.2.17 for the gradient, and we can linearise and simplify our expression to get:

$$0 = \xi_{max} dL + L d\xi_{max} - \frac{L}{\xi_{max}} d\xi_{max}\delta\ell + dL\delta\ell \tag{2.19}$$

Here we recognise $dA^p = \xi_{max} dL + L d\xi_{max}$ with the first two terms. This shows that $dA^p = \mathcal{O}(dL\delta\ell)$, allowing us to write $d\xi_{max}/\xi_{max} = -dL/L$ at leading order. The third term thus becomes: $\frac{L}{\xi_{max}} d\xi_{max}\delta\ell = -dL\delta\ell + \mathcal{O}(dL\delta\ell\frac{\delta\ell}{\xi_{max}})$. This is injected in eq.2.19 and yields:

$$dA^p = -2dL\delta\ell + \mathcal{O}(dL\delta\ell\frac{\delta\ell}{\xi_{max}}) \tag{2.20}$$

Which can be used at leading order in eq.2.16 to finally get:

$$T = 2\gamma_0\delta\ell = \gamma_0 \int_0^{\xi_{max}} ||\boldsymbol{\nabla} h_0||^2 dy \tag{2.21}$$

This expression is in agreement with the demonstration of subsection 2.1.2, and corresponds to twice the excess of surface energy per unit length of the line of tension.

Higher order correction to the surface tension in the thickness jump zone and 2D Laplace law

Let us consider eq.2.13 which gives the profile of surface tension $\delta\gamma$ across the thickness jump zone. We remind:

$$\frac{\delta\gamma}{\gamma_0}(\epsilon) = \frac{1}{2}||\boldsymbol{\nabla} h(\epsilon)||^2 - h\Delta h(\epsilon) + \Gamma_{sup}(\epsilon)$$

for any normal ordinate $\epsilon \in [0, \xi_{max}]$ in the thickness jump zone. This is a development at order $\mathcal{O}(\frac{h^2}{\xi_{max}^2})$, but let us now take a closer look at the higher order term $\Gamma_{sup} = \mathcal{O}(\frac{h^2}{\xi_{max}R})$ (where we recall that $R \gg \xi_{max}$ is the local radius of curvature of $\mathcal{C}$).

By injecting the expression 2.13 of $\delta\gamma$ in eq.2.12, we get:

$$\Gamma_{sup}(\epsilon) = \frac{1}{R}\int_0^{\epsilon} ||\boldsymbol{\nabla} h||^2 \, d\xi \tag{2.22}$$

And if we now look at the difference of surface tension across the whole thickness jump zone, that is $\Delta\gamma_{\mathcal{C}} = \delta\gamma(\xi_{max})$, the first two terms of eq.2.13 on the right hand-side vanish and we have:

$$\Delta\gamma_{\mathcal{C}} = \gamma_0 \times \Gamma_{sup}(\xi_{max}) = \frac{\gamma_0}{R}\int_{\xi_{min}}^{\xi_{max}} ||\boldsymbol{\nabla} h||^2 \, d\xi = \frac{T}{R} \tag{2.23}$$

Which is a 2D Laplace law linking the jump of surface tension γ across a curved line to the line tension T.

2.2 Creating line tension in a foam film: experimental setup

In the previous section 2.1 we predict the presence of a line tension T in the plane of a foam film with two regions of different thicknesses. We provide an expression for it with eq.2.15, and it appears that the knowledge of the thickness profile in the transition zone between the two regions is the key to compute T.

The goal of this section is to create experimentally this situation with two regions, and to measure the thickness profiles in the film to get access to an estimation of the line tension T. We achieved this using a simple setup composed of a single horizontal foam film deformed in a controlled way.

2.2.1 Principle of the experiment, technical limitations and notations

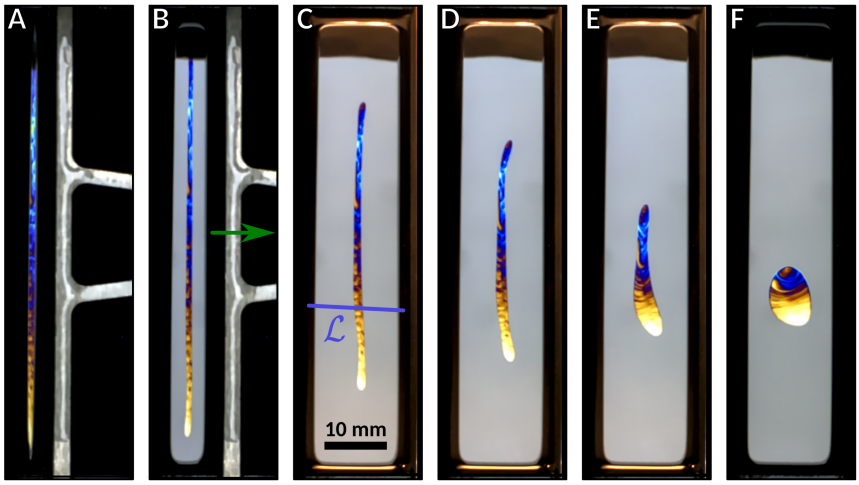

Figure 2.5: Top view of the film, timelapse of the deformation followed by the inner relaxation of the thin coloured patch. Times from A to F: $t = -1,\ -0.6,\ 0,\ 1,\ 3,\ 6$s.

The principle of the experiment is detailed in Fig.2.5 of which we describe the different steps:

- **A:** A horizontal foam film is created very elongated in the rectangular aperture formed by a plastic piece with a squared "U" form and a mobile metallic bar. We create it by bathing

the frame by hand in a soapy solution. We wait for it to drain until it is thin enough to display colours in reflected light.

- **B:** The preexisting film is stretched very rapidly, extracting some new film from the menisci of the frame (appearing in grey in Fig.2.5). This new grey film is a Frankel film, whose dynamics of extraction is detailed in subsection 0.3.2.

- **C:** At the end of the motor motion, which defines the origin of time $t = 0$, the very elongated arena-shaped thin piece of film is surrounded by the thicker film: a line tension exists at the border which tends to minimise its perimeter. We measure its value over the time of the experiment by looking at the thickness profile along $\mathcal{L}$ with the hyperspectral camera.

- **D-F:** The thin film retracts toward a circular shape to achieve its minimum of perimeter. The timescale of the motion is set by a trade-off between the value of T and the damping forces imposed by the viscous air friction.

All notations used to describe our system are shown in Fig.2.6.

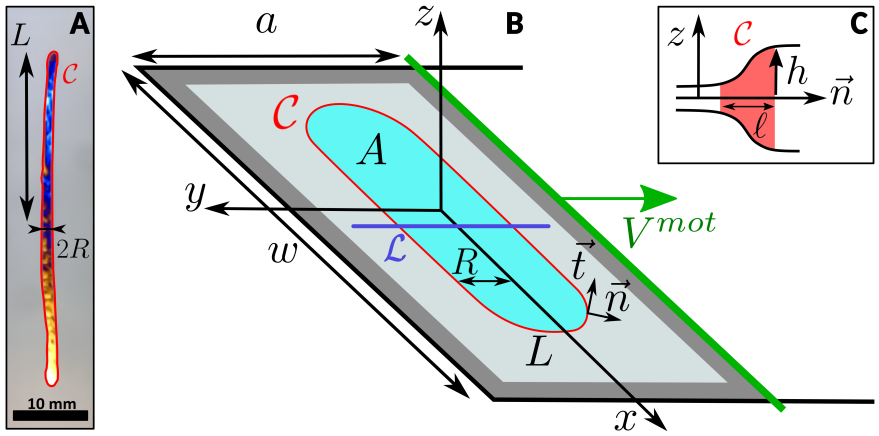

Figure 2.6: Experimental setup and notations used in the chapter.

The foam film is formed with an initial width $a = 2.1\,\mathrm{mm}$. This very narrow configuration only lets a very elongated flat film to exist between the menisci present at each edge of the frame. The film is let to drain for $3\,\mathrm{min}$ to the point that it displays coloured patterns (Fig.2.5A), meaning its thickness has decreased down to a few hundreds of nanometres. The stretching imposed by the motor is performed at $V^{mot} = 10\,\mathrm{mm/s}$ for $1\,\mathrm{s}$ up till the film has a width $a = 12.1\,\mathrm{mm}$. The origin of times $t = 0$ is set at the end of the motor motion, and we show a typical film at this time in Fig.2.6A.

The contrast between the coloured thin film and the thick grey film allow us to estimate the position of the contour $\mathcal{C}$ along which the line tension is applied. The thickness across $\mathcal{C}$ is monitored using a spectral camera along $\mathcal{L}$. The precise localisation of this line from the spatio-spectral image required some work. We found its precise position using a mirror put in the plane of the rectangular frame. With a triangular cache put on the mirror, we were also able to

find the angle $\theta_y = 7^o$ between $\mathcal{L}$ and the y axis (which we tried to lower as much as possible). This angle is neglected hereafter.

In the following, we will only consider the measurement range $t \in [0, 1.5]$s where we measure the relaxations of L and R and the line tension T. This restriction is due to two main factors: ***(i)*** the lamp for the spectral camera radiates quite a lot of heat, we must turn it off before it generates significant thermal Marangoni flows, and ***(ii)*** we will later need the hypothesis $L \gg R$, which is less and less true as the relaxation occurs.

Gravity is neglected throughout this whole study, as the film lies horizontally with a very good precision. This is due to the fact that the thin patch acts as a very sensitive level for the foam film, and the slightest tilt angle leads to a movement toward the menisci at the edges during the relaxation, hindering the measurement. We thus put the deformable frame on three adjustable vertical screws in order to get the right corrections to the horizontality of the setup.

Last problem but not least are the parasitic air movements which we limit by covering the setup with an enclosure as soon as we have created the foam film, and before the deformation.

2.2.2 Setup

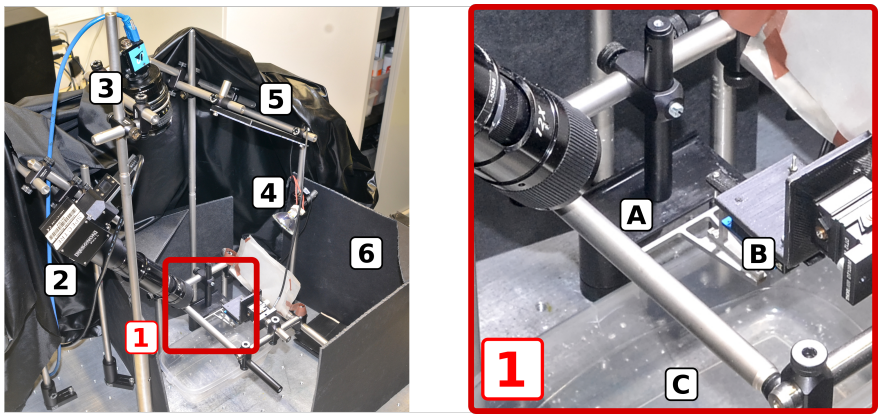

Figure 2.7: Experimental setup used to create the foam film with two regions of different thicknesses. **1-A:** black plastic piece with a squared "U" form (corresponding to the black edges in Fig2.6B). **1-B:** metallic mobile edge (corresponding to the green edge in Fig2.6B) attached to a motor with a wedge-shaped plastic piece. **1-C:** plastic bath containing the soapy solution that we raise by hand to form the foam film on the rectangular deformable frame. **2:** Hyperspectral camera mounted on a navitar objective monitoring the thickness along the line $\mathcal{L}$ of Fig.2.5. **3:** Colour camera monitoring the foam film with reflected light. **4:** White powerful light aligned in reflection with the hyperspectral camera to create interferences against the foam film. **5:** White LED panel aligned in reflection with the colour camera in order to image the coloured reflection of the thin parts of the film. **6:** Cardboard enclosure positioned around the setup during the experiments to mitigate parasitic air movements.

Chemistry

The soapy solutions used to create our flat foam films are SDS/dodecanol mixtures in a solvent made of 75% water 15% glycerol (**NB:** contrary to any other solution used in the frame of this Ph.D work, no fluorescein is added here as we do not need any fluorescent light to image the system). The concentration of SDS is always set at $c_{SDS} = 2.4\,\mathrm{CMC} = 5.6\,\mathrm{g/L}$ while the concentration of dodecanol varies between $c_{DOH} = 0, 15, 35, 50\mathrm{mg/L}$. The protocole to create the soapy solutions is the same as the others.

Deformable frame and motor

The deformable frame used in this set of experiments is made of one single 3D-printed plastic piece with a squared "U" form (Fig2.7A) to which we add a straight metallic part sliding in its arms. This latter is also attached to a PI micromove C-867 motor (Fig2.7B). The result is a rectangular deformable frame with one side of fixed length $w = 62\,\mathrm{mm}$ and the other side with a length varying between $a = 1$ and $25\,\mathrm{mm}$.

Cameras

We use a Resonon Pika L hyperspectral camera mounted on a 12X Navitar objective (Fig2.7**(2)**) to monitor the thickness profile of the foam film along the line $\mathcal{L}$ shown in Fig.2.5**C**. It is aligned with a white light (Fig2.7**(4)**) with respect to the angle of reflection at the surface of the foam film, which acts as a Fabry-Pérot interferometre for the sake of this measurement. The angle of incidence θ with the horizontal plane of the foam film was carefully measured $\theta = 38^o$.

The other (regular) camera we use is an Imaging Source colour DFK 23UM021 camera mounted on a 24-mm Nikon objective (Fig2.7**(3)**) monitoring the foam film from above and the dynamics of retraction of the thin patch toward a circular shape. Fig.2.5 is a timelapse of a typical experiment produced using this camera. To get the contrast of colours at the surface of the foam film, an LED panel is attached in reflection of this camera (Fig2.7**(5)**). In our subsequent usage of this camera, the angle of incidence with the foam film ($\sim 10^o$) will always be neglected with respect to parallax problems.

2.3 Image processing

2.3.1 Detection of the thin region contour and kinematics of the relaxation

In order to study the dynamics of relaxation of the thin film, we start by tracking the area of the thin coloured film. We want to binarise colour images to make contrast between two kinds of pixels: coloured ones (thin film) and grey ones (thick film). The former have very high values in their respective colours (either in R, G or B) but very low values in the others, and the latter have intermediate values in all channels.

We create two sets of three masks:

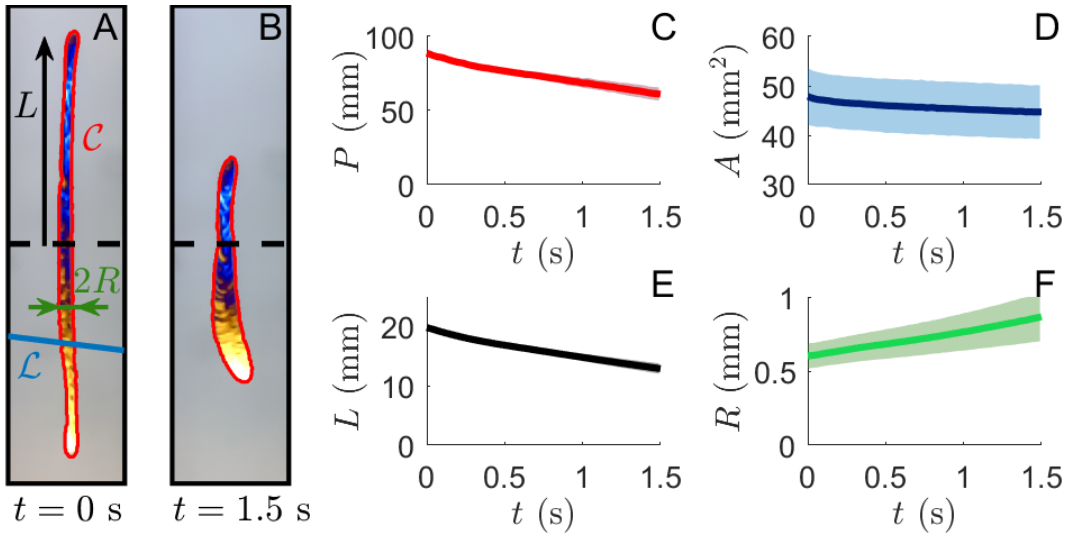

Figure 2.8: Example of contour detection performed on a film with no dodecanol at time $t = 0$. **A:** Image of the film at $t = 0$ recalling the notations used in the text, the detected contour $\mathcal{C}$ is highlighted in red, the line $\mathcal{L}$ along which the thickness profiles are measured is in light blue. **B:** Image of the film at $t = 1.5$ s the end of our measurement range. **C:** Perimeter P of $\mathcal{C}$ as a function of time. **D:** Area A of the interior of $\mathcal{C}$ as a function of time. Mind the ordinate, which is centred around the slightly varying values of A. **E:** Semi-length L of the thin film as a function of time, defined as half the distance between the highest point and the lowest point of $\mathcal{C}$. **F:** Semi-width R of the arena of thin film as a function of time, estimated with the area and the semi-length $R = A/(4L)$. All the uncertainties are represented with shaded areas and evaluated by taking the standard deviation over 13 experiments.

- Set 1 is three masks for the highest values for each RGB channel, each colour with its own threshold. The pixels below the threshold are put to zero, the pixels above subtracted by the threshold. Each mask is thus white where the thin film is of the given colour, black everywhere else.
- Set 2 is three masks for the lowest values for each RGB channel, each colour with its own threshold. The pixels above the threshold are put to zero, the pixels below are kept as they are. Each mask is thus white in the coloured region except for the thresholded colour which is in black. The threshold is chosen so that the grey regions are above it and appear in black.

By summing the masks of Set 1 and 2 by colour, we have three images where the coloured region appears in white, and the grey region appears in black. We average the three masks to get an image which is binarised using a dedicated MATLAB function IM2BW. We fill the gaps in the detected coloured region by dilation-erosion with a small disk of a few pixels in radius.

We then use the contour detection function CONTOURC of MATLAB on the binary image we obtained to get $\mathcal{C}$. A typical frame of the set of experiments without dodecanol taken at time $t = 0$ is shown with its detected contour in Fig.2.8**A**.

From there we can have access to the geometry of the arena of thin film and, by repeating the process over the whole movie, characterise the whole kinematics of the system. All the quantities we extract are shown in Fig.2.8C-F with their uncertainties being the standard deviation over 13 experiments. The perimeter P and the area A are directly extracted from the features of the contour $\mathcal{C}$ and are plotted in Fig.2.8C and D. We see as expected that the perimeter tends to decrease as the thin film relaxes toward a circular shape, while the area remains almost constant (mind the ordinate in graph D) which is a key information allowing us later on to assume the incompressibility of the interfaces.

From $\mathcal{C}$, we also deduce the geometrical parameters L and R. They define an approximate arena-shaped geometry for $\mathcal{C}$, with parallel straight lines of lengths $2L$ connected by semi-circles of radii R. L is estimated by measuring the distance between the highest and lowest point of $\mathcal{C}$ while R is deduce from the measurements of L and A as the area of the arena shape we suppose has the expression for $L \gg R$: $A \simeq 4LR$. We thus see that toward the end of the measurement range we have, we end up with $L(t = 1.5\,\mathrm{s}) \simeq 12\,\mathrm{mm}$ which remains much greater than $R(t = 1.5\,\mathrm{s}) \simeq 1\,\mathrm{mm}$, and our assumption holds for the whole dynamics we study.

2.3.2 Comment on the chemistry

In the previous subsection 2.3.1, we displayed an example of relaxation with a peculiar chemistry that is without dodecanol. We indeed tried to vary this parameter, but ended up with less reliable data and a lack of repeatability arising as soon as we put any concentration of dodecanol, starting from $35\,\mathrm{mg/L}$ up to $200\,\mathrm{mg/L}$.

With dodecanol, the film either undergoes the exact same dynamics as the 13 previous experiments shown in Fig.2.8, or at the opposite shows no relaxation at all. An example is shown in Fig.2.9. In the case with no relaxation, which becomes more prevalent as more dodecanol is added, the thin film remains elongated and eventually destabilises, bending along its length. We hypothesise several origins for this wriggling behaviour during the time range of our measurement:

- Solid-like in-plane motions resisting shear due to heterogeneities of dodecanol concentration at the interfaces. Dodecanol is known to undergo a phase transition at a water-air interface and produce rafts of crystalline 2D phase [102] if concentrated enough. The concentration threshold for this transition is not clear however, even more so in our case where the bulk has SDS micelles, and the dodecanol population is distributed between the interface, the bulk and the SDS micellar phase.

- Air movements at longer times, although in this case our repeatable experiments without dodecanol should also be affected as we witness bending during the same time range as our measurements.

This qualitative lack of repeatability makes us exclude dodecanol as a working parameter, and all the results we will show and discuss in the following will come from the same set of 13 experiments without dodecanol shown in Fig.2.8.

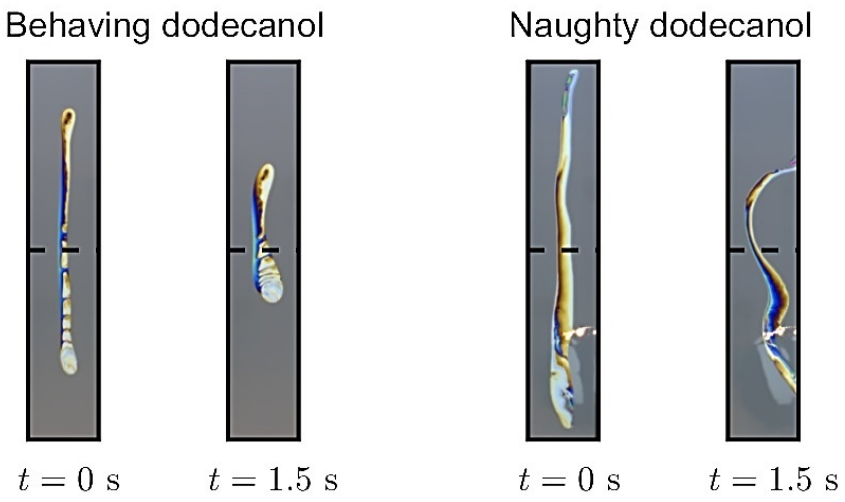

Figure 2.9: Two examples for $[DOH] = 200\,\mathrm{mg/L}$. The repeatability is poor: on the left the thin film relaxes with a kinematics quantitatively very similar to what is shown in Fig.2.8, on the right the thin patch does not relax and eventually bends along its length.

2.3.3 Extracting the thickness profiles

In order to measure the thickness profiles, we collect the movie of the spectra along the line $\mathcal{L}$ of Fig.2.5**C**, of which an example of frame at $t = 1.5\,\mathrm{s}$ is shown in Fig.2.10**A**. We start by finding the average spectrum I_{water} of the lamp and exposition we use by averaging our frames over time and position, yielding the green curve shown in Fig.2.10**B**. Now at a given time and position, we can collect a spectrum $I(\lambda)$ (blue curve in Fig.2.10**B**) and filter it by defining $\tilde{I}(\lambda) = \frac{I}{I_{water}} - \overline{(\frac{I}{I_{water}})}$ where the top bar is an average over λ. The result is shown in Fig.2.10**C**. Given that the foam film behaves for the light as a Fabry-Pérot interferometre of varying thickness $2h(y)$ observed at an angle $\theta = 38^o$, we can directly have a prediction for the intensity:

$$\tilde{I}(k, 2h, \theta) = \tilde{I}_0 \cos\left(4nkh\sqrt{1 - \sin^2\theta/n^2}\right) \tag{2.24}$$

Where n is the refractive index of water and $k = \frac{2\pi}{\lambda}$ is the wavenumber. Thus, from an intensity profile $\tilde{I}(k, 2h) \propto \cos(\alpha k \times 2h)$ with $\alpha = 2n\sqrt{1 - \sin^2\theta/n^2} = 2.36$, we can extract the thickness $2h$. The extraction itself is performed by taking the numerical Fourier transform of $\tilde{I}$ from the wavenumber space k into the thickness space H:

$$\mathcal{F}[\tilde{I}](H) = \int_{k_{min}}^{k_{max}} \tilde{I}(k, 2h) e^{ikH} dk \tag{2.25}$$

Where k_{min} and k_{max} are respectively the minimum and maximum wavenumbers given by the maximum and minimum wavelengths detected by the hyperspectral camera. As eq.2.24 suggests, in the thickness space we expect a dirac function centered around $H = \alpha \times 2h$ convoluted by a cardinal sine of width determined by $k_{max} - k_{min}$, which defines our resolution. Taking into account the geometrical factor α of dilation of our thickness space ($\alpha = 2.36$ in our case with $\theta = 38^o$), the theoretical resolution is $H_{min,th} = \frac{\pi}{\alpha(k_{max} - k_{min})} \simeq 150\,\mathrm{nm}$. However, given the

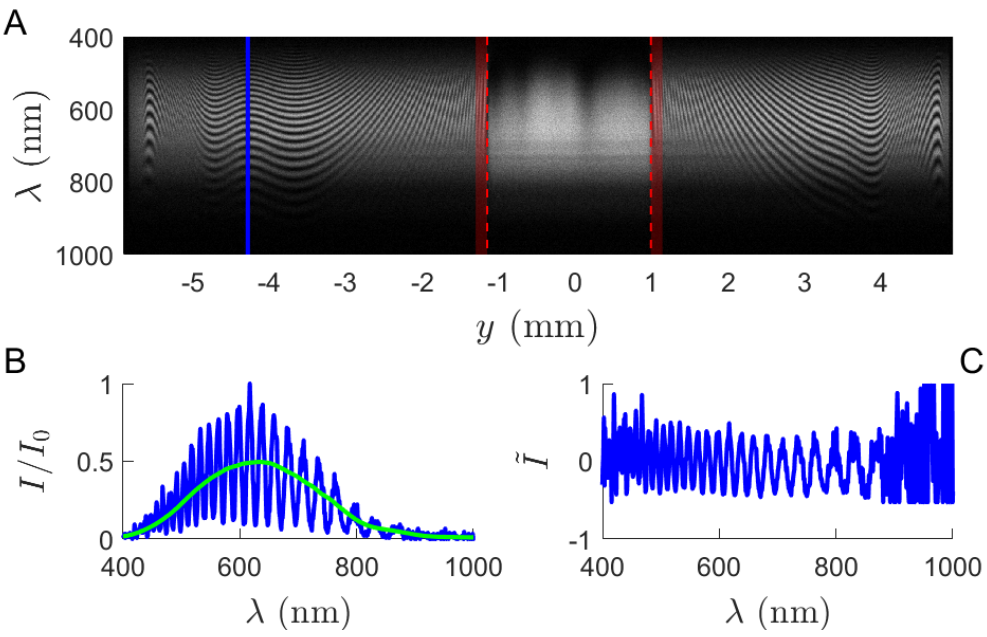

Figure 2.10: Processing of the spectral images obtained for a typical experiment without dodecanol at $t = 1.5\,\mathrm{s}$ toward the end of the measurement range. **A:** Typical image obtained with the spectral camera. The abscissa is the position along the monitored line with its origin set in the middle of the thin film, the ordinate is the wavelength. The central zone displaying a single large interference oscillation and delimited by the vertical red dotted line is the thin film. The red shaded areas are blind zones where it not possible perform the thickness measurement. The blue line is the abscissa y chosen for the example in **B**. **B:** The blue curve is a typical intensity profile taken at a given y shown in **A** by the vertical blue line. The green line is the spectrum of the lamp obtained by averaging the frames in space and time. **C:** Normalised and centred intensity profile $\tilde{I}$ out of which we extract the thickness of the foam film at the given time and position y.

exposure and vanishing spectrum of the lamp at the edges of the spectral range of our camera, our experimental resolution is estimated around $H_{min,exp} = 400\,\mathrm{nm}$.

In the same way, our numerical integration is performed over a wavenumber space with finite steps Δk. Knowing that the difference of λ's from one pixel to the next is always $\Delta\lambda = 1\,\mathrm{nm}$ with a range $\lambda \in [400, 1000]$ nm, the largest step in wavenumber as we integrate is $\Delta k = 2\pi\left(\frac{1}{\lambda_{min}} - \frac{1}{\lambda_{min}+\Delta\lambda}\right) = 4.5 \times 10^4\ \mathrm{rad\,m^{-1}}$. This yields a theoretical maximum detectable value $H_{max,th} = \frac{\pi}{\alpha\Delta k} = 30\,\mu\mathrm{m}$ which is never attained in practice.

In our measurable range $H_{min,exp} = 400\,\mathrm{nm}$ and $H_{max,th} = 30\,\mu\mathrm{m}$, we now work to deduce the profile $2h(y)$ out of the spectra $\mathcal{F}[\tilde{I}](H)$, looking at its highest peak. We also define a second criterion which is a threshold to exceed for a peak to prevent noise. We thus consider both the position and height of the peaks of $\mathcal{F}[\tilde{I}](H)$ in the thickness space H and have the following cases which can be seen in Fig.2.10**A** and Fig.2.11:

- If the peak is above the threshold and positioned at $H \in [H_{min,exp}\ ,\ H_{max,th}]$ in the measurable range, we attribute its position H to the thickness $2h = H$. This is the case in

the outer regions where the intensity profile Fig2.10**B** is taken, it corresponds to the grey thick film and most of the thickness jump zone.

- If the peak is above the threshold and positioned at $H < H_{min,exp}$, it is below our resolution, the peak is too broad to be precise but intense enough thanks to our thresholding to rule out noise to be its cause. A value of zero is attributed to the thickness $2h = 0$. This is the case in the inner region, between the two vertical red dotted lines, where a single well-defined oscillation is measured along the λ axis. It corresponds to the coloured thin flat film, that is located between the red dotted lines in Fig.2.10**A**, or equivalently in the flat segments of Fig.2.11 set to zero.

- If the peak is below the threshold, or above it but located in $H > H_{max,th}$, it is treated as noise and we attribute the value $2h = NaN$. This is what happens in the blind zones, where the thickness profiles become too steep and hinder the measurement (red shaded areas of Fig.2.10**A** or dotted lines of Fig.2.11).

This methodology is applied for each spectrum at each y for the given frame, and repeated for each frame of the movie, building a thickness profile at each time of the experiment. Typical thickness profiles obtained throughout a whole experiment are shown in Fig.2.11. The grey shaded area corresponds to the lower resolution $H_{min,exp}$. The dotted parts of the profiles correspond to the blind zones where the thickness profile is too steep, neighbouring the edges of the thin films. They are parabolic interpolations found by imposing the continuity of thickness $2h$ at both the edge of the thin film ($2h = 0$) and the edge of thick film ($2h > 0$), and the continuity of thickness gradient at the edge of the thick film.

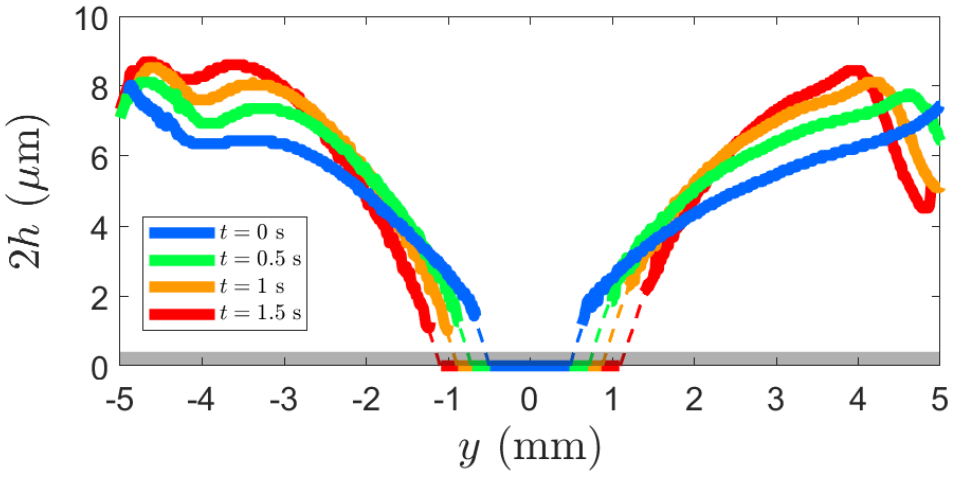

Figure 2.11: Thickness profiles obtained along $\mathcal{L}$ at different times. The origin of time $t = 0$ is set when the motor stops its motion. The red line corresponds to the spectral image taken as an example in Fig.2.10, and is the last thickness profile of our measurement range $t \in [0, 1.5]$s. At this time $t = 1.5$ s, the foam film is in a state close to what is shown in Fig.2.5D.

2.3.4 Computing the resulting line tension

As we have access to the thickness profiles $2h$ during the relaxation (Fig.2.11), we now aim at measuring the line tension T.

Note that we will be able to compute two values of T for each profile, as two thickness jump zones are monitored at the same time by the spectral camera on both sides of the arena. To do so, we provide again the theoretical formula of T, that is eq.2.15:

$$T = \gamma_0 \int_{\xi_{min}}^{\xi_{max}} ||\boldsymbol{\nabla} h(\xi)||^2 \, d\xi$$

The experimental values of the different terms involved in this equation are discussed below.

Surface tension γ_0

The equilibrium surface tension γ_0 is well known for a given chemistry thanks to a pendant drop campaign already described in the Introduction 0 subsection 0.1.3. For our solutions with SDS alone, it is $\gamma_0 = 35\,\mathrm{mN/m}$.

Thickness gradient $||\boldsymbol{\nabla} h||$

First, we identify the y axis of our problem (along which we measure the thickness profiles in Fig.2.11) to the direction of the thickness gradients on both sides of the thin film. We thus define an axis ξ for each semi-profile, one going in the $+y$ direction, the other oriented in the $-y$ direction. Along these axis ξ, we compute the gradients of the semi-profiles $||\boldsymbol{\nabla} h||$. They need to be carefully computed, as any numerical derivative, but especially here that our thickness profiles h have been interpolated in the blind zones where the contributions of the gradient is important.

In the blind zones, we interpolate our thickness profiles by a well-defined parabola imposing continuity of h at both ends of the blind zone and the continuity of $||\boldsymbol{\nabla} h||$ at the thick film edge. These parts of the profiles are analytically well defined, and the computation of the gradient is not a problem. In the thicker zones where we are able to measure h, computing a gradient requires to smooth the profile. To do so, we chose to perform polynomial fits of order 3 starting at the edges of the blind zones and going up til the end of a maximal length of integration ℓ_∞ discussed right after. As we do not constrain the 3rd order polynomial fit to respect any continuity of thickness or thickness gradient, we will be very careful not to integrate the computed gradient at the junction between the blind zone and the measurement zone.

Lower integration boundary

The lower boundary $\xi_{min} = 0$ is always defined as the edges of the thin film, that is the first non-zero values starting from the origin $y = 0$ toward the right or left.

Upper integration boundary

The upper boundary ξ_{max} is a parameter to consider with caution in practice as $||\boldsymbol{\nabla} h||$ vanishes smoothly. To build this discussion, we introduce an auxiliary function $T(\ell_{int})$ defined as:

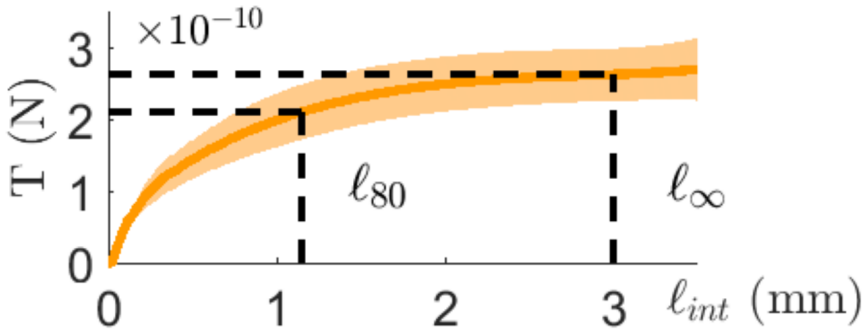

Figure 2.12: Example of the dependence $T(\ell_{int})$ with the length of integration ℓ_{int} (whose retained value for the sake of computing T in the main graph is $\ell_\infty = 3\,\mathrm{mm}$). ℓ_{80} corresponds to the length of integration where T reaches 80% of its maximal value obtained with ℓ_∞. This profile is obtained with the orange thickness profile of Fig.2.11, at $t = 1\,\mathrm{s}$.

$$T(\ell_{int}) = \gamma_0 \int_0^{\ell_{int}} ||\boldsymbol{\nabla} h(\xi)||^2 \, d\xi \tag{2.26}$$

In which the upper bound is a free variable. In Fig.2.12 we show typical measurement $T(\ell_{int})$ made out of the orange curve of Fig.2.11 (averaged on both semi-profiles). We arbitrarily define a length $\ell_\infty = 3\,\mathrm{mm}$ beyond which we risk to start integrating the thickness gradient due to the meniscus on the supporting frame. As expected from the smoothly-vanishing thickness gradients, $T(\ell_{int})$ plateaus smoothly as well.

2.3.5 Results

Measurement of T

The retained value for the line tension T at a given time step is $T(\ell_\infty)$. This is done for each experiment of our set of 13, and the average over them is shown in Fig.2.13 (again the orange dotted line is matched with the previous profiles of h and $T(\ell_{int})$). We thus have an estimate of our line tension $T(t)$ at each time, and we see that we are dealing with a tiny force, of the order of $T \sim 10^{-10}\mathrm{N}$.

Also, we see that it tends to increase with time, which is consistent with the fact that the thickness profiles in Fig.2.11 tend to be steeper over time, leading to more important thickness gradients.

The experimental error is the standard deviation over both semi-profiles of the 13 experiments. In Fig.2.12, the error bars account for the difference in measured line tension between the left and right thickness jump zones monitored by the camera, and a difference up to 20% is observed. This remains under our global error due to statistical repetition which is of the order of 50%. The fact that the measurement is performed in the flat regions of the contour, however, raises a good question: do the curved edges undergo a local compression during the relaxation which would change the local value of T where it effectively applies a force? This conundrum is addressed later on in subsection 2.4.6, as well predictions for the evolution of T with time. In the following,

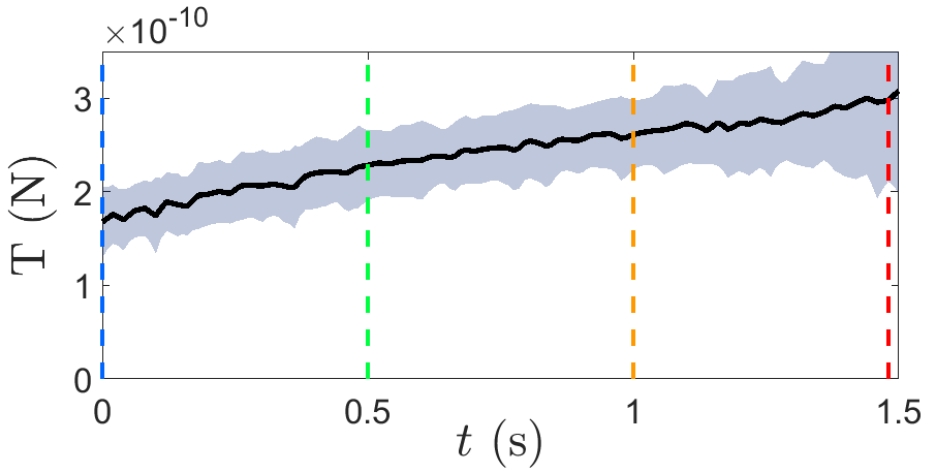

Figure 2.13: Line tension T computed over time on the set of experiments without dodecanol. The error is the standard deviation over the computations for 26 semi-profiles of thickness $2h(\xi)$ which consist of 13 experiments, each with 2 monitored sides of the thin film treated independently. The vertical dashed lines indicating particular times are colour-matched with the thickness profiles given as examples in Fig.2.11.

we will assume that $T(t)$ is a uniform scalar value along the line of tension whose sole dependency is time, given by the experimental data in Fig.2.13.

Location of the force T

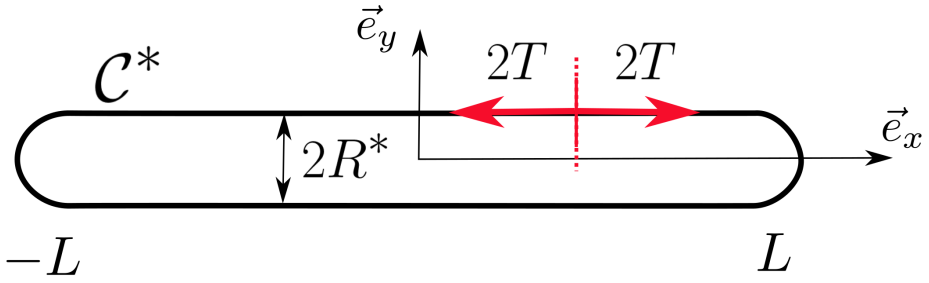

Figure 2.14: First schematic view of the contour $\mathcal{C}^*$ as an arena of semi-width R^*, semi-length L. The line tension T is applied at any point of $\mathcal{C}^*$ (and is supposed uniform along it, the factors 2 accounting for the two interfaces).

As stated in subsection 2.3.1, the thin film contour $\mathcal{C}$ is approximated to an arena with parallel straight lines of lengths $2L$ connected by semi-circles of radii R. **However, the values of R being actually comparable to the typical values ℓ_{int} over which T is integrated, the position where the line tension is applied becomes ill-defined. Thus, we need to distinguish the contour $\mathcal{C}$ from the effective contour $\mathcal{C}^*$ along which we consider the line tension to be applied.**

In Fig.2.14, we define $\mathcal{C}^*$, a similar arena along which we consider that T is effectively applied, with a semi-width R^* defined as:

$$R^* = R + \ell_{80}/2 \tag{2.27}$$

Where ℓ_{80} is the length for a given profile $T(\ell_{int})$ so that $T(\ell_{80}) = 0.8T(\ell_\infty)$, which is graphically represented in Fig.2.12. **Both R and $\ell_{80}/2$ are of the order of $\sim 0.5 - 1\,\mathrm{mm}$ as shown respectively in Fig.2.8F and Fig.2.12.**

2.4 Modelling the relaxation of the thin film: we validate our line tension measurement

Now that we have come up with a measurement for the line tension T (Fig.2.13), which has never been measured before to the best of our knowledge, we want to validate the values we found. To do so, a valuable piece of experimental knowledge is the time evolution of the geometry of the thin patch as it relaxes towards a circular shape. All this information is shown in Fig.2.8.

In this section, we detail the equations leading to a prediction of the dynamics of $L(t)$, the semi-length of the thin patch, knowing the forces in the plane of the foam film. The force here is the line tension, and the dynamics is found to be damped by air friction. We have a quantitative agreement which validates our measurement of T. We first start by writing a general equation of motion for a foam film with a line tension in its plane.

2.4.1 Equation of motion for a foam film with line tension

Let us consider a foam film with the same configuration as in Fig.2.2 Left, except we now keep $\mathcal{C}^*$ as a 1D object subject to a line tension T (mind the * we have now due to the correction of the contour detailed above 2.3.5). Besides the capillary forces we described in section 2.1, the foam film is considered to be subject to friction both in its own plane with an intrinsic surface shear viscosity and with air viscosity. An element of film of area dA taken in the inner or the outer region of $\mathcal{C}^*$ without crossing it have the force balance:

$$\left(2\eta_s \Delta \boldsymbol{v} + 2\boldsymbol{\nabla}\gamma + 2\boldsymbol{f}_g + \boldsymbol{f}_\eta\right) dA = \boldsymbol{0} \tag{2.28}$$

Where $\boldsymbol{v}$ is the 2D velocity field in the plane of the foam film, η_s is the surface shear viscosity, $\boldsymbol{f}_g$ is the friction force on the air for one interface and $\boldsymbol{f}_\eta$ the friction force due to bulk liquid viscosity integrated over the thickness of the film. The factors 2 account for the two water-air interfaces of the film. This equation is a 2D Stokes equation with exterior forces $2\boldsymbol{f}_g$ and $\boldsymbol{f}_\eta$.

If we now choose our element of film dA so that it crosses $\mathcal{C}^*$ at the curvilinear abscissas s and $s + ds$, we must add two terms for the line tension $2T$ (2 interfaces again) acting along $+\boldsymbol{t}(s + ds)$ and $-\boldsymbol{t}(s)$ the tangential directions of $\mathcal{C}^*$. This gives the new balance:

$$\left(2\eta_s \Delta \boldsymbol{v} + 2\boldsymbol{\nabla}\gamma + 2\boldsymbol{f}_g + \boldsymbol{f}_\eta\right) dA = -\frac{\partial(2T\boldsymbol{t})}{\partial s}\, ds \tag{2.29}$$

Which we can rewrite with the normal vector $\boldsymbol{n}$ and the local curvature of $\mathcal{C}^*$ denoted $\kappa(s)$. We also consider T to be constant along $\mathcal{C}^*$, giving:

$$\left(2\eta_s\Delta\boldsymbol{v} + 2\boldsymbol{\nabla}\gamma + 2\boldsymbol{f}_g + \boldsymbol{f}_\eta\right)\, dA = 2T\kappa(s)\boldsymbol{n}(s)\, ds \tag{2.30}$$

This equation can be rewritten globally using a well-defined Dirac distribution. Let us define a set of such functions $\delta_{\mathcal{C}^*}$ defined over $\mathcal{S}$ the whole foam film so that:

$$\forall \boldsymbol{r'} \in \mathcal{C}^*,\ \iint_{\mathcal{S}} \delta_{\mathcal{C}^*}(\boldsymbol{r} - \boldsymbol{r'})d^2\boldsymbol{r} = 1 \tag{2.31}$$

And eq.2.28 and 2.30 can be defined as a single equation at any point $\boldsymbol{r} \in \mathcal{S}$:

$$2\eta_s\Delta\boldsymbol{v}(\boldsymbol{r}) + 2\boldsymbol{\nabla}\gamma(\boldsymbol{r}) + 2\boldsymbol{f}_g(\boldsymbol{r}) + \boldsymbol{f}_\eta(\boldsymbol{r}) = \oint_{\mathcal{C}^*} 2T\kappa(\boldsymbol{r'})\delta_{\mathcal{C}^*}(\boldsymbol{r} - \boldsymbol{r'})\boldsymbol{n}(\boldsymbol{r'})dr' \tag{2.32}$$

This is the general equation for the in-plane motion of a foam film with a line tension acting along a contour $\mathcal{C}^*$ of any shape. This is still a specific case of a more general one, which is a foam film with any thickness field h. In our case, the thickness gradients are very localised in a specific zone, but a more general framework awaits the reader in Appendix 5.

Also, it has to be noted that equation 2.32 must be combined with a relationship between the surface tension and the surface deformation in order to be a closed problem. Let us provide one in the form of the incompressiblity of the interfaces.

2.4.2 Closing the problem: incompressibility of the interfaces

The question of whether the surfactant-laden interfaces we are dealing with are compressible, and to what extent, is one of the main issues we attempt to address in this manuscript for multiple situations. In the previous chapter 1, we considered extensible interfaces and measured their surface elasticity E_f.

In the present case of our thin film relaxing toward a circular shape under the effect of line tension, we will consider incompressible interfaces. To support this assumption, a first physical quantity we can look at is the evolution of the area A of the thin region, shown in Fig.2.8D. It varies slightly throughout the relaxation and we neglect these variations. This incompressibility hypothesis is a key assumption for the model we will use later on. It is questionable however, as a global condition over the conservation of the total area of thin film $\frac{dA}{dt} = 0$ do not exclude local compression and extension to occur. A discussion and additional arguments for this hypothesis awaits the interested reader in subsection 2.4.6.

Thus, we write this condition $\boldsymbol{\nabla}.\boldsymbol{v} = 0$, where we remind that $\boldsymbol{\nabla}$ is a 2D operator in the plane (Oxy) and we have the full set of equations for the relaxation of the arena:

$$\begin{cases} 2\eta_s\Delta\boldsymbol{v}(\boldsymbol{r}) + 2\boldsymbol{\nabla}\gamma(\boldsymbol{r}) + 2\boldsymbol{f}_g(\boldsymbol{r}) + \boldsymbol{f}_\eta(\boldsymbol{r}) = \oint_{\mathcal{C}^*} 2T\kappa(\boldsymbol{r'})\delta_{\mathcal{C}^*}(\boldsymbol{r} - \boldsymbol{r'})\boldsymbol{n}(\boldsymbol{r'})dr' \\ \boldsymbol{\nabla}.\boldsymbol{v} = 0 \end{cases} \tag{2.33}$$

Now that the problem is closed, we need to find the solution for our velocity field $\boldsymbol{v}$. Before looking at the source term on the right-hand side of the first equation, let us have a closer look at the damping forces on the left-hand side. Some simplifications can be made before finding a suitable model for our geometry.

Important remark: In subsection 0.2.5 of the Introduction, I already introduced this limit of incompressible interfaces. There, I also refer to Appendix 2 where I developed a set of equations for compressible interfaces in the limit of high elasticities. The resulting compressible correction to the flow field is computed in Appendix 3, in the specific geometry of the line tension experiment. We found that it is indeed a higher order correction for the sake of studying the relaxation dynamics, and we discard it in the present chapter.

2.4.3 Damping forces: the Boussinesq number Bq

Before applying the above equation to our arena-shaped geometry, let us focus on the left hand-side of eq.2.32. The first, third and fourth terms $2\eta_s\Delta\boldsymbol{v}$, $2\boldsymbol{f}_g$ and $\boldsymbol{f}_\eta$ are dissipative forces respectively accounting for the surface shear viscosity, the friction on the air and the liquid bulk dissipation.

If we want to use it in practice, a natural question about the general framework eq.2.33 is: What is the dominating damping force? This is not an easy question to answer, as surface shear viscosity is highly chemistry-dependent. **In fact, η_s is not well quantified in the case of soluble surfactants, which is our case with SDS alone [36].** On the other hand, the bulk viscosities are well known, but the resulting forces (especially in the gas) need to be treated carefully. Let us define them more accurately and start by comparing these two.

Bulk liquid friction $\boldsymbol{f}_\eta$

As discussed in subsection 0.2.1 of the Introduction, only plug flows in the z direction are allowed in our foam films, far from the menisci. This means that the only liquid bulk viscous contributions to our equations come from the gradients of velocity in the plane of the foam film. They can be integrated over z to give:

$$\boldsymbol{f}_\eta = \int_{-h}^{h} \eta\Delta\boldsymbol{v}dz \tag{2.34}$$

Where Δ and $\boldsymbol{v}$ are here and again only defined in the (Oxy) plane of the foam film. The scaling for this force is thus:

$$f_\eta \sim \eta h\frac{U}{\ell_{xy}^2} \tag{2.35}$$

Where $\eta = 10^{-3}\mathrm{Pa}\cdot\mathrm{s}$ is the bulk viscosity of water, $h \sim 10^{-6}\mathrm{m}$ the thickness of the film, $U \sim 10^{-2}\mathrm{mm/s}$ the typical in-plane velocity, and we need here to provide ℓ_{xy} the typical length scale over which the flow field varies in the plane of the foam film. **We take the experimental order of magnitude $\ell_{xy} \sim R^* \sim 10^{-3}\mathrm{m}$ (*cf.* the experimental section 2.2, subsection 2.3.5).**

Gas friction $\boldsymbol{f}_g$

The tangential force applied by gas friction on an element of interface can be expressed:

$$\boldsymbol{f}_g = \eta_g\frac{\partial\boldsymbol{v}_g}{\partial z}\Big|_{z=\pm h} \tag{2.36}$$

Where z is the normal direction to the median plane (Oxy) of the foam film, η_g is the dynamic viscosity of the gas phase, and $\boldsymbol{v}_g$ is the velocity in the exterior gas phase projected in (Oxy). We suppose in our geometry that $\boldsymbol{v}_g(x,y,z) = \boldsymbol{v}_g(x,y,-z)$ for any (x,y). This force scales as:

$$f_g \sim \eta_g \frac{U}{\ell_z} \tag{2.37}$$

Where $\eta_g = 1.8 \cdot 10^{-5}\mathrm{Pa}\cdot\mathrm{s}$, $U \sim 10^{-2}\mathrm{mm/s}$, and $\ell_z \sim \sqrt{\frac{\eta_g}{\rho_g}\tau}$ is a typical length scale for the vertical gradient of velocity in the gas phase.

Giving an order of magnitude for this latter length raises the question of taking into account gas inertia or not. An estimation of the Reynolds number for the gas in our problem gives:

$$Re = \frac{\rho_g U \ell_{xy}}{\eta_g} \sim 1 \tag{2.38}$$

With $\rho_g \sim 1\,\mathrm{kg/m^3}$ the density of the air.

In this regime of Reynolds numbers, the distance ℓ_z can be chosen as a Blasius length over which a visco-inertial boundary layer develops in the neighbouring gas. Getting an order of magnitude with this scaling means providing a **typical time for our dynamics, which is of the order $\tau \sim 1\,\mathrm{s}$ (Fig.2.8), yielding $\ell_z \sim 10^{-3}\mathrm{m}$.**

In the hypothesis of vanishing Reynolds numbers $Re = 0$, no typical length other than the one imposed by the system can be constructed, and we necessarily have: $\ell_z \sim \ell_{xy} \sim 10^{-3}\mathrm{m}$ which remains of the same order of magnitude! This is important as we will later use in practice a model at $Re = 0$ despite our computation $Re \sim 1$, which is a strong hypothesis in our work.

Comparison between the bulk frictions: gas friction dominates

With the two scalings provided to f_g and f_η, we can now compute their relative importance:

$$\frac{f_\eta}{f_g} \sim \frac{\eta h \ell_z}{\eta_g \ell_{xy}^2} \sim 10^{-1} \tag{2.39}$$

Meaning from now on we can discard the liquid bulk friction term $\boldsymbol{f}_\eta$ from eq.2.33.

The Boussinesq number: comparing gas friction and surface shear viscosity

Thus, the two remaining damping forces are the surface shear viscosity (which depends on the chemistry), and gas friction. In the literature, measurements of η_s for soluble surfactants such as SDS, which we are using, are limited by subphase bulk friction [34, 36], and only upper-bounds can be computed. We face the exact same problem in the case of in-plane motions of foam films, except the subphase here is the gas phase rather than the liquid bulk.

Let us proceed with caution, and define a number to compare these damping forces, which is called a Boussinesq number Bq. This is going to come in handy later on when looking at the damped dynamics of the in-plane motions. Bq is defined in our case as:

$$Bq = \frac{\eta_s}{\ell_{xy}\eta_g} \tag{2.40}$$

Where we again use the experimental coincidence that $\ell_z \sim \ell_{xy}$ for the gas phase. This number will be a central parameter for the Saffman & Hughes model we are about to describe and apply to our case in order to predict the relaxation dynamics.

2.4.4 Mapping on the Saffman and Hughes model

Effective forces in $\mathcal{C}^*$ are applied at the curved edges

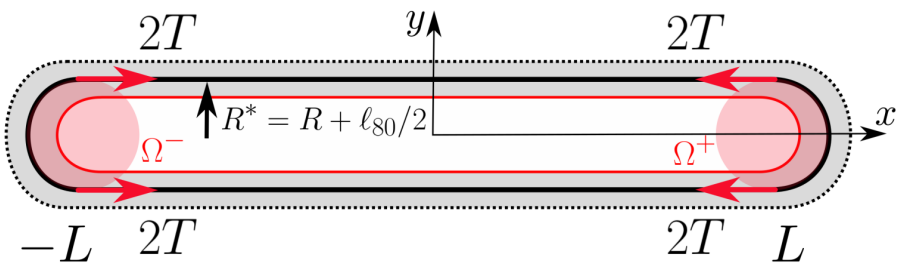

Figure 2.15: Full schematic view of our system. The inner red line is the arena defined by the edge of thin film of semi-width R. The outer black dotted line is the arena defined by the edge of thick film of semi-width $R + \ell_{80}$. The plain black line is the arena of semi-width $R^* = R + \ell_{80}/2$ retained to be the line of tension along which a tension $2T$ is applied (with a factor 2 for the two interfaces). The domains $\Omega^{\pm}$ are the cylindrical domains of fluid where a force $F_x = 4T$ pulls them toward the centre.

In Fig.2.15, we show the two domains $\Omega^{\pm}$ where an effective force is applied in the fluid, that is where the curvature of $\mathcal{C}^*$ is non-zero. These two can be considered as impenetrable cylinders as they both have a homogeneous velocity field of absolute value $|\frac{\mathrm{d}L}{\mathrm{d}t}|$. Thus, eq.2.33 needs only to be solved outside of these domains $\Omega^{\pm}$, where the line tension forces are zero.

Also, by definition of the tension (*cf.* Fig.2.2 and eq.2.9), $\Omega^{\pm}$ are both pulled with a force $4T$ (two pulling edges times two interfaces).

The problem of describing the dynamics of relaxation of $L(t)$ can thus be mapped to the problem of predicting the kinematics of two thin cylindrical patches each pulled towards the other with a force $4T$ in a fluid of surface viscosity η_s and subject to air friction at their circular bases. The two cylinders are far from one another in the sens that $L \gg R^*$, and we anticipate that they can be treated independently, *i.e.* they both generate flow fields that are negligible in the vicinity of their distant counterpart. We will validate this hypothesis later on.

The mobility of an individual cylinder is known

Let us start by considering the problem of a single dragged cylinder depicted in Fig.2.16. An infinite liquid sheet of medium plane (Oxy) and of width $2h$ has a viscosity of η. For scores $|z| > h$ we have a gas phase of viscosity η_g, and the interfaces $\{z = \pm h\}$ are incompressible and have a surface shear viscosity of η_s. We consider a cylinder contained in the liquid sheet of radius

R^* and height $2h$ aligned with the z axis, and subject to a force $\boldsymbol{F}_x = 4T\boldsymbol{e}_x$. No inertia is taken into account, ruling out time as a variable. The velocity of the cylinder is thus colinear to $\boldsymbol{F}_x$ and solving the problem is reduced to finding the friction coefficient ζ ($\mathrm{Pa \cdot m \cdot s}$) defined as:

$$F_x = -\zeta(Bq)\ U_x \tag{2.41}$$

ζ is here a function of the Boussinesq number Bq defined in subsection 2.4.3 comparing surface shear viscosity to gas friction. It comes with the fact that, as demonstrated in 2.4.3, the bulk viscous friction of the cylinder over its lateral area $2\pi R^* h$ on the neighbouring liquid is negligible.

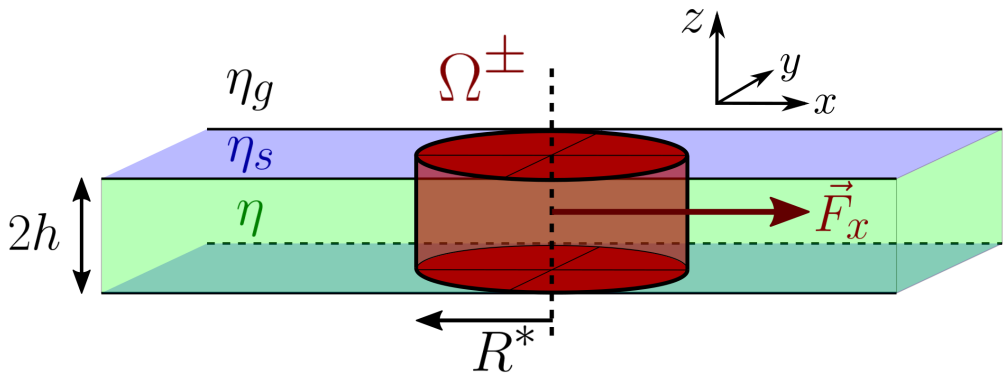

Figure 2.16: Notations used to describe the drag force applied to the cylinders $\Omega^{\pm}$ subject to a force $F_x = 4T$.

An exhaustive resolution of this problem has been developed first by Saffman [103] (1976) in the low Bq regime, followed by Hughes *et al.* [104] (1981) who extended the prediction for any Bq. The interested reader will note that what these studies call a surface shear viscosity is defined in our notations by $\eta_s = 2h\eta$ but they end up in the same physical situation as us, where η_s exists on its own and η is set to zero. They solve for both the rotational and translational problems of a cylinder subject to constant torque and force, but only the latter relates to our situation.

Hughes *et al.* [104] compute the two limits $Bq = 0$ and $Bq \longrightarrow +\infty$, and solve numerically the in-between, yielding the black curve in Fig.2.17. The low limit $\zeta_0 = \zeta(Bq = 0)$ is given by:

$$\zeta_0 = 16\eta_g R^* \tag{2.42}$$

And the asymptotic expression of ζ becomes, for large Bq:

$$\frac{\zeta}{\zeta_0}(Bq \to +\infty) = \frac{\frac{\pi}{4}Bq}{\ln(2Bq) - C_e + \frac{4}{\pi Bq} - \frac{\ln(2Bq)}{2Bq^2}} \tag{2.43}$$

Where $C_e \simeq 0.58$ is the Euler-Mascheroni constant.

These predictions for the friction coefficient $\zeta(Bq)$ will allow us model the relaxation of the thin film, as we measure directly both the force $F_x = 4T$ applied to the edges and their velocity of retraction $U = \frac{\mathrm{d}L}{\mathrm{d}t}$.

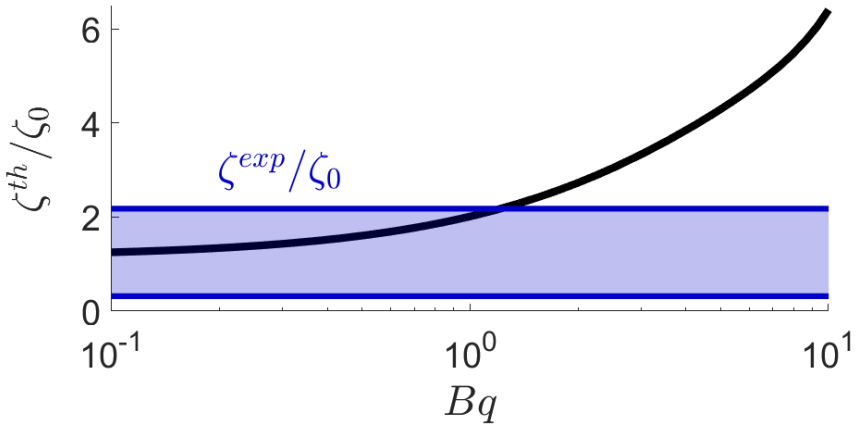

Figure 2.17: Mobility ζ as a function of the Boussinesq number Bq normalised by the low-Bq limit ζ_0. The black line is the theoretical prediction, the blue horizontal lines are the highest and lowest experimental estimations of ζ made throughout the whole relaxation.

The retraction of $\mathcal{C}^*$ can be treated as two independent moving cylinders

As said above, we have separated the problem of solving eq.2.33 into two different subproblems:

- $\Omega^{\pm}$ are individual impenetrable cylinders each pulled with a force $4T$ towards the other.
- The flow field outside these domains can be solved by superimposing the two solutions of eq.2.33 with source terms reduced to the drag of each cylinder.

The former subproblem needs the latter to yield a flow field which becomes negligible at the distance separating the two cylinders. This allows us to see the dynamics of $\Omega^{\pm}$ as two decoupled problems.

The computation of the flow field in outside of $\Omega^{\pm}$ has been done by Stone & Ajdari [105]. Compared to all the cases detailed in this paper, we have here an infinite subphase ($H/R \to +\infty$ with the notations of the paper), and we anticipate that we are in a subphase friction-dominated regime ($\Lambda \gg 1$ in the paper). Fig.7 of the paper shows that in our case, and with our notations now, the amplitude of the velocity field imposed by one domain $\Omega^{\pm}$ in the vicinity of the other is below $0.1|\frac{\mathrm{d}L}{\mathrm{d}t}|$ for $2L > 10R^*$, which is always the case in our measurable range of time.

This validates our assumption that we can treat both domains independently and use the Saffman & Hughes model to look at the dynamics of retraction of $L(t)$.

2.4.5 Quantitative agreement in the air friction-dominated regime

The previous subsection 2.4.4 provides us with a model for the mobility $\zeta(Bq)$ of the edges of the arena $\Omega^{\pm}$ (*cf.* Fig.2.15). Experimentally, we measure at each time step both their velocities $U^{exp}(t) = \frac{\mathrm{d}L}{\mathrm{d}t}$ and the forces applied on them $F_x(t) = 4T(t)$. Thus, for any time t, we now want to compare the value U^{exp} to a theoretical value:

$$U^{th}(t) = \frac{F_x(t)}{\zeta(Bq)} \tag{2.44}$$

Note that the model does not have time as a variable, as no inertia or time-varying forces are among its physical ingredients. Each time step thus represents an independent measure to compare to the model.

To get U^{th}, we now only need to define in what regime of Boussinesq number Bq we are. As discussed in [36], solid experimental clues set an upper bound for η_s in the case of soluble surfactants (and micellar SDS in particular) at $\eta_s \lesssim 10^{-9}\mathrm{Pa\,m\,s}$, allowing us to estimate in our case:

$$Bq = \frac{\eta_s}{R^*\eta_g} \lesssim \frac{10^{-9}}{10^{-3}\times 18\times 10^{-6}} \sim 0.06 \tag{2.45}$$

Meaning we expect to be in an air friction-dominated regime. With this in mind, the model of Saffman & Hughes *et al.* [103, 104] of subsection 2.4.4 gives the expression:

$$U^{th}(t) = \frac{4T(t)}{16\eta_g R^*(t)} \tag{2.46}$$

A comparison with the experimental values $U^{exp}(t) = \frac{\mathrm{d}L}{\mathrm{d}t}$ is shown in Fig.2.18. The middle thicker blue line is the ratio U^{exp}/U^{th} computed with $R^* = R + \ell_{80}/2$, the higher blue line with $R^* = R + \ell_{80}$ and the lower one with $R^* = R$. The uncertainties are shown with shaded areas and correspond to the standard deviation over the 13 repetitions of the experiment, the lower bound being taken with the lower line, the upper bound with the higher line.

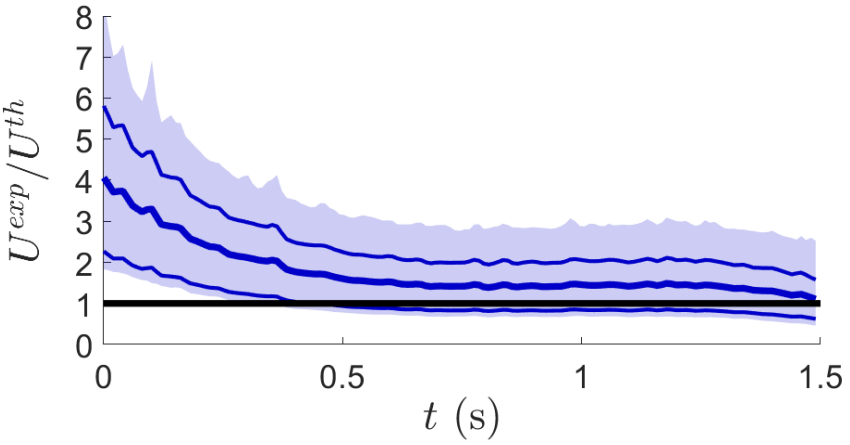

Figure 2.18: Experimental and theoretical comparison for the relaxation speed. The theoretical values U^{th} are computed in the low Boussinesq number limit, which corresponds to an air friction-dominated regime. The three lines correspond each to a different definition of R^*, from top to bottom: $R^* = R + \ell_{80}$, $R^* = R + \ell_{80}/2$ and $R^* = R$. The uncertainties are the extremal values obtained considering all three lines with their respective standard deviations.

The quantitative agreement is good, as for $t > 0.5\,\mathrm{s}$ we have $U^{exp}/U^{th} \simeq 1.5 \pm 1.0$. It means we experimentally validate our measure of line tension T, assuming we are in the low Boussinesq limit thanks to our chemistry. We can also express this in terms of experimental friction coefficient ζ^{exp}:

$$\frac{\zeta^{exp}}{\zeta_0}(t) = \frac{4T(t)}{16\eta_g R^*(t) U^{exp}(t)} \tag{2.47}$$

Where time is again acting as a dummy variable listing independent measurements throughout our working range $t \in [0, 1.5]$ s. The maximum and minimum values for this friction coefficient (taking into account all times $t > 0.5\,\mathrm{s}$ and the uncertainties) are shown with blue lines in Fig.2.17, and correspond as expected to the low Bq regime.

2.4.6 Important remarks and some calculations

Quantitative discrepancy at early times

In Fig.2.18, we see that for $t \in [0, 0.5]$ s, we have a velocity U^{exp} significantly higher than what we expect with our model in the low Boussinesq model.

We are relaxing "too" fast and the explanation cannot be that we have taken the wrong Bq-limit: higher Boussinesq numbers means taking into account the contribution of surface shear viscosity besides air friction, leading to velocities lower than the U^{th} we computed.

The only qualitatively reasonable explanation we have envisioned is an air displacement along the y-axis coming from both directions towards the centre $y = 0$ induced by the displacement of the motor in the $+x$ direction. This would lead to a decrease in the relative velocities between the moving edges of the thin film and the surrounding air, lowering the vertical velocity gradients in the latter and thus lowering the friction.

As for validating this hypothesis... no complex or outlandish experiments trying to control the air movements around the setup were attempted, and so no undergrad interns conducting the experiments were harmed.

Spatial distribution of $T(s)$

The major weakness of the validation of our measurement of the line tension T is that it relies on the bold hypothesis that T is uniform along the contour $\mathcal{C}^*$ (of curvilinear abscissa denoted s). In subsection 2.4.1 we assume this, supported by the fact that the measurement on both sides of the arena are very close. However the line tension responsible for the retraction of the arena is applied at the edges, where we do not measure it, and we have to rely on the assumption $\frac{\partial T}{\partial s} = 0$.

The risk we incur regarding this hypothesis is a local compression of the thickness jump zone during the relaxation as the edges retract. This would lead to different line tensions at the edges (where it applies the driving force) and in the straight parts of the arena (where we measure it).

In Fig.2.19**B**, we show a spatiotemporal image of the interference colours along the red line of **A** and rearranged so that the middle of the arena is at the origin of x (thus correcting for the slight global advection of the arena). The coloured patterns show that the compression ϵ_x is applied in a uniform way along x. This is a solid experimental argument in favour of an equally shared compression of the contour $\mathcal{C}^*$ as it relaxes, and thus a uniform line of tension T.

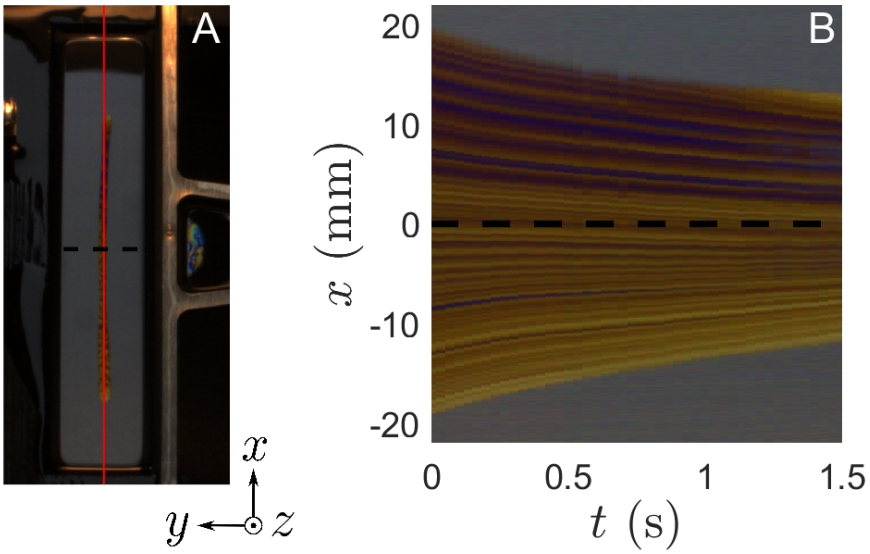

Figure 2.19: Temporal mosaic of the relaxation of the arena. **A:** The red line is the pixel line along which each row of the mosaic is taken at every time step. **B:** Temporal mosaic centred in the frame of the arena (the global advection of the arena in the frame of the camera is corrected).

Time evolution of $T(t)$

In Fig.2.13, we see that the line tension T increases significantly by a factor 2 during the relaxation. We want to rationalise this trend.

Let us first look at the scalings of T with the geometry of the thickness jump zone. If we recall the expression of the line tension, we see that it scales as:

$$T = \gamma_0 \int_0^{\xi_m} ||\boldsymbol{\nabla} h||^2 \, d\xi \sim \gamma_0 \frac{\delta h^2}{w} \tag{2.48}$$

Where δh is the typical difference of thickness between the thin and thick films, and w the typical width of the thickness jump zone.

We can have an experimental access to both δh and w using the thickness profiles of Fig.2.11. w can be estimated with $w = \ell_{80}$ defined in Fig.2.13 as the distance of integration from the edge of the thin film where 80% of the value of T is attained. δh can be estimated as the thickness of the thick film at the position where w is measured. Both are shown in Fig.2.20**A**-**B**, and graph **C** is the normalised line tension defined as:

$$T^* = \frac{wT}{\gamma_0 \delta h^2} \tag{2.49}$$

Which is now constant in time and close to 1, meaning our numerical integration and our evaluation of δh and w went well.

During the relaxation, we see that both δh and w increase by similar factors $\sim 1.5 - 2$, hence the comparable increase of line tension as it scales as $T \sim \delta h^2 / w$. What we want now to rationalise is thus how δh and w grow as the line of tension relaxes.

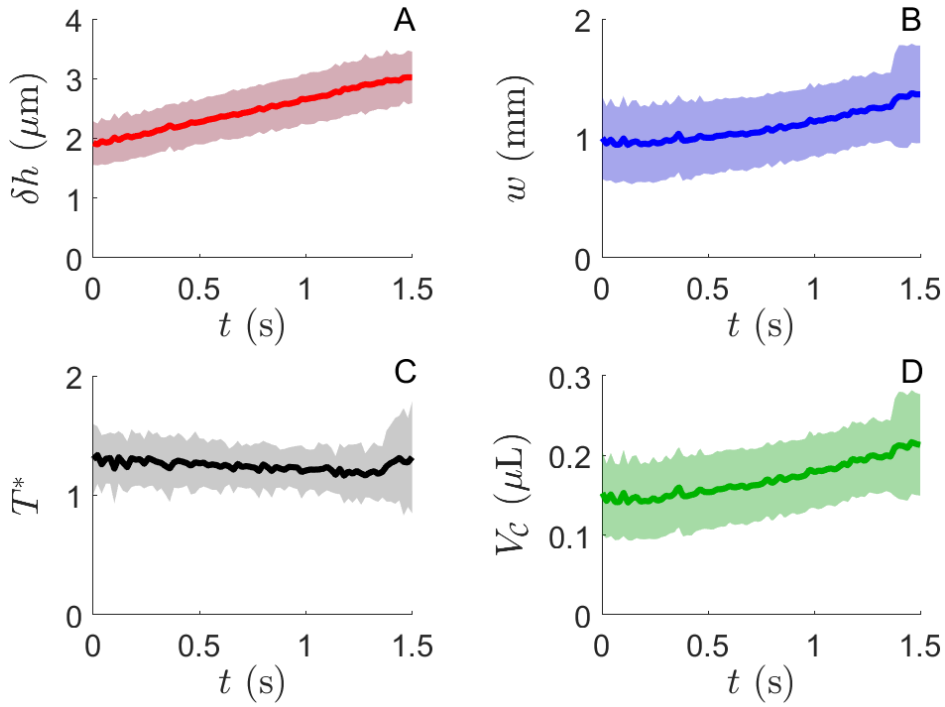

Figure 2.20:

If we get back to our general hypothesis that fluid exchanges between two neighbouring elements of film are infinitely long (due to very slow Poiseuille flows as detailed in 0.2.2) we can think of the thickness jump zone as a closed system, in the sense of volume conservation. Thus, we would assume that $V_{\mathcal{C}^*} = \delta h \times w \times P$ is conserved during the relaxation, and, as the perimeter P is a decreasing function of time (*cf.* Fig.2.8**C**), we would expect δh and/or w to increase over time. However, the volume $V_{\mathcal{C}^*}$ contained in the thickness jump zone, estimated with our measurement of δh and w, is shown in Fig.2.20**D** and increases as well.

This is puzzling, and hinders going further in the reasoning. A potential explanation is a local compression along the direction tangent to $\mathcal{C}^*$ of the thickness jump zone near our line of measurement, which is located in the middle of the arena. Even in this case, what remains unclear is why δh grows over time, as it is basically the thickness of the thick film. The areas of both the thin and thick films being conserved (*cf.* Fig.2.8**D**), the product $\delta h \times A$ should remain constant as well instead of growing because of δh. This could mean that not only the thickness jump zone is being locally compressed, but also the thick film near it. To further advance on this matter, we would need the thickness field everywhere in the foam film, or at least at the edges as well.

Therefore, the function $T(t)$ is assumed uniform along $\mathcal{C}^*$ and its evolution in time is known but not predicted. These are the main flaws of this novel force measurement.

2.5 Conclusions of Chapter 2

- In-plane motions in foam films can be induced by the presence of a line tension T. It originates from localised thickness gradients in the film and tend to minimise the perimeter between pieces of film with different thicknesses.
- For instance, this line tension is relevant for the description of marginal regeneration (*cf.* 0.3.4) where thin patches take circular shapes.
- We managed to create a foam film with a configuration where an elongated arena of thin film is embedded in a thicker film, with a tension line separating them. The thin film relaxes towards a circular shape to minimise the perimeter of the tension line. We are able to measure simultaneously the line tension and the relaxation dynamics of the arena.
- We are speaking of very tiny forces $T \sim 10^{-10}N$, whose precise measurement is a novelty of our work.
- In the frame of our study, using a soluble surfactant (SDS), the in-plane motions are damped by air friction and I analytically predicted the dynamics of relaxation of the arena.
- The measure of our line tension T is in quantitative agreement with the predicted kinematics for the relaxation motion damped by air friction. This validates our new measurement.

3

Dissipative phenomena in an elementary foam: a matter of geometrical frustration

This last chapter is about the core of my experimental work. Here, we will be looking at the rheology of an elementary foam, like my predecessors Adrien Bussonnière and Raphaël Poryles did [4, 6], gathering information on the viscoelastic response of this "local scale of liquid foams". Only now we focus on a system with three films that will allow us to better describe the viscous response of these foams.

In fact, we will be able to quantify the exchanges of surfactants between the films and with the meniscus during the deformation. This is important because a stretched film relaxes by accepting some interface in its plane (*cf.* Frankel films 0.3.2) whereas a compressed film relaxes by giving up some interface. Thus, quantifying the interface balance (*i.e.* the surfactant balance) around the meniscus neighbouring these compressed and stretched films is the key experimental piece of information needed to complete the rheological model developed in our group [4] and before [1, 78].

The main result of this study, and thus of this thesis, is that in the range of strain rate $1-10\,\mathrm{Hz}$, and with all our SDS/DOH mixtures, we only witness film-film exchanges of surfactants, and the meniscus does not play any role of reservoir in this balance.

3.1 Rheology of an elementary liquid foam: geometric frustration

3.1.1 An elementary liquid foam with three films

Our elementary foam is presented schematically in Fig.3.1, as well as the general principle of its deformation.

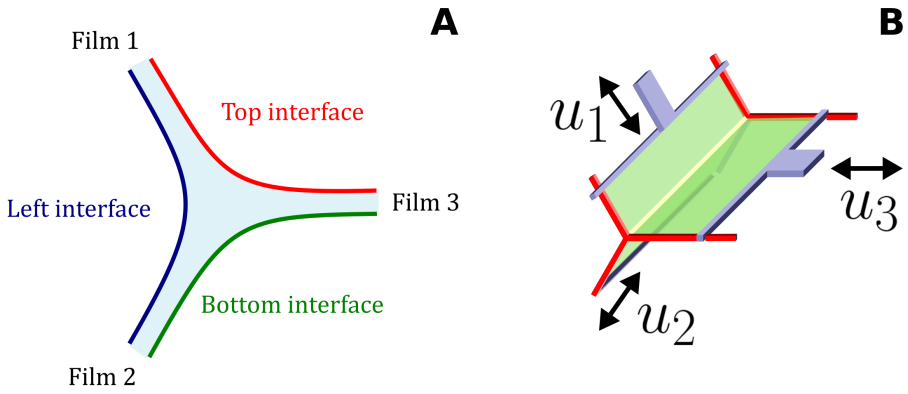

Figure 3.1: Elementary liquid foam with three films. **A:** Side view with the three films (1 for the top left, 2 for the bottom left, 3 for the right) and the three interfaces shared by the films (top, left and bottom interfaces). **B:** Perspective view of the foam, we impose the velocities u_i for each film using three motors. The distance between the two supporting red frames is fixed at 4.2 cm.

Describing this system is equivalent to looking at the local scale of a liquid foam: one meniscus neighboured by three films. In the Introduction 0, subsection 0.4.5, we look at the rheology of an elementary foam with 5 films, and see the viscoelastic response of a Maxwell fluid. Going down to three films and imposing deformations so that $u_1 = u_2 = -u_3$, the response of the difference of tension between film 3 and the two others is similar as shown in Fig.29**A**.

As stated in subsection 0.4.5, the flat deformed foam films have a non-linear elastic response, and the mechanical dissipation is located elsewhere. We expect this region to be very localised near the meniscus and to exist because of what we call a geometric frustration.

Investigating this is the motivation behind passing from 5 to 3 films. We want to be able to better control the deformation state on both side of the meniscus. This was a problem with the 5-films configuration, as we could not deform the central film significantly.

3.1.2 Position of the problem

To understand where lies the problem of the viscous dissipation in our elementary foam, let us look at a peculiar zone, depicted in Fig.3.2: near the meniscus, where **the symmetry of deformation imposes a stagnation point at the interface** (blue cross). Given the three films configuration, the presence of these stopping points is inevitable, and they result in what we call a **geometric frustration**.

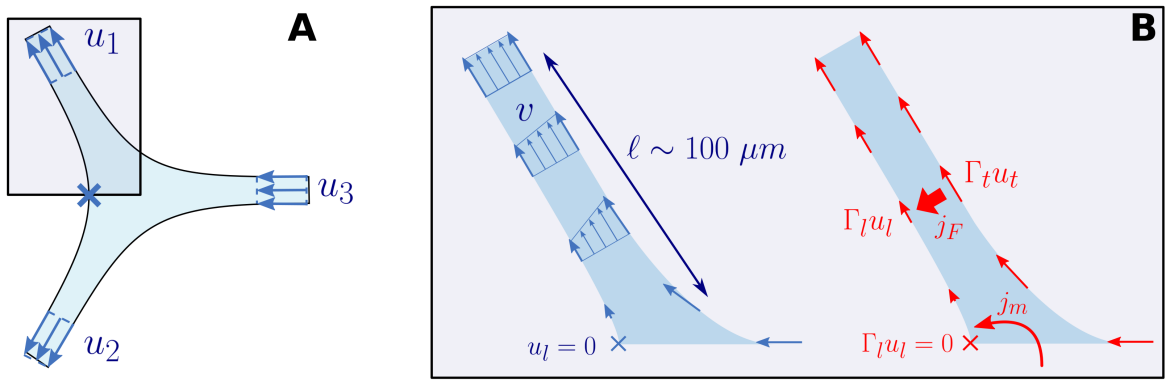

Figure 3.2: Schematic view of the region close to the meniscus as predicted by Bussonnière *et al.* [4]. **A:** Plug flows are imposed far from the meniscus, but because of the symmetry, the left interface has a stagnation point (blue cross). **B:** Zoom near the stagnation point, with the flow field u in blue, the surfactant flux Γu in red. The stagnation point implies the existence of a sheared zone, whose length ℓ can be estimated [4] $\ell \sim 100\,\mu\text{m}$. The stagnation point is also a point of vanishing surfactant flux, and it is yet undetermined in [4] whether the influx of surfactants on the left interface comes from the meniscus (j_m) or from the other film (j_F).

Fig.3.2**B** represents the flow field (blue) and the surfactant transports (red) in the foam near the stagnation point, localised in the middle of the left interface. Most of our experimental results are obtained in the symmetry of deformation and with the direction of the imposed velocities shown in the figure.

The vanishing velocity at the interface imposes the existence of a sheared region near the meniscus of length $\ell \sim 100\,\mu\text{m}$ which is described and estimated by Bussonnière & Cantat [4]. The model behind it and its estimation will be adapted to our own geometry in 3.2.4. This is where the actual viscous dissipation occurs in the system.

The prediction of this length ℓ relies on the surfactant transport map. Here the stagnation imposes the creation of interface on the left, for which we need to provide for its surfactants. Two sources of surfactants can be envisioned here: either the top interface transfers some of its surfactants with a transverse flux j_F, or the meniscus provides for it with a flux j_m. This is where lies the main theoretical conundrum: these two fluxes must enforce the surfactant balance in the system, but how shared is burden? Can we neglect one of them?

The relative importance of these two fluxes j_F and j_m determines the profiles of surface concentrations $\Gamma_{t/l}$ of surfactants along both interfaces, setting the Marangoni stress boundary condition for the shear flow. It thus controls the value of the extension ℓ of the sheared domain and eventually the amount of viscous dissipation in the system.

3.1.3 First hint

In order to get a first qualitative input about these exchanges, we look at the extracted pieces of film in a stretched film and how it may depend on the compression/extension state of its neighbouring films. In Fig.3.3, we impose a fixed deformation ΔL_{in} for a film and a varying

ΔL_{ex} for the two neighbouring films. The three films have initially the same lengths L_{init}. This corresponds to the deformation factors:

$$\epsilon_{in/ex} = \frac{\Delta L_{in/ex}}{L_{init}} - 1 \tag{3.1}$$

And we set a constant $\epsilon_{in} = +0.3$ whereas we vary continuously ϵ_{ex} from -0.5 (compression) to $+0.3$ (extension). This latter case thus corresponds to an isotropic stretching of the elementary foam. The deformations are imposed with fixed velocities so that all deformations have ended at $0.1\,\mathrm{s}$ thus corresponding to a strain rate of $10\,\mathrm{Hz}$.

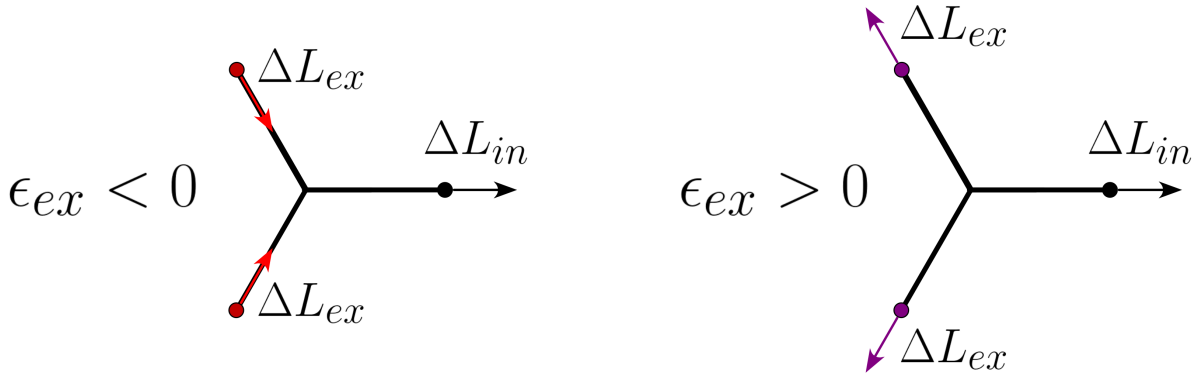

Figure 3.3: Geometry of the deformations applied to the films. All three films start at the same initial length L_{init}. The horizontal film 3 is always stretched in the same way by a distance ΔL_{in}, and we vary the deformation of film 1 and 2 (keeping it with a top-down symmetry) with a distance ΔL_{ex}. The direction of the deformation sets the sign of ϵ_{ex}: negative in compression, positive in extension.

Throughout the deformation, we witness the extraction of pieces of film in the plane of film 3 (undergoing the fixed deformation ϵ_{in}). It is a Frankel film as described in the Introduction in subsection 0.3.2, which has a contrast in fluorescence with the preexisting film 3 due to a difference of thicknesses. This allows us to measure a length L_{out} shown in Fig.3.4**A**, which is a top view of film 3: the large bright fringe on the right is the motor after the stretch, the thin fringe on the middle-left is the free meniscus linking film 3 to its vertical neighbours, film 1 and 2. Fig.3.4**B** shows the quantity L_{out} of Frankel film extracted by stretching film 3 as a function of time for all the range of ϵ_{ex} imposed to its neighbours.

What we immediately see is that the quantity of outgoing film L_{out} heavily depends on the compression state of the neighbouring films. Even more interestingly, L_{out} completely vanishes as the deformation ϵ_{ex} of the neighbouring films tends towards ϵ_{in}, that is the case of an isotropic stretching of the elementary foam. In this specific configuration, the films are unable to exchange any interface by symmetry (we turn j_F off), and **we see that no interface seems to be provided by the meniscus alone, suggesting that the flux j_m is zero.**

This is a first qualitative piece of evidence about the relative importance of these surfactant exchanges. To further investigate this, we need to make the balance between the outgoing quantities of interface of the extracted films as well as the quantitites of interface given up by the compressed films.

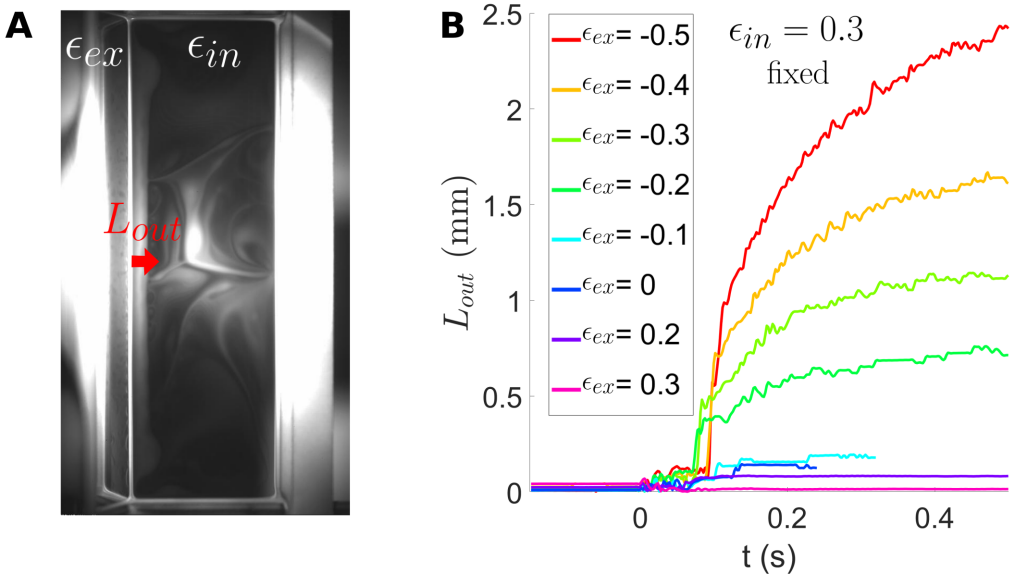

Figure 3.4: Quantifying the length out extracted film in the stretched film 3 depending on the deformation of its neighbours film 1 and 2. **A:** Motor 3 imposes a fixed global deformation $\epsilon_{in} = 0.3$ to film 3, motor 1 and 2 impose the same global deformations $\epsilon_{ex} \in [-0.5, 0.3]$ to film 1 and 2. $L_{out} = f(t)$ is the length of extracted film seen in the plane of film 3 throughout the deformation. **B:** $L_{out} = f(t)$ for the whole range of ϵ_{ex}. The outgoing quantity of film heavily depends on the deformation imposed to the neighbouring films, and vanishes for $\epsilon_{ex} = 0.3 = \epsilon_{in}$ the isotropic deformation. This suggests that the flux j_m (meniscus towards the interfaces) is minimal in the surfactant balance around the meniscus.

First, let us have a closer look at the model for the sheared zone and how j_F and j_m intervene in this theoretical description. It was first developed by Bussonnière & Cantat [4] in the frame of the five films elementary foam. We propose here an adaptation with three films.

3.2 Theoretical state of the art: the Bussonnière & Cantat model for the viscoelasticity of elementary liquid foams

3.2.1 Theoretical description of the flat film, the sheared zone, the dynamic and static menisci

The model developed in [4] will be useful for interpreting my results, and is briefly recalled here for the sake of consistency. As the geometry is different, I have made the necessary minor adaptations.

The model uses the following assumptions :

- The system is invariant by translation in the direction parallel to the free meniscus.

- The shear is mainly localised in a region C (defined in Fig.3.5) where the curvature of the interfaces can be neglected.
- The central piece of the films D undergo plug flows imposed by the motors.
- The dynamic menisci B bridge the sheared zone with the meniscus A. The curvature gradient is localised here.
- The system is supposed in steady state at the time scale of the deformation.
- Most of the surfactants are at the interface, meaning we are in a case where $\Gamma \gg ch$ with h the typical thickness of film and c the bulk concentration of surfactants.

The regions and notations are all shown in Fig.3.5 for our main symmetry of deformation where the stagnation point is on the left interface. Note that all minus/plus signs, in/out exponents and inequalities must be inverted if the directions of the imposed velocities are inverted (if we want $u_{1,2}$ to point inward and u_3 to point outward). **The main studied deformation has this symmetry and these directions for the imposed velocities and is called "Push 3" hereafter**.

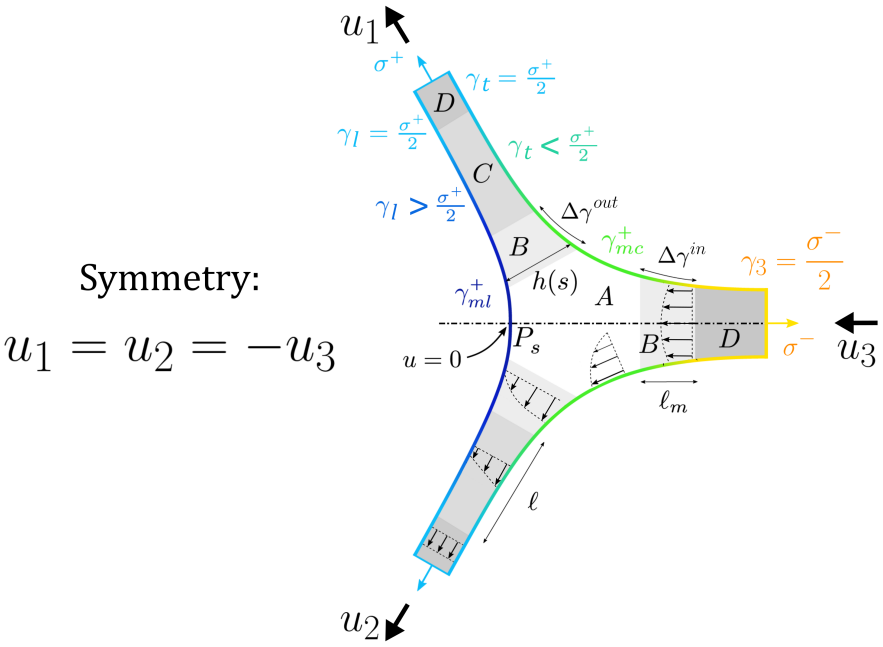

Figure 3.5: Symmetry of the imposed deformation ($u_1 = u_2 = -u_3$) and notations for the different zones considered in the model. γ's are the surface tensions of the interfaces and σ's are the film tensions defined for zones D where the interfaces are symmetrical. Credits to Bussonnière *et al.* [4].

It has to be noted that compared to what is shown in [4], the main difference between the three films case and five films case is that the latter suppose that film 3 (the central horizontal film) remains at rest with no deformation and with the equilibrium tension γ_0. This assumption is supported both by theoretical and experimental arguments detailed in [4]. For the three films

case, film 3 is deformed and the tension conditions for the top/bottom interfaces at infinity in zones C is $\gamma_3 < \gamma_0$. It only requires to redefine the reference tension in the model, which is without important consequences.

3.2.2 Set of equations

Let us now write the coupled equations in region C. We need to write the conservation of momentum, volume, surfactant, as well as the Gibbs identity coupling surface tension with surfactant surface excesses, and the chemical equilibrium beween bulk and surface concentrations of surfactants. The notations for the local frame as well as the boundary conditions in zone C are all shown in Fig.3.6 which is zone C of film 1, with the top and left interfaces.

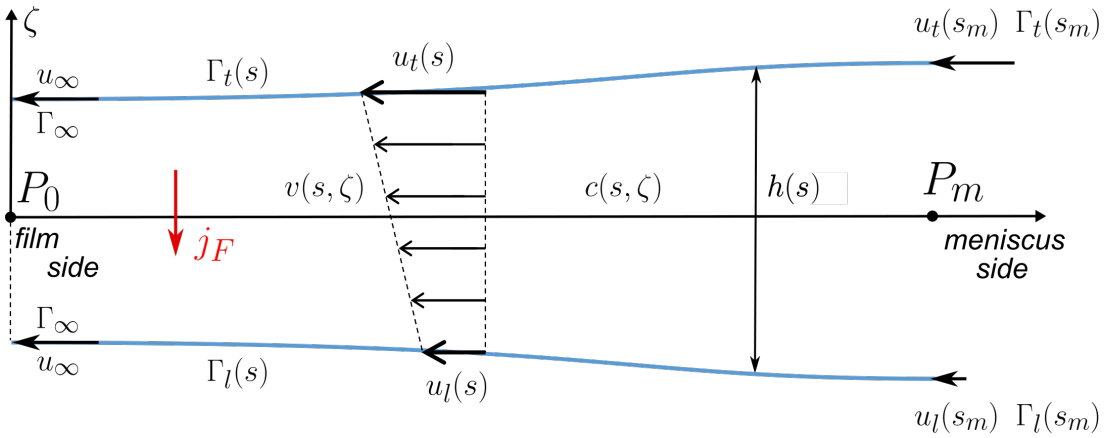

Figure 3.6: Notations for zone C in film 1 (top and left interfaces). P_0 is the junction with zone D, P_m with zone B. The local frame is denoted (s, ζ) and the direction perpendicular to it the direction z along which our system is supposed invariant by translation. $h(s)$ is the thickness of the film, $v(s, \zeta)$ is the flow field, with $u_{t/l}(s)$ denoting its values in $\zeta = \pm\frac{h}{2}$. $c(s, \zeta)$ is the concentration field of surfactants and $\Gamma_{t/l}$ is the surface excess of surfactants at both interfaces. Credits to Bussonnière *et al.* [4].

Let us start by the lubrication equation in the bulk, in which the pressure gradient is zero as curvature is negligible in zone C. Also, the boundary condition for the velocity field at the interfaces is given by the Marangoni stress so that:

$$\partial_{\zeta\zeta} v = 0 \tag{3.2}$$

$$\partial_s \gamma_{t/l} = \pm\eta \partial_\zeta v\Big|_{\pm\frac{h}{2}} \tag{3.3}$$

Where the $\pm$ sign in front of the shear accounts for the fact that the surfaces are oriented towards $\pm\zeta$ on the top and left interfaces.

Eq.3.2 comes with the direct consequence that the flow field is a simple shear flow of equation:

$$v(s, \zeta) = \frac{\Delta u^f}{h}\zeta + u_m \tag{3.4}$$

Where $\Delta u^f(s) = u_t - u_l$ is the difference of velocities between the interfaces and $u_m(s) = (u_t + u_l)/2$ is the mean velocity across the film. Mass conservation thus writes:

$$Q = \int_{-\frac{h}{2}}^{\frac{h}{2}} v(s,\zeta)d\zeta = u_m h = \text{cst} \tag{3.5}$$

Which can be recast using the boundary condition at $s \to -\infty$ (towards domain D) where $v(s,\zeta) = u_\infty$ and $h(s) = h_\infty$:

$$u_\infty h_\infty = \frac{h}{2}(u_t + u_l) \tag{3.6}$$

Now with eq.3.3, we must balance the stress in the simple shear flow with the Marangoni stress, leading to:

$$\partial_s \gamma_t = \eta \frac{\Delta u^f}{h} \quad \text{and} \quad \partial_s \gamma_l = -\partial_s \gamma_t \tag{3.7}$$

This is where we are able to see the beauty of shearing a foam film: the opposed gradients of surface tension at the two interfaces means a difference of surfactant populations, and surfactant transport from one interface to the other and at the boundary of C is what will completely determine the shear in the end. And thus the viscous dissipation. We write this further using the Marangoni modulus to link $\gamma_{t/l}$ and $\Gamma_{t/l}$:

$$\gamma_{t/l} = \gamma_0 - E_M \frac{\Gamma_{t/l} - \Gamma_0}{\Gamma_0} \tag{3.8}$$

Where Γ_0 is the equilibrium surfactant population at rest and E_M the Marangoni modulus of the interface defined in the Introduction 0.1.4 with eq.11. This leads directly to, using eq.3.7:

$$-\frac{E_M}{\Gamma_0}\partial_s \Gamma_t = \eta \frac{\Delta u^f}{h} \quad \text{and} \quad \partial_s \Gamma_l = -\partial_s \Gamma_t \tag{3.9}$$

Meaning that the quantity $\Gamma_t + \Gamma_l = 2\Gamma_\infty$ is conserved along s in region C.

The next set of equations we can write in order to close the system is the diffusion field of surfactants in the film as well as its conservation at the interface. As discussed in subsection 0.2.2, diffusion along ζ is considered to be instantaneous while diffusion along s is infinitely long. We thus write:

$$\partial_{\zeta\zeta} c = 0 \tag{3.10}$$

$$\partial_s(\Gamma_{t/l} u_{t/l}) = \mp D \partial_\zeta c \Big|_{\pm\frac{h}{2}} \tag{3.11}$$

Eq.3.10 yields a linear profile of c in the bulk for which the boundary conditions are given by providing an additional equation for the chemical equilibrium, that is:

$$c(s, \pm\frac{h}{2}) = c_0 + \frac{\Gamma_{t/l} - \Gamma_0}{h_\Gamma} \tag{3.12}$$

This is the simplest model linking c to Γ, a more refined one was developed in chapter 1 and the physical interpretation of h_Γ for SDS/DOH mixtures is discussed in subsection 0.2.3. Solving eq.3.10 with these two boundary conditions allows us to write the full field of bulk concentration:

$$c(s,\zeta) = c_0 + \frac{\Gamma_t + \Gamma_l - 2\Gamma_0}{2h_\Gamma} + \frac{\Gamma_t - \Gamma_l}{hh_\Gamma}\zeta \tag{3.13}$$

Combining this with eq.3.11, we arrive at:

$$\partial_s(\Gamma_t u_t) = -D\frac{\Gamma_t - \Gamma_l}{hh_\Gamma} \quad \text{and} \quad \partial_s(\Gamma_l u_l) = -\partial_s(\Gamma_t u_t) \tag{3.14}$$

Meaning that the quantity $\Gamma_t u_t + \Gamma_l u_l$ is also conserved along s.

In the end, the conservation laws of momentum and surfactants can be written using the boundary condition at $s \to -\infty$ (zone D) where we have a plug flow between identical interfaces, leading to:

$$\Gamma_t + \Gamma_l = 2\Gamma_\infty \tag{3.15}$$
$$\Gamma_t u_t + \Gamma_l u_l = 2\Gamma_\infty u_\infty \tag{3.16}$$

Which allows us to substitute Γ_l and u_l in the other equations, finally yielding a set of four equations bearing on Γ_t, u_t, Δu^f and h:

$$\partial_s\Gamma_t = -\frac{\eta\Gamma_0}{E_M}\frac{\Delta u^f}{h} \tag{3.17}$$
$$\partial_s(\Gamma_t u_t) = -2D\frac{\Gamma_t - \Gamma_\infty}{hh_\Gamma} \tag{3.18}$$
$$\Delta u^f = (u_t - u_\infty)\frac{2\Gamma_\infty}{2\Gamma_\infty - \Gamma_t} \tag{3.19}$$
$$h = \frac{h_\infty u_\infty(2\Gamma_\infty - \Gamma_t)}{\Gamma_\infty u_\infty + u_t(\Gamma_\infty - \Gamma_t)} \tag{3.20}$$

3.2.3 Boundary condition on the meniscus side $s \to s_m$: the surfactant flux j_m as an unknown parameter

In order to close the problem, we need to provide for boundary conditions on the meniscus side of the problem. To do so, we first need to define properly the curvilinear abscissa s_m of point P_m at which these conditions are applied.

This abscissa does **not** correspond to the point P_s of Fig.3.5, as the vanishing Laplace pressure condition of region C becomes invalid in region B, the dynamic meniscus. P_m defines the frontier between C and B where we suppose that the tension of the top free interface reaches the tension of film 3: $\gamma_t(s_m) = \gamma_3 + \Delta\gamma^{out} + \Delta\gamma^{in}$ besides two additional terms $\Delta\gamma^{out/in}$ corresponding to the tension jump due to the dynamic menisci (*cf.* Fig.3.5). These two terms have been computed in 0.3.2, and an estimate in [4] allows us to neglect them, leading to the final definition of P_m, or abscissa s_m so that: $\gamma_t(s_m) = \gamma_3$. This can be equivalently rewritten as:

$$\Gamma_t(s_m) = \Gamma_3 \tag{3.21}$$

This definition itself is not a sufficient condition to close the problem however, and we also need to provide a condition for the left interface in s_m. As beyond s_m the top interface is considered to be at its final value of surface excess of surfactant Γ_3, the surfactant flux towards the left interface necessarily comes from the meniscus and not the top interface. This takes the form:

$$\Gamma_l(s_m)u_l(s_m) + j_m = 0 \tag{3.22}$$

Where j_m is the *ad hoc* flux from the meniscus bulk to the left interface between P_m and P_s (introduced qualitatively in subsection 3.1.2). A phenomenological description of j_m is developed in [4], by writing it as :

$$j_m = -U_m\Big(\Gamma_l(s_m) - \Gamma_0\Big) \tag{3.23}$$

where $U_m = r_m/\tau$ is a typical transport velocity with r_m the meniscus curvature and τ a typical time of adsorption of surfactants. This time can be estimated with a blasius layer of diffusion of surfactant in the meniscus, knowing the typical interface velocities and diffusion coefficient D. All these details are given in [4], but will not be of particular importance for the following of this thesis work.

3.2.4 Numerical resolution of the system

The system made of eq.3.17-3.20 along with the boundary conditions eq.3.15, 3.16, 3.21 and 3.22 can eventually be solved numerically. **The control parameter here is the surface excess Γ_∞ and the sought quantity is u_∞.**

Fig.3.7 shows the resolution of the system. Blue colours stand for the "Push 3" case we are mostly interested in, where $u_\infty < 0$ (represented in Fig.3.5 and 3.6), orange colours stand for the other case where all velocities in films 1, 2 and 3 are of the opposite sign (same symmetry for the stopping point).

Velocities $U_c = E/\eta$ and $U_d = D/h_\Gamma$ are respectively a capillary and a diffusion velocity defining a normalising velocity $\sqrt{U_c U_d}$. The solid lines stand for the case where j_m is neglected. The dotted lines stand for the case where j_m is non-zero with U_m imposed at: $U_m \sim \sqrt{U_c U_d}$. All curves end in $s = s_m$ where the condition 3.21 is met. **Finding s_m also leads, after redimentionalisation, to an estimate for the length ℓ of zone C, and [4] yields $\ell \sim 100\,\mu\mathrm{m}$.**

First thing to notice for the vanishing j_m case (solid lines) is that u_l vanishes in $s = s_m$, meaning that we do not have a stopping point in P_s but rather a stagnant cap from P_m to P_s. This is expected: without j_m, the flux $\Gamma_l u_l(s_m)$ is zero: if not for Γ_l, then the interface velocity $u_l(s_m)$ must vanish.

Much less intuitive is the fate of h close to the meniscus: it thins out if film 1 is compressed and it thickens if it is stretched! This is an indirect consequence of surfactant fluxes imposing an extension to the mean flux $u_m = (u_t + u_l)/2$ in zone C with a sign opposite to that of zone D.

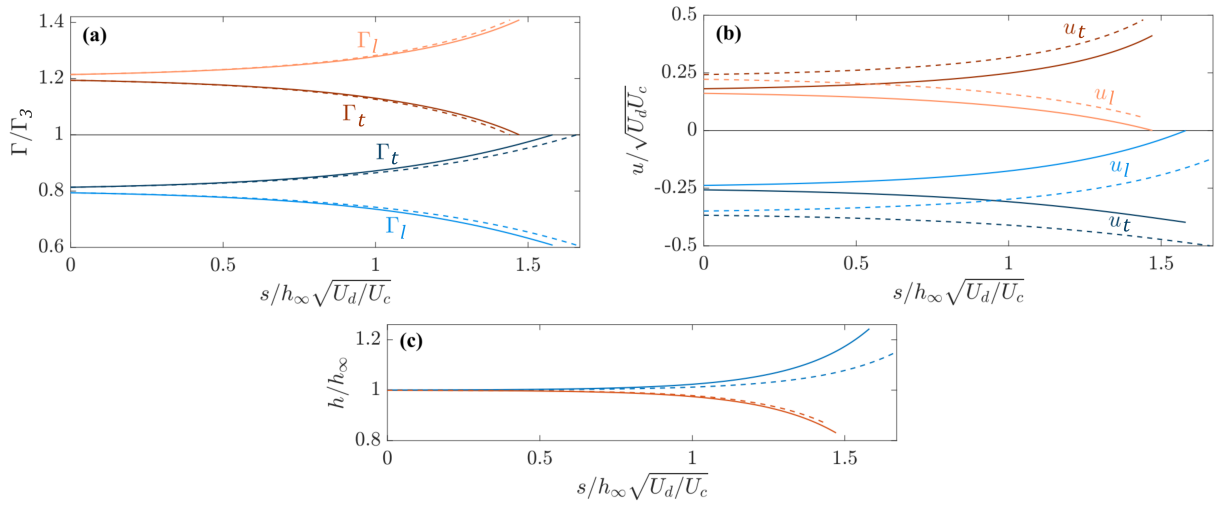

Figure 3.7: Numerical resolutions for: **(a)** the surface concentrations of surfactants, **(b)** the interface velocity fields and **(c)** the thickness profile. Credits to Bussonnière *et al.* [4].

In the end, the numerical resolution gives a relationship $u_\infty = f(\Gamma_\infty)$ with Γ_∞ being the control parameter in the system. This relationship is rather presented in the form of graph $\Delta\sigma = f(U)$ where $\Delta\sigma$ is the difference of tension between film 1 and 3 (directly linked to the difference $\Gamma_\infty - \Gamma_3$ through the Marangoni modulus) and $U = u_t(s_m)$ is found by solving the system and finding u_∞. We show the results for the case of negative u_∞ (stretching film 1) in Fig.3.8. The leftmost blue curve corresponds to vanishing U_m (thus vanishing j_m), the rightmost red one to $U_m = 1000\sqrt{U_c U_d}$.

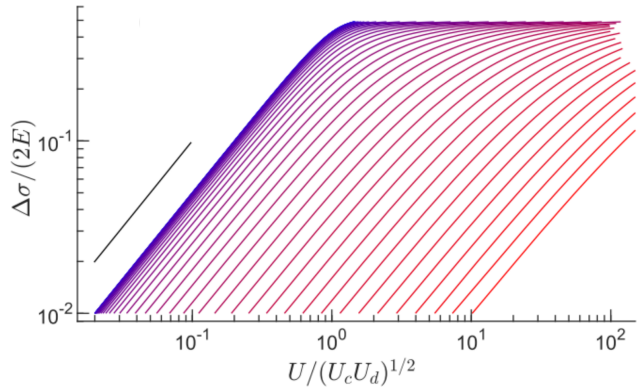

Figure 3.8: Numerical resolution of the differences of tension $\Delta\sigma$ as a function of the interface velocity $U = u_t(s_m)$. The colours are for different values of U_m from (blue) $U_m \to 0$, no exchanges with the meniscus, to (red) $U_m = 1000\sqrt{U_c U_d}$ dominating exchanges with the meniscus. Credits to Bussonnière *et al.* [4].

These stress-strain curves $\Delta\sigma = f(U)$ characterise the rheological response of the elementary liquid foam. Thus, finding the value for the numerical free parameter U_m (and the flux j_m behind it) is the key to predict them.

3.3 Experimental challenge: measuring j_m

Knowing the value of j_m is thus the experimental challenge we face in the frame of this thesis work. To investigate this, we now need to relate this quantity to experimentally measurable quantities. The surfactant exchanges take the form of creation (resp. destruction) of interfaces in the plane of the stretched film 1 (resp. compressed film 3). Below, we relate the amount of surfactants leaving and entering the films to measurable lengths in these films.

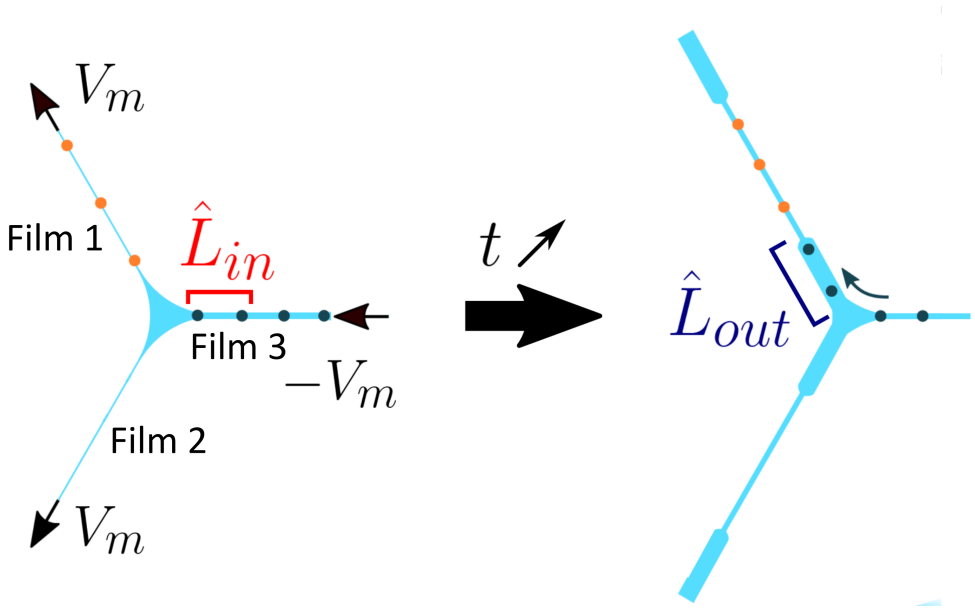

Figure 3.9: Schematic view of the time evolution of the elementary liquid foam. The dots are material points attached to the top interface. As film 3 is compressed with a motor velocity $-V_m$, it gives up a certain length $\hat{L}_{in}$ of interface, whereas film 1 (stretched with motor 1 at $+V_m$) accepts a certain length $\hat{L}_{out}$ in its plane.

The two lengths of interface we are interested in in the frame of this balance are $\hat{L}_{out}(t)$ and $\hat{L}_{in}(t)$ (mm) which are represented in Fig.3.9 during a "Push 3" experiment where the hats indicate the actual lengths we measure. Note that $\hat{L}_{out}$ is directly measurable in the stretched films as it is the length of a well defined piece of film. We define $\hat{L}_{in}$ in the same way, but it has no physical existence as it leaves the compressed film. It is actually the length that would have the piece of film which disappeared if it was still in the film. They are time dependent quantities as the deformation takes place and respectively carry the quantities $N_{out}(t)$ and $N_{in}(t)$ (mol) of surfactants which write:

$$N_{out}(t) = 2\Gamma_1(t) \times \hat{L}_{out}(t) \tag{3.24}$$

$$N_{in}(t) = 2\Gamma_3(t) \times \hat{L}_{in}(t) \tag{3.25}$$

$$\tag{3.26}$$

Where $\Gamma_1(t)$ and $\Gamma_3(t)$ are the surface concentrations of surfactants as defined earlier (Γ_1 corresponds to the Γ_∞ of the model). Here, they are time dependent variables, as the central

region (region D in the model) of film 1 and 3 undergo stretching/compression during the deformation. This last point rises a subtlety: $N_{out}(t)$ and $N_{in}(t)$ are not directly proportional to the lengths of interface $\hat{L}_{out}(t)$ and $\hat{L}_{in}(t)$ as time goes by. To solve this problem, we must relate $\Gamma_1(t)$ and $\Gamma_3(t)$ to quantities we can measure experimentally. This is doable by looking back at eq.1.17 from chapter 1 section 1.3, where we define a film elasticity E_f, which can be related to the definition of the Marangoni modulus eq.11:

$$\sigma^f = \sigma_0 + E_f \frac{\epsilon}{1+\epsilon} = \sigma_0 - 2E_M \frac{\Gamma - \Gamma_0}{\Gamma_0} \tag{3.27}$$

Where we suppose that $E_f = 2E_M$ in presence of poorly soluble surfactants such as dodecanol which dominates the elastic response, as discussed in 1.2.2. This allows us to write directly for both films, 1 and 3:

$$\Gamma = \frac{\Gamma_0}{1+\epsilon} \tag{3.28}$$

Thus, the lengths of interface at rest we will have to compare are $L_{out}(t)$ and $L_{in}(t)$ (mm) which are the actual lengths of films corrected by the deformation factor of the film:

$$L_{out}(t) = \frac{\hat{L}_{out}(t)}{1+\epsilon_1(t)} = \frac{N_{out}}{2\Gamma_0} \tag{3.29}$$

$$L_{in}(t) = \frac{\hat{L}_{in}(t)}{1+\epsilon_3(t)} = \frac{N_{in}}{2\Gamma_0} \tag{3.30}$$

$$\tag{3.31}$$

Which are the relevant quantities to measure. **This is experimentally demanding as we need to simultaneously measure the lengths of exchanged films as well as their states of extension/compression.**

On the other hand, we need now to relate the quantities of exchanged surfactants $N_{out}(t)$ and $N_{in}(t)$ to j_m. Let us define the time $t = t_1$ when the deformation starts, and where we impose constant and equal velocities $\pm V_m$ at the ends of film 1 and 3. Two precautions: first the motor velocities $\pm V_m$ are not directly the velocities $u_1 = u_\infty$ and $u_3 = u_t(s_m)$ as the zone D undergoes extension (*cf.* chapter 1 where we study the elastic contribution of zone D). Second, we consider that the velocities u_i are uncontrolled time-dependent variables imposing $u_\infty(t)$ and $u_t(s_m, t)$ in our model, and each time t is instantly at the relevant steady state given the imposed velocities. In this frame, the quantities $N_{out}(t)$ and $N_{in}(t)$ as we defined them can be written as time integrals:

$$N_{out}(t) = -\int_{t_1}^{t} \Big[\Gamma_t u_t(s_m, t') + \Gamma_l u_l(s_m, t')\Big] dt' \tag{3.32}$$

$$N_{in}(t) = -2\int_{t_1}^{t} \Gamma_t u_t(s_m, t') dt' \tag{3.33}$$

Where the factor 2 for N_{in} comes from the symmetry of "Push 3" imposing identical top and bottom interfaces and where we identify the second term of the right hand-side of N_{out} using eq.3.22: $\Gamma_l u_l(s_m, t') = -j_m(t')$. This leads to the interface balance:

$$N_{out}(t) = \frac{1}{2}N_{in}(t) + \int_{t_1}^{t} j_m(t')dt' \tag{3.34}$$

Which is directly:

$$L_{out}(t) = \frac{1}{2}L_{in}(t) + \frac{1}{2\Gamma_0}\int_{t_1}^{t} j_m(t')dt' \tag{3.35}$$

This is the key equation to solve our experimental conundrum: quantifying L_{out} and L_{in} allows us to deduce directly j_m and the quantities of surfactant exchanged with the meniscus during the deformation. Besides, two limit cases for these film-meniscus exchanges can be envisioned. Fig.3.10 gives a schematic view of both of them.

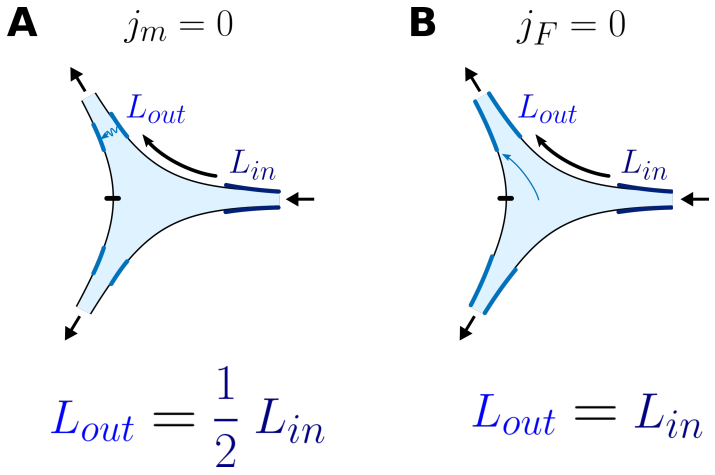

Figure 3.10: Two extreme cases if: **A** The flux of surfactants from the meniscus to the left interface is zero $j_m = 0$, then we need to create 4 L_{out}'s out of 2 L_{in}'s, and $L_{out} = \frac{1}{2}L_{in}$; **B** The flux of surfactants from the top/bottom interfaces to the left interface vanishes near the meniscus $j_F(s = s_m) = 0$, then the meniscus provides 2 L_{out}'s and we have $L_{out} = L_{in}$.

Vanishing flux from the meniscus $j_m = 0$

In the case where the meniscus does not provide any surfactant to the frustrated interface, that is $j_m = 0$ (Fig.3.10**A**), the only ingoing surfactant flux for film 1 comes from the top interface coming from film 3, and we directly have through eq.3.35:

$$L_{out}(t) = \frac{1}{2}L_{in}(t) \tag{3.36}$$

The simple and intuitive way to interpret this result is to see that if not for the meniscus, we need to create 4 interfaces L_{out} out of 2 interfaces L_{in}, hence the factor $1/2$.

Large flux j_m

If on the contrary we allow the meniscus to provide as much surfactants as possible (meaning the factor U_m in the model is as large as we want in eq.3.23), the model eq.3.17-3.20 leads to:

$$L_{out}(t) = L_{in}(t) \tag{3.37}$$

Again, the intuitive interpretation is to see that at best, the meniscus provides for as many surfactants as the ingoing interface L_{in} in order to allow the creation of the interface L_{out} on the frustrated side. Providing more than that (*i.e.* $L_{out} > L_{in}$) is unphysical as the frustrated interface is slower than the free one $|u_l(s_m)| \leq |u_t(s_m)|$ and its surfactant population lower or equal $\Gamma_l(s_m) \leq \Gamma_t(s_m)$.

The next sections 3.4-3.5 are about describing the setup and experimental protocols we used to quantify the exchanges of surfactants, and how we simultaneously monitor the rheological response of the system under deformation. The sections after, 3.6-3.8, detail all the data processing and necessary precautions associated with the quantification of L_{out} and L_{in}. **Section 3.9 shows and discusses the results.**

3.4 Experimental setup and notations

As the state of the art of elementary liquid foams suggests, the number of coupling between the physical ingredients at play in our system is high and the geometry already complex at this scale. Although being the most elementary foam we can think of, three films connected by a meniscus, this system shows all the couplings we can dream of!

In that respect, collecting a lot of different data in a very well controlled and reliable way is a necessity if we want to better understand these couplings. The price we paid for that is a strong automation of our experimental setup, and a lot of different cameras around it, which needed to be synchronised very accurately (at the μs scale). Also, space management was the key... both in terms of bulkiness of the different elements and in terms of lighting. The experimental set-up allows us to measure the meniscus size and position, the film thicknesses and the velocity fields in the films.

And thus what we reaped has proved to be highly reproducible. This is even surprising, because some phenomena such as marginal regeneration seem to be quite turbulent and non-reproducible. Despite all that, the measurements of deformations, deformation rates, and film tensions in particular, have a good reproducibility for a given chemistry.

3.4.1 Chemistries

In the continuity of the experimental campaigns led with the five films rheometer in chapter 1 and [6], we use SDS/dodecanol mixtures to create our three films elementary foam. Thus, we will know what to expect when it will come to measure the elasticities of our films. Note however that contrary to this campaign we removed the glycerol and work with water-based solutions only. Here are the characteristics of the solutions we use followed by the protocol:

- $1\,\mathrm{L}$ of demineralised water (with a resistivity as a proxy for its purity of $18\,\mathrm{M\Omega \cdot cm}$)
- A concentration of SDS $c_{SDS} = 5.6\,\mathrm{g/L} = 19.4\,\mathrm{mmol/L} = 2.4\,\mathrm{CMC}$

- A concentration of dodecanol which varies from no dodecanol to $c_{DOH} = 50\,\mathrm{mg/L} = 0.27\,\mathrm{mmol/L}$
- A concentration of fluorescein $c_{fluo} = 0.8\,\mathrm{g/L} = 2.4\,\mathrm{mmol/L}$

We weight and put all the solid parts of the recipe ($m_{SDS} = 5.6\,\mathrm{g}$, $m_{DOH} = \{0\ ,\ 5\ ,\ 15\ ,\ 35\ ,\ 50\}\mathrm{mg}$ and $m_{fluo} = 0.8\,\mathrm{g}$) in a bottle thoroughly cleaned with one rinse with acetone followed by several rinse with demineralised water of the same quality as used in the next step. Dodecanol melting at $23 - 24\,^{\circ}\mathrm{C}$, it is cooled down in a fridge in advance if need be to allow a precise weighing (which didn't happen many times thanks to one other parameter being living in Brittany). We then take one litre of demineralised water using a volumetric flask cleaned with the same protocol as the bottle. The litre of water is then carefully added to the bottle containing the solids by ensuring the water is flowing gently along the walls of the bottle to avoid excessive foaming, which could lead to an inhomogeneous mixing by entrapping dodecanol crystals. We add a magnetic rod to the bottle and put it on a heating magnetic stirrer at $50\,^{\circ}\mathrm{C}$ for $2\,\mathrm{h}$. The bottle is stored in a dry place at room temperature. Mixtures of SDS/dodecanol being subject to aging in a matter of days (even hours for refined physico-chemistry), the timing which is roughly respected is a solution made between 2PM and 4PM used in the experiment the next day morning at around 10AM.

NB: to cope with the aging problem, we tried different chemistries knowing that we need to fill a $1\,\mathrm{L}$ tank of solution and allow the creation of centimetric foam films lasting tens of seconds. The use of negatively charged fluorescein (which is conditioned by our cyan laser) prohibits the use of cationic surfactants such as the TABs surfactants, as they interact with fluorescein and hinder the fluorescence. Non-ionic surfactants were ruled out because of the foaming problem, and no non-ageing anionic surfactant was found at a reasonable cost given the rather large quantities we need. Thus, we kept on using SDS.

3.4.2 Notations for the 3-films elementary foam

The notations for the axis of the main frame (x, y, z) are shown in Fig.3.11, with x being perpendicular to the free meniscus, parallel to the plane of film 3 and oriented towards motor 3. The system is supposed invariant by translation along z, the direction parallel to the free meniscus (this invariance is discussed later in subsection 3.7).

Also, we will need to define local frames (x_i, y_i) for film 1 and 2, with in each case x_i oriented towards motor i. All these notations are shown in Fig.3.11**A**.

Eventually, we need some notations for the positions, angles and lengths in the system, as the motors and the free meniscus all move during the deformations we impose. The origin of the main frame is set at the initial position of the meniscus before we start any deformation. This initial time will be made explicit later in subsection 3.5 while describing the protocol of the deformation. The lengths $L_{m,i}$ between the motors and the origin are the lengths actually imposed in the system by moving the motors (see Fig.3.11**B**). The meniscus position is denoted (X_{BP}, Y_{BP}) and is used to define all the other quantities: the lengths of the films denoted L_i, that is the length between the motors and the free meniscus, θ the bisector angle between film

1 and 2, and θ_3 the angle between film 3 and the bisector line of film 1 and 2. These two last angles will be relevant to project the forces acting on the meniscus and thus to compute the difference of tension in the system.

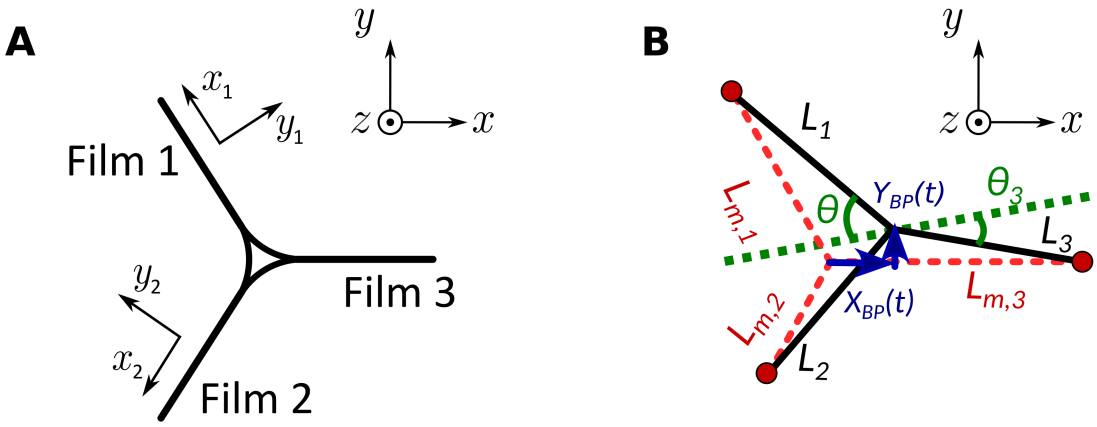

Figure 3.11: **A:** Notations for the local axis for all the films. **B:** Definitions of the different lengths in the system, illustrated for an arbitrary deformation. The motors are the red disks, here placed at arbitrary positions. The three foam films 1, 2 and 3 are the black lines, of respective lengths L_1, L_2 and L_3. The red dotted lines link the three motors to the centre of the deformable frame, their lengths are denoted $L_{m,1}$, $L_{m,2}$ and $L_{m,3}$, and are the lengths imposed experimentally in our setup. The centre of the deformable frame defines the origin of the x and y axis, and we define the position of the free meniscus with the coordinates (X_{BP}, Y_{BP}).

3.4.3 Motors, optics and photobleaching setup

Motors

The three moving edges of the supporting frame for the foam are attached to three independent and identical motors PI mikromove C-867 PI-line M-663.5U. Macros defining their velocities and position instructions are preloaded on them, and they are all synchronised with a DAQ card National Instruments USB-6343. The velocity instructions can go up to $V = 100\,\mathrm{mm/s}$, but we will keep it below $V = 50\,\mathrm{mm/s}$, as we start having significant discrepancies between the required ramp and the effective movements of the motors at $V = 60\,\mathrm{mm/s}$.

Note that in the following, we extensively use "motor" for "mobile edge of the frame" by metonymy.

PF Camera

Our main camera monitoring film 3 by fluorescence, named "PF Camera" hereafter, is a Photon Focus MV1-D1312-160-CL. Its field of view encompasses the whole film 3 with a pixel ratio of $21.8\,\mathrm{px/mm}$, recording $950 \times 544\,\mathrm{px}$ frames at a rate of $278\,\mathrm{Hz}$. It looks at the system from above, thus, the bath of soapy solution being in its optical axis, we need to cover the latter

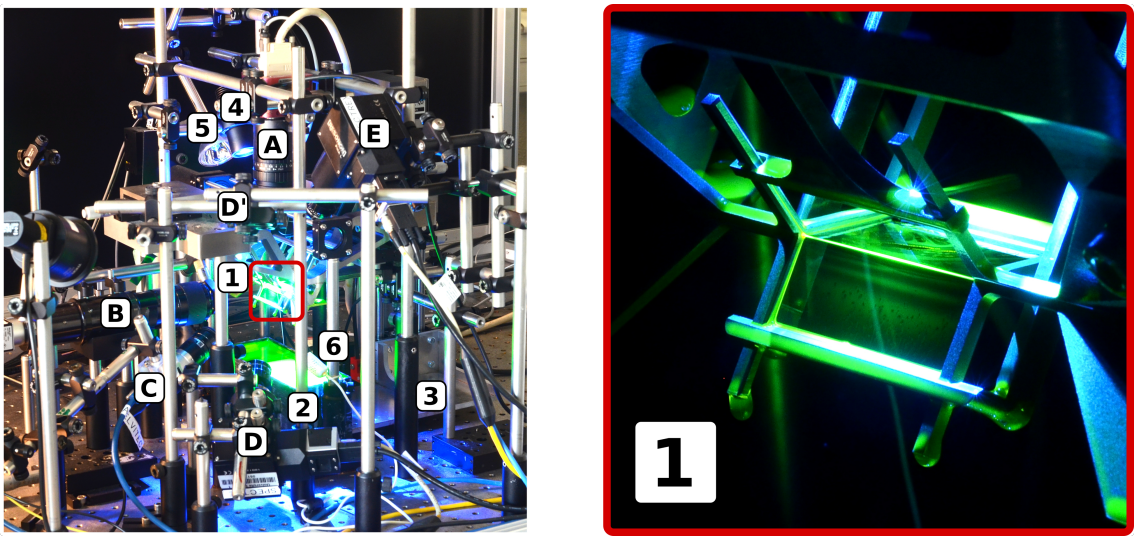

Figure 3.12: Picture of the whole setup, letters are for cameras, numbers for other experimental tools. **A:** Photon focus fluorescence camera "PF", looking at film 3 from the top. **B:** Plateau border camera "BP", looking at the free meniscus from the side. **C:** Top fluorescence camera "TPF", looking at film 1. **D-D':** Hyperspectral camera 1 "SP1" looking at the thickness profile along a line contained in the plane of film 1. **D'** is the other position on the experimental setup where "SP1" can be attached to look at film 2. **E:** Hyperspectral camera 2 "SP2" looking at the thickness profile of film 3. **1:** Deformable frame where the elementary foam is created. The foam films fluoresce green-yellow light, and the saturated line connecting the triple points of the three-pointed stars is the free meniscus hanging in the air. **2:** Tank for the soapy solution, lying on a horizontal plate **3** moving up and down using a stepper motor. **4-5:** Blue and white lights used respectively for fluorescence imaging and hyperspectral imaging. A second white lamp aligned with "SP1" is present but hidden by the setup. **6:** Temperature and humidity sensor positioned as close as possible to the elementary foam.

with a printed cache so that we avoid stray fluorescent light. The trigger of the camera and the collection of frames are all done through the DAQ card, with a precision on the synchronisation and the timestamps of the frames on the order of a µs. A typical frame recorded by this camera is shown in Fig.3.13.

BP Camera (Bord de Plateau)

The camera monitoring the free meniscus by fluorescence from the side, named the "BP Camera" hereafter (for Bord de Plateau), is a Basler 1920-155uc camera mounted on a 12X Navitar objective. Ingoing light is filtered using an orange filter to ensure that we only see the fluoresced light of the elementary foam. The field of view is focused on a portion of a few millimetres of free meniscus at the centre of the foam along the z axis, with a pixel ratio in the range $690 - 1300\,\mathrm{px/mm}$ and recording $1920 \times 860\,\mathrm{px}$ frames at a rate of $150\,\mathrm{Hz}$. The synchronisation and collection of frames is done through the DAQ, with the same precision and in the same way as for the PF camera.

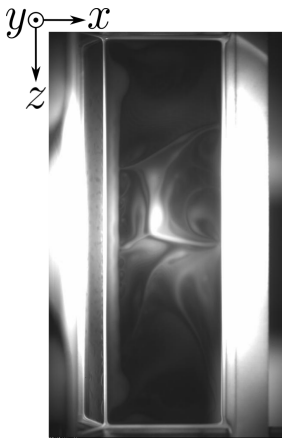

Figure 3.13: Typical frame recorded with the PF camera. Film 3 is the rectangle in the middle, bordered on the right by motor 3 (thick saturated vertical fringe) and by the free meniscus on the left (thin saturated vertical fringe).

One goal of this recording is to measure the radius of curvature of the free meniscus by looking at the shape of the intensity profile. In order to get a clear signal, we need to remove the light coming from film 3, whose plane contains the optical axis of the camera, parasiting the fluoresced light from the free meniscus itself. While using this camera, a horizontal cache is placed between film 3 and the blue LED lighting the system, so that only the free meniscus fluoresces toward the BP camera.

An example of a full frame picture is shown in Fig.3.14A, along with the intensity profile $I(y)$ averaged over z in Fig.3.14B.

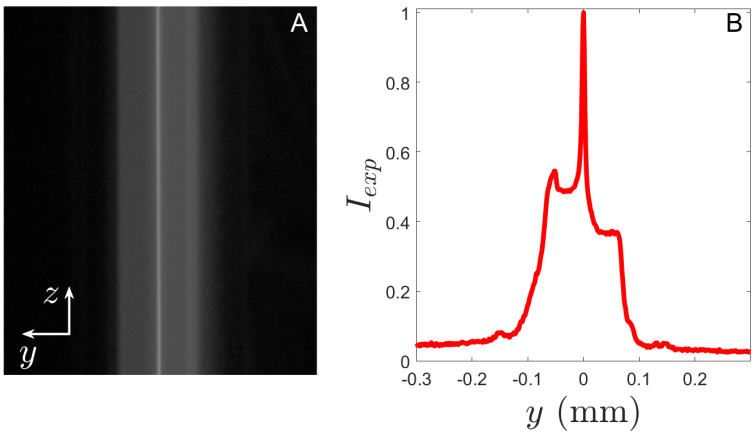

Figure 3.14: **A** Typical frame obtained with the BP camera. The very thin saturated fringe in the middle localise the position of film 3, whose plane contains the optical axis of the camera. **B** Intensity profile $I(y)$ averaged along z. The positions of the shoulders of the signal will allow us to compute the radius of curvature of the meniscus.

SP1 and SP2 Cameras (for SPectral)

We use two hyperspectral cameras to monitor the three films, with "SP1" having two positions, one for film 1, one for film 2, and "SP2" monitoring film 3. These cameras are Resonon Pika L hyperspectral cameras mounted on $23\,\mathrm{mm}$ Schneider High Resolution VIS-NIR objectives. Along a physical line of length $1024\,\mathrm{px}$, they monitor the light intensity received for each wavelength, with 600 pixels, each one dedicated to a wavelength $\lambda \in [400, 1000]\mathrm{nm}$ with a constant step of $1\,\mathrm{nm}$ between each. Depending on the zoom applied, the physical line can be seen with a pixel ratio ranging from $20 - 30\,\mathrm{px/mm}$. The scale is found by placing a mirror in the plane of the foam film, on which a narrow strip of tape is affixed, aligned with z and of a well-known width.

TPF Camera (ToP Fluorescence)

Film 1 is imaged using a Basler 1920-155uc camera mounted on a 25mm Fujifilm objective (Fig.3.12C) with $1920 \times 800\,\mathrm{px}$ at a rate of $150\,\mathrm{Hz}$. Ingoing light is filtered using a similar orange filter as the one used with the "BP" camera. The "TPF" camera could not be aligned with the normal y_1 to film 1 because of a lack of space in the setup due to other cameras. However, it was put as close as possible from it so that the parallax problem remains negligible for the sake of our measurement, which is in the vicinity of the centre of the free meniscus. This is where the pixel ratio is computed (33 or $35\,\mathrm{px/mm}$ depending on the set of experiments). The synchronisation and collection of data is ensured using the DAQ just as for the other cameras. This camera does not need any cache to remove stray fluoresced light (however a mat strip of tape was placed on a metallic surface aligned with the optical axis to remove an inopportune reflection). A typical frame recorded by this camera is shown in Fig.3.15.

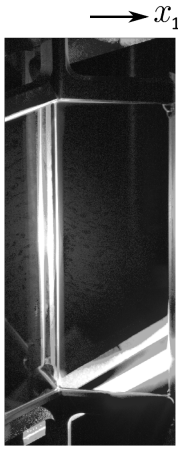

Figure 3.15: Typical frame recorded with the TPF camera. Film 1 is the rectangle in the middle.

Photobleaching setup

To describe the velocity fields in the planes of the films of the elementary foam, we need to create passive tracers in the film that do not change the state of its interfaces. Thickness heterogeneities which can be imaged by fluorescence could be a lead, but what we need here is a reliable and

very localised information on the velocity field (at a scale smaller than the typical heteogeneity). Thus, the group developed a photobleaching setup designed to locally deactivate fluorescein using a cyan laser excitted at $488\,\mathrm{nm}$ to create tiny pieces of non-fluorescing bulk to track (kudos to Jacopo Seiwert, Adrien Bussonnière, former post-docs of our group, and Emmanuel Schaub, the research engineer of the soft matter department at the IPR). This setup was first developed in 2015 and a proof of concept was made with a study of convective transport in vertical foam films by J. Seiwert *et al.* [106]. The main contribution in the frame of my Ph.D was to develop its automation and to allow drawing arrays of dots with the life-saving help of Emmanuel Schaub.

The optical path of the laser is directed using small mirrors, passing through an acousto-optic modulator AOTFnC-400.650-TN which serves as a very responsive shutter. Toward the end of the path, the laser hits a mirror attached to a galvanometric scanning head dynAXIS to apply tiny changes to its direction and is eventually directed down on film 3 to photobleach it from the top. The shutter and scanning head responsiveness and their synchronisation allow us to shoot in a reliable way down to $\sim 10\,\mathrm{ms}$ per dot, which happened to be the minimal time it takes to create a dark enough dot in the film.

The laser is used at a power of $120\,\mathrm{mW}$ that requires optical protections in the form of glasses and a special cage covering the optical path of the laser. The acousto-optic modulator and the mirror with the galvanometric scanner are synchronised with a dedicated channel of the DAQ card to emit localised flashes at specified positions on film 3 to photobleach them. The result is a 2×8 rectangular grid of dark dots of typical diameter $\sim 100\,\mu\mathrm{m}$ shot with a precision of the same order of magnitude which we made separate by $\Delta x = \Delta z = 400\,\mu\mathrm{m}$ in both directions. It is placed near the meniscus and with the two columns aligned with the z-axis. A typical frame recorded by this camera is shown in Fig.3.16.

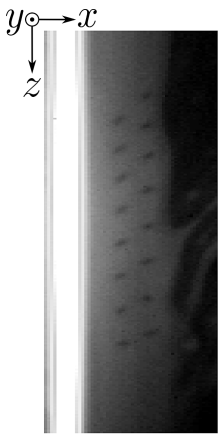

Figure 3.16: Zoomed image of the photobleached dots performed with the PF camera. The saturated vertical fringe on the left is the free meniscus.

3.4.4 Interfacing and synchronising the experiment

The cameras, the motors (both for the deformable frames and to lift the soapy solution bath) and all the photobleach-related devices are connected to the DAQ card for the synchronisation and interfaced with LabView.

The main code is fed with all the parameters: times, motors, cameras, photobleaching setup and save paths. The motors are loaded with individual macros specifying their positions, velocities and when to wait for a trigger to be synchronised together. The DAQ card is linked to all cameras and motors and it triggers the different elements at the times specified by the parameters.

Regarding the cameras, it only launches the beginning of the recording, and the internal clock of the cameras maintains the framerate. Each frame is collected with its timestamp, thus preventing a mismatch between times and frames in case of frame skipping, which can happen if the buffer is overfilled due to random RAM mismanagement events.

The movies, the positions of the motors and their timestamps are collected and stored as binary files.

3.5 Detailed protocol for the "Push 3" experiment

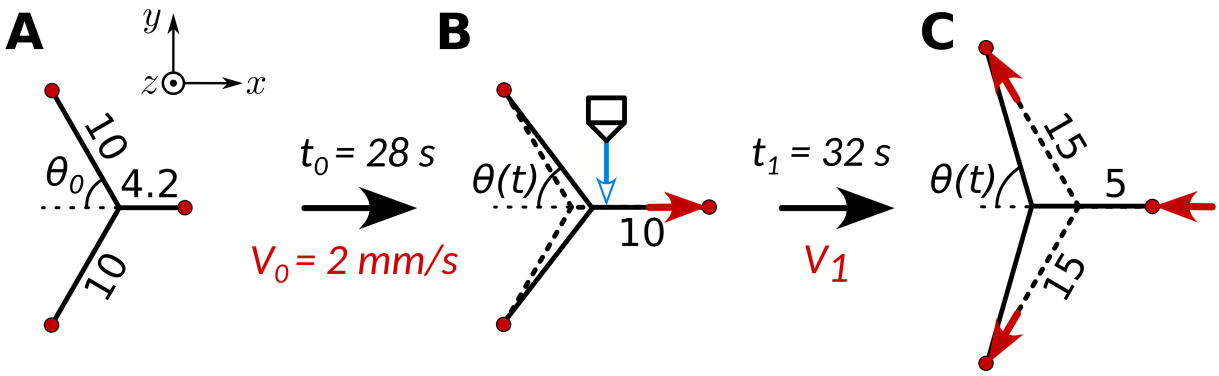

Figure 3.17: Description of the "Push 3" experiment. **A** is the initial shape of the film assembly, as extracted from the bath. **B** represents the preparation stage, which is required to control the initial thickness of film 3. **C** is the deformation we want to address. All numbers given along the different films are the lengths (in mm) between the centre of the frame (triple point of the plain lines for $t < t_0$, of the dotted line for $t > t_0$) and the motors. The red lines indicate which motors are involved at each step, along with their velocities in red as well. The cyan cursor pointing downwards accounts for the photobleaching step occurring at $t = 31\,\mathrm{s}$. θ is defined as the semi-angle between the vertical films 1 and 2.

The main results of this chapter are obtained in a specific deformation configuration referred to as "Push 3", as mentioned earlier and detailed below. In this configuration, films 1 and 2 are stretched, and film 3 is compressed over the same amplitude, at the same velocities, and at the same times. The protocol is illustrated in Fig.3.17. Other types of deformations have been investigated and will be compared to "Push 3" later on, as we will detail our results.

Before launching the code and the automated part, we start by cleaning the surface of the bath with a custom squeegee (removing bubbles and impurities) and by setting the right light given the choice of camera for the experiment. Note that because of RAM management and lighting, we can only turn on one camera at a time during the experiments.

The PF, BP and TPF cameras require blue light to image the system by fluorescence, and we turn on the blue LED right from the start. The SP1 and SP2 cameras require white lights specifically aligned with them for their interferometric measurement of thickness. These white lights produce a lot of heat, thus we only turn them by hand during the main deformation as specified later.

Then we launch the main LabView code with all the parameters we need, which are defined in the following. The motor of the bath rises up til it immerses the deformable frame, for $5\,\mathrm{s}$, then goes down at a well-controled and low velocity of $30\,\mathrm{mm/s}$ to wet the frame in reproducible way and avoid bubble formation. The trigger sent by the DAQ card to command the motor to go down is the origin of times $t = 0$ for the experiment. Once the bath is down again, we may put on different caches depending on the cameras (as discussed individually in section 3.4.3).

At this point the films are too heterogeneous in thickness to proceed to the main deformation, because of the broken invariance by translation along z and that would lead to a lack of reproducibility of the experiments. The state of the horizontal film 3 is crucial in particular, as the main deformation consists in compressing it after it has been photobleached. Right after the formation of the elementary foam, film 3 can be seen in Fig.3.18A: the thickness distribution in the film ranges from hundreds of nanometers to tens of microns. Patches of same thicknesses tend to regroup for energy reasons (the same as what drives the relaxation of the thin film in chapter 2) and the thicker ones are evacuated towards the menisci at the edges, replaced by thinner patches (by the marginal regeneration instability discussed in 0.3.4).

We first let the film drain until $t = t_0$ (Fig.3.18B and Fig.3.17B), then it is stretched slowly. The result is Fig.3.18C, where the red arrows are the newly created films extracted from the menisci (Frankels films *cf.* 0.3.2) which have the major advantage to be very homogeneous and reproducible. The photobleaching step and the main deformation can be made from this state at $t = t_1$ as depicted in Fig.3.17C. The deformation performed at t_1 is our actual measurement, and varying the velocity of deformation V_1 is our second parameter besides chemistry.

All the lengths $L_{m,i}$ imposed between the centre of the frame and the motors i at all times are given in Fig.3.17, as well as the velocities imposed.

NB: All the waiting to ensure a controlled state for the horizontal film 3 also has repercussions on the other films 1 and 2:

- As gravity drainage occurs, it tends to make the top film 1 thinner and the bottom film 2 thicker. This has a direct impact on their respective elasticities, as a thinner film is also stiffer as expected with our model of chapter 1 section 1.2.2. This dependency is quite "slow" however, and one order of magnitude in thickness yields a factor two on the elasticity. Boundaries can be set to this problem by monitoring mean thicknesses of both film 1 and 2, which we will do using camera SP1.

- Allowing the menisci to drain for extended periods of time lead to the formation of thin patches near the edges of the film (see 0.3.3). For menisci located at the bottom of their films (the free meniscus for film 1, the meniscus supported by its motor for film 2) the 2D Rayleigh-Taylor instability occurs (*cf.* section 0.3.5). This leads to the constant presence

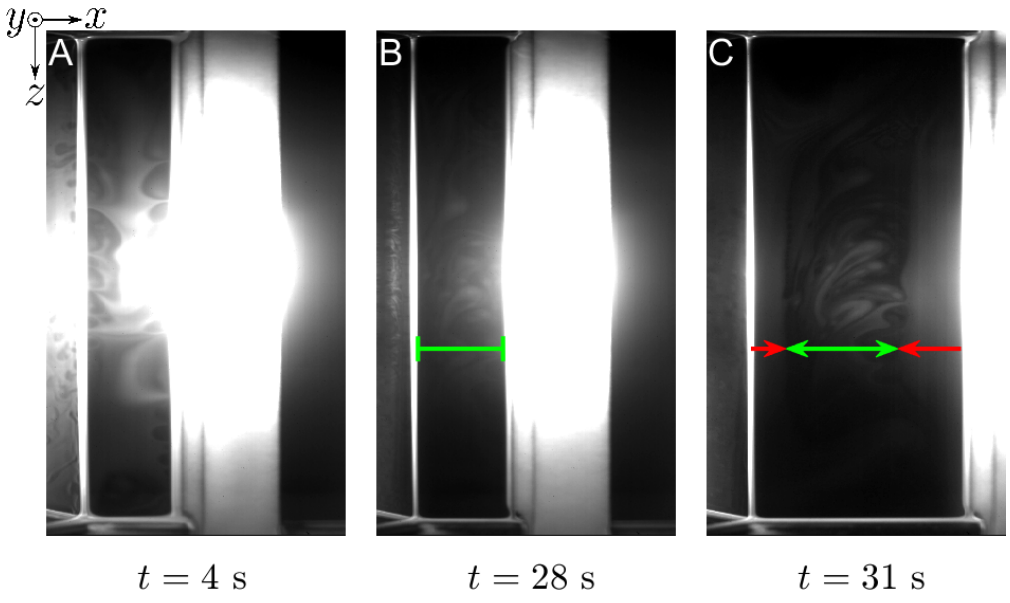

Figure 3.18: Fluorescence images of the horizontal film 3 (top view using the PF camera) during the preparation phase. **A:** Right after the elementary foam is formed, the film 3 (indicated by the green line in B) is very heterogeneous in thickness (Fig.3.17A). **B:** Right before the preparatory stretch, the film has drained and is more homogeneous in thickness although some patterns are still visible. **C:** Right after the preparatory stretch (Fig.3.17B), some newly created film went out of the menisci, identified with the red arrows. The pre-existing film (which is a bit stretched in the process) is identified by the green line and double arrows. The extracted Frankel films are very homogeneous and invariant along z.

of thin patches advected upwards, which has consequences for image processing in the non-horizontal films.

3.6 Data and image processing

In this section, we will detail how we process the different movies to extract all the physical quantities we need to describe our system. All the following numerical methods will be detailed for the "Push 3" experiment, which is the main studied deformation of our elementary liquid foam described in section 3.5. Other deformations such as "Push 1" and "Pull 3" require some adjustments in movie processing, but the numerical methods remain broadly the same.

3.6.1 Tracking of the free meniscus in the horizontal plane

Extracted ingredient: X_{BP} the horizontal position of the meniscus

When the films are pushed or stretched and the forces they exert on their neighbours change, the free meniscus moves. The meniscus position will be related quantitatively to the tensions in

the films in section 3.8. Here we focus on its horizontal motion by computing its position X_{BP} on the x axis.

As discussed in Bussonnière *et al.* [4] and seen experimentally in Fig.3.19A-B, the free meniscus curves in the z-direction as it moves, taking a roughly parabolic shape $X(z)$, and the position $X_{BP} = \delta_1 + \delta_2$ as we define it in Fig.3.19 is the position of its apex. Although we have $\delta_1 \simeq \delta_2$, taking into account the parabolic shape for the sake of computing the angle θ between the film leads to a negligible correction which has been computed and represents less than 1% of deviation throughout the measurement. This correction had already been investigated and computed in Bussonnière *et al.* [4] in a similar configuration, where the interested reader can find its formula with the same notations for δ_1 and δ_2. In this study, we will thus only measure the apex position X_{BP} and not the whole meniscus shape.

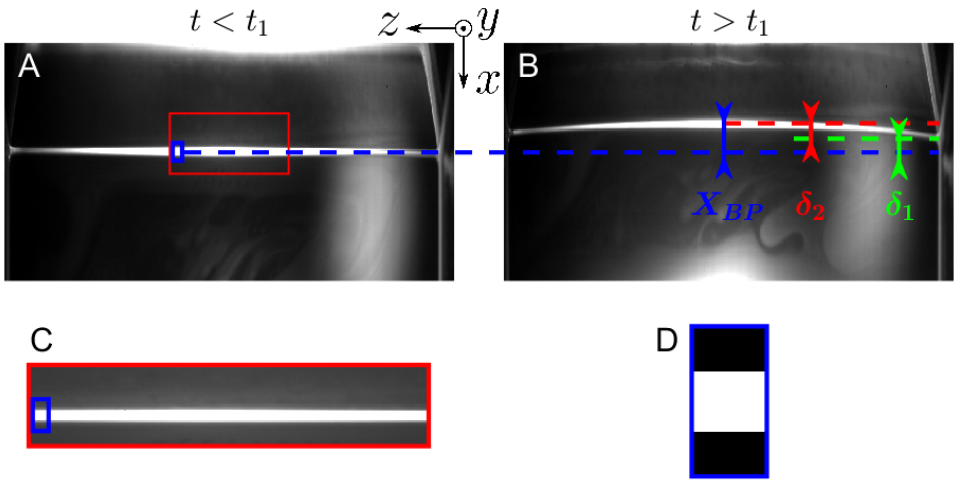

Figure 3.19: Tracking of the free meniscus horizontal displacement, example with $[DOH] = 50\,\mathrm{mg/L}$ at $V_1 = 50\,\mathrm{mm/s}$. **A-B:** Top view (PF camera) of the system respectively right before ($t = 31.99\,\mathrm{s}$) and just after ($t = 32.1\,\mathrm{s}$) the main deformation occurring at $t_1 = 32\,\mathrm{s}$. The aspect ratio of the picture is deformed to better see the curvature of the free meniscus as it moves. We directly see that the total displacement of the apex of the meniscus $X_{BP} = \delta_1 + \delta_2$ is the sum of δ_1 the displacement of the free meniscus as a whole and δ_2 the displacement of the apex due to the free meniscus curving in the z direction. Both contributions are of comparable amplitudes. **C:** Zoom in the region of the apex of the free meniscus of **A** with an aspect ratio faithful to reality. This zone is where we look for the maximum of correlation of the binary mask **D** along x for each position z to estimate the position of the apex of the parabola.

In order to track the position of the apex of the free meniscus, we use a correlation technique with a correlation mask which is a bright vertical saturated segment with a well chosen width and length on a black background (*cf.* Fig3.19D). For each position z in the region of the apex of the free meniscus (Fig3.19C), we look for the maximum of correlation along x of our binary mask. The value X_{BP} is obtained with an average over z over the region encompassed by the red rectangle in Fig.3.19A. This process is repeated for each frame individually, with the same region of interest and the same binary mask.

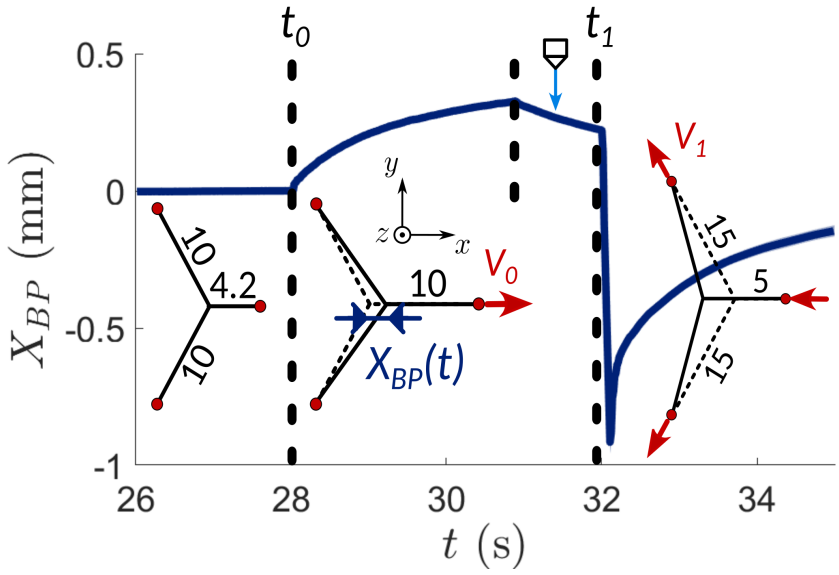

Figure 3.20: Typical curve $X_{BP} = f(t)$ obtained for $V_1 = 50\,\text{mm/s}$ and $[DOH] = 50\,\text{mg/L}$. The error is smaller than the width of the curve. Each step of the deformation is placed at its time of occurrence, see section 3.5. The preparation phase starting at $t_0 = 28\,\text{s}$ ends around $t = 31\,\text{s}$ and we photobleach film 3 between $t = 31.5\,\text{s}$ and $32\,\text{s}$.

Eventually, the origin of X_{BP} is set so that at $t < t_0 = 28\,\text{s}$ we consider it to be at its rest position, the centre of the deformable frame as shown in Fig.3.20. No drift of the meniscus position has been witnessed before that time, and this initial position appears as the right criterion to define when the films meet with an angle of 120^o. Thus we set $X_{BP}(t = t_0) = 0$.

3.6.2 Tracking the vertical position of the free meniscus and its radius by ray tracing

Extracted ingredients:

- Y_{BP} **(mm) the vertical position of the meniscus**
- R **(mm) the curvature radius of the meniscus**

To determine Y_{BP} and R, we use the BP camera, located on the side of the meniscus and whose a typical frame is displayed in Fig.3.14A. The intensity profiles are obtained by first averaging each frame along the z direction, as shown in Fig.3.14B. The maximum of intensity of each frame is tracked and corresponds to the centre of the meniscus, determining its ordinate Y_{BP} (Fig.3.22A). This tracking is done without any correlation technique, as the resolution is much greater than with the PF camera used for X_{BP}, and we only look at the maximum of I for each frame. Also, the displacements along the y direction are much smaller than in the x direction due to the symmetry of the "Push 3" deformation, and the curvature of the meniscus in the y direction does not need to be quantified.

Finding R is more indirect, as we need to look at the shape of the intensity profile and relate

it to the shape of the meniscus. As depicted in Fig.3.21, a ray-tracing simulation was necessary to link R to the profile I_{fluo}. I developed the simulation with the following assumptions:

- The meniscus has its equilibrium section, that is three sectors of three circles of radii R tangentially connecting one another (*cf.* left of Fig3.21)
- We only consider the fluoresced light, which is supposed to be emitted in an homogeneous and isotropic way in the volume of the meniscus. Each emitted ray is subject to reflection/refraction laws at the three curved water/air interfaces.
- We only collect the rays going out of the meniscus horizontally, which we retrace back in the volume. Each segment of their trajectories contributes to the intensity proportionally to its length and the number of reflections (where most of the intensity is lost) before going out towards the camera.

The resulting intensity profile I_{fluo} shown in Fig.3.21A closely resembles the experimental observations depicted in Figure 3.21B, with a sudden drop of intensity beyond an ordinate $y = 0.208R$ from the centre. This decrease is noticeable in the simulation as soon as we consider the first reflection within the meniscus. Including more than the second reflection did not result in a significant modification of the intensity pattern.

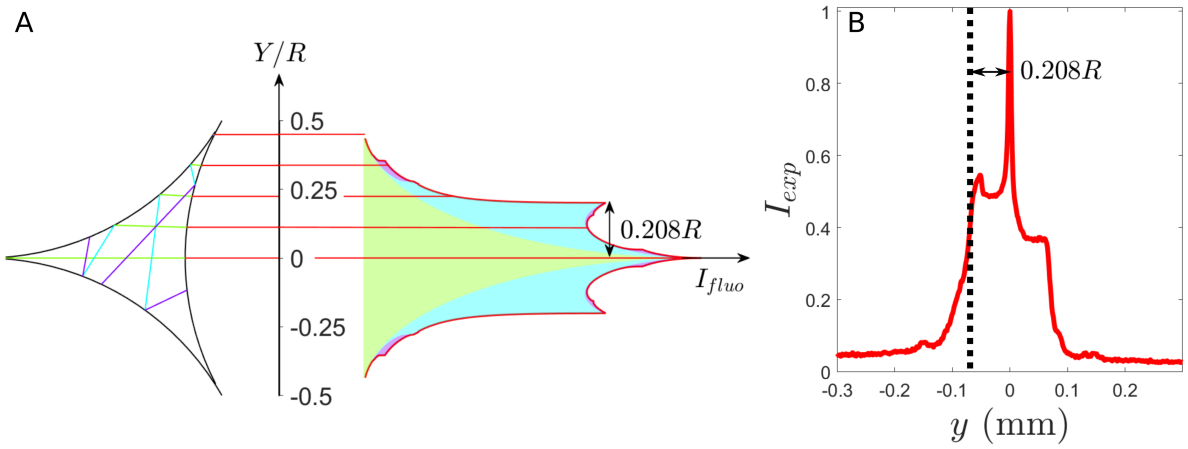

Figure 3.21: Ray tracing simulation for a fluorescent meniscus. **A:** we define an ideal free meniscus composed of three interfaces of curvatures R in contact. The red lines are the outgoing rays seen by the side. On the right, the resulting intensity profile as a function of the ordinate (normalised by R), where the shaded coloured areas are the contributions of the different rays: ray without reflection (green), with one reflection (light blue), or two reflections (purple). **B:** Identification of the intensity drop on experimental data.

The global maximum of $I(y)$ sets the origin of y for the sake of computing R (Fig.3.21B). The intensity drops are then detected on each semi profile at $y_{drop} = 0.208R$ allowing us to measure R. This detection is realised by looking at the lowest absolute values of y where the absolute value of the gradient of intensity $\nabla I = \partial_y I$ exceeds a certain threshold, which sets the

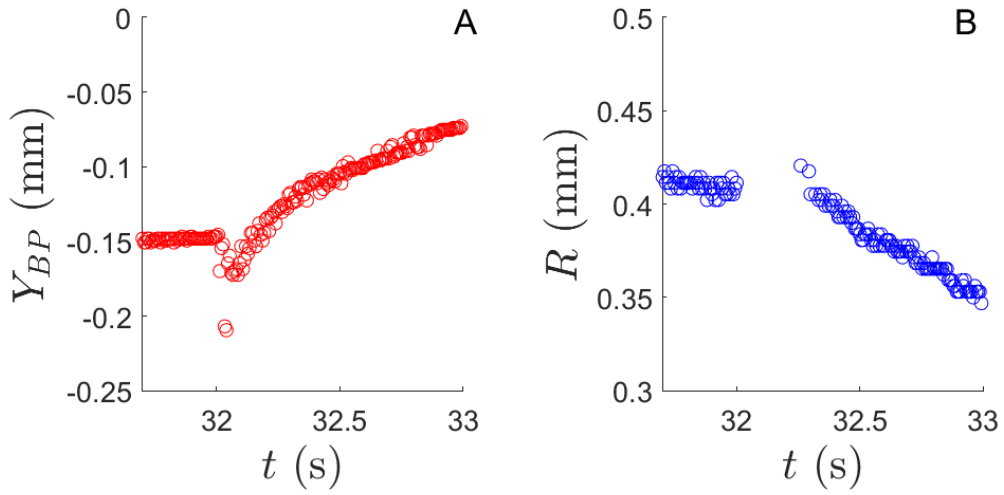

Figure 3.22: Results of the detection via the side camera "BP" for an experiment at $[DOH] = 35\,\mathrm{mg/L}$ and $V_{def} = 50\,\mathrm{mm/s}$. **A:** Ordinate of the free meniscus as a function of time around the time of deformation. $Y_{BP} = 0$ is set at $t_0 = 28\,\mathrm{s}$ the time of preparation. **B:** Radius of curvature of the free meniscus measured over time. During the deformation itself (between $t_1 = 32\,\mathrm{s}$ and $t = 32.1\,\mathrm{s}$), the free meniscus goes too far off focus, leading to the presence of a blind zone in the detection.

edge of the drop in intensity of the semi-profile. From this detection, we extract for each frame two radii of curvature (for the top and bottom semi-profiles) which are very close in practice, and we define for each frame the radius $R(t)$ as the mean between the two. A typical profile is shown in Fig.3.22B. Note that we have a blind zone during the deformation, as the meniscus goes too far off focus (and probably out of our equilibrium assumption for the geometry), hindering the measurement of R.

3.6.3 Tracking the edges of Frankel films in the horizontal film 3

Extracted ingredient:

- $L_{Fr,3}$ **(mm) the length of Frankel film near the free meniscus in film 3.**
- $L_{Fr,3,ext}$ **(mm) the length of film between the edge of the free meniscus and the Frankel film bordering motor 3.**

After the preparation phase at $t_0 = 28\,\mathrm{s}$, two Frankel films are created in the plane of film 3, one at the free meniscus, one at the edge of the motor (see Fig.3.23C). Their respective areas decrease during the main deformation as we compress film 3. Our goal is to track the edges of these films during the main deformation. We will define all the positions we extract with respect to the edge of the free meniscus. The boundaries between the thin/thick pieces of film are material points (*cf.* subsection 0.3.2), they are highly relevant to track the in-plane motions in the x direction.

The exact edge of the free meniscus is hard to find experimentally however, as the meniscus is saturated in fluorescent light, being much thicker than its neighbouring foam films, thus hindering

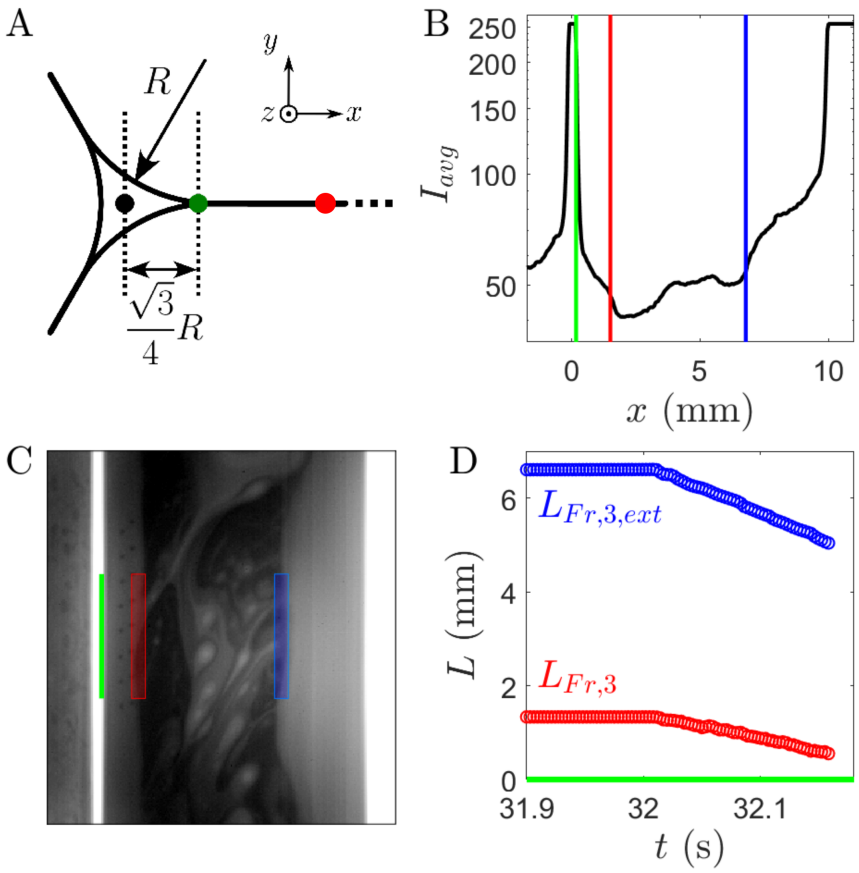

Figure 3.23: **A**: Geometry of the free meniscus of radius of curvature R. The black dot is the centre of the meniscus located in (X_{BP},Y_{BP}), the green one the edge of the flat film, the red one the edge of the Frankel film produced during the preparation step. **B**: Intensity profile of **C** averaged in the z direction taken at $t = 31.9\,\mathrm{s}$. **C**: Film 3 at $t = 31.9\,\mathrm{s}$ (*i.e.* before the deformation) seen from the fluorescent camera PF from the top. The green line is the edge of the free meniscus. The red rectangle is where the correlation mask is chosen to track the Frankel film $L_{Fr,3}$. Similarly the blue rectangle is the correlation mask used to track the edge of the Frankel film bordering the motor to get $L_{Fr,3,ext}$. **D**: Positions of the edges of the Frankel films detected over the deformation. They are defined with respect to the edge of the free meniscus. The example we give is for a solution of concentration $[DOH] = 35\,\mathrm{mg/L}$ whose films are deformed at $V_{def} = 20\,\mathrm{mm/s}$.

a sharp measurement of its edge. To solve this problem, we must rely on the estimation of the curvature radius R (determined in section 3.6.2) to be able to localise the edge. As shown in Fig.3.23A if we consider that the meniscus remains close to its equilibrium geometry, the meniscus edge is located in $X_{BP} + \frac{\sqrt{3}}{4}R$ (green dot in the figure), which we estimate using the radius $R(t_1 = 32\,\mathrm{s})$ found right before the deformation. This $\frac{\sqrt{3}}{4}R$ correction represents up to 10% of the values of $L_{Fr,3}$ shown in Fig.3.23D, and thus is better known than let to the uncertainties. Besides, we see with Fig.3.22B that the meniscus radius R has varied little during the deformation (which is a blind zone for the measurement), thus we choose a single value R

for this correction that is the value at $t_1 = 32\,\mathrm{s}$.

The tracking of $L_{Fr,3}$ is performed by image correlation on successive frames. We initialise the procedure right before the main deformation at $t = 31.9\,\mathrm{s}$ by taking the intensity profile I_{avg} averaged over the z direction, with z in the range delimited by the coloured rectangles shown in Fig.3.23. Note that the lighting increases from left to right in Fig.3.23B, leading to the intensity gradient of fluoresced light, but both Frankel films at both edges have very similar thicknesses as shown later in section 3.6.5. Using the first and second derivatives $\partial_x I_{avg}$ and $\partial_{xx} I_{avg}$, we look where we have simultaneously a negative enough slope (with a well-chosen threshold) and an inflection point on the second derivative. The lowest x position is retained as the initial position of the Frankel film on the free meniscus side and is shown in Fig.3.23B with the vertical red line. Once this initial position is found, a first correlation mask is defined around it by cropping the image with an area shown in red in Fig.3.23C. Each following frame is then compared with this mask, where the maximum of correlation along the x-axis is found and set to be the new position of the edge of Frankel film, allowing us to draw $L_{Fr,3}(t)$. The mask is refreshed every few frames in order to keep an accurate detection.

The detection of $L_{Fr,3,ext}(t)$ by tracking the edge of Frankel film at motor 3 (blue lines and mask in Fig.3.23) is done in a similar fashion. The only difference is the initialisation done by clicking directly on the intensity profile Fig.3.23B while monitoring the frame Fig.3.23C. This is due to a less repeatable initial state: the initial position of this Frankel film can vary by up to a millimetre, and be neighboured by a central film of different thickness heterogeneities pattern.

3.6.4 Tracking the Frankel film in the top left film 1

Extracted ingredient: $L_{Fr,1}$ (mm) the length of Frankel film going out of the free meniscus at the bottom of film 1 as it is stretched during the main deformation.

In this subsection, we detail how we detect the outgoing Frankel film in the stretched film 1 using the TPF camera.

In Fig.3.24A-C we detail the relative position of the camera with respect to the films, and show a typical image obtained as we record. For each frame, we first detect the position of the free meniscus which we set to be the origin of the local axis x_1 as shown in Fig3.24D. This is done by looking at the position of the middle of the rightmost saturated continuum of the cropped frame Fig.3.24C. As the image of motor 3 is also saturated, this works only when both domains are separated (see Fig.3.24C). At longer times, motor 3 becomes too close and only the right edge of the saturated fringe of the meniscus can be distinguished. Thus we keep memory of the semi-length of the free meniscus (which varies very little throughout the experiment), and place the origin of x_1 with respect to the rightmost edge of saturation by retrieving the stored semi-width.

The detection of the edge of the Frankel film located along the free meniscus in film 1 is based on the same principle as the initialisation of the algorithm of the previous subsection 3.6.3.

The detected edge of Frankel film allows us to define $L_{Fr,1}$ as the length between it and the edge of free meniscus, whose position is deduced in the same way as for the previous subsection 3.6.3 by taking into account the length $\frac{\sqrt{3}}{4}R$. We plot an example of result in Fig.3.24E where

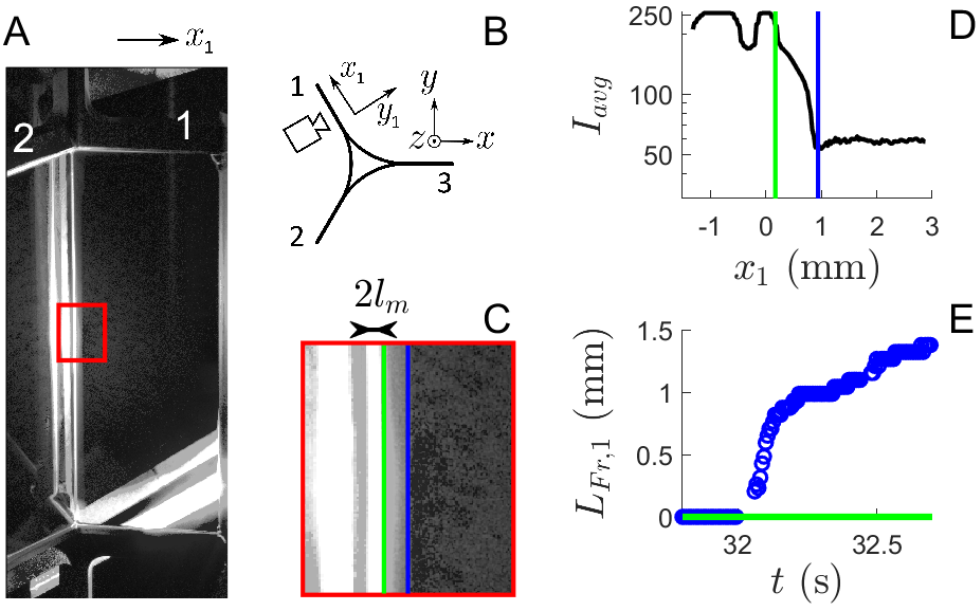

Figure 3.24: Detection process of the outgoing Frankel film in film 1, the example is given for an experiment at $[DOH] = 35\,\mathrm{mg/L}$ and $V_1 = 50\,\mathrm{mm/s}$. **A:** Full frame image of film 1 at $t = 32.1\,\mathrm{s}$ at the end of the main deformation. Film 2 is also visible on the left. **B:** Schematic position of the camera with respect to the elementary foam. **C:** Cropped portion of the frame used to detect the outgoing Frankel film. **D:** Intensity profile I_{avg} obtained by averaging **C** over the z axis. The leftmost saturated fringe is motor 3 entering the field of view at the end of the deformation, the rightmost one whose centre is set at $x_1 = 0$ is the free meniscus. The green line is the edge of the free meniscus, the blue one is the detected position of the edge of outgoing Frankel film. **E:** Detected length of outgoing Frankel film $L_{Fr,1}(t)$ as a function of time. It is defined with respect to the edge of the free meniscus. At the earliest times of deformation the detection is hindered by the saturating brightness of the free meniscus.

$t_1 = 32\,\mathrm{s}$ is the time of deformation. It has to be noted however that at earliest times after $t_1 = 32\,\mathrm{s}$, when the deformation as begun, the edge of Frankel film is not detected as it is too close from the saturated fringe of the free meniscus, hence the presence of a blind zone in Fig.3.24E.

3.6.5 Thickness profiles with hyperspectral cameras

Extracted ingredients:

- $H_1(x_1, t)$ **(µm) the thickness profiles of film 1 before the main deformation (for** $t < t_1 = 32\,\mathrm{s}$**).**
- $H_2(x_2, t)$ **(µm) the thickness profiles of film 2 before the main deformation (for** $t < t_1 = 32\,\mathrm{s}$**).**

- $H_3(x_3, t)$ **(µm) the thickness profiles of film 2 before the main deformation (for** $t < t_1 = 32\,\mathrm{s}$**).**

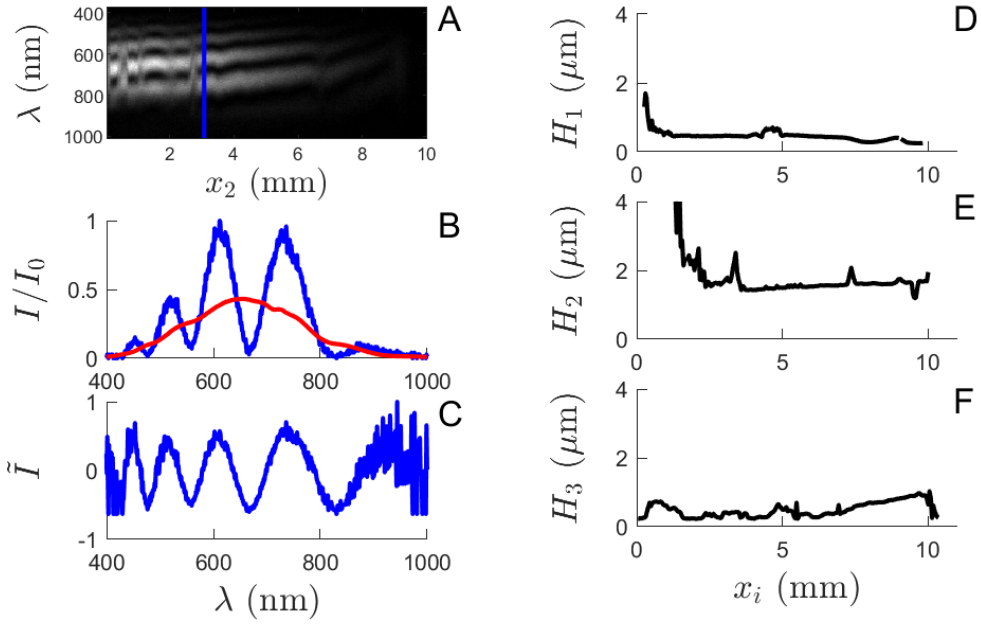

Figure 3.25: Example of thickness profiles measurements on $[DOH] = 35\,\mathrm{mg/L}$ at $t = 31.9\,\mathrm{s}$ just before the deformation. **A:** Spectral image of film 2. x_2 is the local abscissa aligned with the axis of deformation of the film defined so that $x_2 = 0$ is the position of the free meniscus (*cf.* Fig.3.11). The ordinate is the wavelength λ for each value of which we measure the light intensity. **B:** In blue, we show a typical spectrum obtained at a given position $x_2 = 3$ mm located on **A** by the blue line. In red, we show the average light spectrum, obtained by averaging the spectra over time and x_2. **C:** Filtered spectrum extracted from **B** which varies as $cos(\alpha H/\lambda)$ from which we extract the thickness H. **D-E:** Thickness profiles obtained for the 3 different films along their respective local abscissas x_1, x_2 and x_3 (with $x_3 = x$) at $t = 31.9\,\mathrm{s}$ just before the deformation.

We probe the system with our hyperspectral cameras to get the initial distributions of thicknesses of the three different films before deforming them at various velocities. This will allow to monitor the differences of initial states between the films, as gravity drainage occurs before we start deforming the films at $t_1 = 32\,\mathrm{s}$. However, measuring during the deformation was not possible, and motion blur could be a reason.

In order to measure the profiles, we collect the movies of the spectra for the three films, of which an example of frame right before the deformation at $t = 31.9\,\mathrm{s}$ is shown in Fig.3.25A. **The procedure is then similar to what is detailed in chapter 2, subsection 2.3**: The raw intensity profiles I (Fig.3.25B) are processed in order to get the normalised and centred profiles $\tilde{I}$ (Fig.3.25C) from which a thickness $H(y, t)$ is extracted.

Fig.3.25D-F show the typical profiles measured for the three films of the elementary foam at $t = 31.9\,\mathrm{s}$ for the chemistry $[DOH] = 35\,\mathrm{mg/L}$. These are the profiles right before the main

deformation at $t_1 = 32\,\mathrm{s}$, and we see that film 2 (at the bottom) is twice as thick as the other films because of gravity drainage.

3.6.6 Tracking of the photobleached dots

Extracted ingredients:

- $L_{c,1}$ **(mm) the distance between the edge of the free meniscus and the first column of dots.**
- $L_{c,2}$ **(mm) the distance between the edge of the free meniscus and the second column of dots.**
- **(**X_k**,**Z_k**) (mm) with** $k = [\![1, 16]\!]$ **the positions of the photobleached dots**

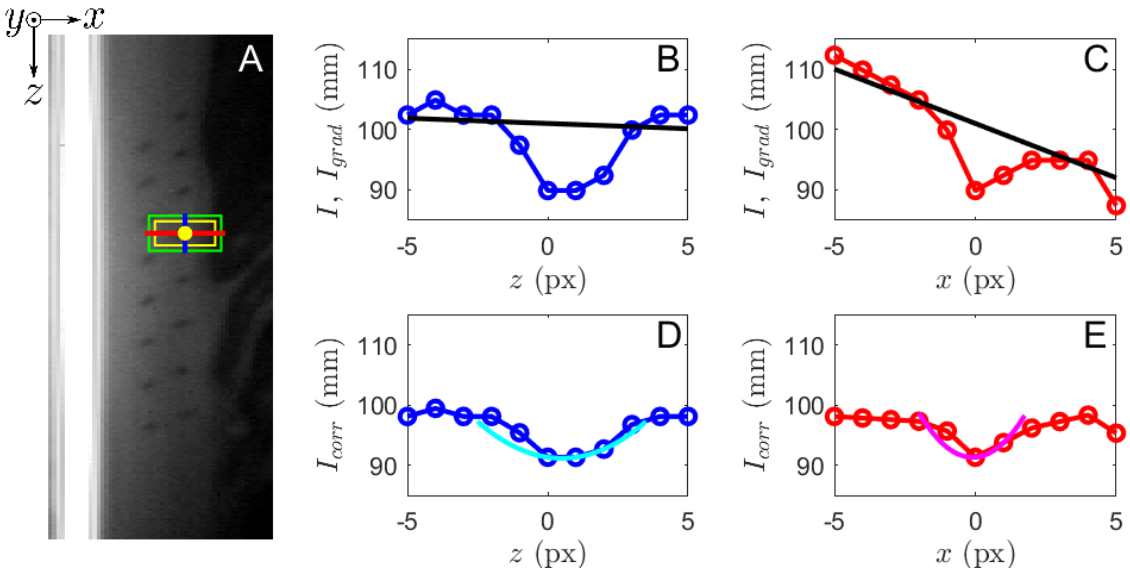

Figure 3.26: Example given on $[DOH] = 35\,\mathrm{mg/L}$ at $t = 31.99\,\mathrm{s}$ just before the deformation. **A:** Zoomed frame of the PF camera in the region where the photobleached dots are created, near the free meniscus, which appears as the vertical saturated fringe. The yellow disk is the position of a dot, the yellow rectangle is the correlation mask chosen around this position, and the green rectangle is the correlation area where the mask will be moved in the next frame to seek the new position of the dot. **B-C:** Intensity profiles I along the x and z axis taken along the lines of matching colours in **A**. The coloured lines are only here as guides for the eye. The black lines are the affine profiles I_{grad} computed using the average profiles over both directions of the correlation area. This correction is especially necessary in the x direction as the free meniscus fluoresces much more than the foam film. **D-E:** Corrected profiles I_{corr} where we suppress the local gradient along the given axis in order to better localise the local minimum of intensity. The apex of the parabolic fits gives a subpixellar estimation of the position.

After the preparation phase at $t_0 = 28\,\mathrm{s}$, which ends at around $t = 31\,\mathrm{s}$, the system is let to relax around one second before the deformation at $t_1 = 32\,\mathrm{s}$. In the mean time, we use our cyan laser to photobleach two rows of dots in the Frankel film bordering the free meniscus in film 3. Once the last dot is shot, we start tracking them individually via the PF camera. They remain aligned in their respective rows as they are pushed towards the free meniscus when the "Push 3" deformation occurs with a very good repeatability. The initial positions at $t = 31.9\,\mathrm{s}$ are roughly determined by clicking all the dots of each first frame of each experiment. The true initial positions are found by looking for the local minimum of intensity in the close vicinity of the clicked pixels.

Once the initial position of a dot is given, we start by defining a correlation mask around it, shown in the form of a yellow square in Fig.3.26A. We then look in the next frame the position where it correlates the most in a wider correlation area defined by the green rectangle in Fig.3.26A. This gives a first estimate of the next position of the dot, however, we need to look around it for the real local minimum of intensity, as even an offset of one pixel would rapidly lead to a misalignment between the centre of the next correlation mask and the centre of the tracked dot.

In order to do so, we look at the intensity profiles $I_{avg,z}(x)$ and $I_{avg,x}(z)$ averaged and computed over the dimensions of our correlation area and we compute their respective gradients. This leads to the definition of a correcting intensity surface, which is a tilted planar surface we retrieve to the original intensity surface. In Fig.3.26B-C two examples of raw intensity profiles $I(x)$ and $I(z)$ are chosen respectively along the blue and red lines of Fig.3.26A. In black, we display the calculated gradients of the average profiles, and in Fig.3.26D-E, we have the corrected profiles along the same lines. Using these last two, we can find the pixel of the local minimum of intensity, which will be defining the next correlation mask.

Eventually, we estimate the position of the local minimum with a subpixellar resolution by fitting the intensity profiles along x and z with two parabolas around the pixel of minimum of intensity. The coordinated found by doing so are stored as the X_k and Z_k positions of dot k for the given time of the frame.

Using these positions, we are be able to evaluate $L_{c,1}$ and $L_{c,2}$ (Fig.3.27) the distance between the edge of the free meniscus and the average position of each column 1 and 2 (containing 8 dots each), with whom we will later try to evaluate the compression of film 3 ϵ_3. The positions of the dots Z_k along z will also allow us to monitor the nullity of the compression ϵ_z along z, which is a key measurement to ensure our invariance by translation along this direction (see section 3.7).

3.7 Monitoring the invariance by translation along z

All the experiments and result we aim to establish have been thought as invariant by translation along the z axis. The main direct consequence of this sought invariance is to allow us to write all compressions happening in the film as uniaxial compressions, meaning any surface compression can be written discarding the z terms:

$$\frac{1}{A}\frac{dA}{dt} = \frac{\partial v_x}{\partial x} \tag{3.38}$$

Where A is an area of a piece of film and v_x the local velocity along the x axis.

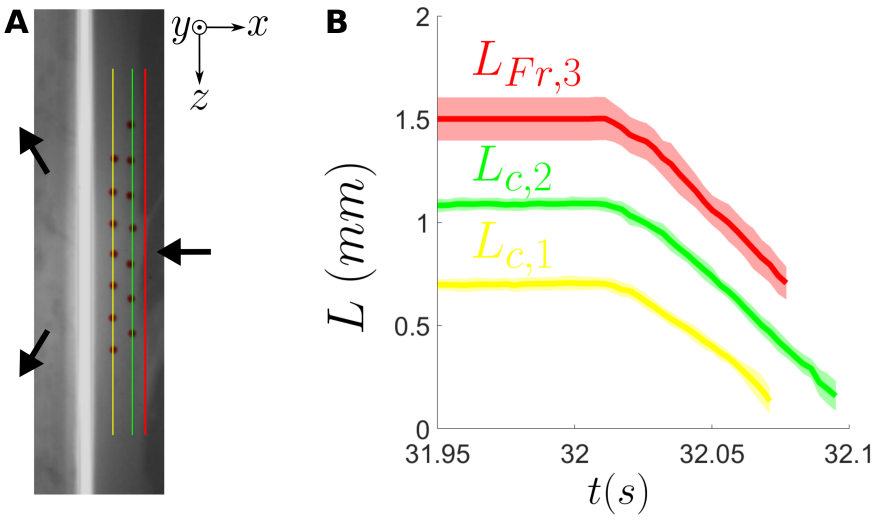

Figure 3.27: Monitoring the positions of the edge of prepared Frankel film and the photobleached columns. **A:** Zoom near the meniscus in film 3. The vertical bright fringe on the middle left is the free meniscus, film 3 is on its right. The red line localises the detected edge of prepared Frankel film, whose distance from the edge of free meniscus is $L_{Fr,3}$, the green and yellow lines localise the two columns of photobleached dots, whose distances from the edge of meniscus are $L_{c,1}$ and $L_{c,2}$. **B:** Time evolution of the distances defined in **A**. The main deformation happens at $t_1 = 32\,\mathrm{s}$, where film 3 is compressed.

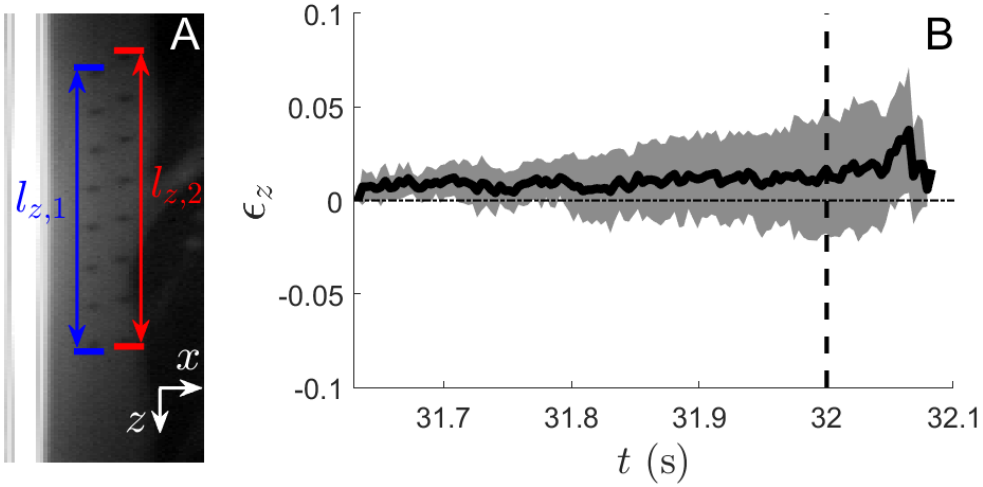

Figure 3.28: Measurement of the compression along the z axis on an example of $[DOH] = 35\,\mathrm{mg/L}$ at $V_1 = 35\,\mathrm{mm/s}$. **A:** We track the lengths $l_{z,1}$ and $l_{z,2}$ defined as the distances between the upper and lower dots of each column throughout the whole experiment. **B:** We define the deformation along z, $\epsilon_z = l_z/l_{z,init} - 1$ and make an average of this quantity over both column and over all the repetitions of the experiments. The error is the standard deviation associated with this average. The vertical black dotted line is the time $t_1 = 32\,\mathrm{s}$ at which the main deformation starts.

The main indicator that it is verified is by monitoring with the photobleached dots that the compression ϵ_z along z is close to zero. This could be defaulted by two main reasons more or less easy to identify.

Two possible causes for a broken invariance

- A local one: the meniscus-flat film junction instability, which tends to create semicircular patches of thin film spontaneously going out of the meniscus (see section 0.3.4 relying on the work of Trégouët *et al.* [66], Gros *et al.* [107]). This one can be easily seen once it is triggered, as the thin semicircles are regularly dispatched along the z axis and hinder thicker film to approach the meniscus.

- A global one: the relaxation of the thick Frankel film we created next to the free meniscus during the preparation. Due to the presence of a line tension between the thick prepared Frankel film and the thin film preexisting the preparation phase of "Push 3"(see section 3.5 for the preparation step, chapter 2 section 2.2 for the line tension), the Frankel film tends to relax at longer times. This can be directly seen far from the centre, where the lighting is poor, making this cause for a broken invariance less obvious and more dangerous.

In both cases, measuring that the field ϵ_z is null is the main indicator that these phenomena do not hinder the measurement.

Control of the invariance

In order to do so, we use our photobleached dots and define the distances l_z between dots aligned along the z axis as illustrated in Fig.3.28A. The deformation along z is thus defined as:

$$\epsilon_z = \frac{l_z}{l_{z,init}} - 1 \tag{3.39}$$

Where $l_{z,init}$ is the initial length taken right at the beginning of the dot tracking, that is after the preparation phase. Thus it does not take into account the pre-deformation applied to film 3 during this phase. However, it shows how little it varies anyway during the main deformation. In Fig.3.28B, we see that ϵ_z remains of the order of a few percents, and does not vary significantly during the main deformation occurring at $t_1 = 32\,\mathrm{s}$. With the given example, the deformation lasts until $t = 31.14\,\mathrm{s}$, but tracking the dots becomes impossible before this time, hence the range of time we display in the figure.

These values are to be compared to the deformation seen on the other axis of the foam film, that is along x, where we anticipate that the deformations $\epsilon_x \gg \epsilon_z$ will be much greater as shown later in subsection 3.8.2. In the following, we will assume this invariance along z to hold, and we will resume discussing its validity later while computing the ϵ_x's. We also extend this hypothesis of invariance to the preparation phase, before we are able to create the dots, which is reasonnable although not measured directly.

3.8 Computing tensions, deformations and elasticites of the films

This section details how we use the processed data from section 3.6 to extract the relevant physical quantities with respect to the model presented in section 3.2.

The first quantity is the ratio of tensions σ_3/σ_1 between the compressed/stretched films. Theoretically, it gives the boundary conditions $s \to \pm\infty$ for region C in terms of surface tensions $\gamma = \sigma/2$. Experimentally, it is extracted by monitoring the angle θ between the films 1 and 2.

The second kind of quantities are the deformations of the films ϵ_1 and ϵ_3. Theoretically, they give access to the quantities L_{out} and L_{in} of interface exchanged between the films, enabling the quantification of the flux j_m. Experimentally, they are first deduced by tracking the lengths of well-identified pieces of film (seen as closed systems).

The third and last quantity is the film elasticity of our elementary foam E_f. It allows us to refine our measurements of the deformations ϵ_1 and ϵ_3, and to have access to the individual absolute tensions σ_1 and σ_3, using their ratio found with the angle measurement. Experimentally, it is found with a linearisation of our quantities around a specific time of the experiment, which is more detailed later.

Note that our data processing contains several redundancies, which we consider of high importance to ensure the robustness and consistency of the analysis. The film elasticity is thus measured *in situ*, and compared to the values obtained in chapter 1.

3.8.1 Relative tensions between the films

As the films are stretched and compressed, their tensions change, leading to a change in the angle between the films as the meniscus at the triple point has to maintain its force balance. This change in angle results in a displacement of the meniscus, which we measure, as shown in section 3.6. In this subsection, we detail how we start from our displacement measurement (X_{BP}, Y_{BP}) to be able to compute a ratio of tensions $\sigma_3/\sigma_{1,2}$ between the stretched film 3 and the compressed films 1 and 2.

Raw data and minor corrections

Let us start with the horizontal displacement X_{BP} as it carries most of the information on the angle between the film, considering the configuration of the "Push 3" deformation. In Fig.3.29, we show a typical graphs $X_{BP} = f(t)$ for various velocities of deformation V_1 at a given chemistry ($[DOH] = 50\,\mathrm{mg/L}$). The uncertainty on the reproducibility is of the order of 0.5%, which is a key indicator that the experimental reproductibility is excellent and the sub-pixellar correlation techniques detailed in subsection 3.6.1 went well.

A zoom in the very early times of deformations at t_0 and t_1 in Fig.3.30 reveals two things:

- A very short delay followed by oscillations, mainly due to the inertia of both the motors and the meniscus.

- An apparent free slip of the free meniscus of the order of $10\,\mu m$ in the frame of the cameras as it starts to move.

The inertial oscillations are small in comparison with the main deformation and the meniscus acceleration will be neglected in the following. The apparent slip is negligible too, but its origin is more puzzling. the existence of this slip is clearly due to an initial repositioning of the films with respect to their meniscii at the motor edges. This slip is suspected to occur also at $t_1 = 32\ s$ in the opposite direction as motor 3 pushes back its film. We choose to correct the horizontal positions and to use $X_{BP,corr}$, where we removed a $+\Delta X_{slip} \sim 30\,\mu m$ jump at $t_0 = 28\,s$, and a $-\Delta X_{slip}$ jump at $t_1 = 32\,s$. This correction is very small in any case. A zoom at $t_0 = 28\,s$ is shown in Fig.3.30 to illustrate this procedure.

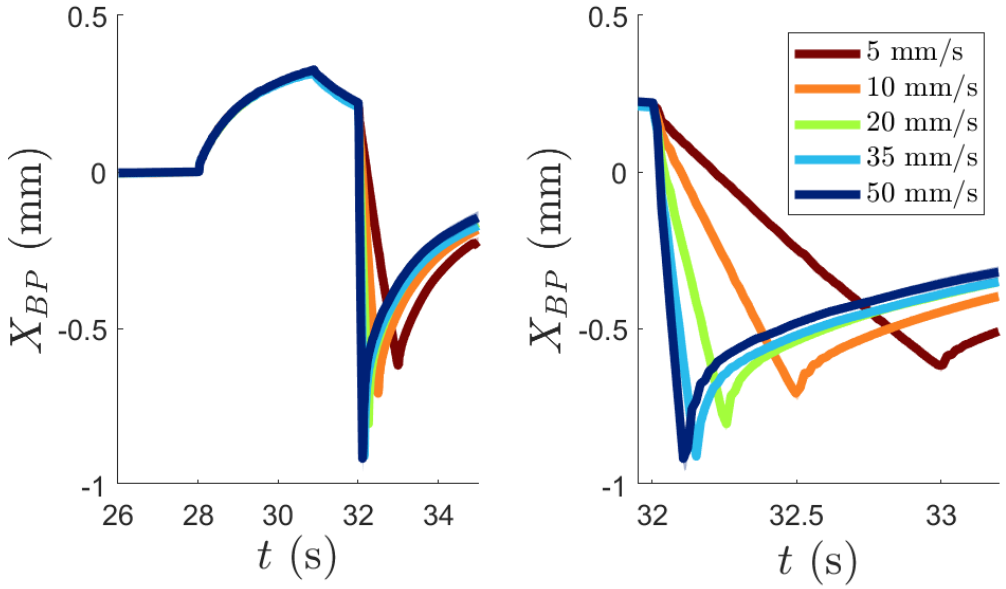

Figure 3.29: Horizontal displacement of the free meniscus throughout the whole "Push 3" experiment, for $[DOH] = 50\,mg/L$ and a varying velocity of main deformation V_1. The figure on the right is just a zoom around $t_1 = 32\,s$ of the figure on the left. At $t_0 = 28\,s$, the horizontal film 3 is prepared, meaning it is being stretched at $V_0 = 2\,mm/s$ from $4.2\,mm$ to $10\,mm$, leading to a first displacement of the free meniscus in $+x$. At $t_1 = 32\,s$, the main deformation of the "Push 3" experiment is performed at V_1 varying between $5 - 50\,mm/s$.

The other component of the displacement of the meniscus, Y_{BP}, which is measured using the BP camera as detailed in subsection 3.6.2. Given the geometry of the "Push 3" deformation, a non-zero vertical displacement represents a breaking of symmetry for the system induced by gravity. In Fig.3.31, we show a typical trajectory for the meniscus throughout the whole experiment, and we make sure that our assumption of a top-down symmetry remains valid as we have $X_{BP} \gg Y_{BP}$. Y_{BP} remains small, and no slipping behaviour as for X_{BP} was observed at our resolution (even though it is one order of magnitude greater than on the x axis, given the configuration of the PF and BP cameras).

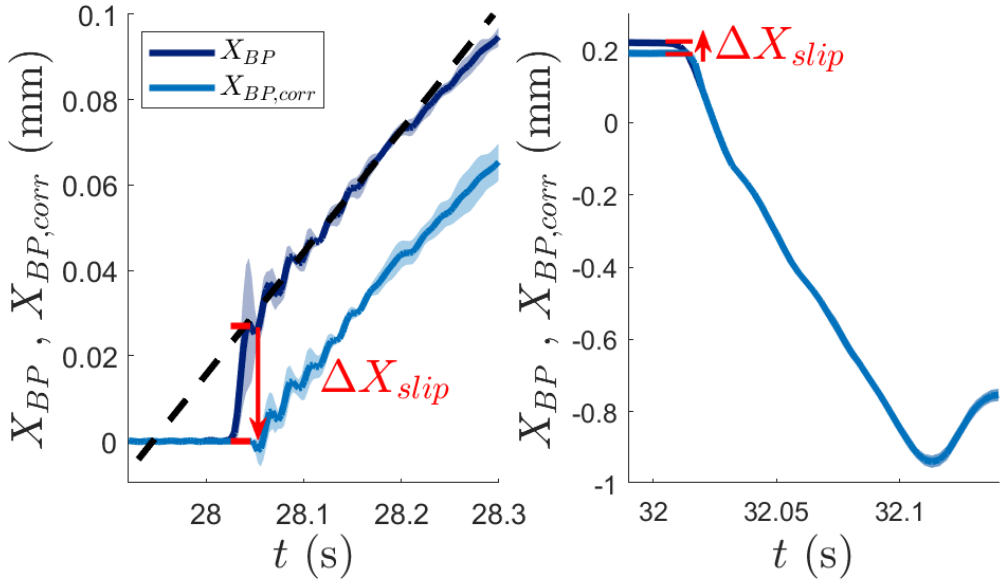

Figure 3.30: Correction because of the apparent free slip. The dark blue data are the uncorrected positions X_{BP}, the light blue data are the corrected $X_{BP,corr}$ taking into account the slips at $t_0 = 28\ s$ and $t_1 = 32\ s$.

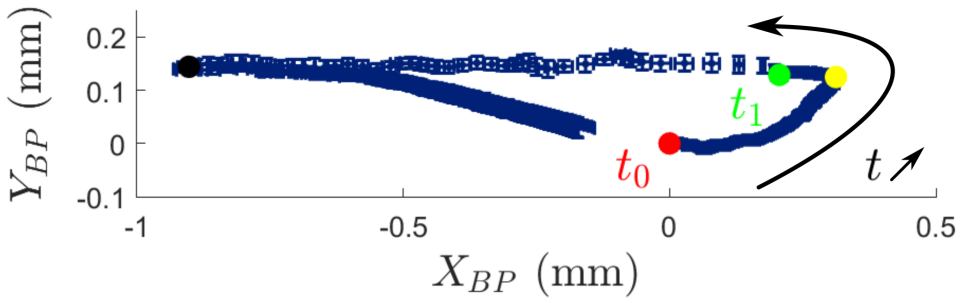

Figure 3.31: Position of the free meniscus in the Oxy plane with scale-matched axis on an example of $[DOH] = 50\,\text{mg/L}$ at $V_1 = 35\,\text{mm/s}$. The red dot is the beginning of the preparation step $t_0 = 28\,\text{s}$ which defines equilibrium position of the meniscus. The yellow dot is the end of the preparation phase at $t = 30.9\,\text{s}$. The green dot is the deformation time $t_1 = 32\,\text{s}$ at which the main deformation occurs. The black dot is the end of the main deformation, which is $t = 32.14\,\text{s}$ in this specific case of $V_1 = 35\,\text{mm/s}$.

Computing the tension ratio

Now that we have the corrected positions $(X_{BP}(t), Y_{BP}(t))$, we can compute the angle θ between the vertical films 1 and 2. Knowing at all times the lengths $L_{m,1}(t)$ and $L_{m,2}(t)$ imposed between the edges of the motors and the centre of the deformable frame, we can measure the vectors $\boldsymbol{L}_1(t)$ and $\boldsymbol{L}_2(t)$ linking the centre of the meniscus to the edges of the motors (**see Fig.3.32 for**

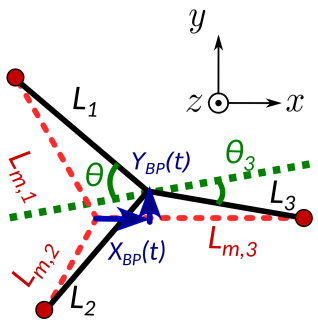

Figure 3.32: Definitions of the different lengths in the system, illustrated for an arbitrary deformation. This is a reminder of Fig.3.11B.

angles and lengths notations):

$$\boldsymbol{L}_1 = X_1\boldsymbol{e}_x + Y_1\boldsymbol{e}_y = \Big(- L_{m,1}\ cos(\theta_0) - X_{BP}\Big)\boldsymbol{e}_x + \Big(L_{m,1}\ sin(\theta_0) - Y_{BP}\Big)\boldsymbol{e}_y \tag{3.40}$$

$$\boldsymbol{L}_2 = X_2\boldsymbol{e}_x + Y_2\boldsymbol{e}_y = \Big(- L_{m,2}\ cos(\theta_0) - X_{BP}\Big)\boldsymbol{e}_x + \Big(- L_{m,2}\ sin(\theta_0) - Y_{BP}\Big)\boldsymbol{e}_y \tag{3.41}$$

With $\theta_0 = 60^o$ being the rest semi-angle between the films. The angle θ we seek is given through the scalar product of these two vectors, and we have:

$$\theta = \frac{1}{2}\mathrm{Arccos}\Big(\frac{\boldsymbol{L}_1.\boldsymbol{L}_2}{L_1 L_2}\Big) \tag{3.42}$$

Typical measurements of θ are shown in Fig.3.33 Left for various velocities at a given chemistry ($[DOH] = 50\,\mathrm{mg/L}$).

Eventually, we are able to compute a ratio between the tensions σ_i of the films. In the general case, without the assumption of a top/down symmetry (because of the vertical displacement), the angle θ we defined is the semi-angle between film 1 and 2 and the angle θ_3 is the angle of film 3 with the bisector line of film 1 and 2 as shown in Fig.3.32. A projection along the bisector line of $\boldsymbol{L}_1$ and $\boldsymbol{L}_2$ of the forces acting on the meniscus yields the balance:

$$\sigma_3 \cos\theta_3 = (\sigma_1 + \sigma_2)\cos\theta \tag{3.43}$$

Estimating the small angle θ_3, we reach at max: $\theta_{3,max} = \mathrm{Arcsin}(\frac{Y_{BP}}{L_3}) + \frac{X_1 Y_{BP}}{Y_1^2} \sim 4^o$ whose cosine remains very close to 1 with a 0.5% error, and so we write:

$$\sigma_3 = 2\bar{\sigma}\cos\theta \tag{3.44}$$

With $\bar{\sigma} = \frac{\sigma_1+\sigma_2}{2}$ the average of the tensions between the films 1 and 2. As we cannot work with both σ_1 and σ_2, and because the vertical displacement Y_{BP} remains small compared to X_{BP}, **we will assume in the following** $\sigma_1 = \bar{\sigma}$. This choice is consistent with the assumption of top/down symmetry made on some other parameters which are obtained only on film 1 but not on film 2. Under these assumptions, the ratio between the tension of the compressed film 3 and the tension of the stretched films 1 and 2 is simply given by:

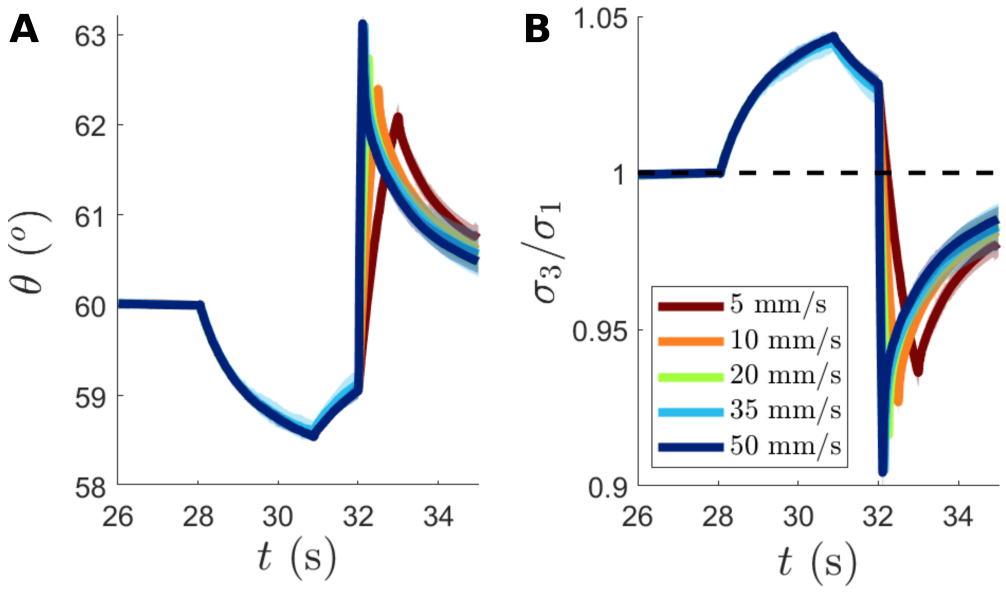

Figure 3.33: Example for $[DOH] = 50\,\mathrm{mg/L}$ and a varying velocity of main deformation V_1. **A:** Semiangle θ between film 1 and 2. At the initial state $t_0 = 28\,\mathrm{s}$, right before the preparation, the angle meets the Plateau's law. Its deviation from this law arise because of a difference of the tension between film 1 (or 2), and film 3. **B:** Tension ratio between film 3 and 1 (or 2 equivalently) deduced from the angle measurement.

$$\frac{\sigma_3}{\sigma_1} = 2\cos\theta \tag{3.45}$$

Using this relation, we compute the ratios in Fig.3.33 Right from the set shown on its Left.

3.8.2 Deformation of film 3 ϵ_3 and film 1 ϵ_1

To further describe our system, we now want to look at the states of deformation of our films ϵ_i. In fact, the elastic response of a single foam film due to insoluble surfactants can be captured with the expression used in chapter 1 (eq.1.17):

$$\sigma = \sigma_0 + E_f \frac{\epsilon}{1+\epsilon} \tag{3.46}$$

Thus, measuring the deformations ϵ_1 and ϵ_3 of film 1 and 3 and using the tension ratio σ_3/σ_1, we will be able to determine the elasticity E_f of our films.

Determination of ϵ_3

We start by computing the deformation ϵ_3 of the horizontal film 3. Before the preparation step at $t_0 = 28\,\mathrm{s}$, film 3 is at rest with a repose length $L_{i,3}$. As it is stretched during the preparation phase, two thicker new films are created in the plane of film 3 with a clear contrast with the preexisting film. The result can be seen in Fig.3.23C. During this preparation phase, film 3 has

been only accepting interface (either from the menisci or the other films) so that all the matter initially present before the preparation remained in the film. The initial film, between the two Frankel films, is thus a closed system that can be used to determine ϵ_3.

The total deformation ϵ_3 of film 3 is *a priori* defined as the sum of the deformation along both axis x and z of its plane: $\epsilon_3 = \epsilon_{3,x} + \epsilon_{3,z}$. The second term $\epsilon_{3,z}$ can be discarded thanks to the invariance by translation along z which we discussed and verified in section 3.7.

Thus, we only need to compute the first term $\epsilon_{3,x}$. By tracking the edges of Frankel films in film 3, as illustrated in Fig.3.23, we deduce the length $L_{c,3} = L_{Fr,ext,3} - L_{Fr,3}$ of the closed system along x. Knowing that it was equal to the length imposed to film 3 before the preparation $L_{i,3} = 4.2\,\mathrm{mm}$, we have a direct experimental access to $\epsilon_{3,x}$ and ϵ_3:

$$\epsilon_3(t) = \epsilon_{3,x}(t) = \frac{L_{c,3}(t)}{L_{i,3}} - 1 \tag{3.47}$$

This quantity is defined as long as we are able to track the edges of both Frankel films. This lasts up till the Frankel film next to the free meniscus completely disappears in it, or until the thin film instability occurs at the edge of the free meniscus as discussed in section 3.7.

A result of the calculation of ϵ_3 is shown in Fig.3.34 (red curve), where we see that film 3 starts from a stretched state due to the preparation phase, and is being compressed as we push on it during the main deformation at $t_1 = 32\,\mathrm{s}$.

A unique value for the film elasticity E_f?

The full determination of the absolute tensions and deformations relies on the assumption that the film elasticity E_f is the same for the three films.

This hypothesis of unique E_f is not straightforward as the elasticity of a single film depends on its thickness which varies from one film to another due to the gravity drainage for instance. However, by looking at the initial state of our system using the spectral cameras, we see in Fig.3.25D-F that right before the main deformation at $t_1 = 32\,\mathrm{s}$, the three films have a factor 2 to 4 of difference in thickness. As discussed in Chapter 1 and in Poryles *et al.* [6], the thinner a foam film, the stiffer it is. This dependency is very slow however, as a factor 4 on the thickness leads to a 15% change in stiffness only.

A direct experimental evidence that the three elasticities are very close in our case is that the angle θ_3 (see Fig.3.32) remains very small compared to θ. An even faster way to control this symmetry between the films is to see in Fig.3.31 that the displacement along y of the meniscus is small compared to the displacement along x.

Thus, we will assume that E_f is the same for the three films and that the relationship between the tension and the deformation of each film is the same and given by eq.3.46.

A first determination $\epsilon_{1,a}$ of ϵ_1

In order to compute ϵ_1, we define a closed system that is the piece of film present in the plane of film 1 when the main deformation starts at $t_1 = 32\,\mathrm{s}$. At later times, its length along the local abscissa x_1 is denoted $L_{1,close}(t)$ and can be written as:

$$L_{1,close}(t) = L_1(t) - 2L_{Fr,1}(t) \tag{3.48}$$

Which is the distance between motor 1 and the free meniscus to which we retrieve the length of Frankel film going out of the edges. The factor 2 in front of $L_{Fr,1}$ is there to take into account the Frankel film going out of the supported meniscus of motor 1, which is assumed to be equal to the Frankel film going out of the free meniscus.

Important remark: **Assuming that the Frankel film at the motor is equal to the Frankel film at the free meniscus is a crude proxy. As we aim at avoiding such hypotheses, ϵ_1 will be re-estimated later on, using only the film elasticity E_f we are about to compute in a time range where $L_{Fr,1}$ is negligible.**

Its reference length $L_{1,close,0}$, *i.e.* the length it would have at the reference tension is unknown, as film 1 is *a priori* pre-stretched during the preparatory phase. This is not obvious, but stretching film 3 alone at $t_0 = 28\,\mathrm{s}$ (*cf.* Fig.3.17) means stretching the top and bottom interfaces of the elementary foam, the former being shared with film 1. The deformation ϵ_1 is thus defined as:

$$\epsilon_1(t) = \epsilon_{1,x_1}(t) = \frac{L_{1,close}(t)}{L_{1,close,0}} - 1 \tag{3.49}$$

The quantity that remains to be found is $L_{1,close,0}$. In order to estimate it, we can see in Fig3.33B that at some crossing time during the deformation $t_c > t_1 = 32\,\mathrm{s}$, the tension ratio is $\sigma_3/\sigma_1 = 1$, meaning that the tension σ_1 of film 1 is the same as the tension σ_3 of film 3, of which we know the deformation ϵ_3 at all times. Knowing with eq.3.46 that we also have $\epsilon_1(t_c) = \epsilon_3(t_c)$ we can write:

$$L_{1,close,0} = \frac{L_1(t_c) - 2L_{Fr,1}(t_c)}{1 + \epsilon_3(t_c)} \simeq \frac{L_1(t_c)}{1 + \epsilon_3(t_c)} \tag{3.50}$$

Where at this particular time t_c which is always at the very beginning of the deformation, the term $L_{Fr,1}(t_c) \ll L_1(t_c)$ can be discarded as the Frankel films are barely out of their menisci. Eventually, we have the expression:

$$\epsilon_{1,a}(t) = \Big(1 + \epsilon_3(t_c)\Big)\frac{L_1(t) - 2L_{Fr,1}(t)}{L_1(t_c)} - 1 \tag{3.51}$$

This first estimation $\epsilon_{1,a}$ is also shown in Fig.3.34 (light blue). The time at which it crosses the red curve ϵ_3 is t_c the crossing time indicated with a short pointed line. It is important to note that at some time during the deformation, indicated by the tall vertical dashed lines in Fig.3.34, we start detecting $L_{Fr,1}$, leading to a sudden drop in the value of $\epsilon_{1,a}$ as we take $L_{Fr,1} = 0$ before that time.

With these deformations $\epsilon_{1,a}$ and ϵ_3 and with the ratio of the tensions σ_3/σ_1, we now have all we need to compute E_f the elastic modulus of our films.

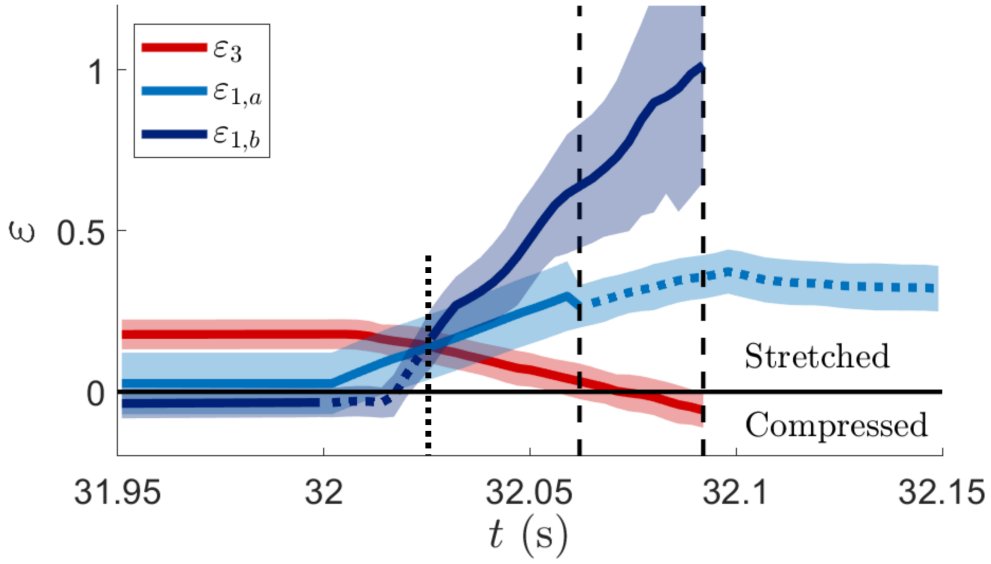

Figure 3.34: Example given on $[DOH] = 35\,\mathrm{mg/L}$ and $V_1 = 50\,\mathrm{mm/s}$. Red is the deformation ϵ_3 of film 3, Light Blue the first estimation of the deformation $\epsilon_{1,a}$ of film 1 and Dark Blue the corrected deformation $\epsilon_{1,b}$ of film 1. The leftmost dotted line is t_c the crossing time. The dashed lines encompass the time at which we simultaneously measure the ingoing and outgoing films.

3.8.3 Determination of the film elasticity E_f

To estimate the film elasticity E_f, we linearize all our quantities around t_c, defining a new time scale $\hat{t} = t - t_c$:

$$\begin{cases} \epsilon_{1,a}(\hat{t}) & = \epsilon_0 + \lambda_1 \hat{t} \\ \epsilon_3(\hat{t}) & = \epsilon_0 + \lambda_3 \hat{t} \\ \frac{\sigma_3}{\sigma_1}(\hat{t}) & = 2\cos\theta = C + \lambda_\theta \hat{t} \end{cases} \tag{3.52}$$

In the vicinity of this crossing time $\hat{t} = 0$, which is located in Fig.3.34 where all curves intersect with an ordinate ϵ_0, we consider that we have $\epsilon_{1,a},\ \epsilon_3 \ll 1$. Thus, we linearize eq.3.46 and get:

$$\frac{\sigma_3}{\sigma_1}(\hat{t}) = \frac{\sigma_0 + E_f\ \epsilon_0 + E_f\ \lambda_3 \hat{t}}{\sigma_0 + E_f\ \epsilon_0 + E_f\ \lambda_1 \hat{t}} \tag{3.53}$$

And a development at first order in $\hat{t}$ leads to the expression:

$$E_f \simeq \frac{\sigma_0 \lambda_\theta}{\lambda_3 - \lambda_1} \tag{3.54}$$

In which all quantities can be estimated. The equilibrium tension σ_0 depends on the chemistry only and is already characterised in Chapter 1 with a pendant drop method. The slopes λ_1, λ_3 and λ_θ are found with a linear regression for $\hat{t}$ comprised between $\hat{t} = 0$ the crossing time and

the detection time of the Frankel film for film 1 (leftmost vertical dotted line in Fig.3.34). We compute the elasticities E_f for all chemistries and velocities of deformation V_1 and plot them in Fig.3.35.

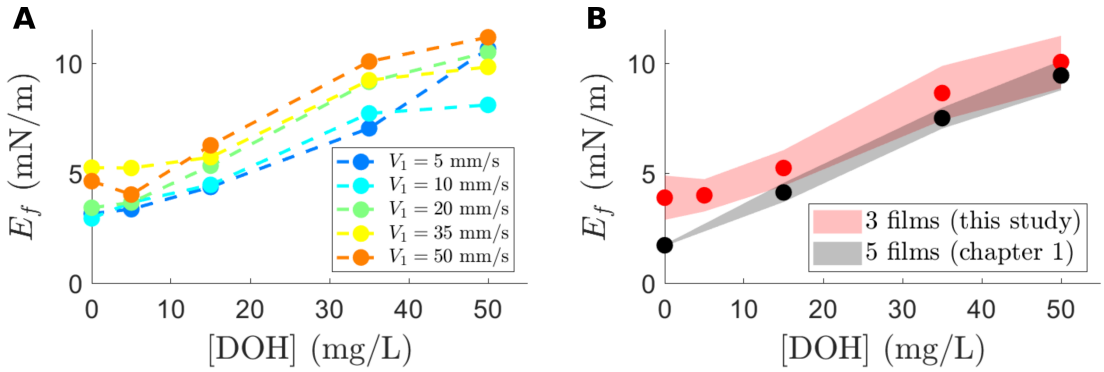

Figure 3.35: **A:** Measured film elasticity as a function of the dodecanol concentration of the solution for different velocities of deformation. **B:** Red is graph **A** averaged over all velocities, and we compare it to the Black, the elasticities measured with the setup of chapter 1 (*cf.* [6])

As we can see in Fig.3.35A, our measures seem to depend on V_1 with the trend "the faster, the stiffer". At first glance, we could think that this is coherent with the fact that the faster the interfaces are deformed, the lower is the time given to bulk-interface exchanges, which would tend to compensate for the gain/loss of surface concentration of surfactants, lowering the change in surface tension and thus lowering the apparent elasticity of the interfaces. This reasoning would be valid if the interfaces were in contact with an infinitely thick bulk phase, however as seen in Chapter 1, the elasticity we observe is expected to be caused by the finite amount of dodecanol present in the bulk. Besides, the interface is supposed to be at equilibrium with the bulk at all times given the very short times of diffusion through the foam films for a common surfactant such as SDS or dodecanol $\tau_{eq} \sim L^2/D \sim 1\,\mathrm{ms}$. This is much smaller than the smaller time of deformation $\tau_{def} \sim 100\,\mathrm{ms}$, thus ruling out unsteady populations of classical surfactants as an explanation for varying elasticity.

The explanation for this dependency is actually unclear, and could originate from very insoluble and large impurities present in the air which would take an infinite time to diffuse through the bulk.

We see that with the same chemistries and the same range of film thicknesses, we recover values for E_f which are very close to what was measured in previous works (see Poryles *et al.* [6] and Fig.3.35B). In the following, we take our measurements averaged over the velocities as our reference elasticities E_f depending only on the chemistry.

Also, this elasticity measurement allows us to get the absolute tensions σ. We first compute σ_3, as the measurement of ϵ_3 is the most reliable of all deformations. This writes:

$$\sigma_3 = \sigma_0 + E_f \frac{\epsilon_3}{1+\epsilon_3} \tag{3.55}$$

Getting σ_1 can be performed by then using the ratio $\sigma_3/\sigma_1 = 2\cos\theta$, which is our reliable force measurement shown in Fig.3.33. **This will be useful in the form of re-measuring a**

corrected $\epsilon_{1,b}$ knowing σ_1 and E_f precisely.

3.8.4 A second estimation of the deformation $\epsilon_{1,b}$

We see that now we have computed σ_3 we just defined a path to compute the absolute tension σ_1 without relying on the estimation of a deformation factor ϵ_1 for the vertical films. In fact, the first estimation $\epsilon_{1,a}$ at large times (dashed lines in Fig.3.34) depends on two things:

- Our capability to measure as early as possible the Frankel film $L_{Fr,1}$ going out of the free meniscus as film 1 is stretched.
- A strong assumption that the Frankel film going out on the side of motor 1 is the same in length as the one we measure at the free meniscus.

Thus, we can now try to work the opposite way to avoid making these assumptions: using σ_3 and the ratio $\sigma_3/\sigma_1 = 2\cos\theta$ which is known with a high precision, we can deduce the absolute tension σ_1. With σ_1, we can now deduce another estimation $\epsilon_{1,b}$ using the equation:

$$\epsilon_{1,b} = \frac{\sigma_1 - \sigma_0}{E_f - (\sigma_1 - \sigma_0)} \tag{3.56}$$

Whose computation is shown in Fig.3.34 (dark blue). Note that the earlier points, before the crossing time, are shown with a dotted line as this is where the reliability of our angle measurement is the weakest because of the slip described and discussed at the beginning of section 3.8.1. Between the crossing time and the time of detection of the Frankel films in film 1, both estimations are expected to be reliable, and we indeed see that they remain quite close. These two estimations differ however, and the conclusions we make on the interface transfer properties remains the same using either one estimation of ϵ_1 or the other.

The points in which we are the most interested in are between the two black vertical dotted lines: after the time at which we start measuring some Frankel film going out of the free meniscus in film 1, and before the end of tracking of the edge of Frankel film at the free meniscus in film 3. **In this range, $\epsilon_{1,b}$ is the most reliable estimation of ϵ_1.**

3.9 Results: Surfactant balance and the fate of j_m

3.9.1 Computing L_{in} and L_{out}

Now that we have carefully computed the deformations of the films ϵ_1 and ϵ_3, and that we have given ourselves the lengths of film $L_{Fr,1}$ and $L_{Fr,3}$ involved in the interface balance, it is time to compute the proper balance between L_{out} and L_{in} as promised in subsection 3.3.

Computing the outgoing quantity of interface $L_{out}(t)$

The length of outgoing interface $\hat{L}_{out}(t)$ is directly given by the length of Frankel film detected near the free meniscus in film 1: $\hat{L}_{out} = L_{Fr,1}$ (*cf.* subsection 3.6.4).

Computing the length of interface at rest L_{out} also requires to know the extension state ϵ_1 of the film:

$$L_{out}(t) = \frac{\hat{L}_{out}}{1+\epsilon_1} = \frac{L_{Fr,1}(t)}{1+\epsilon_1(t)} \tag{3.57}$$

In section 3.8, we estimate ϵ_1 twice: $\epsilon_{1,a}$ is computed with eq.3.51 using the tension ratio between the films and the length of Frankel film $L_{Fr,1}$, whereas $\epsilon_{1,b}$ is computed with eq.3.56 using the absolute tension of film 1 once the film elasticity is computed. Both quantities are represented with an example in Fig.3.34, and we see that these two measurements may differ by up to a factor 2. They make different hypotheses, detailed above, and although $\epsilon_{1,b}$ seems to have the most parsimonious set of assumptions, we keep both of them and will compute $L_{out,a,b}$ twice as well.

Computing the ingoing quantity of interface $L_{in}(t)$

It is not directly possible to compute $\hat{L}_{in}$, as we track a film which is simultaneously compressed and evacuated from film 3 out of the sight of the camera. To circumvent the problem, we compute the difference of lengths of interface at rest. To do so, we use the prepared Frankel film of length $L_{Fr,3}(t)$ (*cf.* subsection 3.6.3), and knowing the state of compression $\epsilon_3(t)$ of film 3 (*cf.* subsection 3.8.2) we write:

$$L_{in}(t) = \frac{\hat{L}_{in}}{1+\epsilon_3} = \frac{L_{Fr,3}(t_1)}{1+\epsilon_3(t_1)} - \frac{L_{Fr,3}(t)}{1+\epsilon_3(t)} \tag{3.58}$$

The underlying assumption of this method is to consider that the thick prepared Frankel film $L_{Fr,3}$ has the same state of compression as the thin central film $L_{c,3}$ preexisting the preparation from which ϵ_3 is computed through 3.47.

This uniformity of compression state ϵ_3 between the two kinds of film is not obvious but well-founded. As discussed in subsection 0.2.4, tension is uniform in the plane of a foam film, whatever the thickness of the different patches. With eq.3.46, we see that the condition of uniform ϵ_3 is that both kinds of film have the same film elasticity E_f. This latter depends on the film thickness!

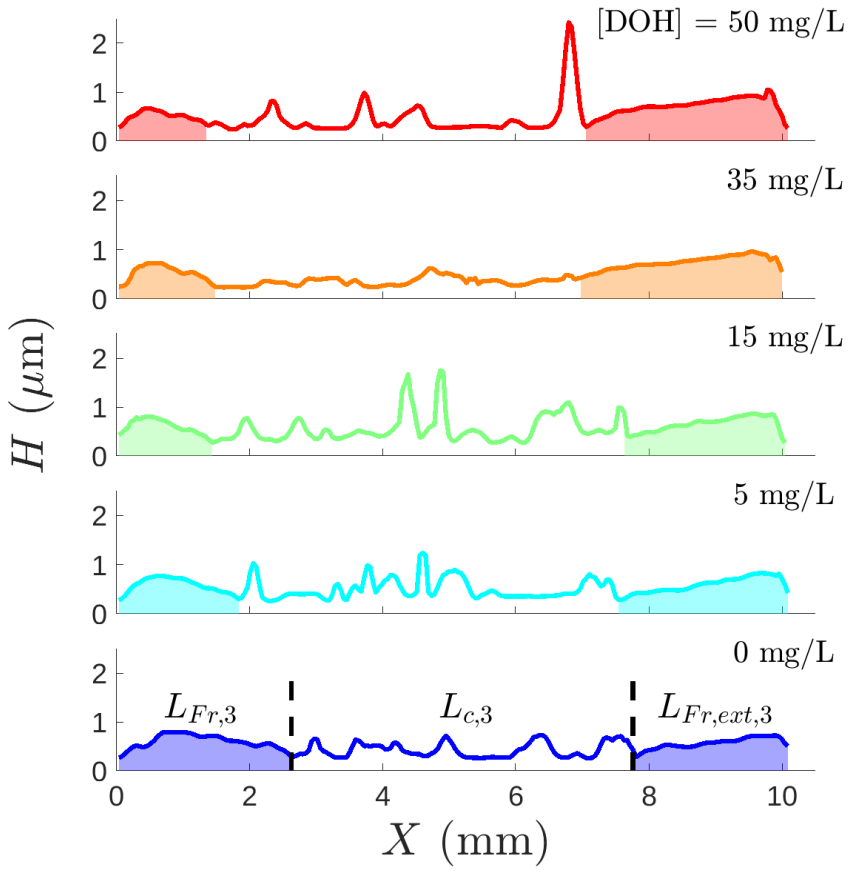

Figure 3.36: Thickness profiles of prepared film 3 right before the main deformation at $t_1 = 32\,\mathrm{s}$ using the hyperspectral cameras SP1 and SP2. The shaded areas are the Frankel films extracted during the preparation phase. $x = 0$ is the free meniscus, $x = 10\,\mathrm{mm}$ is the edge of motor 3.

However, as seen in Fig.1.3B of subsection 1.2.1, elasticity is a slowly varying function of thickness. In the present case, typical thickness profiles right before t_1 the deformation time are shown in Fig.3.36 for all chemistries. We identify the thick Frankel films $L_{Fr,3}$ and $L_{Fr,3,ext}$ with respectively the left and right coloured shaded areas.

We see that the central film is thinner on average by less than a factor $1/2$, which corresponds to a difference of elasticities E_f of less than 10%. This means that at maximum, we make an error of 10% on the estimation of the ϵ_3 for the ingoing Frankel film $L_{Fr,3}$. This remains within our errorbars for the estimation of L_{in}, as this relative error is mitigated by the fact that L_{in} depends on $1 + \epsilon_3$, hence our assumption.

Results

In Fig.3.37, we show all the computable L_{in} and $L_{out,b}$: we managed to get them for the range $[DOH] = 15, 35, 50\,\mathrm{mg/L}$ in chemistry, and $V_1 = 10, 20, 35$ and $50\,\mathrm{mm/s}$ for the velocity of deformation.

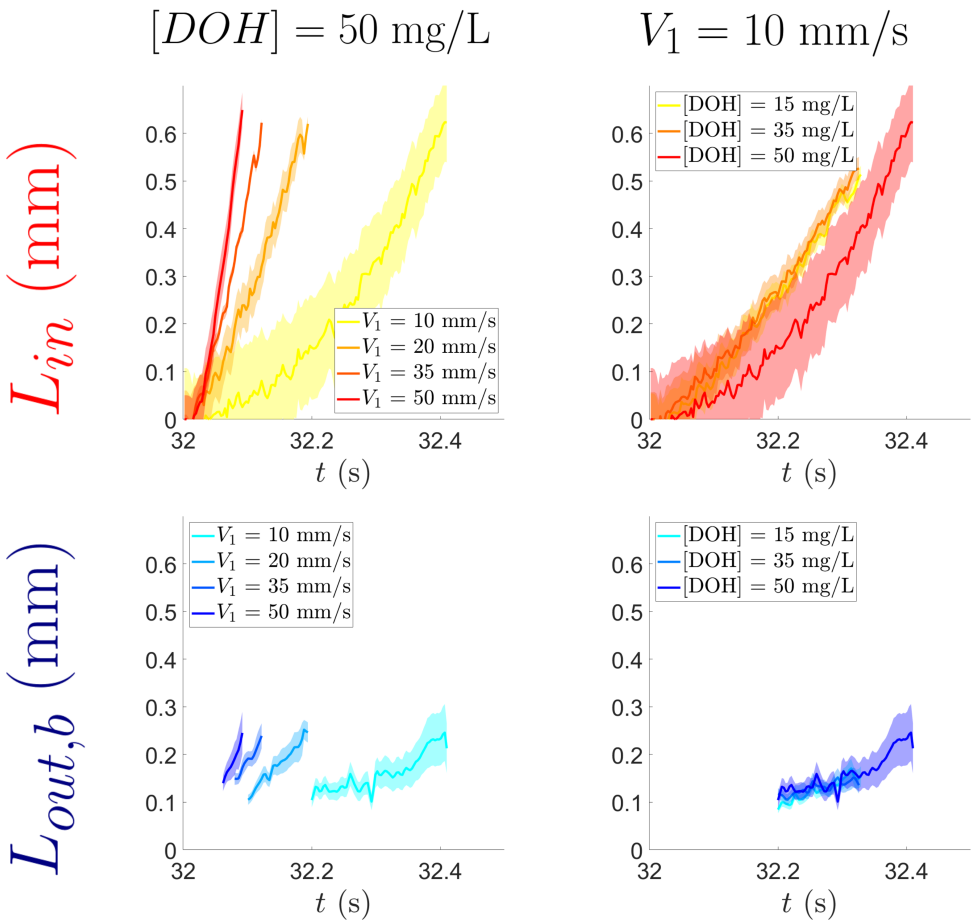

Figure 3.37: All exchanged lengths $L_{in}(t)$ and $L_{out,b}(t)$ in the ranges of chemistry $[DOH] = 15, 35, 50\,\mathrm{mg/L}$ and of velocities of deformation $V_1 = 10, 20, 35$ and $50\,\mathrm{mm/s}$.

Now we have ways to compute $L_{in}(t)$ and $L_{out}(t)$, and we show a typical result in Fig.3.38 which contains the averaged curves for $V_1 = 50\,\mathrm{mm/s}$ and $[DOH] = 50\,\mathrm{mg/L}$. At this velocity, the deformation takes place between $t_1 = 32\,\mathrm{s}$ and $t = 32.1\,\mathrm{s}$.

Our goal is now to compare simultaneously $L_{in}(t)$ and $L_{out}(t)$ over the same time range, which is shown with the shaded orange area. Before this time range, we are limited by the fact that we start detecting the outgoing film $L_{Fr,1}$ during the deformation and L_{out} cannot be defined. The end of this time range is set by the end of the detection of the ingoing Frankel film $L_{Fr,3}$, hindering the measurement of L_{in} as well as the estimation of the corrected deformation ϵ_1, and thus of $L_{out,b}$.

3.9.2 Vanishing flux j_m

In Fig.3.39 we show the two quantities $L_{out} = f(L_{in})$ plot against each other, for the two computations $L_{out,a}$ (Fig.3.39**A**) and $L_{out,b}$ (Fig.3.39**B**). **These constitute the main result of this manuscript.**

The yellow area corresponds to the expected range for the interface balance. We recall that

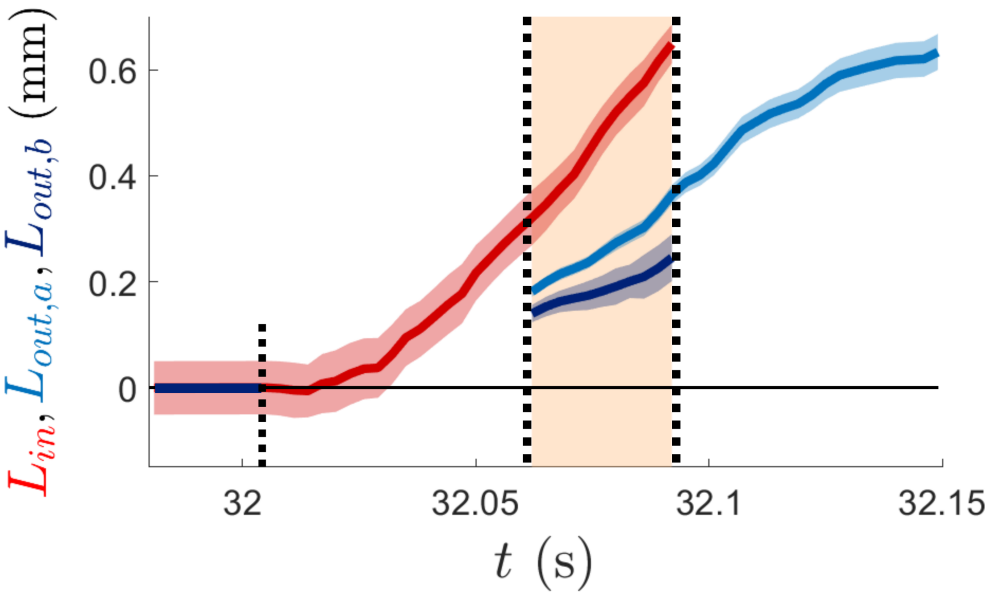

Figure 3.38: Typical graph of interface lengths obtained for $[DOH] = 50\,\mathrm{mg/L}$ and a velocity of main deformation $V_1 = 50\,\mathrm{mm/s}$. L_{in} is computed from ϵ_3, $L_{out,a}$ from $\epsilon_{1,a}$ and $L_{out,b}$ from $\epsilon_{1,b}$. The shaded area corresponds to the time range over which both the ingoing and outgoing quantities of surfactants are measurable simultaneously.

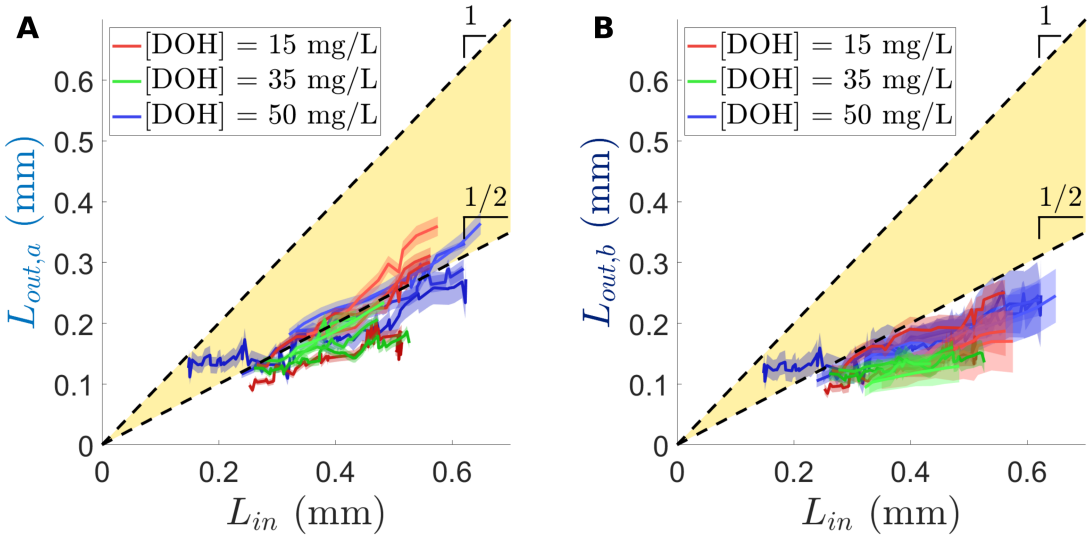

Figure 3.39: Comparison of the outgoing quantities of surfactants as a function of the ingoing ones $L_{out} = f(L_{in})$ for various chemistries and for the velocities $V_1 = 10, 20, 35$ and $50\,\mathrm{mm/s}$. **A:** $L_{out,a}$ is computed with $\epsilon_{1,a}$; **B:** $L_{out,b}$ with $\epsilon_{1,b}$. The shaded area corresponds to the range of expected balance, with $y = x$ the limit of no film-film exchanges, and $y = 0.5x$ the limit of no exchanges with the meniscus.

the upper limit $L_{out}(t) = L_{in}(t)$ corresponds to the extreme case where the meniscus provides

for as many surfactants as the free interface, the lower limit $L_{out}(t) = \frac{1}{2}L_{in}$ to the case where the flux of surfactants from the meniscus is zero. All this is detailed in subsection 3.3.

In our range of measurement, all velocities and chemistries are on the lower bound, suggesting that the flux of surfactants from the meniscus is null in all cases: $j_m = 0$.

This is the key information we needed to further advance on the theoretical descriptions of flows in sheared foams. This is also the main experimental result of this thesis work.

Important remarks

- Our result is verified in quite a narrow range of velocities of deformations, from $V_1 = 10$ to $50\,\mathrm{mm/s}$, corresponding to strain rates of $\dot{\epsilon} = 2 - 10\,\mathrm{Hz}$ given our geometry. At lower strain rates, we lose the invariance by translation along z before being able to measure L_{in} and L_{out} simultaneously. Higher strain rates cannot achieve reliable measurements, either because the motors are limited at $V_1 = 50\,\mathrm{mm/s}$ or because smaller amplitudes of deformations make it impossible to measure L_{in} and L_{out}.

- This result is heavily chemistry dependent to the best of our knowledge, as all hidden time variables allowing/excluding the existence of a j_m are adsorption, desorption or diffusion times of surfactants. Notably, even changing the direction of deformation, and thus the sign of the potential j_m, could lead to very different results under the same deformation conditions. Adsoption and desorption dynamics are known to be very different. This is a bit explored in section 3.10, where we look at other deformations, unfortunately without achieving measuring the interface balance as we did here.

- The balance computed with the corrected $\epsilon_{1,b}$ shown in Fig.3.39B is a bit below the lower bound of our model. This is puzzling, as it would suggest a j_m of the opposite sign (from the interface to the meniscus in this case, which is excluded). It might be caused by the fact that we neglect the exchanges in the dynamic menisci, the $\Delta\gamma^{in/out}$ of Fig.3.5 which have been neglected and which correspond both to a $\Delta\Gamma^{in/out}$ not taken into account in the surfactant balance. This assumption is more discussed in [4], and could explain this discrepancy.

3.10 Other deformations

3.10.1 "Push 1": Potential influence of gravity

In the "Push 1" experiments the geometry of deformation remains exactly the same as in "Push 3" but the roles of the different films are interchanged so that we look at the same system with the direction of gravity changed. The protocol is shown in Fig.3.40. As discussed in subsections 0.2.4 and 0.3.5, what we expect gravity to change here is:

- Giving different initial thicknesses for the compressed/stretched films. Figs.3.6.5 D-F show how different are the films whose roles have been interchanged between "Push3" and "Push1".

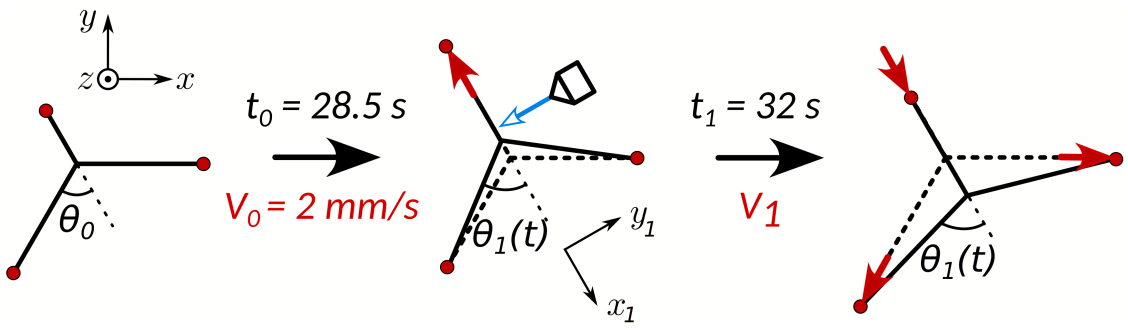

Figure 3.40: Protocol for the "Push 1" experiment. The prepared film is now film 1, where we photobleach 10 dots. The angle followed during the main deformation becomes $\theta_1(t)$. This protocol corresponds exactly to the "Push 3" protocol with interchanged roles for the films to probe the effect of gravity.

- Redistribute pieces of films as we deform them, the thicker ones being advected down, the thinner one advected up.

This second point is quite important, as we want to prepare a thick Frankel film in the plane of film 1. Stretching a vertical film means having a Frankel film at both the free meniscus and the motor at the top, and this last one, thicker than the central part, is not in a stable position with respect to gravity (*cf.* 0.3.5). Thus, the initial recirculations in film 1 induced by the preparation step excluded the least mobile interfaces (*i.e.* with dodecanol), because the top Frankel film falls slower in the form of chimneys, making the prepared state not reproducible. Without dodecanol, the top thick patches are evacuated faster, seemingly along the solid frame, and a reproducible prepared state is possible. The only change compared to the "Push 3" protocol is a shift of $0.5\,\mathrm{s}$ of the preparation time to $t_0 = 28.5\,\mathrm{s}$.

Besides, we managed to photobleach dots in the prepared film, but tracking them and the edge of the prepared film throughout the main deformation at t_1 was a problem, leading to a big experimental noise hindering the measurement of $L_{in}(t)$.

For the sake of measuring the tensions however, the measurement remained possible by tracking the angle between film 2 and 3 in this case. We plot in Fig.3.41 the film tension ratio between the compressed film and the stretched film for both "Push 3" (in blue, σ_3/σ_1) and "Push 1" (in red, σ_1/σ_3). The chemistry is with $[DOH] = 0$ and a velocity of deformation $V_1 = 35\,\mathrm{mm/s}$. A few observations:

- The preparation of film 1 in "Push 1", although identical to the preparation of film 3 in "Push 3", has a slightly lower amplitude.
- "Push 1" has larger initial slips in $t_0 = 28.5\,\mathrm{s}$ and $t_1 = 32\,\mathrm{s}$.
- The measurement is less reproducible, leading to a bigger experimental error.
- The slopes in time of the ratios are the same past the slip in $t_1 = 32\,\mathrm{s}$.
- The tension ratio relaxes towards 1 after the deformation in the same amount of time.

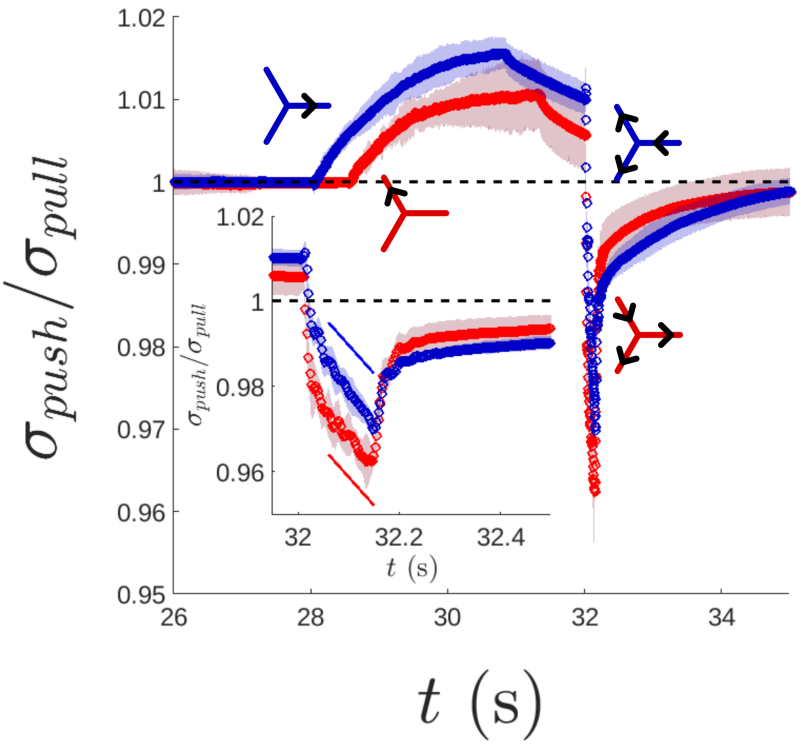

Figure 3.41: Comparison of the tension ratio in the "Push 3" (Blue) and "Push 1" (Red) experiments for the same chemistry $[DOH] = 0$ and velocity of main deformation $V_1 = 35\,\mathrm{mm/s}$. The tension ratio is σ_3/σ_1 for "Push 3" and σ_1/σ_3 for "Push 1". The inset is a zoom on the main deformation at $t_1 = 32\,\mathrm{s}$.

The main conclusion of this comparison is that gravity does not seem to play a major role for the rheology of our elementary foam, although its centimetric dimensions raised the question. However, it poses a lot of major experimental problems for the sake of tracking the patches of exchanged films and we cannot conclude on the robustness of our quantification of the interface exchanges under changing gravity.

3.10.2 "Pull 1": Same symmetry, opposite directions for the imposed velocities

The "Pull 1" experiment aims at looking at the interface exchanges with the same symmetry as "Push 3", but with minus signs on the imposed velocities. To do so, we designed the protocol detailed in Fig.3.42. The main fundamental difference with "Push 3" is that the preparation does not respect the axial symmetry of the main deformation as it still bears on the compressed film 3.

We thus manage to photobleach in film 3 as we previously did for "Push 3", and to track simultaneously the columns of dots and the prepared Frankel film as the film is compressed. A zoom on the region of film 3 neighbouring the free meniscus right before the deformation is shown

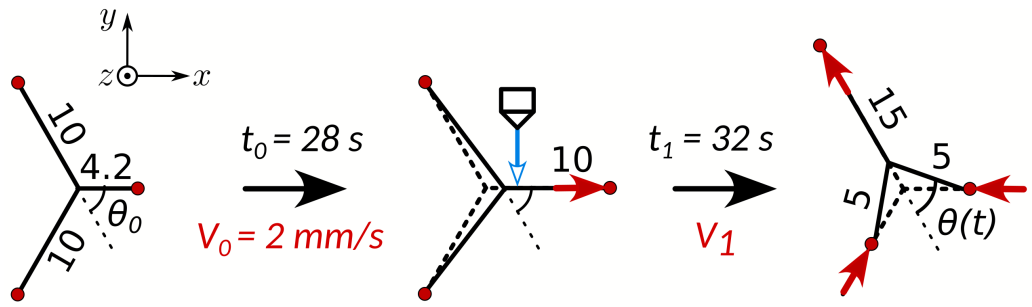

Figure 3.42: Protocol for the "Pull 1" experiment. The prepared film is film 3, where we photobleach 16 dots. Compared to "Push 3", we only swap the direction of deformation film 2. The relevant angle to track θ is the semiangle between film 2 and 3.

in Fig.3.43A with the arrows showing the direction of deformations for each film. Fig.3.43B shows the raw data of the distances between the matching coloured lines in A and the edge of the free meniscus as the film is compressed. Also, we show the length of outgoing Frankel film $L_{Fr,1}$ detected in film 1. The repeatability of these experiments is limited at longer times by something that we did not face with "Push 3": Marginal regeneration. In Fig.3.43C, we show how this phenomenon takes place, with the semicircular thin patched going out of the free meniscus. For more details about it, *cf.* subsection 0.3.4.

Actually, it is retrospectively surprising that no marginal regeneration takes place in "Push 3"! This even constitutes a result. The main difference in the case of "Pull 1" is that the compressed film has one frustrated interface and one free, whereas for "Push 3" both are free to slide on the free meniscus. This requires more investigation.

In the meantime, marginal regeneration is a source of low reproducibility for our experiments, and "Pull 1" yields noisy deformations ϵ_3 for the compressed film, as shown in Fig.3.44, inducing an even bigger error on the quantity of ingoing interface L_{in} which we did not manage to compute. Besides, computing the ratio of tension becomes tricky here, as the preparation step breaks the symmetry between film 2 and 3 compared to the main deformation. This would require to compute separately σ_2 and σ_3 by computing another angle in the problem, which is achievable but not done yet.

This is as far as we could go on the "Pull 1" experiments on that date, and more refined specific data processing could lead to better computations of the deformation and significant quantities of exchanged interface. For now, the L_{in}'s I tried to compute were so noisy that I do not dare showing them in this manuscript.

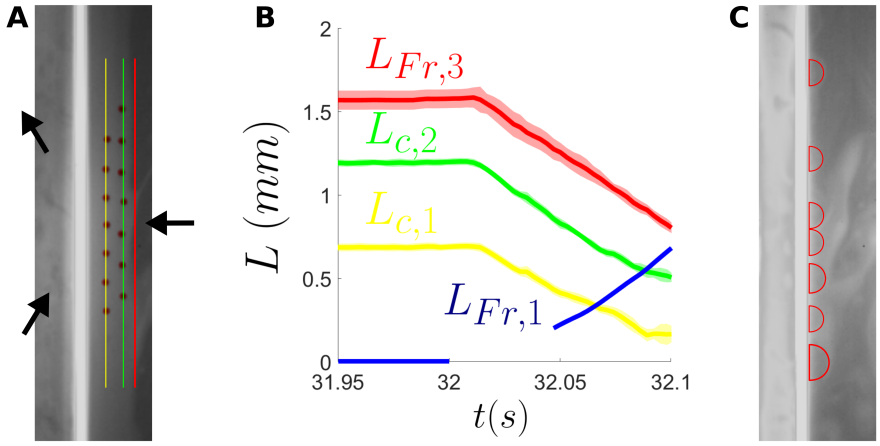

Figure 3.43: Positions of the edge of prepared Frankel film and the photobleached columns. **A:** Zoom near the meniscus in film 3. The vertical bright fringe on the middle left is the free meniscus, film 3 is on its right. The red line localises the detected edge of prepared Frankel film, whose distance from the edge of free meniscus is $L_{Fr,3}$, the green and yellow lines localise the two columns of photobleached dots, whose distances from the edge of meniscus are $L_{c,1}$ and $L_{c,2}$. **B:** Time evolution of the distances defined in **A** as well as $L_{Fr,1}$ (blue) the outgoing length of interface in film 1. The main deformation happens at $t_1 = 32\,\mathrm{s}$, where film 3 is compressed and film 1 is stretched. **C:** Towards the end of the deformation, the marginal regeneration instability appears, breaking our invariance by translation and thus stopping the measurement of the exchanged quantities of interface.

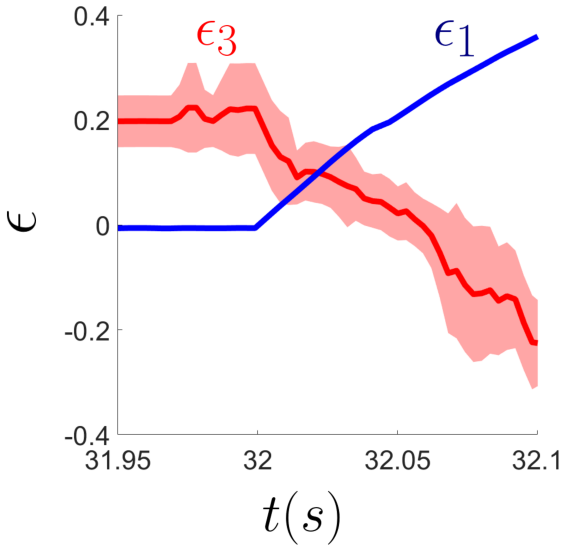

Figure 3.44: Example given on the chemistry $[DOH] = 35\,\mathrm{mg/L}$ and a velocity of main deformation $V_1 = 50\,\mathrm{mm/s}$ for the deformations of film 3 and 1. It was not possible to compute the corrected ϵ_1 in this deformation, and we show here the deformation equivalent to the $\epsilon_{1,a}$ of "Push 3".

3.11 Conclusions of Chapter 3

- The fluid mechanics behind the visco-elasticity of elementary liquid foams is not completely settled.
- The elastic contributions are well understood and originate from the finite-sized reservoir effects of the foam films. This was the subject of chapter 1.
- The viscous contributions are suspected to originate from a very localised sheared zone near the meniscus, of size $\ell \sim 100\,\mu\mathrm{m}$. The existence of this zone is imposed by the presence of a stagnation point at the interface of the elementary foam, and a theoretical model already exists to describe it [4].
- The flow field in this zone is fully determined by the Marangoni stresses at the interfaces, which are set by the dynamics of exchange of the surfactants in this zone.
- The quantity of surfactants exchanged with the meniscus was a free parameter of the model which could lead to very different predictions for the dissipation occurring in the elementary foam.
- By looking simultaneously at the quantities of surfactants going in and out of the meniscus during the deformation of the foam, **I was able to measure the nullity of the quantity of surfactants exchanged with the meniscus.**
- This result is robust even if we vary the velocity of deformation or the chemistry of the foam. I need now to put it back into the theoretical model to close it, and to compare it to the experimental rheological data I also measured during my experimental campaign.

Conclusion

The common denominator to all my thesis work is the study of in-plane flows within foam films. This is a hydrodynamicist's point of view to help better understanding the ageing and rheology of liquid foams, starting from a single film and scaling up to what we called an elementary liquid foam. The subjects I covered in my Introduction are part of the work of a whole (welcoming) community which has developed the field of foam film hydrodynamics for decades now.

My three chapters are three modest stones that I have the chance to place at three distinct points of this edifice.

Chapter 1 is about the elasticity of a single foam film. Because the bulk is very thin, it is a finite-sized reservoir for the sake of populating the water-air interfaces sandwiching it. This is responsible for an effective elastic contribution under deformation which has already been predicted and measured by Prins *et al.* [5] in 1967 in the submicellar regime. **Here, I provided an extension of this model to the micellar regime in presence of poorly soluble surfactants. I also compared this new thermochemical model to experimental data from Isabelle's group, and found that we could predict the elasticity of the different solutions based on their chemistry.** The results were published in *Soft Matter* [6].

Chapter 2 is about a novel measurement of a line tension force $T \sim 10^{-10}\mathrm{N}$ in the plane of foam films. It originates from the thickness gradients present in the film along a contour and sets it in motion in order to minimise its perimeter. These motions are observed during the marginal regeneration instability for instance, where thin patches take a circular shape because of this force, and are advected up in the film, thus being an important mechanism for its ageing. Another example is the use made of in-plane motions of foam films as a proxy for atmospheric turbulent flows, where this line tension could represent a non-negligible force potentially harming the analogy. **I supervised the experimental campaigns where we created the foam film subject to this line tension. We looked at a configuration where we were able to simultaneously measure the force and monitor the relaxation of the in-plane motions. Our force measurement was validated by a quantitative agreement with the witnessed relaxation, which I modelled analytically knowing that the damping mechanism was air friction.** The results have been accepted by *Physical Review Letters* by the time I write this manuscript [99].

Chapter 3 is about the main experimental contribution of my thesis. The effective viscosity of an elementary liquid foam is thought to originate from a very localised sheared zone near the meniscus linking the foam films. The exchanges of surfactants there, between the interfaces, the bulk and the meniscus, entirely determine the shear flow responsible for the mechanical dissipation. Adrien Bussonnière and Isabelle Cantat developed a theoretical model for all that [4], but one

parameter was left free because of a lack of experimental information: **how much surfactants are exchanged with the meniscus? I adapted the experimental setup to perform this measurement and found that there were no exchanges in all the range of strain rates and chemistries I tried.**

The next step of this study is to look back at the theoretical model, setting the flux of surfactants towards the meniscus to zero. This will allow us to predict stress curves $\Delta\sigma = f(U)$ which we can then compare to the unused experimental data measured in my campaigns besides the surfactant exchanges. Notably, I measured the film elasticities with my setup (validated by our previous works in chapter 1) and computed the film deformations. We thus have access to the absolute tensions σ of each film of the elementary foam, which will be a valuable piece of knowledge for the comparison with the theoretical predictions.

Appendix

Appendix 1: Derivation of compressible Navier-Stokes equation in 2D

Same derivation than Chapter II of the Landau Lifchitz [108], adapted in 2D. Conservation of momentum in 2D writes:

$$\rho \frac{D\boldsymbol{v}}{Dt} = \boldsymbol{\nabla}_s \gamma + \boldsymbol{\nabla}_s \cdot \overline{\overline{\boldsymbol{\tau}}}_s + \boldsymbol{f}_{ext} \tag{3.59}$$

Where $\overline{\overline{\boldsymbol{\tau}}}_s$ is the rheological stress tensor (**NB:** compared to section 0.1.4, we dispatched the stress tensor so that $\overline{\overline{\boldsymbol{\sigma}}}_s = \gamma \overline{\overline{\boldsymbol{I}}}_s + \overline{\overline{\boldsymbol{\tau}}}_s$):

$$\overline{\overline{\boldsymbol{\tau}}}_s = \eta_s \Big(\overline{\overline{\boldsymbol{\nabla}}}_s \boldsymbol{v} + {}^t \overline{\overline{\boldsymbol{\nabla}}}_s \boldsymbol{v} \Big) + \mu_s \boldsymbol{\nabla}_s \cdot \boldsymbol{v}\ \overline{\overline{\boldsymbol{I}}}_s \tag{3.60}$$

Where η_s is the surface shear viscosity and μ_s a coefficient associated to the viscous response to dilation. It is not yet the dilatational surface viscosity though, as we need first to separate among these terms the pure dilatational contribution from the pure shear contributions. To do so, we compute the isotropic part of the tensor:

$$\bar{\tau} = \frac{\tau_{xx} + \tau_{yy}}{2} = \mu_s \boldsymbol{\nabla}_s \cdot \boldsymbol{v} + \frac{\eta_s}{2} \Big(2\partial_x v_x + 2\partial_y v_y \Big) = (\mu_s + \eta_s) \boldsymbol{\nabla}_s \cdot \boldsymbol{v} \tag{3.61}$$

Thus, let $\kappa_s = \mu_s + \eta_s$ be the surface dilatational viscosity. We can rewrite the tensor $\overline{\overline{\boldsymbol{\tau}}}_s$ as:

$$\overline{\overline{\boldsymbol{\tau}}}_s = \eta_s \Big(\overline{\overline{\boldsymbol{\nabla}}}_s \boldsymbol{v} + {}^t \overline{\overline{\boldsymbol{\nabla}}}_s \boldsymbol{v} - \boldsymbol{\nabla}_s \cdot \boldsymbol{v}\ \overline{\overline{\boldsymbol{I}}}_s \Big) + \kappa_s \boldsymbol{\nabla}_s \cdot \boldsymbol{v}\ \overline{\overline{\boldsymbol{I}}}_s \tag{3.62}$$

Its contribution to eq.3.59 can thus be expressed on the x axis:

$$\boldsymbol{\nabla}_s \cdot \overline{\overline{\boldsymbol{\tau}}}_s|_x = \partial_x \tau_{xx} + \partial_y \tau_{xy} = \partial_x \Big(\kappa_s \boldsymbol{\nabla}_s \cdot \boldsymbol{v} + \eta_s (2\partial_x v_x - \partial_x \boldsymbol{\nabla}_s \cdot \boldsymbol{v}) \Big) + \partial_y \Big(\eta_s (\partial_y v_x + \partial_x v_y) \Big) \tag{3.63}$$

$$= \kappa_s \partial_x \boldsymbol{\nabla}_s \cdot \boldsymbol{v} + \eta_s \Big(2\partial_{xx} v_x - \partial_x \boldsymbol{\nabla}_s \cdot \boldsymbol{v} + \partial_{yy} v_x + \partial_{yx} v_y \Big) \tag{3.64}$$

$$= \kappa_s \partial_x \boldsymbol{\nabla}_s \cdot \boldsymbol{v} + \eta_s \Delta v_x + \eta_s \Big(\partial_{xx} v_x + \partial_{xy} v_y - \partial_x \boldsymbol{\nabla}_s \cdot \boldsymbol{v} \Big) \tag{3.65}$$

$$= \kappa_s \partial_x \boldsymbol{\nabla}_s \cdot \boldsymbol{v} + \eta_s \Delta v_x \tag{3.66}$$

Which can be recast in eq.3.59 as a general vectorial expression on all axis:

$$\rho\frac{D\boldsymbol{v}}{Dt} = \boldsymbol{\nabla}_s\gamma + \kappa_s\boldsymbol{\nabla}_s\Big(\boldsymbol{\nabla}_s\cdot\boldsymbol{v}\Big) + \eta_s\Delta_s\boldsymbol{v} + \boldsymbol{f}_{ext} \tag{3.67}$$

Which is a general 2D Navier-Stokes equation when associated with a surface conservation law.

NB: This computation deviates from the 3D one when we compute the isotropic part of $\overline{\overline{\boldsymbol{\tau}}}$ to find the dilatational viscosity (or second viscosity), as a 3D tensor would mean hitting a factor $(\mu + \frac{2}{3}\eta)$ instead. This defines $\kappa = \mu + \frac{2}{3}\eta$ the second bulk viscosity to inject in the expression of $\overline{\overline{\boldsymbol{\tau}}}$ and the end of the computation leads to a term $(\kappa + \frac{1}{3}\eta)\boldsymbol{\nabla}(\boldsymbol{\nabla}\cdot\boldsymbol{v})$ for the viscous forces associated with dilation.

Appendix 2: Limit of high elasticities for the in-plane motions of a foam film

The fact that the film elasticity E_f dominates even for small deformations is a key ingredient in all the models we will develop in the frame of this thesis work. Most of the time, we will even assume the film to be incompressible, as in the following sections. However, before taking this limit, it has to be noted that the first limit of very high elasticities for a deformable film yields interesting results for the description of the kinematics of the film in-plane motions. In fact we will see here that we can decompose our velocity field in an irrotational component and an incompressible component, the former being simple, expressed at the lower order with elasticity, the latter being the solution of a more simple equation at higher order.

In the general case, the uniformity of film tension found in subsection 0.2.4 can be written:

$$\boldsymbol{\nabla}_s\sigma^f = \boldsymbol{0} \tag{3.68}$$

If we consider a film formed of two flat symmetrical interfaces, thus removing capillary stress from the equation, the film tension σ^f is then "just" twice the surface tension of both interfaces. This encompasses the elastic and viscous responses of the film, and the uniformity equation 3.68 can be rewritten as twice eq.10 where the exterior forces $\boldsymbol{f}_{g,s}$ have been discarded and surface tension expressed with $E_f = 2E_M$ (*cf.* eq.11) in the insoluble limit in the form $\frac{\mathrm{d}\gamma}{\mathrm{d}t} = E_f\Big(\boldsymbol{\nabla}_s\cdot\boldsymbol{v}_s\Big)$, yielding:

$$\boldsymbol{0} = E_f\boldsymbol{\nabla}_s\int_t\Big(\boldsymbol{\nabla}_s\cdot\boldsymbol{v}_s\Big)dt + 2\kappa_s\boldsymbol{\nabla}_s(\boldsymbol{\nabla}_s\cdot\boldsymbol{v}_s) + 2\eta_s\boldsymbol{\Delta}_s\boldsymbol{v}_s \tag{3.69}$$

Where $E_f = 2E_M$ is the film elasticity, which is uniform and independent of time in the present case.

We first start by doing a Helmholtz-Hodge decomposition of our vector field: $\boldsymbol{v}_s = \boldsymbol{v}_{irr} + \boldsymbol{v}_{inc}$, where $\boldsymbol{v}_{irr} = \boldsymbol{\nabla}_s\phi$ is an irrotational velocity field written as a gradient and $\boldsymbol{v}_{inc} = \boldsymbol{\nabla}_s\times\psi$ [1] is

[1] In 2D, the curl of a vector is usually a scalar. The Helmholtz decomposition is generalised in 2D with an alternative definition of this operator which takes a scalar as input and outputs a vector [109]: $(\boldsymbol{\nabla}_s\times) : \psi(x,y) \longrightarrow (-\partial_y\psi, \partial_x\psi)$. Thus, we will implicitly use both definitions $\boldsymbol{\nabla}_s\times$ and $\nabla_s\times$ with or without the bold nabla depending on the kind of 2D curl.

an incompressible velocity field written as a 2D curl.

This is where we use our hypothesis that film elasticity is bigger than any other force: $E_f \gg \frac{\kappa_s}{\tau_{def}}$, $\frac{\eta_s}{\tau_{def}}$ to write at lowest order only the first term of the right-hand side of eq.3.69:

$$\mathbf{0} = \boldsymbol{\nabla}_s \int_t \Big(\boldsymbol{\nabla}_s \cdot \boldsymbol{v}_s\Big) dt = \boldsymbol{\nabla}_s \int_t \Big(\boldsymbol{\nabla}_s \cdot \boldsymbol{v}_{irr}\Big) dt \tag{3.70}$$

As $\boldsymbol{v}_{irr}$ is the non-vanishing component of $\boldsymbol{v}_s$ when we take the divergence. We also need to anticipate that $\boldsymbol{v}_{irr}$ will also have a higher order component and we write $\boldsymbol{v}_{irr} = \boldsymbol{v}_{irr,0} + \boldsymbol{v}_{irr,1}$ with $\boldsymbol{v}_{irr,0}$ being the lower order term, and by differentiating eq.3.70 with respect to time:

$$\boldsymbol{\nabla}_s\Big(\boldsymbol{\nabla}_s \cdot \boldsymbol{v}_{irr,0}\Big) = \mathbf{0} \implies \boldsymbol{\nabla}_s \cdot \boldsymbol{v}_{irr,0} = K(t) \tag{3.71}$$

This leads directly to a Poisson equation for the velocity potential $\Delta\phi = K(t)$ where the source term is necessarily the deformation rate $K(t) = \dot{\epsilon}$ in order to respect area conservation in the problem. To be solved, this part of the velocity field requires us to know the imposed velocity at the edges of the film, as the Poisson problem can be solved using Neumann boundary conditions for ϕ, that is knowing $\frac{\partial \phi}{\partial n_s}.\boldsymbol{n}_s = \boldsymbol{v}_s\Big|_{\text{edge}}$ (where $\boldsymbol{n}_s$ is the normal vector to the edge of the foam film seen as a 2D domain). This is exactly what we know in practice when we deform a foam film, and we have a complete set of equations for $\boldsymbol{v}_{irr}$:

$$\begin{cases} \frac{\partial \phi}{\partial n_s}.\boldsymbol{n}_s \text{ is known at the edges} \\ \Delta\phi = \dot{\epsilon} \end{cases} \tag{3.72}$$

This set gives a unique solution $\boldsymbol{v}_{irr,0}$ which can be easily found in practice for simple geometries of deformation. Now that this component is found, we go at higher order in eq.3.69:

$$\mathbf{0} = E_f \boldsymbol{\nabla}_s \int_t \Big(\boldsymbol{\nabla}_s \cdot (\boldsymbol{v}_{irr,1} + \boldsymbol{v}_{inc})\Big) dt + 2\eta_s \boldsymbol{\Delta}_s \boldsymbol{v}_{inc} \tag{3.73}$$

Where the terms of $\boldsymbol{v}_{irr}$ linked to the instrinsic viscosities κ_s, η_s vanish after some reorganisations using $\boldsymbol{\Delta}_s = \boldsymbol{\nabla}_s \boldsymbol{\nabla}_s \cdot - \boldsymbol{\nabla}_s \times \nabla_s \times$. On the other hand, the incompressibility of $\boldsymbol{v}_{inc}$ allows us to write the set of equations as:

$$\begin{cases} \boldsymbol{\nabla}_s \cdot \boldsymbol{v}_{inc} = 0 \\ \boldsymbol{\nabla}_s \gamma_{inc} + \eta_s \boldsymbol{\Delta}_s \boldsymbol{v}_{inc} = \mathbf{0} \end{cases} \tag{3.74}$$

Where $\gamma_{inc} = E_f \int_t \boldsymbol{\nabla}_s \cdot \boldsymbol{v}_{irr,1} \, \mathrm{d}t$ is a Lagrange multiplier of a 2D Stokes equation for $\boldsymbol{v}_{inc}$, enforcing the incompressibility condition. Thus we do not need to make the higher order field $\boldsymbol{v}_{irr,1}$ explicit to compute the dominant term $\boldsymbol{v}_{inc}$ of $\boldsymbol{v}_s \simeq \boldsymbol{v}_{inc} + \boldsymbol{v}_{irr,0}$.

Thus, even if a foam film is being stretched, meaning the velocity at its edges is non-zero, we can still compute the total velocity field $\boldsymbol{v}_s = \boldsymbol{v}_{inc} + \boldsymbol{v}_{irr}$. This is thanks to the film elasticity being dominant for any small deformation, allowing us to decompose the problem on different orders, the lower order giving the compressible field $\boldsymbol{v}_{irr}$ taking into account the global deformation of the foam film, the higher order giving the incompressible field $\boldsymbol{v}_{inc}$ which is a solution of a 2D Stokes equation.

Note that this result remains valid even if we keep exterior forces $\boldsymbol{f}_{ext,s}$ such as air friction, as long as they remain of higher order than the film elasticity E_f. We only need to add them to eq.3.74 when we need to solve for the incompressible field.

Appendix 3: Compressible correction for the flow field of the line tension experiment

In section 2.4 of Chapter 2, we suppose the incompressibility of the interfaces based on the fact that the area A of the thin film is almost constant in time, as recalled with Fig.3.45**C**. However, it undergoes a slight compression, even though the motors have stopped moving.

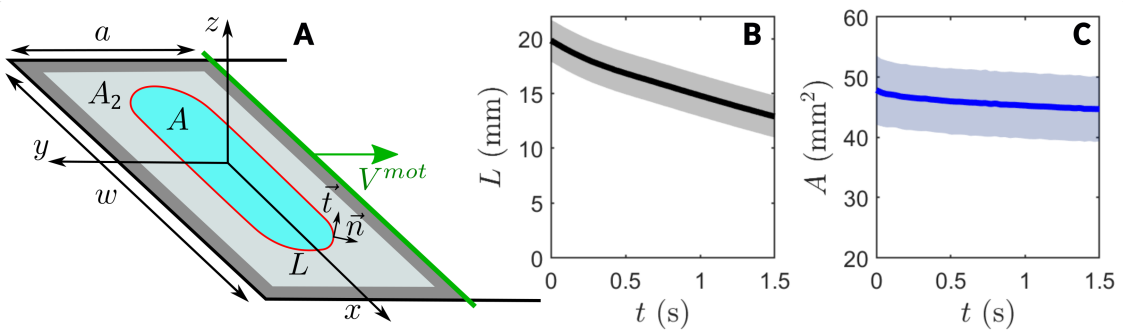

Figure 3.45: Recalling the notations and some experimental data from chapter 2 section 3.4: **A** Notations for the deformable frame; **B** Semi-length L of the arena of thin film throughout its relaxation; **C** Area A of the thin film during the experiment.

This is due to some Frankel film extraction, which happens mostly during the stretching to create the thick film of area $A_2 = aw - A$ (as shown in Fig.3.45**A**), but which also continues after the deformation for $t > 0$. To try and take this into account for the sake of describing the velocity field in the plane of the foam film, we use the development for the limit of high elasticities led in the Appendix 2. This latter established that we can decompose the velocity field into two components: a compressible one corresponding to a pure stretching, and an incompressible one corresponding to the resolution of a 2D Stokes equation with the exterior forces. **The goal of this Appendix is to apply this decomposition to our concrete problem and to validate that the compressible term can effectively be discarded in our case, as we assumed in section 2.4.**

This decomposition is conditioned by the fact that the in-plane forces are much lower than the film elasticity. In the case of chapter 2, these are the exterior friction forces and the line tension.

First, the friction in this case is dominated by air friction (*cf.* 2.4.4, and is of the order of magnitude: $f_g \sim \eta_g U/\delta \sim 10^{-4}\mathrm{Pa}$ with $\eta_g \sim 10^{-5}\mathrm{Pa}\cdot\mathrm{s}$ the air viscosity, $U \sim 10^{-2}\mathrm{m/s}$ the typical velocity for the in-plane motions and $\delta \sim 10^{-3}\mathrm{m}$ the typical width of the sheared air layer (all recalled from 2.4.3). Second, the line tension forces are of the order $T/R^2 \sim 10^{-3}\mathrm{Pa}$ with $T \sim 10^{-9}\mathrm{N}$ the line tension and $R^2 \sim 10^{-3}\mathrm{m}$ the typical curvature radius of the line of tension.

These forces are to be compared to the elastic forces at stake while deforming the foam film globally by stretching it and inducing film extraction. This yields forces of the order of $E_f/L \sim 1\,\mathrm{Pa}$ with $E_f \sim 10^{-2}\mathrm{N/m}$ the film elasticity and $L \sim 10^{-2}\mathrm{m}$ the typical length of the foam film. The elastic forces dominate all the others and thus the decomposition of Appendix 2 can be applied.

Note that in the following, time may appear as it is a constant of our experimental problem. Our model though is independent of time, and t acts as a dummy variable listing all the resolutions of the flow field at each time step.

Compressible component for the uniaxial stretching

Let us first start by computing the compressible velocity field using the set of eq.3.72. In the specific case of the experiment of chapter 2, the foam film is rectangular and went through a uniaxial deformation which is well known. After the motor has stopped, some Frankel film are still being extracted at the four edges. We make the assumption that the tension is uniform along the four menisci at the straight edges, and the tension being uniform in the film, the velocity of Frankel film extraction V_{Fr} is uniform along the rectangular frame, leading to the explicit conditions for the velocity potential ϕ:

$$\begin{cases} \boldsymbol{v}_0 = \boldsymbol{\nabla}\phi \\ \partial_x\phi(x=0) = V_{Fr} \ ; \ \partial_x\phi(x=w) = -V_{Fr} \\ \partial_y\phi(y=0) = V_{Fr} \ ; \ \partial_y\phi(y=a) = V_{mot} - V_{Fr} \\ \Delta\phi = \frac{1}{A_2}\frac{\mathrm{d}A_2}{\mathrm{d}t}(t) \end{cases} \tag{3.75}$$

Where V_{Fr} is known by looking at the compression state of the film with the last equation. V_{mot} is the velocity of the motor at the time at which we solve the system, and for our measurable range $t > 0$: $V_{mot} = 0$. The system has a solution for a compressible velocity field $\boldsymbol{v_0}$ that is:

$$\begin{cases} v_{0,x} = V_{Fr} + \frac{x}{w}\Big(- 2V_{Fr}\Big) \\ v_{0,y} = V_{Fr} + \frac{y}{a}\Big(V_{mot} - 2V_{Fr}\Big) \end{cases} \tag{3.76}$$

This velocity field must now be associated with the incompressible flow which we compute in section 2.4.

Superposition with the incompressible flow field and importance of this correction for the relaxation dynamics

The computation of the incompressible velocity field $\boldsymbol{v_{inc}}$ is given equivalently in subsection 2.4.2, eq.2.33, by considering a γ_{inc} that takes into account the compressible flow field, or by Appendix 2, eq.3.74, by adding $\boldsymbol{f_g}$ the air friction and the line tension integral as higher order forces in the system. They both give:

$$\begin{cases} \boldsymbol{\nabla}_s \cdot \boldsymbol{v}_{inc} = \boldsymbol{0} \\ \eta_s \boldsymbol{\Delta}_s \boldsymbol{v}_{inc} + \boldsymbol{\nabla}_s \gamma_{inc} + \boldsymbol{f}_g = \oint_{\mathcal{C}^*} T\kappa(\boldsymbol{r'})\delta_{\mathcal{C}^*}(\boldsymbol{r} - \boldsymbol{r'})\boldsymbol{n}(\boldsymbol{r'})dr' \end{cases} \tag{3.77}$$

This problem is solved in section 2.4.4 in a form that allows us to get an expression for the time evolution of L with eq.2.46. With the compressible component, we have:

$$\dot{L}(t) = -\frac{T(t)}{4R(t)\eta_{air}} - \frac{2L(t)}{w}V_{Fr}(t) \tag{3.78}$$

Where the first term of the right hand-side is given by eq.2.46 and the second term is the compressible contribution. Experimentally, we define $U^{exp} = \dot{L}$ in section 2.4.4, and here we also define a corrected velocity:

$$U^{exp}_{corr}(t) = U^{exp}(t) + \frac{2L(t)}{w}V_{Fr}(t) \tag{3.79}$$

Which now takes into account the compression of the thin film as more thick film is extracted. This is the corrected velocity that may be taken into account for the sake of quantifying the relaxation dynamics associated with the line tension forces.

We compute the ratio U^{exp}_{corr}/U^{exp} and plot it in Fig.3.46. Mind that $U^{exp} = \dot{L} < 0$ and $V_{Fr} > 0$, hence the ratio below one. **We directly see that it is a correction of 15% at best, which is a useful correction in general, but given the present experimental uncertainties associated with the line tension measurement (of the order of 50%...), it has been discarded for the sake of simplicity in the story of chapter 2.**

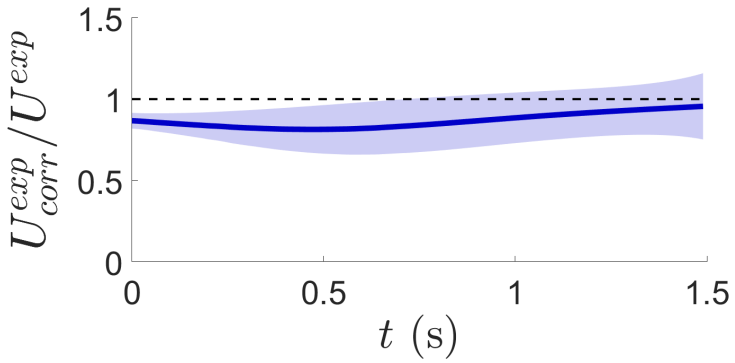

Figure 3.46: Ratio of the corrected velocity U^{exp}_{corr} by the experimental velocity U^{exp} retained in chapter 2. The correction is of the order of 15%.

Appendix 4: 2D Stokes equation and derivation of its Green function

Let us consider a 3D viscous fluid of viscosity η, to which we apply a force perpendicular to a segment localized by the vector $\boldsymbol{r}_1 = (x_1, y_1)$ in the (Oxy) plane, and by the z-scores $z_1 \in [-M, M]$. We denote f^{lin} the force per unit length applied on a part of the segment, and $\boldsymbol{u}$ the unit vector of the direction of the force. M is arbitrarily large. The Stokes equations governing the motion and the pressure field is then:

$$\Delta \boldsymbol{v}(\boldsymbol{r}) - \boldsymbol{\nabla}\frac{p(\boldsymbol{r})}{\eta} = -\frac{f^{lin}}{\eta}\int_{-M}^{M} \delta_{3D}(\boldsymbol{r}-\boldsymbol{r}_1)dz_1\ \boldsymbol{u} \tag{3.80}$$

$$\boldsymbol{\nabla}.\boldsymbol{v} = 0 \tag{3.81}$$

The dirac delta function δ_{3D} is defined so that its integration over the volume of definition $\mathcal{R}^3$ is unity. In this case, the Green function of the Stokes equation is integrated over the segment and yields:

$$\boldsymbol{v}(\boldsymbol{r}) = +\frac{f^{lin}}{\eta}\int_{-M}^{M} \overline{\overline{\boldsymbol{G}}}_{3D}(\boldsymbol{r}-\boldsymbol{r}_1).\boldsymbol{u}\ dz_1 \tag{3.82}$$

Where $\mathbf{G}_{3D}$, the Oseen tensor, is defined as:

$$G_{3D,ij}(\boldsymbol{r}) = \frac{1}{8\pi}\Big(\frac{\delta_{ij}}{|\boldsymbol{r}|} + \frac{r_i r_j}{|\boldsymbol{r}|^3}\Big) \tag{3.83}$$

Where δ_{ij} is the Kronecker symbol. We now seek an analogy between this 3D mathematical problem in order to solve for a point force 2D problem whose Stokes equations can be written:

$$\Delta \boldsymbol{v}(\boldsymbol{r}) + \boldsymbol{\nabla}\frac{\gamma(\boldsymbol{r})}{\eta_s} = -\frac{T}{\eta_s}\delta_{2D}(\boldsymbol{r}-\boldsymbol{r}_1)\boldsymbol{u} \tag{3.84}$$

$$\boldsymbol{\nabla}.\boldsymbol{v} = 0 \tag{3.85}$$

Where $\frac{\gamma}{\eta_s} = -\frac{p}{\eta}$ defines by analogy a surface tension and a surface shear viscosity, T is a force, and the new dirac function δ_{2D} is now defined over the (Oxy) plane. The mathematical analogy between the problems can be written so that the Green function of the 2D problem is defined as:

$$\frac{f^{lin}}{\eta}\int_{-M}^{M} \overline{\overline{\boldsymbol{G}}}_{3D}(\boldsymbol{r}-\boldsymbol{r}_1).\boldsymbol{u}\ dz_1 = \frac{T}{\eta_s}\overline{\overline{\boldsymbol{G}}}_{2D}(\boldsymbol{r}_{\parallel}-\boldsymbol{r}_{1,\parallel}).\boldsymbol{u} \tag{3.86}$$

The $\parallel$ index symbolizing the fact that the vector is projected in the (Oxy) plane. Computing the integral for each coordinate and identifying the terms for the tensor $\overline{\overline{\boldsymbol{G}}}_{2D}$, we get for $\boldsymbol{r} \in \mathcal{R}^2 = (Oxy)$:

$$G_{2D,ij}(\boldsymbol{r}) = \frac{1}{4\pi}\Big(\delta_{ij}\ \ln\Big(\frac{2M}{|\boldsymbol{r}|}\Big) + \frac{r_i r_j}{|\boldsymbol{r}|^2}\Big) \tag{3.87}$$

Which is the solution to eq. 3.84 yielding the 2D velocity field:

$$\boldsymbol{v}(\boldsymbol{r}) = +\frac{T}{\eta_s}\overline{\overline{\boldsymbol{G}}}_{2D}(\boldsymbol{r}-\boldsymbol{r}_1).\boldsymbol{u} \tag{3.88}$$

Appendix 5: A more general equation of motion for foam films with any field of thickness h

In a more general case than presented in subsection 2.4.1, the thickness gradients are not localised along a contour. We can still write the equation of motion for any thickness field h in the foam film. We can do so by adding directly the viscous stress tensor $\overline{\overline{\boldsymbol{\sigma}}}_{visc}$ for two viscous 2D interfaces to the capillary stress tensor $\overline{\overline{\boldsymbol{\sigma}}}_{cap}$ computed in eq.2.7 of section 2.1:

$$\overline{\overline{\boldsymbol{\sigma}}}_{visc} = 2\eta_s\left(\overline{\overline{\boldsymbol{\nabla}}}\boldsymbol{v} + {}^t\overline{\overline{\boldsymbol{\nabla}}}\boldsymbol{v}\right) \tag{3.89}$$

Where $\boldsymbol{v}$ is the 2D velocity field shared by both interfaces, as we put ourselves in the case where only plug flows are allowed as discussed in 0.2.1 (potentially extensional plug flows though). Also, the factor 2 in $\overline{\overline{\boldsymbol{\sigma}}}_{visc}$ is here to take into account the two interfaces.

We now write the conservation of momentum in the film neglecting its inertia:

$$\boldsymbol{0} = \boldsymbol{\nabla}.\left(\overline{\overline{\boldsymbol{\sigma}}}_{cap} + \overline{\overline{\boldsymbol{\sigma}}}_{visc}\right) + \boldsymbol{f}_{ext} \tag{3.90}$$

Where $\boldsymbol{f}_{ext} = 2\boldsymbol{f}_g$ accounts for the exterior forces acting on the film, which in the present case are only $2\boldsymbol{f}_g$ the friction forces of the two interfaces on the neighbouring gas phase. Taking the divergence of both the capillary and viscous stress tensors, we have:

$$2\eta_s\Delta\boldsymbol{v} + 2\boldsymbol{\nabla}\gamma + 2\gamma_0 h\boldsymbol{\nabla}(\Delta h) + 2\boldsymbol{f}_g = \boldsymbol{0} \tag{3.91}$$

The first two terms correspond to the terms of a 2D Stokes equation in which the role of the classical pressure gradient in 3D is held by the Marangoni stress here in 2D. The third term comes from the divergence of the capillary stress tensor alone, where a simplification occurs between $\boldsymbol{\nabla}.\overline{\overline{\boldsymbol{\sigma}}}^{\,*}_{cap}$ and $\boldsymbol{\nabla}.(\sigma^f\overline{\overline{\boldsymbol{I}}}_2)$ with the terms depending on h. Note that we can write equivalently with both notations $\boldsymbol{\nabla}\delta\gamma$ as in eq.2.7 or $\boldsymbol{\nabla}\gamma$ as in eq.2.32, as only the deviation from the equilibrium value matters here.

This equation is the general equation of in-plane motion of a foam film with any thickness field h and two interfaces of surface viscosity η_s subject to the friction of the neighbouring gas phase. Is has been already derived by Bruinsma *et al.* [64] using another approach.

The specific case of eq.2.32 where we defined a line tension can be recovered by injecting a thickness field h whose gradient is non-zero in very localised regions only. If we do so (as we did in section 2.4.1), we need to be careful as not only the third term of eq.3.91 matters in the non-zero gradient of thickness zones, but also $\boldsymbol{\nabla}\gamma$ as discussed in section 2.1.2.

Bibliography

[1] M. Durand and H. A. Stone, "Relaxation time of the topological $t1$ process in a two-dimensional foam," *Phys. Rev. Lett.*, vol. 97, p. 226101, Nov 2006.

[2] S. Besson, G. Debrégeas, S. Cohen-Addad, and R. Höhler, "Dissipation in a sheared foam: From bubble adhesion to foam rheology," *Phys. Rev. Lett.*, vol. 101, no. 21, p. 214504, 2008.

[3] A. Titta, M. Le Merrer, F. Detcheverry, P. D. M. Spelt, and A.-L. Biance, "Level-set simulations of a 2d topological rearrangement in a bubble assembly: effects of surfactant properties," *Journal of Fluid Mechanics*, vol. 838, p. 222–247, 2018.

[4] A. Bussonnière and I. Cantat, "Local origin of the visco-elasticity of a millimetric elementary foam," *Journal of Fluid Mechanics*, vol. 922, p. A25, 2021.

[5] A. Prins, C. Arcuri, and M. Van Den Tempel, "Elasticity of thin liquid films," *Journal of Colloid and Interface Science*, vol. 24, no. 1, pp. 84–90, 1967.

[6] R. Poryles, T. Lenavetier, E. Schaub, A. Bussonnière, A. Saint-Jalmes, and I. Cantat, "Non linear elasticity of foam films made of sds/dodecanol mixtures," *Soft Matter*, vol. 18, no. 10, pp. 2046–2053, 2022.

[7] I. Cantat, S. Cohen-Addad, F. Elias, F. Graner, R. Höhler, O. Pitois, F. Rouyer, and A. Saint-Jalmes, *Les mousses: structure et dynamique*. Belin, 2010.

[8] J. W. Gibbs, "On the equilibrium of heterogeneous substances," 1879.

[9] R. C. Tolman, "Consideration of the gibbs theory of surface tension," *The journal of chemical physics*, vol. 16, no. 8, pp. 758–774, 1948.

[10] V. Bergeron and C. Radke, "Equilibrium measurements of oscillatory disjoining pressures in aqueous foam films," *Langmuir*, vol. 8, no. 12, pp. 3020–3026, 1992.

[11] V. Bergeron and C. Radke, "Disjoining pressure and stratification in asymmetric thin-liquid films," *Colloid and Polymer Science*, vol. 273, pp. 165–174, 1995.

[12] B. Derjaguin and L. Landau, "Theory of the stability of strongly charged lyophobic sols and of the adhesion of strongly charged particles in solutions of electrolytes," *Progress in Surface Science*, vol. 43, no. 1-4, pp. 30–59, 1993.

[13] E. J. W. Verwey, "Theory of the stability of lyophobic colloids.," *The Journal of Physical Chemistry*, vol. 51, no. 3, pp. 631–636, 1947.

[14] C. Stubenrauch and R. V. Klitzing, "Disjoining pressure isotherms of thin liquid films - new concepts and perspectives," vol. 15, pp. R1197–R1232, 2003.

[15] Y. Zhang and V. Sharma, "Nanoridge formation and dynamics of stratification in micellar freestanding films," *Langmuir*, vol. 34, no. 3, pp. 1208–1217, 2018.

[16] S. Yilixiati, E. Wojcik, Y. Zhang, and V. Sharma, "Spinodal stratification in ultrathin micellar foam films," *Molecular Systems Design & Engineering*, vol. 4, no. 3, pp. 626–638, 2019.

[17] J. D. Berry, M. J. Neeson, R. R. Dagastine, D. Y. Chan, and R. F. Tabor, "Measurement of surface and interfacial tension using pendant drop tensiometry," *Journal of Colloid and Interface Science*, vol. 454, pp. 226–237, 2015.

[18] J.-C. Michel, L.-M. Riviere, and M.-N. Bellon-Fontaine, "Measurement of the wettability of organic materials in relation to water content by the capillary rise method," *European journal of soil science*, vol. 52, no. 3, pp. 459–467, 2001.

[19] A. Ward and L. Tordai, "Time-dependence of boundary tensions of solutions i. the role of diffusion in time-effects," *The Journal of Chemical Physics*, vol. 14, no. 7, pp. 453–461, 1946.

[20] H. Manikantan and T. M. Squires, "Surfactant dynamics: hidden variables controlling fluid flows," *Journal of Fluid Mechanics*, vol. 892, p. P1, 2020.

[21] J. Lu, I. Purcell, E. Lee, E. Simister, R. Thomas, A. Rennie, and J. Penfold, "The composition and structure of sodium dodecyl sulfate-dodecanol mixtures adsorbed at the air-water interface: a neutron reflection study," *Journal of Colloid and Interface science*, vol. 174, no. 2, pp. 441–455, 1995.

[22] V. Fainerman, D. Vollhardt, and G. Emrich, "Dynamics and phase transition in adsorbed monolayers of sodium dodecyl sulfate/dodecanol mixtures," *The Journal of Physical Chemistry B*, vol. 105, no. 19, pp. 4324–4330, 2001.

[23] M. Boussinesq, "Speed of the slow, uniform fall of a liquid spherical drop in a viscous fluid of lesser specific weight," *Ann. Chim. Phys*, vol. 29, pp. 364–371, 1913.

[24] L. Scriven, "Dynamics of a fluid interface equation of motion for newtonian surface fluids," *Chemical Engineering Science*, vol. 12, no. 2, pp. 98–108, 1960.

[25] J. Lopez and A. Hirsa, "Direct determination of the dependence of the surface shear and dilatational viscosities on the thermodynamic state of the interface: Theoretical foundations," *Journal of Colloid and Interface Science*, vol. 206, no. 1, pp. 231–239, 1998.

[26] J. T. Petkov, T. D. Gurkov, B. E. Campbell, and R. P. Borwankar, "Dilatational and shear elasticity of gel-like protein layers on air/water interface," *Langmuir*, vol. 16, no. 8, pp. 3703–3711, 2000.

[27] E. Aumaitre, D. Vella, and P. Cicuta, "On the measurement of the surface pressure in langmuir films with finite shear elasticity," *Soft Matter*, vol. 7, no. 6, pp. 2530–2537, 2011.

[28] Y. Couder, J. Chomaz, and M. Rabaud, "On the hydrodynamics of soap films," *Physica D: Nonlinear Phenomena*, vol. 37, no. 1, pp. 384–405, 1989.

[29] J. M. Chomaz and B. Cathalau, "Soap films as two dimensional classical fluids," vol. 41, p. 2243, 1990.

[30] J. M. Chomaz, "The dynamics of a viscous soap film with soluble surfactant," vol. 442, p. 387, 2001.

[31] M. v. d. Tempel, J. Lucassen, and E. Lucassen-Reynders, "Application of surface thermodynamics to gibbs elasticity," *The Journal of Physical Chemistry*, vol. 69, no. 6, pp. 1798–1804, 1965.

[32] B. Noskov and T. Zubkova, "Dilational surface properties of insoluble monolayers," *Journal of colloid and interface science*, vol. 170, no. 1, pp. 1–7, 1995.

[33] C. Barentin, C. Ybert, J.-M. Di Meglio, and J.-F. Joanny, "Surface shear viscosity of gibbs and langmuir monolayers," *Journal of Fluid Mechanics*, vol. 397, p. 331–349, 1999.

[34] W. Drenckhan, H. Ritacco, A. Saint-Jalmes, A. Saugey, P. McGuinness, A. van der Net, D. Langevin, and D. Weaire, "Fluid dynamics of rivulet flow between plates," *Physics of Fluids*, vol. 19, p. 102101, 10 2007.

[35] H. A. Stone, "Interfaces: in fluid mechanics and across disciplines," *Journal of Fluid Mechanics*, vol. 645, p. 1–25, 2010.

[36] Z. A. Zell, A. Nowbahar, V. Mansard, L. G. Leal, S. S. Deshmukh, J. M. Mecca, C. J. Tucker, and T. M. Squires, "Surface shear inviscidity of soluble surfactants," *Proceedings of the National Academy of Sciences*, vol. 111, no. 10, pp. 3677–3682, 2014.

[37] I. Langmuir, "The constitution and fundamental properties of solids and liquids. ii. liquids.," *Journal of the American chemical society*, vol. 39, no. 9, pp. 1848–1906, 1917.

[38] K. B. Blodgett, "Films built by depositing successive monomolecular layers on a solid surface," *Journal of the American Chemical Society*, vol. 57, no. 6, pp. 1007–1022, 1935.

[39] A. Renault, J.-F. Rioux-Dube, T. Lefevre, S. Pezennec, S. Beaufils, V. Vie, M. Tremblay, and M. Pezolet*, "Surface properties and conformation of nephila clavipes spider recombinant silk proteins at the air- water interface," *Langmuir*, vol. 25, no. 14, pp. 8170–8180, 2009.

[40] D. Vollhardt, V. Fainerman, and G. Emrich, "Dynamic and equilibrium surface pressure of adsorbed dodecanol monolayers at the air/water interface," *The Journal of Physical Chemistry B*, vol. 104, no. 35, pp. 8536–8543, 2000.

[41] J. Fang and P. Joos, "The dynamic surface tension of sds—dodecanol mixtures: 1. the submicellarsystems," *Colloids and surfaces*, vol. 65, no. 2-3, pp. 113–120, 1992.

[42] J. P. Fang and P. Joos, "The dynamic surface tension of SDS- dodecanol mixtures. 2. Micellar SDS-dodecanol mixtures," *Colloids and Surfaces*, vol. 65, no. 2-3, pp. 121–129, 1992.

[43] P.-G. de Gennes, ""young" soap films," *Langmuir*, vol. 17, no. 8, pp. 2416–2419, 2001.

[44] G. I. Taylor, "The dynamics of thin sheets of fluid. iii. disintegration of fluid sheets," vol. 253, no. 1259, pp. 313 – 321, 1959.

[45] F. E. C. Culick, "Comments on a ruptured soap film.," vol. 31, p. 1128, 1960.

[46] H. Lhuissier and E. Villermaux, "Bursting bubble aerosols," vol. 696, pp. 5–44, 2012.

[47] K. Mysels, "Shinoda, I (., and frankel, s.,"," *Soap films. Study of their thinning and a bibliography." Pergamon, London*, 1959.

[48] K. J. Mysels and M. C. Cox, "An experimental test of frankel's law of film thickness," *Journal of Colloid Science*, vol. 17, no. 2, pp. 136–145, 1962.

[49] K. J. Mysels, "Dynamic processes in soap films," *The Journal of general physiology*, vol. 52, no. 1, pp. 113–124, 1968.

[50] A. Prins and M. Van den Tempel, "Composition and elasticity of thin liquid films," *The Journal of Physical Chemistry*, vol. 73, no. 9, pp. 2828–2834, 1969.

[51] J. Seiwert, B. Dollet, and I. Cantat, "Theoretical study of the generation of soap films: role of interfacial visco-elasticity," *Journal of Fluid Mechanics*, vol. 739, p. 124–142, 2014.

[52] L. Champougny, B. Scheid, F. Restagno, J. Vermant, and E. Rio, "Surfactant-induced rigidity of interfaces: a unified approach to free and dip-coated films," *Soft matter*, vol. 11, no. 14, pp. 2758–2770, 2015.

[53] A. Bérut and I. Cantat, "Marangoni stress induced by rotation frustration in a liquid foam," *Soft Matter*, vol. 15, no. 7, pp. 1562–1570, 2019.

[54] A. Oron, S. H. Davis, and S. G. Bankoff, "Long-scale evolution of thin liquid films," vol. 69, no. 3, p. 931, 1997.

[55] C. J. W. Breward and P. D. Howell, "The drainage of a foam lamella," vol. 458, pp. 379–406, 2002.

[56] L. Landau and B. Levich, "Dragging of a liquid by a moving plate," in *Dynamics of curved fronts*, pp. 141–153, Elsevier, 1988.

[57] J. D. McGraw, T. Salez, O. Bäumchen, E. Raphaël, and K. Dalnoki-Veress, "Self-similarity and energy dissipation in stepped polymer films," vol. 109, no. 12, p. 128303, 2012.

[58] A. Aradian, E. Raphaël, and P.-G. de Gennes, ""marginal pinching" in soap films," *Europhysics Letters*, vol. 55, p. 834, sep 2001.

[59] E. Chatzigiannakis, P. Veenstra, D. ten Bosch, and J. Vermant, "Mimicking coalescence using a pressure-controlled dynamic thin film balance," vol. 16, pp. 9410–9422, 2020.

[60] E. Chatzigiannakis, N. Jaensson, and J. Vermant, "Thin liquid films: Where hydrodynamics, capillarity, surface stresses and intermolecular forces meet," *Current Opinion in Colloid & Interface Science*, vol. 53, p. 101441, 2021.

[61] I. U. Vakarelski, R. Manica, X. Tang, S. J. O'Shea, G. W. Stevens, F. Grieser, R. R. Dagastine, and D. Y. C. Chan, "Dynamic interactions between microbubbles in water," vol. 107, no. 25, pp. 11177–11182, 2010.

[62] S. I. Karakashev and E. D. Manev, "Hydrodynamics of thin liquid films: Retrospective and perspectives," *Advances in colloid and interface science*, vol. 222, pp. 398–412, 2015.

[63] P. Howell and H. A. Stone, "On the absence of marginal pinching in thin free films," *European Journal of Applied Mathematics*, vol. 16, no. 5, pp. 569–582, 2005.

[64] R. Bruinsma, "Theory of hydrodynamic convection in soap films," *Physica A: Statistical Mechanics and its Applications*, vol. 216, no. 1, pp. 59–76, 1995.

[65] V. A. Nierstrasz and G. Frens, "Marangoni flow driven instabilities and marginal regeneration," vol. 234, no. 1, pp. 162 – 167, 2001.

[66] C. Trégouët and I. Cantat, "Instability of the one-dimensional thickness profile at the edge of a horizontal foam film and its plateau border," *Phys. Rev. Fluids*, vol. 6, p. 114005, Nov 2021.

[67] J. Miguet, M. Pasquet, F. Rouyer, Y. Fang, and E. Rio, "Marginal regeneration-induced drainage of surface bubbles," *Physical Review Fluids*, vol. 6, no. 10, p. L101601, 2021.

[68] E. Shabalina, A. Bérut, M. Cavelier, A. Saint-Jalmes, and I. Cantat, "Rayleigh-taylor-like instability in a foam film," *Phys. Rev. Fluids*, vol. 4, p. 124001, Dec 2019.

[69] L. Champougny, J. Miguet, R. Henaff, F. Restagno, F. Boulogne, and E. Rio, "Influence of evaporation on soap film rupture," *Langmuir*, vol. 34, no. 10, pp. 3221–3227, 2018.

[70] J. A. F. Plateau, *Statique expérimentale et théorique des liquides soumis aux seules forces moléculaires*, vol. 2. Gauthier-Villars, 1873.

[71] F. J. Almgren and J. E. Taylor, "The geometry of soap films and soap bubbles," *Scientific American*, vol. 235, no. 1, pp. 82–93, 1976.

[72] S. A. Khan and R. C. Armstrong, "Rheology of foams: Ii. effects of polydispersity and liquid viscosity for foams having gas fraction approaching unity," *Journal of Non-Newtonian Fluid Mechanics*, vol. 25, no. 1, pp. 61–92, 1987.

[73] D. Buzza, C.-Y. Lu, and M. E. Cates, "Linear shear rheology of incompressible foams," vol. 5, pp. 37 – 52, 1995.

[74] D. Weaire and J. Kermode, "The evolution of the structure of a two-dimensional soap froth," *Philosophical Magazine B*, vol. 47, no. 3, pp. L29–L31, 1983.

[75] H. Princen, "Rheology of foams and highly concentrated emulsions: I. elastic properties and yield stress of a cylindrical model system," *Journal of Colloid and interface science*, vol. 91, no. 1, pp. 160–175, 1983.

[76] A. M. Kraynik, "Foam flows," *Annual Review of Fluid Mechanics*, vol. 20, no. 1, pp. 325–357, 1988.

[77] A. L. Biance, S. Cohen-Addad, and R. Höhler, "Topological transition dynamics in a strained bubble cluster," vol. 5, pp. 4672 – 4679, 2009.

[78] S. Besson and G. Debrégeas, "Statics and dynamics of adhesion between two soap bubbles," *The European Physical Journal E*, vol. 24, pp. 109–117, Oct 2007.

[79] M. Fortes and P. Teixeira, "Triple-line decoration and line tension in simple three-dimensional foam clusters," *Physical Review E*, vol. 71, no. 5, p. 051404, 2005.

[80] J. Lucassen, "Adsorption kinetics in micellar systems," *Faraday Discussions of the Chemical Society*, vol. 59, pp. 76–87, 1975.

[81] J. Lucassen and M. Van Den Tempel, "Dynamic measurements of dilational properties of a liquid interface," *Chemical Engineering Science*, vol. 27, no. 6, pp. 1283–1291, 1972.

[82] R. I. Saye and J. A. Sethian, "Multiscale modeling of membrane rearrangement, drainage, and rupture in evolving foams," vol. 340, no. 6133, pp. 720–724, 2013.

[83] S. Ishida, P. Synak, F. Narita, T. Hachisuka, and C. Wojtan, "A model for soap film dynamics with evolving thickness," *ACM Transactions on Graphics (TOG)*, vol. 39, no. 4, pp. 31–1, 2020.

[84] N. D. Denkov, S. Tcholakova, K. Golemanov, K. P. Ananthapadmanabhan, and A. Lips, "Viscous friction in foams and concentrated emulsions under steady shear," vol. 100, p. 138301, 2008.

[85] S. Cohen-Addad, R. Höhler, and Y. Khidas, "Origin of the slow linear viscoelastic response of aqueous foams," vol. 93, p. 028302, 2004.

[86] K. Krishan, A. Helal, R. Höhler, and S. Cohen-Addad, "Fast relaxations in foam," *Phys. Rev. E*, vol. 82, p. 011405, 2010.

[87] S. Costa, S. Cohen-Addad, A. Salonen, and R. Höhler, "The dissipative rheology of bubble monolayers," vol. 9, no. 3, pp. 886–895, 2013.

[88] F. Elias, J. Crassous, C. Derec, B. Dollet, W. Drenckhan, C. Gay, V. Leroy, C. Noûs, J. Pierre, and A. Saint-Jalmes, "The acoustics of liquid foams," *Current Opinion in Colloid & Interface Science*, vol. 50, p. 101391, 2020.

[89] H. Lhuissier and E. Villermaux, "Soap films burst like flapping flags," *Physical review letters*, vol. 103, no. 5, p. 054501, 2009.

[90] R. Höhler and S. Cohen-Addad, "Rheology of liquid foam," *Journal of Physics: Condensed Matter*, vol. 17, no. 41, p. R1041, 2005.

[91] A. Saint-Jalmes and C. Trégouët, "Foam coarsening under a steady shear: interplay between bubble rearrangement and film thinning dynamics," *Soft Matter*, vol. 19, no. 11, pp. 2090–2098, 2023.

[92] L. Braun, M. Kühnhammer, and R. von Klitzing, "Stability of aqueous foam films and foams containing polymers: Discrepancies between different length scales," *Current Opinion in Colloid & Interface Science*, vol. 50, p. 101379, 2020.

[93] G. Czichocki, D. Vollhardt, and H. Much, "Determination of dodecanol traces in sodium dodecyl sulfate," *Journal of colloid and interface science*, vol. 95, no. 1, pp. 275–276, 1983.

[94] D. Bethell, R. E. Fessey, E. Namwindwa, and D. W. Roberts, "The hydrolysis of c 12 primary alkyl sulfates in concentrated aqueous solutions. part 1. general features, kinetic form and mode of catalysis in sodium dodecyl sulfate hydrolysis," *Journal of the Chemical Society, Perkin Transactions 2*, no. 9, pp. 1489–1495, 2001.

[95] P. Joos and H. Deelstra, "Effect of minor components on the surface tension of micellar dodecyl sulfate solutions," *Bulletin des Sociétés Chimiques Belges*, vol. 84, no. 3, pp. 189–195, 1975.

[96] D. Vollhardt and G. Czichocki, "Effect of isomeric alcohols as a minor component on the adsorption properties of aqueous sodium alkyl sulfate solutions," *Langmuir*, vol. 6, no. 2, pp. 317–322, 1990.

[97] D. Vollhardt and G. Emrich, "Coadsorption of sodium dodecyl sulfate and medium-chain alcohols at the air–water interface," *Colloids and Surfaces A: Physicochemical and Engineering Aspects*, vol. 161, no. 1, pp. 173–182, 2000.

[98] A. Rahman and C. Brown, "Effect of ph on the critical micelle concentration of sodium dodecyl sulphate," *Journal of Applied Polymer Science*, vol. 28, no. 4, pp. 1331–1334, 1983.

[99] T. Lenavetier, G. Audéoud, M. Berry, A. Gauthier, R. Poryles, C. Trégouët, and I. Cantat, "Line tension in a thick soap film," *(preprint)*, 2023.

[100] M. Pasquet, F. Restagno, I. Cantat, and E. Rio, "Thickness profiles of giant soap films," *Physical Review Fluids*, vol. 8, no. 3, p. 034001, 2023.

[101] F. Seychelles, Y. Amarouchene, M. Bessafi, and H. Kellay, "Thermal convection and emergence of isolated vortices in soap bubbles," *Phys. Rev. Lett.*, vol. 100, p. 144501, Apr 2008.

[102] G. Sefler, Q. Du, P. Miranda, and Y. Shen, "Surface crystallization of liquid n-alkanes and alcohol monolayers studied by surface vibrational spectroscopy," *Chemical Physics Letters*, vol. 235, no. 3, pp. 347–354, 1995.

[103] P. G. Saffman, "Brownian motion in thin sheets of viscous fluid," *Journal of Fluid Mechanics*, vol. 73, no. 4, pp. 593–602, 1976.

[104] B. D. Hughes, B. A. Pailthorpe, and L. R. White, "The translational and rotational drag on a cylinder moving in a membrane," *Journal of Fluid Mechanics*, vol. 110, p. 349–372, 1981.

[105] H. A. Stone and A. Ajdari, "Hydrodynamics of particles embedded in a flat surfactant layer overlying a subphase of finite depth," vol. 369, pp. 151–173, 1998.

[106] J. Seiwert, R. Kervil, S. Nou, and I. Cantat, "Velocity field in a vertical foam film," *Phys. Rev. Lett.*, vol. 118, p. 048001, Jan 2017.

[107] A. Gros, A. Bussonnière, S. Nath, and I. Cantat, "Marginal regeneration in a horizontal film: Instability growth law in the nonlinear regime," *Phys. Rev. Fluids*, vol. 6, p. 024004, Feb 2021.

[108] L. D. Landau and E. M. Lifshitz, *Fluid Mechanics: Landau and Lifshitz: Course of Theoretical Physics, Volume 6*, vol. 6. Elsevier, 2013.

[109] E. Glötzl and O. Richters, "Helmholtz decomposition and rotation potentials in n-dimensional cartesian coordinates," 12 2020.

Université de Rennes

Titre : Mouvements aux interfaces de mousses liquides élémentaires

Mots clés : films de savon, mousses liquides, surfactants, rhéologie de surface, tension de ligne, interfaces liquides

Résumé : Les modèles physiques visant à prédire les propriétés mécaniques et rhéologiques des mousses liquides sont encore en développement. Une échelle locale pertinente pour attaquer ce problème du point de vue hydrodynamique est la mousse liquide élémentaire : quelques films de savon reliés entre eux par un ou deux ménisques. Ces travaux portent sur les écoulements dans de tels systèmes, plus précisément sur les mouvements dans les plans de ses différents films de savon. Il comporte essentiellement trois contributions.

La première porte sur le comportement élastique individuel des films sous étirement. Nous avons étendu un modèle connu à une gamme de chimie plus large et plus commune, et avons pu mesurer les modules élastiques effectifs de nos solutions.

La seconde porte sur la mise en évidence et la quantification d'une tension de ligne d'origine purement capillaire dans le plan d'un film de savon d'épaisseur hétérogène. En modélisant les mouvements de relaxation dans le plan du film de savon, nous validons cette mesure inédite par un accord quantitatif avec la dynamique observée.

Enfin, la troisième contribution porte sur les échanges de surfactants entre films de savon voisins lorsque la mousse élémentaire est soumise à une contrainte mécanique. Le résultat principal de cette partie, et de cette thèse, est que le ménisque séparant les films n'intervient pas dans cet échange. Ceci est une information importante qui permet de fermer un modèle théorique préexistant qui vise à prédire la viscosité effective des mousses liquides.

Title : Interfaces in motion in elementary liquid foams

Keywords : soap films, liquid foams, surfactants, surface rheology, line tension, liquid interfaces

Abstract : Models aiming to predict the mechanical and rheological properties of liquid foams are still under development. A relevant local scale to tackle this issue from a hydrodynamic perspective is the elementary liquid foam: a few foam films connected by one or two menisci. This work focuses on flows in such systems, specifically on movements within the planes of their foam films. It comprises three main contributions.

The first focuses on the individual elastic behaviour of films under stretching. We extended a known model to a broader and more common chemical range and were able to measure the effective elastic moduli of our solutions.

The second highlights and quantifies a line tension of purely capillary origin within the plane of a foam film with heterogeneous thickness. By modelling the relaxation movements within the plane of the foam film, we validate this novel measurement through a quantitative agreement with the observed dynamics.

Finally, the third contribution addresses surfactant exchanges between foam films when the elementary foam undergoes mechanical constraint. The main result of this part, and of this thesis, is that the meniscus separating the films does not play any role in this exchange. This is crucial information to close an existing theoretical model aiming to predict the effective viscosity of liquid foams.